

Deep Near-Infrared Spectroscopy of High-Redshift Galaxies: the Physical Growth of Passive Systems

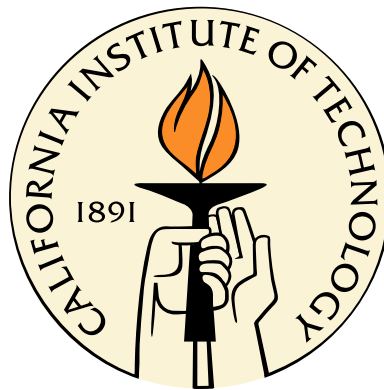
Thesis by

Sirio Belli

In Partial Fulfillment of the Requirements

for the Degree of

Doctor of Philosophy



California Institute of Technology

Pasadena, California

2016

(Defended July 21, 2015)

*A Kristen,
per gli sprazzi di bellezza*

Acknowledgments

Richard Ellis, the best advisor I could have asked for. His enthusiasm for pure research and love for adventure inspired me to become an astronomer and continue to inspire me every day. He also is *il miglior fabbro* – without his editing this thesis would have been twice as long and half as clear.

Drew Newman, who taught me everything I always wanted to know but I was afraid to ask about quiescent galaxies, and went from being a mentor to a colleague to a friend. Tucker Jones, who guided me through my first nights at Palomar – a truly mystical experience.

The incredibly friendly and efficient staff at Keck and Caltech – special thanks to Judy McClain and Gita Patel.

The friends at Caltech with which I shared the journey. Mislav, Antonija, Allison, Gwen, Ryan, Swarnima, Teja, Amir, Ben, Sebastian, Jackie, Howard, Anna, Masha, and many others.

The traditions of the astronomy department. The ski trips to Mammoth, the Halloween parties, the celebrations at the Ath, the softball games. Monday wine and cheese, Tuesday tea, Wednesday colloquium, Thursday donuts, Friday beer. Espresso after lunch. A ping-pong game, every single day.

Los Angeles. The 2 to the 134 every morning, the 110 at night. Vermont between Franklin and Hollywood. The Vista, the Los Feliz, the Laemmle, the Arclight, and the Egyptian.

The old friends. Andrea Civitarese. Filo, Zà, Marty. Chiara Daraio, for having brought me to Caltech the first time.

Michael Bottom for (or despite?) five years of office sharing. Trevor David for disagreeing with me on everything, every time. Federico Tadei for the nights out. Saman Saeedi and Matt Schenker for all sorts of things, including many Sundays on the golf course.

My parents for their unconditional support throughout the last 29 years.

And, above all, Kristen Boydston.

Abstract

The assembly history of massive galaxies is one of the most important aspects of galaxy formation and evolution. Although we have a broad idea of what physical processes govern the early phases of galaxy evolution, there are still many open questions. In this thesis I demonstrate the crucial role that spectroscopy can play in a physical understanding of galaxy evolution. I present deep near-infrared spectroscopy for a sample of high-redshift galaxies, from which I derive important physical properties and their evolution with cosmic time. I take advantage of the recent arrival of efficient near-infrared detectors to target the rest-frame optical spectra of $z > 1$ galaxies, from which many physical quantities can be derived. After illustrating the applications of near-infrared deep spectroscopy with a study of star-forming galaxies, I focus on the evolution of massive quiescent systems.

Most of this thesis is based on two samples collected at the W. M. Keck Observatory that represent a significant step forward in the spectroscopic study of $z > 1$ quiescent galaxies. All previous spectroscopic samples at this redshift were either limited to a few objects, or much shallower in terms of depth. Our first sample is composed of 56 quiescent galaxies at $1 < z < 1.6$ collected using the upgraded red arm of the Low Resolution Imaging Spectrometer (LRIS). The second consists of 24 deep spectra of $1.5 < z < 2.5$ quiescent objects observed with the Multi-Object Spectrometer For Infra-Red Exploration (MOSFIRE). Together, these spectra span the critical epoch $1 < z < 2.5$, where most of the red sequence is formed, and where the sizes of quiescent systems are observed to increase significantly.

We measure stellar velocity dispersions and dynamical masses for the largest number of $z > 1$ quiescent galaxies to date. By assuming that the velocity dispersion of a massive galaxy does not change throughout its lifetime, as suggested by theoretical studies, we match galaxies in the local universe with their high-redshift progenitors. This allows us to derive the *physical* growth in mass and size experienced by individual systems, which represents a substantial advance over photometric inferences based on the overall galaxy population. We find a significant physical growth among quiescent galaxies over $0 < z < 2.5$ and, by comparing the slope of growth in the mass-size plane $d \log R_e / d \log M_*$ with the results of numerical simulations, we can constrain the physical process responsible for the evolution. Our results show that the slope of growth becomes steeper at higher

redshifts, yet is broadly consistent with minor mergers being the main process by which individual objects evolve in mass and size.

By fitting stellar population models to the observed spectroscopy and photometry we derive reliable ages and other stellar population properties. We show that the addition of the spectroscopic data helps break the degeneracy between age and dust extinction, and yields significantly more robust results compared to fitting models to the photometry alone. We detect a clear relation between size and age, where larger galaxies are younger. Therefore, over time the average size of the quiescent population will increase because of the contribution of large galaxies recently arrived to the red sequence. This effect, called *progenitor bias*, is different from the physical size growth discussed above, but represents another contribution to the observed difference between the typical sizes of low- and high-redshift quiescent galaxies. By reconstructing the evolution of the red sequence starting at $z \sim 1.25$ and using our stellar population histories to infer the past behavior to $z \sim 2$, we demonstrate that progenitor bias accounts for only half of the observed growth of the population. The remaining size evolution must be due to physical growth of individual systems, in agreement with our dynamical study.

Finally, we use the stellar population properties to explore the earliest periods which led to the formation of massive quiescent galaxies. We find tentative evidence for two channels of star formation quenching, which suggests the existence of two independent physical mechanisms. We also detect a mass downsizing, where more massive galaxies form at higher redshift, and then evolve passively. By analyzing in depth the star formation history of the brightest object at $z > 2$ in our sample, we are able to put constraints on the quenching timescale and on the properties of its progenitor.

A consistent picture emerges from our analyses: massive galaxies form at very early epochs, are quenched on short timescales, and then evolve passively. The evolution is passive in the sense that no new stars are formed, but significant mass and size growth is achieved by accreting smaller, gas-poor systems. At the same time the population of quiescent galaxies grows in number due to the quenching of larger star-forming galaxies. This picture is in agreement with other observational studies, such as measurements of the merger rate and analyses of galaxy evolution at fixed number density.

Contents

Acknowledgments	v
Abstract	vi
1 Introduction	1
1.1 Quiescent Galaxies in the Local Universe	1
1.1.1 Dynamics	2
1.1.2 Stellar Populations	5
1.1.3 How did Quiescent Galaxies Form?	8
1.2 Quiescent Galaxies at High Redshift	9
1.2.1 The Evolution over $0 < z < 1$	9
1.2.2 Galaxies at $z > 1$: the Redshift Desert	11
1.2.3 The Size Evolution of Quiescent Galaxies	12
1.2.4 Open Questions	16
1.3 Goals of this Thesis	16
2 Testing the Universality of the Fundamental Metallicity Relation at High Redshift Using Low-Mass Gravitationally Lensed Galaxies	18
Abstract	18
2.1 Introduction	19
2.2 Data	21
2.2.1 Sample Selection	21
2.2.2 Spectroscopy	23
2.2.3 Imaging	27
2.2.3.1 Archival Data	27
2.2.3.2 Palomar Observations	27
2.3 Properties of Stellar Populations	27
2.3.1 Photometry	27
2.3.2 SED Fitting	28

2.4	Spectroscopic Diagnostics	31
2.4.1	Dust Extinction	31
2.4.2	Lack of AGN Contribution	33
2.4.3	Metallicities	33
2.4.4	Star Formation Rates	37
2.4.5	Line Widths	38
2.5	Results	38
2.5.1	The Mass–Metallicity Relation	38
2.5.2	Star Formation Rate versus Stellar Mass	40
2.5.3	The Fundamental Metallicity Relation	41
2.5.4	The Scatter in the Fundamental Metallicity Relation	42
2.6	Discussion	43
2.7	Summary	44
3	Velocity Dispersions and Dynamical Masses for a Large Sample of Quiescent Galaxies at $z > 1$: Improved Measures of the Growth in Mass and Size	46
	Abstract	46
3.1	Introduction	47
3.2	Data	49
3.2.1	Sample Selection	49
3.2.2	Spectroscopic Observations and Data Reduction	50
3.2.3	Auxiliary Data	51
3.2.4	SDSS Data	51
3.2.5	Selecting Quiescent Galaxies	54
3.3	Physical properties of the sample	55
3.3.1	Size Measurement	59
3.3.2	SED fitting	59
3.3.3	Velocity Dispersions	61
3.4	Dynamical Masses	62
3.4.1	The Stellar Mass-Dynamical Mass Relation	64
3.4.2	The Redshift Evolution of the Mass Ratio	64
3.4.3	Testing Inferred Velocity Dispersions	66
3.5	The size growth of quiescent galaxies	67
3.5.1	The Progenitor Bias	67
3.5.2	Evolution at Fixed Velocity Dispersion	68
3.5.2.1	The Evolution of Dynamical and Stellar Masses	70

3.5.2.2	Inferring the Size Growth	72
3.5.3	Evolution at Fixed Ranking in Velocity Dispersion	74
3.6	Summary and Discussion	75
Appendix 3.A	Photometric Data	78
Appendix 3.B	Galaxy Structure and Dynamical Masses	79
4	Stellar Populations from Spectroscopy of a Large Sample of Quiescent Galaxies at $z > 1$: Measuring the Contribution of Progenitor Bias to Early Size Growth	82
	Abstract	82
4.1	Introduction	83
4.2	Data	85
4.3	Derivation of Physical Properties	87
4.3.1	Stellar Populations	87
4.3.2	[OII] Emission	89
4.4	The Red Sequence	91
4.4.1	Diversity among Quiescent Galaxies	92
4.4.2	Reconstructing the Quiescent Population	94
4.5	Size Evolution on the Red Sequence	98
4.5.1	The Size-Age Relation	98
4.5.2	The Contribution of Progenitor Bias to the Size Growth	99
4.6	Summary and Discussion	101
4.6.1	Two Pathways to Quenching?	102
Appendix 4.A	The Spectroscopic Sample is Unbiased	104
5	New MOSFIRE Spectroscopy of Quiescent Galaxies at $1.5 < z < 2.5$. Evolution of Stellar Populations and Dynamical Properties	109
	Abstract	109
5.1	Introduction	110
5.2	Data	113
5.2.1	Target Selection and Ancillary Data	113
5.2.2	MOSFIRE Spectroscopy	113
5.3	Physical Properties	117
5.3.1	Structural Properties	117
5.3.2	Velocity Dispersions	118
5.3.3	Stellar Populations	118
5.3.4	Emission Lines	119
5.3.5	AGN activity in 35616	121

5.4	Dynamical Analysis	121
5.4.1	The Stellar-to-Dynamical Mass Ratio	123
5.4.2	Galaxy Evolution at Fixed Velocity Dispersion	124
5.5	Analysis of the Stellar Populations	126
5.5.1	The Ages of High-Redshift Quiescent Galaxies	126
5.5.2	Constraining the Recent Star Formation Activity of a Massive Galaxy at $z = 2.09128$	
5.6	Summary and Discussion	131
6	Conclusions and Future Work	134
6.1	The Growth of Massive Galaxies	134
6.2	The Formation and Quenching of the First Galaxies	137
6.3	Future Work	140

List of Figures

1.1	The fundamental plane	3
1.2	The color-magnitude relation	6
1.3	Redshift evolution of the fundamental plane	10
1.4	Mass - size relation at $z \sim 2$	13
1.5	Absorption line spectrum of a $z = 2.19$ quiescent galaxies	15
2.1	<i>HST</i> image stamp, Triplespec spectrum, and SED fit for each gravitational arc	24
2.1	Continued.	25
2.1	Continued.	26
2.2	Dust extinction $E(B - V)$	34
2.3	BPT diagram	34
2.4	Gas metallicity derived from emission line flux ratios	36
2.5	Comparison of SFR derived from $H\alpha$ and from SED fitting	37
2.6	Mass-metallicity relation	39
2.7	Star formation rate versus stellar mass	39
2.8	Observations vs. prediction of the fundamental metallicity relation	41
3.1	Redshift distribution of the sample	50
3.2	LRIS spectra and <i>HST</i> cutouts	52
3.2	Continued.	53
3.3	Selection of the quiescent subsample in the <i>UVJ</i> diagram	55
3.4	Mass-size relation	60
3.5	Stellar mass vs. dynamical mass	63
3.6	Distribution of sizes, stellar masses, and velocity dispersions	63
3.7	Evolution of the stellar-to-dynamical mass ratio	65
3.8	Inferred vs. observed velocity dispersions	66
3.9	Velocity dispersion vs. effective radius	69
3.10	Stellar-to-dynamical mass ratio vs. velocity dispersion	70
3.11	Matching galaxies at fixed velocity dispersion	72

3.12	Matching galaxies at fixed ranking in velocity dispersion	74
3.13	Stellar vs. dynamical mass as a function of morphology	80
3.14	Inferred vs. observed velocity dispersions as a function of morphology	80
4.1	Illustration of the spectral fitting technique	86
4.2	Illustration of the posterior distributions	88
4.3	Comparison of star formation rates	89
4.4	Distribution of stellar population parameters on the UVJ plane	90
4.5	The τ - age plane	92
4.6	Stacked LRIS spectra	93
4.7	Reconstructed evolution on the UVJ diagram	95
4.8	Reconstructed number density evolution	96
4.9	Relation between mass, size, and age	97
4.10	Reconstructed evolution of the average size	99
4.11	Comparison between the properties of the LRIS sample and the 3D-HST reference sample	105
5.1	MOSFIRE spectra of $1.5 < z < 2.5$ quiescent galaxies	116
5.2	UVJ diagram for the MOSFIRE sample	117
5.3	$H\alpha$ emission in a quiescent galaxies	120
5.4	Absorption and emission lines in a quiescent galaxies	120
5.5	Physical properties of the MOSFIRE sample	122
5.6	Redshift evolution of the stellar-to-dynamical mass ratio	123
5.7	Evolution of quiescent galaxies in the mass-size plane	125
5.8	Galaxy age vs. age of the universe	127
5.9	Galaxy age vs. age of the universe, by stellar mass	127
5.10	Spectral fit to COSMOS-31719	129
5.11	Posterior distribution for the age and intensity of the burst for COSMOS-31719 . . .	130
6.1	Inside-out growth of massive galaxies	136
6.2	Velocity dispersions vs stellar mass for compact star-forming and quiescent galaxies .	138
6.3	Sub-millimeter galaxies and red nuggets: distribution in star formation rates	140
6.4	A gravitationally-lensed compact quiescent galaxy	142
6.5	Simulated Keck NIRES spectrum.	143

List of Tables

2.1	Sample of Gravitational Arcs	22
2.2	TripleSpec Observations	22
2.3	Emission Line Fluxes	30
2.4	Physical Properties of the Sample of Star-Forming Galaxies	32
3.1	LRIS Observations	50
3.2	Physical Properties of the Sample of Quiescent Galaxies	56
3.2	Physical Properties of the Sample of Quiescent Galaxies	57
3.2	Physical Properties of the Sample of Quiescent Galaxies	58
4.1	Stellar Population Properties of the Sample of Quiescent Galaxies	106
4.1	Stellar Population Properties of the Sample of Quiescent Galaxies	107
4.1	Stellar Population Properties of the Sample of Quiescent Galaxies	108
5.1	MOSFIRE Observations	114

Chapter 1

Introduction

Soon after obtaining the first conclusive measurements of the distance to nearby galaxies (Hubble, 1925), thus confirming their extragalactic nature, Edwin Hubble noticed that galaxies can be divided into different types according to their appearance, and eventually proposed his famous tuning-fork diagram (Hubble, 1936). He speculated that elliptical and lenticular galaxies represent an early stage, while spirals (with and without bars) are the late stage in the same evolutionary sequence. Although this simple scenario proved to be wrong, the names early-type and late-type are still used today to classify galaxy morphology.

The dichotomy in the observed morphology is only one aspect of a much deeper *bimodality* that has been later discovered in the distribution of many important physical properties of local galaxies (starting from Baade, 1944). Most notably, the distributions of colors, surface brightness, and star formation rate are all clearly bimodal (e.g., Blanton et al., 2003; Driver et al., 2006; Noeske et al., 2007). Typically, early-type galaxies are red, have high Sérsic (1963) index, and are quiescent (meaning that their star-formation rate is low), while late-type galaxies are blue, with low Sérsic index and high star formation rate.

While star-forming galaxies are characterized by a large amount of gas, which is responsible for prominent emission lines in their optical spectra, quiescent galaxies are mainly composed of stars and dark matter, and their spectra show numerous absorption features. In the present work we will mainly focus on the evolution and formation of quiescent galaxies.

1.1 Quiescent Galaxies in the Local Universe

One of the most important components of galaxies is their stellar content. Besides the physical properties of individual stars such as age and metallicity, stellar populations are also characterized by their dynamical state. In particular, stellar orbits can be orderly distributed on a thin disk or be randomly distributed in the 3D space, or any combination of the two. Observing the spectrum of a galaxy in the appropriate wavelength range (typically optical and near-infrared) can shed light

on both sets of properties, and represents one of the most powerful tools for extragalactic studies.

Here we summarize the properties of local quiescent galaxies, focusing on both the dynamical state and the stellar population properties, and then we review the theoretical ideas that have been developed with the goal of understanding the formation and subsequent evolution of these systems.

1.1.1 Dynamics

For star-forming galaxies the main component of the motion of stars and gas is generally the circular velocity on a relatively thin disk. Early spectroscopic measurements led to the discovery of a tight correlation between the luminosity and the rotation velocity of disk galaxies (Tully & Fisher, 1977). At about the same time, the Faber & Jackson (1976) relation was discovered for elliptical galaxies, for which the luminosity correlates with velocity dispersion (which is a statistical measure of the typical velocity of stars in the galaxy) according to a power law: $L \propto \sigma^\alpha$. Initially the importance of these relations was due to their use as a way to measure distances. By measuring the velocity dispersion and the *apparent* luminosity, it is easy to derive the distance that makes the *absolute* luminosity in agreement with the Faber-Jackson relation. This type of measurement is possible because of the intrinsic tightness of the relation, which yields a small uncertainty on the derived distance.

Another scaling relation for elliptical galaxies discovered in these early investigations is the correlation between surface brightness and size: $I_e \propto R_e^{-\beta}$ (Kormendy, 1977), where R_e is the effective, or half-light, radius. This relation was, again, used mainly to derive distances, since it links a distance-independent quantity (the surface brightness) with one that scales with distance (the size). However, surface brightness is directly connected to luminosity L (in a given band):

$$I_e \equiv \frac{L}{2\pi R_e^2}. \quad (1.1)$$

It is easy to see, then, that the Faber-Jackson and the Kormendy relations are just two different projections of one three-dimensional relation between size, velocity dispersion, and luminosity. This relation has been observationally confirmed to be well described by a plane in the logarithmic space, called the *fundamental plane* (Djorgovski & Davis, 1987; Dressler et al., 1987):

$$\log R_e = a \log \sigma + b \log I_e + c. \quad (1.2)$$

This relation is remarkably tight and therefore represented an important method for measuring distances. Additionally, the small intrinsic scatter of this relation contains precious information on the formation and evolution of elliptical galaxies. Today the focus has shifted toward understanding the fundamental plane rather than just using it to determine distances. For this purpose, it is better

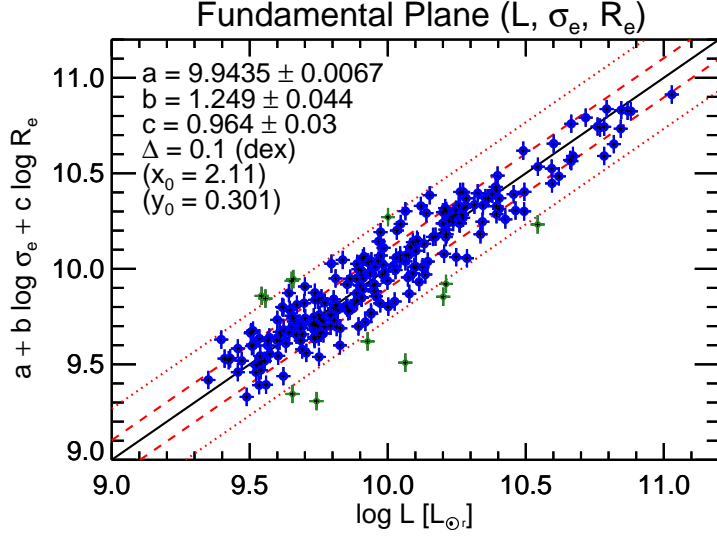


Figure 1.1 The fundamental plane of local quiescent galaxies, from Cappellari et al. (2013). The relation between luminosity and a combination of size and velocity dispersion is very tight, with an observed scatter of only 0.10 dex.

to write the relation in terms of luminosity rather than surface brightness:

$$\log L = A \log \sigma + B \log R_e + C . \quad (1.3)$$

Recent measurements (Cappellari et al., 2013), shown in Figure 1.1, yield the following result:

$$L \propto \sigma^{1.25} R_e^{0.96} . \quad (1.4)$$

Since its original discovery, the existence of a tight relation between these three physical properties of elliptical galaxies has been understood as a consequence of the virial theorem. For a system in equilibrium, the stellar kinetic energy T and the gravitational energy U satisfy the following equation:

$$2T + U = 0 . \quad (1.5)$$

We now make the simplifying assumption that the kinetic energy is related to the central velocity dispersion σ and the mass M by a simple relation:

$$T = C_K \frac{1}{2} M \sigma^2 , \quad (1.6)$$

and similarly the gravitational energy is simply related to the galaxy's mass and size:

$$U = -C_U \frac{GM^2}{R_e} . \quad (1.7)$$

Adopting these relations, the virial theorem becomes:

$$M = \frac{C_K C_U}{G} \sigma^2 R_e . \quad (1.8)$$

In order to compare the theoretical prediction with the observational results, we need to transform from mass to luminosity. We therefore define the mass-to-light ratio as

$$\Gamma \equiv \frac{M}{L} , \quad (1.9)$$

and we can rewrite Equation 1.8 as

$$L = \frac{C_K C_U}{G \Gamma} \sigma^2 R_e . \quad (1.10)$$

The parameters C_K , C_U , and Γ depend on the detailed properties of the stellar orbits and the stellar populations. If these properties are the same for all elliptical galaxies, independently on their size and mass, then we have a perfect *homology*, and the virial theorem implies $L \propto \sigma^2 R_e$. However, this prediction is significantly different from the observed fundamental plane (Equation 1.4). This discrepancy is often referred to as the *tilt* of the fundamental plane. Understanding the physical origin of this tilt has been the focus of a large number of theoretical and observational works (see Ciotti, 2009, for a review).

One way to reconcile the predicted relation with the observed fundamental plane is to assume that $C_K C_U$ varies smoothly with velocity dispersion. This type of weak homology implies that elliptical galaxies are not identical, scaled systems, but a one-dimensional family parameterized by the velocity dispersion. Physically, this might be caused by a variation of the density and pressure tensor distributions with galaxy mass (e.g., Ciotti et al., 1996; Bertin et al., 2002; Trujillo et al., 2004). A different approach, instead, is to assume that galaxies are structurally homologous, but the mass-to-light ratio Γ varies as a function of the velocity dispersion (e.g., Renzini & Ciotti, 1993). This could be achieved either by varying the stellar ages (and metallicities), or by allowing a non-universal initial mass function (IMF). Also, a systematically different dark matter contribution to the central density may be responsible for a smoothly varying mass-to-light ratio.

Recently, a consistent picture is emerging from observational studies. Using detailed 2D kinematic data and realistic dynamical modeling, Cappellari et al. (2006) measured the masses of nearby early-type galaxies and found that $\Gamma \propto \sigma^{0.84 \pm 0.07}$, which is exactly what is needed to explain the difference between the observed relation (Equation 1.4) and the theoretical one (Equation 1.10). This

result, which highlights the fundamental role of velocity dispersion in understanding the differences between early-type galaxies, has been confirmed by independent studies in which the masses were derived via strong gravitational lensing analysis (Bolton et al., 2007; Auger et al., 2010). Furthermore, by including dark matter in their dynamical models, Cappellari et al. (2013) showed that the mass-to-light ratio variation is not due to a different dark matter fraction, but to a change in the stellar population properties. This might be due to differences in age or IMF, with the latter being the explanation favored by an analysis of the observed colors.

Since dynamical non-homology has been shown not to be a significant contribution to the tilt of the fundamental plane, it is now common to refer to the *mass plane*, defined in the stellar mass - velocity dispersion - size space (Bolton et al., 2007; Cappellari et al., 2013) (however, for a different view see Taylor et al., 2010a). The mass plane is equivalent to a comparison of the stellar mass with the *dynamical mass*, defined as $M_{\text{dyn}} = K\sigma^2 R_e/G$. Cappellari et al. (2006) showed that adopting $K = 5$ this simple virial mass estimate reproduces very accurately the total mass derived with a detailed analysis of resolved kinematic data.

1.1.2 Stellar Populations

It has been known for a long time that elliptical galaxies present a relation between color and magnitude (Baum, 1959), and that if such relation is tight enough, it could be used to measure distances (Sandage, 1972). Brighter galaxies are redder, and this is generally attributed to a relation between metallicity and mass, since more massive galaxies are expected to retain a higher fraction of the metals formed by supernovae (e.g., Arimoto & Yoshii, 1987).

However, it was only with the landmark study of Bower et al. (1992) that the color-magnitude relation was first used to put quantitative constraints on the formation of early-type galaxies. First, the authors showed that precision photometry of the elliptical galaxies in the Virgo and Coma clusters revealed a remarkably tight sequence, with an intrinsic scatter (i.e., not due to observational errors) in the $U - V$ color smaller than 0.04 mag. The fact that the relation is identical in both clusters strongly suggests that such color-magnitude relation and its tightness are universal. Such uniformity in colors implies that galaxies of the same mass (or magnitude) must have formed in a similar way at a similar cosmic epoch.

In order to constrain the formation epoch, Bower et al. (1992) used the models from Bruzual (1983) to calculate the rate in the $U - V$ evolution as a function of the age t_F for a simple stellar population, shown in Figure 1.2. Clearly, the color evolution is very slow after a few Gyr from the initial burst. Assuming that the observed scatter in the color-magnitude relation is entirely due to a variation in formation time among different galaxies of a given mass, we can write

$$\text{observed scatter in } U - V = \frac{\partial(U - V)}{\partial t} \times \text{spread in formation times} . \quad (1.11)$$

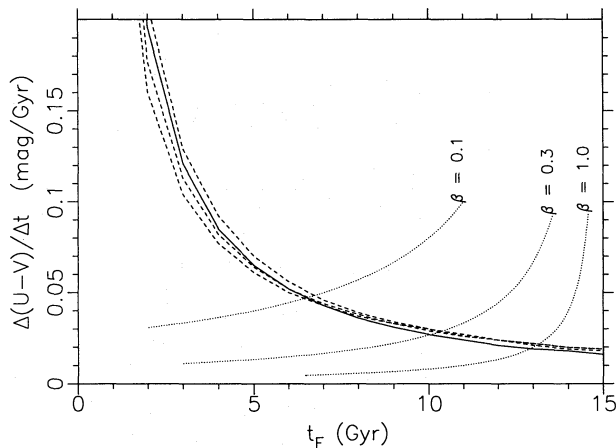


Figure 1.2 Evolution of the rate of change in color as a function of the stellar population age t_F (solid line), from Bower et al. (1992). The dashed lines represent the evolution for models with different IMF. After the first 5 Gyr, the $U - V$ color changes very little with time: less than 0.05 mag per Gyr. Assuming that galaxies at a given mass formed when the Universe had an age $t_H - t_F$ over a timescale given by $\beta(t_H - t_F)$, then the observed scatter constrains the formation time. The three thin dotted lines show the expected scatter for three values of β . The point where they intersect the thick line is the most recent lookback time at which galaxies could have formed. Note that the age of the universe is assumed to be $t_H = 15$ Gyr.

If we parameterize the scatter in formation times as a fraction β of the corresponding age of the universe (spread in formation times = $\beta(t_H - t_F)$, where t_H is the current age of the universe), and we use the observed value of 0.04 mag as an upper limit on the intrinsic scatter, we then obtain

$$\frac{\partial(U - V)}{\partial t} \times \beta(t_H - t_F) < 0.04 \text{ mag} . \quad (1.12)$$

The curves $0.04/\beta(t_H - t_F)$ are plotted in Figure 1.2 for three values of β . The points where these curves intersect the color evolution for a simple stellar population represent lower limits to the age of the quiescent population. For example, if galaxies formed randomly during an early epoch, then $\beta = 1$, and they must have formed over the very first few Gyr. If $\beta = 0.1$, on the other hand, then galaxy formation happened over a very short timescale, and the typical age can be much lower, around 5 Gyr.

The remarkable uniformity of the colors of quiescent galaxies represents an important constraint for models of galaxy formation and evolution; however, the study of broadband photometry has inherent limitations due to its poor spectral resolution. For example, red colors might be caused by dust extinction or old ages, and this degeneracy cannot be broken with photometric data alone. The bulk of the information on the stellar populations is contained in galaxy spectra.

The optical spectrum of quiescent galaxies presents many features, some of which are particularly

useful as proxies for galaxy properties: for example, the Balmer lines are an excellent age indicator, while the Mgb and $\langle Fe \rangle$ lines are closely related to the metal abundances. Measuring these and other Lick/IDS indices, first introduced by Burstein et al. (1984), and comparing the results with grids obtained from model spectra allowed the first measurements of ages and metallicities for individual galaxies, although this procedure is typically affected by significant degeneracies (e.g., Renzini, 2006). In order to overcome this issue, Thomas et al. (2005) looked at the distribution of the Lick indices for a large sample of early-type galaxies, and derived robust trends of age and metallicity as a function of velocity dispersion σ , once more confirming the role of velocity dispersion as one of the most fundamental galaxy properties. In particular, they find that more massive galaxies (with larger velocity dispersion) formed stars at an earlier epoch and on shorter timescales.

In recent years, the advent of reliable libraries of stellar population templates (e.g., Bruzual & Charlot, 2003; Maraston, 2005) together with the adoption of full spectrum fitting (e.g., Cid Fernandes et al., 2005; Conroy et al., 2014) have led to significant progress in our understanding of the ages, metallicities, and star formation histories of local quiescent galaxies. The stellar chemical composition can now be measured to a remarkable level of detail: the state-of-the-art analysis of local quiescent galaxies includes measured abundances for 16 chemical elements (Conroy et al., 2014). However, if we want to understand the early evolution of quiescent galaxies, this *archaeological* approach presents significant limitations.

First, the analysis of spectra observed in local galaxies is plagued by the so-called outshining effect, i.e., the large difference in luminosity between young and old stars. For example, the mass-to-light ratio in the V band for a simple stellar population with an age of 100 Myr is 30 times lower than that for a 10 Gyr old population (Bruzual & Charlot, 2003). This implies that most of the light observed in old massive galaxies can in principle be due to a small amount of recently-formed stars, whose contribution to the total mass is negligible. As a result, spectral analysis can only yield a lower limit on the age of the stellar population.

Second, even in the ideal case where no contamination from younger stars took place, measuring the ages of old galaxies is challenging because of the lack of evolution in the spectra of old populations. This is true for both the shape of the continuum (i.e., the color, as shown in Figure 1.2), and for the narrow absorption features. For example, the strength of the Balmer lines evolves by the same amount during the time interval between 1 and 2 Gyr of age as in the following 10 Gyr (e.g., Vazdekis et al., 2010). As a result, ages become increasingly uncertain for older systems. Even if spectroscopic data are used, it is very difficult to distinguish between a formation redshift of, e.g., $z = 2$ and $z = 3$.

Finally, a third problem is the degeneracy between the mass *formation* history and the mass *assembly* history. Even when a reliable star formation history is found, it is not possible to know whether the various episodes were due to *in-situ* star formation or to the contribution of stars formed in other systems that then merged with the galaxy under study. Being able to directly probe

these different scenarios is fundamental for our understanding of galaxy formation.

These limitations of archaeological studies can only be overcome by direct observations of the high-redshift universe.

1.1.3 How did Quiescent Galaxies Form?

Since the existence of spiral and elliptical galaxies was noted, the question of how galaxies formed and evolved has been considered to be one of the main goals of extragalactic astronomy (Hubble, 1936). Historically, two alternative scenarios have been proposed to explain the formation of spheroidal galaxies. In the monolithic collapse model, massive galaxies are formed via a global starburst when the universe was very young, and their subsequent evolution is purely passive (Eggen et al., 1962; Larson, 1974; Rees & Ostriker, 1977; Arimoto & Yoshii, 1987). On the other hand, in the hierarchical growth model galaxies assemble slowly over time via mergers with other systems (Toomre, 1977; White & Rees, 1978; White & Frenk, 1991; Kauffmann, 1996; Cole et al., 2000).

An important turning point in galaxy formation studies was the development of a widely accepted cosmological model based on dark energy and cold dark matter (Λ CDM). Since dark matter is completely governed by gravitation, it is relatively easy to model its evolution. One of the most robust predictions of numerical simulations, in fact, is that dark matter halos follow a simple hierarchical growth driven by mergers with other halos (Mo et al., 2010, and references therein). The hierarchical merging scenario, therefore, seems to be strongly favored by the accepted cosmological model.

However, as we discussed above, one of the main results from the archaeological investigations of quiescent galaxies is that their stellar ages are very old. Also, more massive galaxies are found to host systematically older stars compared to less massive systems. This behavior, dubbed *downsizing* in star formation (Cowie et al., 1996), is apparently in contradiction with a hierarchical scenario, in which more massive galaxies are supposed to be the last to form. This apparent discrepancy is easily resolved if one distinguishes between the epoch at which galaxies were assembled in their current state from the epoch of formation of their stars. In fact, the highest density peaks in the early universe collapsed first, and transformed gas into stars on a shorter timescale compared to regions with lower density. As massive galaxies grow out of these early peaks, their stellar content will naturally present old ages. Theoretical models of galaxy formation based on hierarchical merging and Λ CDM cosmology can easily reproduce the observed downsizing in star formation (e.g., De Lucia et al., 2006).

Besides the merger history, predicting other observable galaxy properties such as the star formation rate, color, and morphology is not a trivial task, because the complex baryonic physics must be taken into account. Although numerical simulations have dramatically improved in the past decade, modeling the observed galaxy population remains one of the most difficult challenges in contempo-

rary astrophysics. By tuning the detailed treatment of the many physical processes involved, models are now able to qualitatively match the observations, but we are still far from a complete understanding of the formation and evolution of galaxies in the context of a Λ CDM cosmology (Somerville & Davé, 2014, and references therein). One particularly important aspect that is lacking a satisfactory explanation is the existence of two fundamentally different types of galaxies. It is generally understood that gas-rich systems at some point turn off their star formation and become quiescent galaxies, but the physical processes responsible for this dramatic change, called galaxy *quenching*, have not been identified yet. Many scenarios have been proposed to stop the accretion of cold gas, including major mergers, quasar-mode AGN feedback, stellar winds, disk instability, and cosmic starvation (e.g., Hopkins et al., 2008; Feldmann & Mayer, 2015). Furthermore, after gas accretion is terminated, the gas consumption rate should permit star-formation for a long time. Additional processes are needed to prevent the residual cold gas forming stars; possibilities include radio-mode AGN feedback or stellar feedback (e.g., Croton et al., 2006).

1.2 Quiescent Galaxies at High Redshift

Observations of the local population of quiescent galaxies are able to set useful constraints on theoretical models. The tightness of the scaling relations and the results of archaeological studies, for example, must be explained by a successful model of galaxy formation and evolution. However, observations of high-redshift galaxies are needed to complement our understanding of the local universe. By probing galaxy properties at earlier cosmic times we can directly test theories on how structures formed and evolved.

1.2.1 The Evolution over $0 < z < 1$

In the 1990s, the development of the 8-10 m class telescopes and the launch of *HST* made finally possible the exploration of quiescent galaxies at higher and higher redshift, up to $z \sim 1$ (for a review, see Renzini, 2006).

The fundamental plane of elliptical galaxies was studied first in clusters and then in the field population up to $z \sim 1$ (e.g., van Dokkum & Franx, 1996; Kelson et al., 2000; van Dokkum & Ellis, 2003). These studies consistently found that a thin plane exists at high redshift as well, and it is parallel to the one found at $z \sim 0$. However, the plane shifts to larger luminosities at increasingly higher redshift, in a way that is fully consistent with the fading of old stellar populations formed at high redshift. Using a large sample of galaxies over the range $0.2 < z < 1.2$, Treu et al. (2005a,b) were also able to detect a differential evolution of the mass-to-light ratio (see Figure 1.3), which suggests that galaxies with larger masses (and velocity dispersions) formed earlier. This directly confirms the downsizing in star formation observed in archaeological studies.

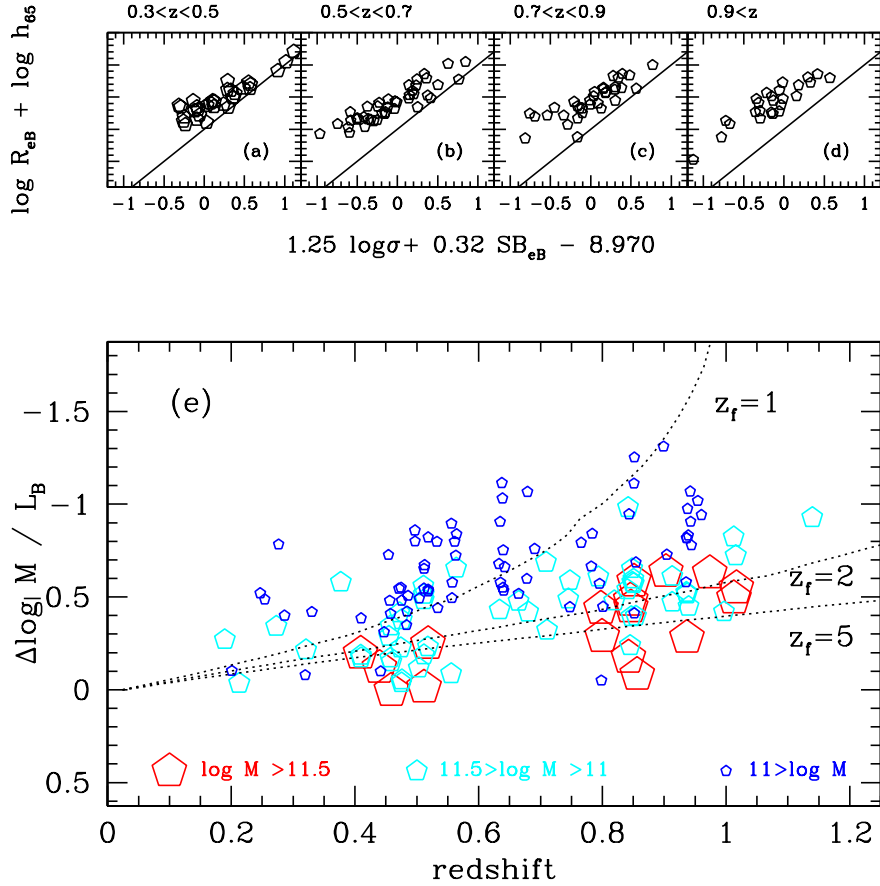


Figure 1.3 Redshift evolution of the fundamental plane, from Treu et al. (2005a). Top: Edge-on view of the fundamental plane in redshift bins, over $0.3 < z < 0.9$. The solid line is the local relation. Bottom: Offset from the local fundamental plane, in terms of mass-to-light ratio. Dotted lines show the expected trend for single burst models with different formation redshift. Note that the evolution is steeper and the scatter larger for less massive galaxies. At large masses, the data are consistent with a very early formation followed by passive evolution.

Observing the color-magnitude relation at high redshift is the best way to disentangle the degeneracy between early formation and late, synchronized formation of quiescent galaxies that limited the study of Bower et al. (1992). Since a tight red sequence is found in galaxy clusters (Ellis et al., 1997; Stanford et al., 1998) and in the field (Bell et al., 2004) up to $z \sim 1$, the star formation phase for quiescent galaxies must have been completed earlier than $z \sim 3$. Furthermore, Kodama & Arimoto (1997) were able to prove that the color-magnitude relation is caused by a trend of metallicity rather than age, since the red sequence does not steepen with redshift.

Studies of the Lick indices also confirmed the old ages and the passive evolution of quiescent galaxies up to $z \sim 1$ (Bender et al., 1996; Kelson et al., 2001). The most recent results using improved models and much larger samples confirm the passive evolution with a high degree of accuracy at least up to $z \sim 0.7$ (Choi et al., 2014; Gallazzi et al., 2014).

These independent and complementary analysis give a consistent picture in which the massive, quiescent galaxies that are found at $z \sim 1$ formed at even higher redshift and then passively evolved into the local population. However, an important point to keep in mind is that not all the local quiescent galaxies need to be descendants of the high-redshift quiescent galaxies, since it is conceivable that some star-forming systems were quenched at intermediate or low redshift. This difficulty in connecting galaxy populations at different redshifts, called *progenitor bias* by van Dokkum & Franx (1996), is one of the most challenging aspects of any observational study of galaxy evolution.

Finally, the development of wide photometric surveys allowed the determination of the number density of a given population of galaxies as a function of redshift. The earlier studies found that the luminosity function of quiescent galaxies remain approximately constant over $0 < z < 1$ (Lilly et al., 1995). Since the luminosity of a passive population fades with time, it is more instructive to look at the distribution of the stellar masses, which can be measured by fitting models of stellar populations to the observed broadband photometry, a technique first applied to high-redshift systems by Brinchmann & Ellis (2000). The observed stellar mass function (e.g., Drory et al., 2004; Pozzetti et al., 2010; Ilbert et al., 2013) shows that the number of quiescent galaxies slowly declines with redshift, but the rate is strongly mass-dependent: the more massive systems are already in place at $z \sim 1$ while the less massive galaxies formed at later times. Furthermore, the mass function of star-forming galaxies seems to be remarkably constant up to $z \sim 1$. Since star-forming galaxies continuously increase their mass with new stars, these observations require a substantial amount of quenching, i.e., of transformation from star-forming to quiescent systems (e.g., Faber et al., 2007).

1.2.2 Galaxies at $z > 1$: the Redshift Desert

The spectral features that contain most of the information on the dynamics and stellar populations of quiescent galaxies are the CaII H and K absorption lines, the Balmer series, and the 4000Å break. At $z > 1.3$ these features are redshifted into the observed near-infrared, where spectroscopic

observations are limited by poor detector sensitivity and strong sky emission. For this reason the $z > 1.3$ epoch has been called the *redshift desert*. The first observations of this epoch, therefore, probed the rest-frame near-UV, where Fe and Mg absorption lines allow one to measure spectroscopic redshifts and estimate stellar ages. UV features allowed the first discovery of passive galaxies at $1.6 < z < 1.9$ (Cimatti et al., 2004; Glazebrook et al., 2004), which turned out to be as massive as the largest systems in the local universe, with stellar masses above $10^{11} M_{\odot}$.

Although different selection of red galaxies based on the observed colors were proposed (e.g. Cimatti et al., 2002; Franx et al., 2003; Daddi et al., 2004a), only with the use of efficient near-infrared imaging and spectroscopy the presence of a red sequence at $z \sim 2$ could be confirmed (Kriek et al., 2006, 2008). This confirms the archaeological evidence for an early formation of quiescent galaxies. Moreover, the existence of massive systems already assembled at such early epochs suggests a downsizing in *mass assembly*. This is qualitatively different from the previously known downsizing in star formation, and is not consistent with a hierarchical merging scenario for the formation of galaxies. Such discrepancy between theory and observations represents one of the most important challenges for models based on the Λ CDM cosmology.

Interestingly, mass function studies found that most of the massive galaxies even at $z > 1$ are already quiescent (Pozzetti et al., 2003). However, the number evolution steepens at high redshift: the number density of quiescent galaxies compared to $z \sim 0$ is 2-3 times smaller at $z \sim 1.5$ (Daddi et al., 2005; Saracco et al., 2005; Drory et al., 2005), and 10 times smaller at $z \sim 2$ (Muzzin et al., 2013; Ilbert et al., 2013).

1.2.3 The Size Evolution of Quiescent Galaxies

Once the population of massive galaxies was identified at high redshift, and it was established that most of these systems are passively evolving, an interesting and unexpected result emerged from the study of their structure. Using space-based *HST* and ground-based adaptive optics imaging, a number of groups measured the sizes of massive galaxies first at $1 < z < 2$ (Daddi et al., 2005; Trujillo et al., 2006a, 2007; Longhetti et al., 2007; Cimatti et al., 2008) and then at $z > 2$ (Zirm et al., 2007; Toft et al., 2007; van Dokkum et al., 2008). These studies consistently found that massive galaxies are significantly smaller at high redshift than at $z \sim 0$. At a given stellar mass, $z > 2$ systems are about 3-5 times smaller than their local counterparts, and their central density is larger by an order of magnitude.

Since most of the massive galaxies have already been quenched at high redshift and show signs of passive evolution, they are not expected to undergo a physical growth. Additionally, some of them are already as massive as the largest local ellipticals: their compact nature at high redshift suggests a peculiar type of growth in which the size increases by a factor of a few, while the stellar mass remains virtually unchanged. The inferred growth of these galaxies, dubbed *red nuggets* (Damjanov

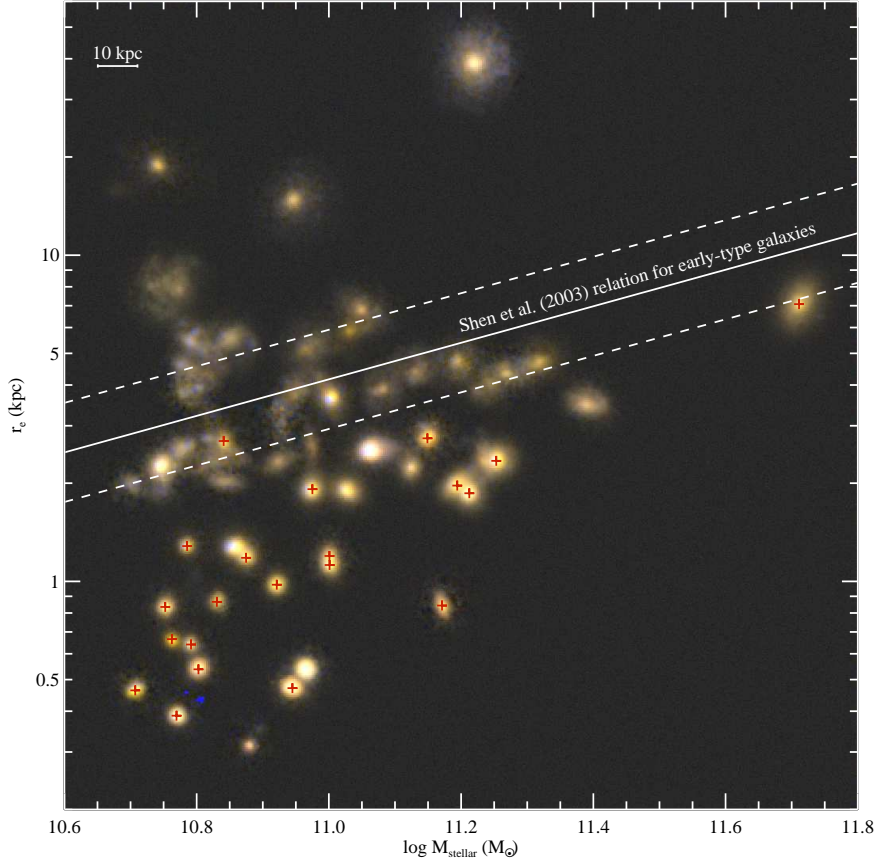


Figure 1.4 Mass - size relation for galaxies at $1.5 < z < 2.5$, from Szomoru et al. (2012). The color images are composites of rest-frame UBg observations taken with *HST*. Quiescent galaxies are marked with a red cross, and the local relation for early-type galaxies from Shen et al. (2003) is shown in white. Clearly, quiescent galaxies are much smaller at high redshift than in the local universe. Also, at $z \sim 2$ there is a clear relation between size and morphology (or star formation activity), with quiescent galaxies being smaller than star-forming galaxies at any stellar mass.

et al., 2009), is therefore quite puzzling.

Given the unexpected nature of this compactness, the possibility that the difference in structure between local and high-redshift quiescent galaxies might be explained partially or fully by observational uncertainties has been considered. On one hand, the sizes might be underestimated because of the low signal-to-noise ratio, which would cause observations to miss low-surface brightness halos at large radii, or maybe because of strong color gradients, which yield different sizes at different rest-frame wavebands; on the other hand, the stellar mass measurements could be biased because the templates usually adopted for studies of local galaxies might not work for high-redshift systems, particularly due to the increased importance of the post-AGB phase in younger galaxies (Mancini et al., 2010; Hopkins et al., 2010). However, a systematic analysis of the uncertainties involved in the SED fitting, such as the choice of stellar population models, initial mass function, and star formation history, reveals that the mass-size relation at $z \sim 2$ is offset towards smaller sizes by

at least a factor of three (Muzzin et al., 2009). Additionally, the installation of the near-infrared Wide Field Camera 3 onboard the *HST* allowed the detailed study of the structure of red nuggets in the rest-frame optical. Deep imaging data showed that the surface brightness profile of these systems is well-behaved out to large radii, and yielded effective sizes in agreement with the previous measurements, thus confirming the significant offset of the $z \sim 2$ quiescent population from the local mass-size relation (Cassata et al., 2010; Szomoru et al., 2010, 2012, see Figure 1.4). Therefore the observational uncertainties are too small to explain the remarkable compactness of high-redshift quiescent galaxies. At this point, only two possible explanations are left.

In the *physical growth* scenario, the compact sizes of individual quiescent galaxies grow with time because of some physical process. There are two main candidates for such process. One is a puffing-up growth, where an internal mechanism (such as AGN feedback or stellar evolution) expels large quantities of gas. This gas in turn can alter the distribution of the stars (Fan et al., 2008, 2010), or form new stars at larger radii (Ishibashi et al., 2013); either way, the final size as measured from the stellar light distribution will be larger. The other candidate is galaxy merging. When a galaxy merges with another, the mass always increases, while the size growth is determined by the amount of gas and the mass ratio between the two systems. If the merger is dry, i.e., no gas is involved, then the final size will be always larger than the initial one. Moreover, the smaller the density of the satellite (or equivalently its mass), the steeper will be the size growth (e.g., Naab et al., 2009; Bezanson et al., 2009).

Alternatively, in the *progenitor bias* scenario, the compact red nuggets observed at high redshift do not physically grow in size, and they evolve into the most compact systems in the local universe (e.g., Carollo et al., 2013). This is possible because the population of quiescent galaxies at $z \sim 0$ is significantly more numerous than its analog at $z \sim 2$, as extensively shown by mass function studies (e.g., Muzzin et al., 2013). Therefore, *most* of the local quiescent galaxies were not quiescent at $z \sim 2$. Furthermore, at any redshift quiescent and spheroidal galaxies are smaller compared to disks and star-forming systems (Franx et al., 2008; Buitrago et al., 2008; Williams et al., 2010).

Distinguishing between physical growth and progenitor bias is particularly important because of its consequences on our understanding of the passive evolution of massive galaxies. However, this relatively simple question has been very challenging from the observational point of view. The most direct way to validate the physical growth scenario is to look for compact galaxies in the local universe: if they are not found, or are far less numerous than the compact population at high redshift, then we must conclude that those galaxies did evolve into larger systems. Unfortunately, measuring and comparing number densities at different redshifts is extremely difficult because of the systematics involved. As a result, different studies, sometime performed on the same dataset, yielded very different results (Trujillo et al., 2009; Taylor et al., 2010b; Carollo et al., 2013; Poggianti et al., 2013).

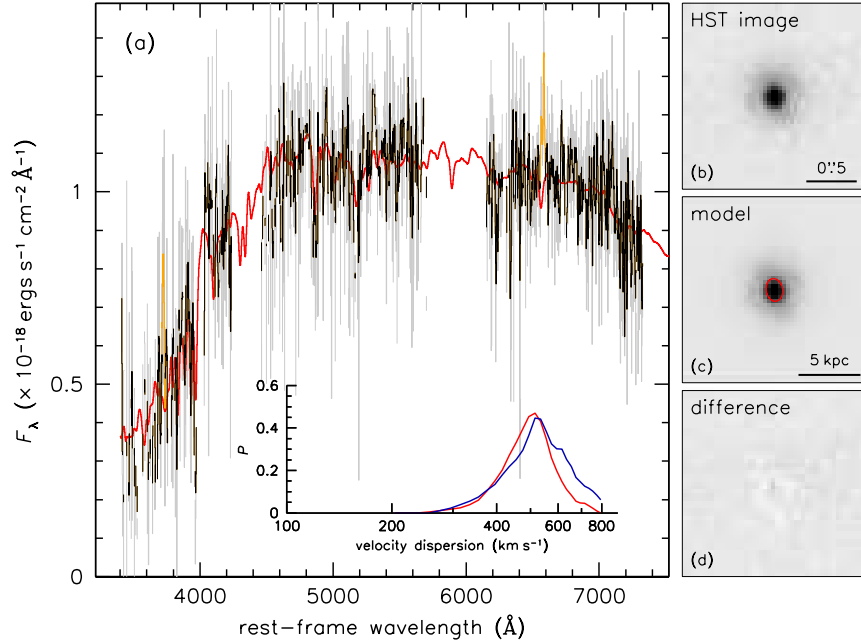


Figure 1.5 Ultra-deep spectrum of a quiescent galaxies at $z = 2.19$, from van Dokkum et al. (2009). A 29-hour exposure in the near-infrared with the Gemini telescope was necessary to achieve enough signal-to-noise ratio to allow for an estimate of the velocity dispersion. The *HST* cutout shows that this is a typically compact galaxy.

A different approach is to try and connect galaxies at different redshifts according to a physically motivated method. The simplest way to compare galaxies is at fixed stellar mass; this might work for quiescent galaxies that evolve in isolation, but mergers will add mass even to passive systems and invalidate this method. A better way is to compare galaxies *at fixed velocity dispersion*. Observational studies have shown that velocity dispersion is one of the most fundamental quantities of galaxies, yielding the cleanest correlations with other properties such as mass-to-light ratio, color, and star formation history (e.g., Thomas et al., 2005; Cappellari et al., 2006; Franx et al., 2008; Graves et al., 2009a; Wake et al., 2012). Furthermore, numerical simulations have proved that while the stellar mass can increase because of mergers, the velocity dispersion of a spheroidal remains approximately constant throughout its lifetime (e.g., Nipoti et al., 2003; Hopkins et al., 2009b; Oser et al., 2012).

However, while measuring the stellar mass can be done in a reliable way with just a few photometric measurements, the velocity dispersion measurement requires deep absorption-line spectroscopy, which is particularly difficult to achieve at $z > 1$, where the rest-frame spectrum is redshifted into the observed near-infrared. Because of technological limitations, progress in near-infrared spectroscopy has been extremely slow until recently, and only few years ago the first absorption lines could be detected at a redshift $z > 2$ (van Dokkum et al., 2009; Kriek et al., 2009). An ultra-deep exposure (see Figure 1.5) was required to obtain the spectrum of a single galaxy, from which velocity

dispersion and stellar population properties could be measured. However, in the last few years an impressive progress in near-infrared detectors has finally allowed spectroscopic studies of $z > 2$ quiescent galaxies (Newman et al., 2010; Toft et al., 2012; van de Sande et al., 2013; Bezanson et al., 2013), starting an exciting new era for observational studies of galaxy evolution.

1.2.4 Open Questions

We can summarize the main open questions about the formation and evolution of quiescent galaxies in the following points:

- When did massive galaxies form their stars? And when did they assemble their total mass? If their assembly was completed at very early times, as observations suggest, how can we reconcile this with a hierarchical growth of structures, which is a clear prediction of the Λ CDM cosmological model?
- What are the physical processes responsible for the quenching of star formation in galaxies?
- Why are high-redshift quiescent galaxies much smaller than their local counterpart? How could they form with such high central densities?
- How did quiescent galaxies grow in size without correspondingly increasing their mass? More generally, do quiescent galaxies undergo a purely passive evolution?

1.3 Goals of this Thesis

The main goal of the present thesis is to take advantage of the recent progress in the near-infrared capabilities of large telescopes to probe the physical properties of high-redshift galaxies, with a particular focus on the size growth of quiescent galaxies.

As an illustration of the possibilities opened up by near-infrared observations, in Chapter 2 we present a study of the rest-frame optical emission lines for star-forming galaxies at $1.5 < z < 3$ based on data collected at the Palomar telescope with the Triplespec instrument. By measuring the fluxes of the strongest nebular lines, such as $[\text{OII}]\lambda 3726, 3729$, $[\text{OIII}]\lambda 5007$, $\text{H}\alpha$, and $\text{H}\beta$, we derive star formation rates and gas-phase metallicities, with the goal of testing the recent claims of a universal relation between mass, metallicity, and star formation rate (Mannucci et al., 2010).

The remaining part of this thesis is a study of deep spectra of quiescent galaxies at $z > 1$. As extensively discussed in this introduction, spectra allow one to study both the dynamical structure and the stellar population content of quiescent galaxies, and represent one of the key tools for observers to explore the physical properties of galaxies and their evolution with cosmic time.

In Chapter 3 we present the largest sample of quiescent galaxies at $1 < z < 1.5$ for which deep spectroscopic data are available. These observations, based on the preliminary study by Newman et al. (2010), were made possible by the upgrade of the red arm of the LRIS multi-object spectrograph at Keck, which extended the usable wavelength range into the near-infrared, up to $1\mu\text{m}$. The deep rest-frame optical spectra allow us to measure velocity dispersions, which are important for two reasons. First, from the velocity dispersions and the effective sizes derived from *HST* imaging, we can calculate dynamical masses and compare them to stellar masses. This constitutes a test of the accuracy of stellar masses, and at the same time extends previous studies of the mass plane evolution to higher redshift. Second, as shown by numerous studies and described above, velocity dispersions represent one of the most fundamental properties of spheroidal galaxies, and are thought to remain relatively constant with cosmic time. They can therefore be used as a sort of label to trace galaxy populations at different cosmic times, and avoid the contribution of progenitor bias to the inferred evolution of galaxy properties. The main goal of this chapter is in fact to measure the size evolution of quiescent galaxies *at fixed velocity dispersion* rather than at fixed stellar mass.

The stellar populations of the same sample are explored in Chapter 4. By measuring the star formation histories of individual systems, we can identify those galaxies that were only recently quenched, and compare their sizes with those for the overall population. This is a novel look at the effect of progenitor bias on the size growth of quiescent galaxies. Furthermore, exploring the properties of stellar populations at such early cosmic time can offer important insights on the quenching mechanism.

With the new generation of near-infrared instruments, observers are finally able to explore the redshift desert with an unprecedented level of detail. The new MOSFIRE instrument at Keck is arguably the best spectrograph for studies that aim at a relatively large number of deep near-infrared spectra. In Chapter 5 we present MOSFIRE observations of quiescent galaxies at $1.5 < z < 2.5$ and extend the previous analysis to higher redshift. This sample represents a significant step forward in the study of quiescent systems in this critical redshift range. The spectra are used to derive both velocity dispersions and stellar population properties, and give us a first look at the formation of the very first massive galaxies.

Finally, in Chapter 6 we summarize the results of this thesis, present the current state of the field, and discuss future directions for observational studies.

Chapter 2

Testing the Universality of the Fundamental Metallicity Relation at High Redshift Using Low-Mass Gravitationally Lensed Galaxies

Abstract

We present rest-frame optical spectra for a sample of 9 low-mass star-forming galaxies in the redshift range $1.5 < z < 3$ which are gravitationally lensed by foreground clusters. We used Triplespec, an echelle spectrograph at the Palomar 200-inch telescope that is very effective for this purpose, as it samples the entire near-infrared spectrum simultaneously. By measuring the flux of nebular emission lines we derive gas phase metallicities and star formation rates, and by fitting the optical to infrared spectral energy distributions we obtain stellar masses. Taking advantage of the high magnification due to strong lensing we are able to probe the physical properties of galaxies with stellar masses in the range $7.8 < \log M_*/M_\odot < 9.4$ whose star formation rates are similar to those of typical star-forming galaxies in the local universe. We compare our results with the locally determined relation between stellar mass, gas metallicity, and star formation rate. Our data are in excellent agreement with this relation, with an average offset $\langle \Delta \log(\text{O}/\text{H}) \rangle = 0.01 \pm 0.08$, suggesting a universal relationship. Remarkably, the scatter around the fundamental metallicity relation is only 0.24 dex, smaller than that observed locally at the same stellar masses, which may provide an important additional constraint for galaxy evolution models.

A version of this chapter has been published as Belli, S., Jones, T., Ellis, R. S., & Richard, J. 2013, ApJ, 772, 141

2.1 Introduction

The gas-phase metallicity represents a fundamental property of galaxies and can be used to investigate the complex physical processes that govern galaxy evolution. It mainly traces the star formation history, as metals produced in stars are ejected into the interstellar medium (ISM), but the exchange of material between the galaxy and the intergalactic medium (IGM) also plays an important role. The accretion of metal-poor gas from the IGM can dilute the metal content of the gas in a galaxy. Also, stellar winds can substantially lower the metallicity by ejecting metals.

Despite the complexity of these processes, a clear relation between galaxy luminosity and metallicity has been known since the work of Lequeux et al. (1979). Recently, thanks to the vast amount of spectroscopic and photometric data available from the Sloan Digital Sky Survey (SDSS), it has become clear that the physical parameter that correlates most strongly with metallicity is the galaxy stellar mass (Tremonti et al., 2004). This mass-metallicity relation, in which galaxies of higher masses contain larger metallicities, is remarkably tight over 3 orders of magnitude in stellar mass, with a dispersion of only 0.10 dex in metallicity.

A natural explanation for the observed mass-metallicity relation is the outflow of metal-enriched gas driven by star formation. Because of the lower gravitational potential, low-mass galaxies lose a higher fraction of their gas, with a consequent decrease in metallicity (Larson, 1974; Garnett, 2002; Tremonti et al., 2004). An alternative possibility is that lower mass galaxies are less metal-rich because their star formation history has been developed more gradually (Ellison et al., 2008), in agreement with the now-familiar effect of *downsizing* (Cowie et al., 1996).

Different models of galaxy formation and evolution are able to match the mass-metallicity relation in the local universe, but have dissimilar predictions for high redshift galaxies (e.g., De Lucia et al., 2004; Davé & Oppenheimer, 2007; Tassis et al., 2008; Davé et al., 2011a; Yates et al., 2012). Observing the redshift evolution of the mass-metallicity relation can therefore differentiate these models. Observations at different redshifts have shown a clear evolution with cosmic time, with lower metallicity at higher redshift, for a fixed mass (Savaglio et al., 2005; Erb et al., 2006a; Maiolino et al., 2008; Mannucci et al., 2009; Zahid et al., 2011; Yuan et al., 2013).

However, it is important to recognize that high-redshift studies target galaxy populations that are different from those found typically in the local Universe. The evolution of the mass-metallicity relation could then be the result of a selection effect rather than a change in the physical properties of the galaxies with cosmic time.

Among the differences between local and high-redshift galaxies, star formation activity is one of the most important. At earlier cosmic times, the star formation rate (SFR) was on average much higher than today, because galaxies contained a larger amount of cold gas. Also, most of the high-redshift surveys are magnitude-limited in the rest-frame UV, and therefore tend to select

galaxies with high SFR. The combination of these two effects makes it very difficult to compare the metallicity of galaxies at different redshifts with the same stellar mass and star formation rate. It is then essential to study the relation between SFR and metallicity, since this could have important consequences on the interpretation of the observed evolution of the mass-metallicity relation.

In fact, Mannucci et al. (2010) found that the local mass-metallicity relation is different for samples of galaxies with different star formation rates. Furthermore, they showed that the SDSS galaxies lie on a tight 3D surface in the mass-metallicity-SFR space, with a dispersion of only 0.053 dex in metallicity (see also Lara-López et al., 2010). According to this *fundamental metallicity relation* (FMR), at fixed stellar mass SFR and metallicity are anti-correlated. If this relation holds independently of cosmic time, a galaxy population at high redshift will tend to have a low average metallicity because of its high SFR. In this scenario the evolution of the mass-metallicity relation is driven by the shifting of galaxy populations on the SFR-mass plane, rather than being directly caused by the evolution of some physical process. Clearly, testing the fundamental metallicity relation at different redshifts is of primary importance.

The redshift evolution of the FMR was first explored by Mannucci et al. (2010) using samples from the literature, and they concluded that the local relation is a good fit for any star-forming galaxy up to $z \sim 2.2$. But high-redshift observations are biased towards high-SFR galaxies, and a direct test using galaxies with the same range of star formation rates that is seen in the SDSS sample ($\text{SFR} < 10 M_{\odot}/\text{yr}$) is still lacking. Additional difficulties come from the fact that to measure the metallicity one needs the rest-frame optical emission lines, which at $z \sim 2$ are redshifted into the near-infrared, a spectral region where sky emission is strong.

One way to probe lower star formation rates with the current technology is to take advantage of strong gravitational lensing. The magnification induced by foreground galaxy clusters allows one to reach faint objects, corresponding to stellar masses and SFRs (on average) lower than the values achievable without lensing. Recent studies of the FMR for high-redshift lensed galaxies found a general agreement with the local relation, although with a very large scatter (Richard et al., 2011; Wuyts et al., 2012b; Christensen et al., 2012).

Testing the universality of the fundamental metallicity relation is important not only for understanding the evolution of the mass-metallicity relation, but also to constrain models of galaxy evolution. For example, Davé et al. (2011a) consider a simple model in which inflow, outflow, and star formation are in equilibrium and determine the gas metallicity. This scenario can qualitatively explain the dependence of the mass-metallicity relation on the star formation rate: at a fixed stellar mass a high SFR is caused by a large inflow, which in turn implies a low metallicity. If a galaxy is perturbed, e.g., by a merger, it will move away from the FMR and, after some time, will return to the equilibrium configuration. This equilibrium timescale determines the scatter in the mass-metallicity-SFR relation. So long as the yield of metals per unit star formation and the mass loading factor

(i.e., the ratio between outflow and star formation) are constant, the equilibrium relation implies a universal FMR independent of redshift. Although this and other simple analytic models (Dayal et al., 2012; Davé et al., 2012) succeed in explaining the local fundamental metallicity relation, we are still far from a detailed understanding of the relevant physical processes. High-redshift observations are essential for quantitative tests of hydrodynamical simulations of galaxy evolution.

In this work we study a sample of low-luminosity, $z \sim 2$ gravitational arcs with magnification factors of ~ 10 – 100 . We used the Triplespec spectrograph on the Palomar 200-inch telescope that features a good sensitivity and covers the full near-infrared wavelength range. This characteristic makes it an ideal instrument for such a study, because it allows us to observe all diagnostic lines of interest simultaneously. In addition to the efficiency of observation, a particular benefit is the ability to measure emission line ratios, the diagnostics of gas-phase metallicities, in a single exposure, mitigating uncertainties that arise from variations in weather conditions. Also, we mainly rely on the emission lines [OIII] λ 5007, [OII] λ 3726, 3729, H α and H β for measuring the metallicity, so that we are not limited by the requirement of detecting the faint [NII] λ 6584 line. For these reasons we probe stellar masses and star formation rates that are on average lower than the ones of previously studied samples of lensed galaxies.

The sample of gravitational arcs, the spectroscopic observations, and data reduction are described in Section 2. In Section 3 we present the photometric measurements and the fitting of the spectral energy distribution, while in Section 4 we explore the galaxy physical properties using the measured line fluxes. We discuss the constraints of these measurements on the evolution of the fundamental metallicity relation in Section 5, and the implications for galaxy evolution models in Section 6. We assume a Λ cold dark matter (Λ CDM) cosmology with $\Omega_\Lambda = 0.7$, $\Omega_m = 0.3$ and $H_0 = 70 \text{ km s}^{-1}\text{Mpc}^{-1}$. Magnitudes are given in the AB system.

2.2 Data

2.2.1 Sample Selection

We selected our sample of gravitational arcs from the literature according to the following three criteria.

First, we considered only galaxy clusters with a well-constrained lens model. This allowed us to select arcs of known magnification $\mu \gtrsim 10$.

Second, the observed (i.e., not corrected for lensing) arc magnitude must be $R \lesssim 23$, so that observations with Triplespec at Palomar are feasible. This means that we can probe intrinsic magnitudes $R \gtrsim 25.5$, fainter than the limits of typical non-lensing surveys.

Third, the arc should have a known spectroscopic redshift such that the emission lines from [OII] to H α fall in the wavelength range observable with Triplespec. The ideal range is $2 < z < 2.5$, but

Table 2.1. Sample of Gravitational Arcs

Cluster	Arc	μ^a	Reference	Run	Exp. Time	Redshift ^b
A611	1.2, 1.3	19.6 ± 3.0	Newman et al. (2009) ^c	B	1h20min	1.4902
RXJ2129	1.1, 1.2	61 ± 17	Richard et al. (2010)	A	5h30min	1.5221
A1413	2.1, 2.2	23.9 ± 6.4	Richard et al. (2010)	B, D	3h00min	2.0376
A1835	7.1	88 ± 30	Richard et al. (2010)	B	1h45min	2.0733
RXJ1720	1.1, 1.2	22.5 ± 9.1	Richard et al. (2010)	A	4h00min	2.2200
A773	1.1, 1.2	27.9 ± 7.9	Richard et al. (2010)	C	3h15min	2.3032
MACS0717	13.1	7.2 ± 3.0	Limousin et al. (2011)	C, D	5h30min	2.5515
A383	3C, 4C	23.9 ± 3.3	Newman et al. (2011)	C	2h00min	2.5771
A1689	1.1, 1.2	57 ± 23	Coe et al. (2010)	D	6h30min	3.0421
A1703	3.1, 3.2	46 ± 20	Richard et al. (2009)	B	3h30min	3.2847

^aGravitational magnification. For multiply imaged sources, this is the sum of the magnifications.

^bRedshifts measured from [OIII] λ 5007, except for RXJ1720, for which H α was used. The uncertainties are always less than 0.0003.

^cMagnification factor calculated after updating the lensing map with the new arc redshift, see Section 2.4.

Table 2.2. Triplespec Observations

Run	Date	Seeing (arcsec)
A	2010 August 23, 25, 26	0.9 - 1.3
B	2011 April 10, 11, 12, 13	0.9 - 1.3
C	2012 January 12, 13, 14	1.1 - 2.0
D	2012 April 29, 30, May 1	0.9 - 1.5

Note. — The seeing was measured in the K_S band.

we can measure metallicities and star formation rates using lines available for galaxies from $z \sim 1.5$ to $z \sim 3$.

This selection provides us with 10 sources viewed through 10 distinct clusters (see Table 2.1). For the arc in RXJ1720 only $H\alpha$ is observable because the other diagnostic lines are unfortunately obscured by night sky emission. We do not attempt any analysis on this object, but we include it in Table 2.1 because ours is the first redshift measurement for this arc obtained from a rest-frame optical emission line.

From now on we will refer to the gravitational arcs by the names of the corresponding galaxy clusters, e.g., A1835 for A1835 arc 7.1.

2.2.2 Spectroscopy

All spectroscopic data were taken with Triplespec on the 200-inch Hale Telescope at Palomar Observatory over the course of four observing runs (see Table 2.2). Triplespec is a near-infrared cross-dispersed spectrograph that simultaneously covers the wavelength range 1–2.4 μm with a resolution $R \sim 2700$ (Herter et al., 2008).

The 1×30 arcsec long slit was positioned on the targets as shown in Fig. 2.1 via a blind offset from a bright star. For each target we typically undertook many exposures of 300–450 seconds each, using a two-point dithering pattern. The position of the target along the slit and the dithering offset were carefully chosen for each arc, avoiding any overlap of the arc with foreground cluster galaxies, and leaving enough blank sky along the slit to reliably measure and subtract background emission. When it was possible to arrange a multiply imaged system in the slit, the spectra, if resolved, were reduced and extracted separately and then combined.

The spectroscopic data were reduced using a modified version of *Spextool* (Cushing et al., 2004; Vacca et al., 2004). For each target we extracted the spectrum from each A–B pair and then combined the 1D spectra. The aperture for the boxcar extraction was defined using the [OIII] emission profile in the stack of many A–B pairs, since the line emission is rarely detected in single frames.

Flux calibration and correction for telluric absorption were performed using Elias et al. (1982) A-type standard stars. Note that this procedure also corrects for the variation of effective seeing with wavelength. Although the absolute flux calibration can be very uncertain, it affects only the emission line fluxes but not their ratios, which are used in calculating gas-phase metallicities. This is one of the main advantages of using Triplespec, which allows one to observe the entire near-infrared spectrum at once. However, SFR measurements are affected by absolute flux calibration, which therefore needs to be carefully quantified.

The accuracy of the absolute flux calibration is limited by many factors. First, the observing conditions were not always photometric, and a good fraction of our observations was affected by

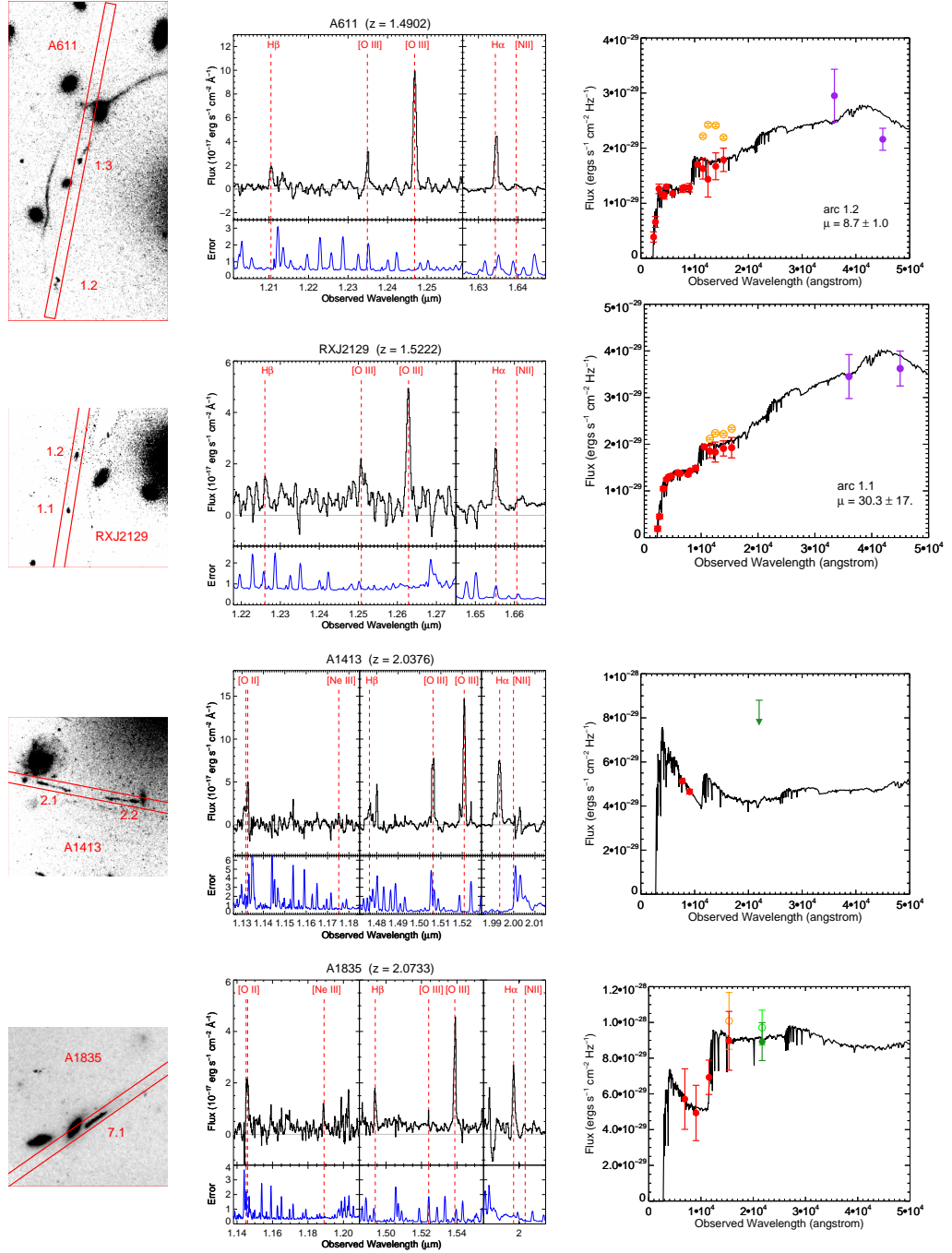


Figure 2.1 *HST* image stamp, Triplespec spectrum, and SED fit for each gravitational arc. *Left*: The *Hubble Space Telescope* images (F702W or F775W) show the position of the Triplespec slit. Each square is 15 arcseconds on the side. *Center*: Each spectrum has been inverse-variance smoothed using a 5-pixel window, and the bottom panels show the $1\text{-}\sigma$ error in the same units as the flux. When multiple images are present on the slit, the spectrum shown is the combined spectrum. *Right*: The photometry from (observed) UV to infrared is plotted as filled points, and the color corresponds to the type of data: red for *HST*, green for ground-based near-infrared, and purple for *Spitzer* IRAC images. The empty, lighter-colored points are photometric measurements not corrected for emission line flux (see Section 2.3.2), and the best-fit synthetic spectrum is shown as a solid line. For objects with two gravitational images, the SED is plotted only for the one that is less contaminated by foreground galaxies, and its magnification factor is shown. Spectra and photometry are not corrected for the lensing magnification.

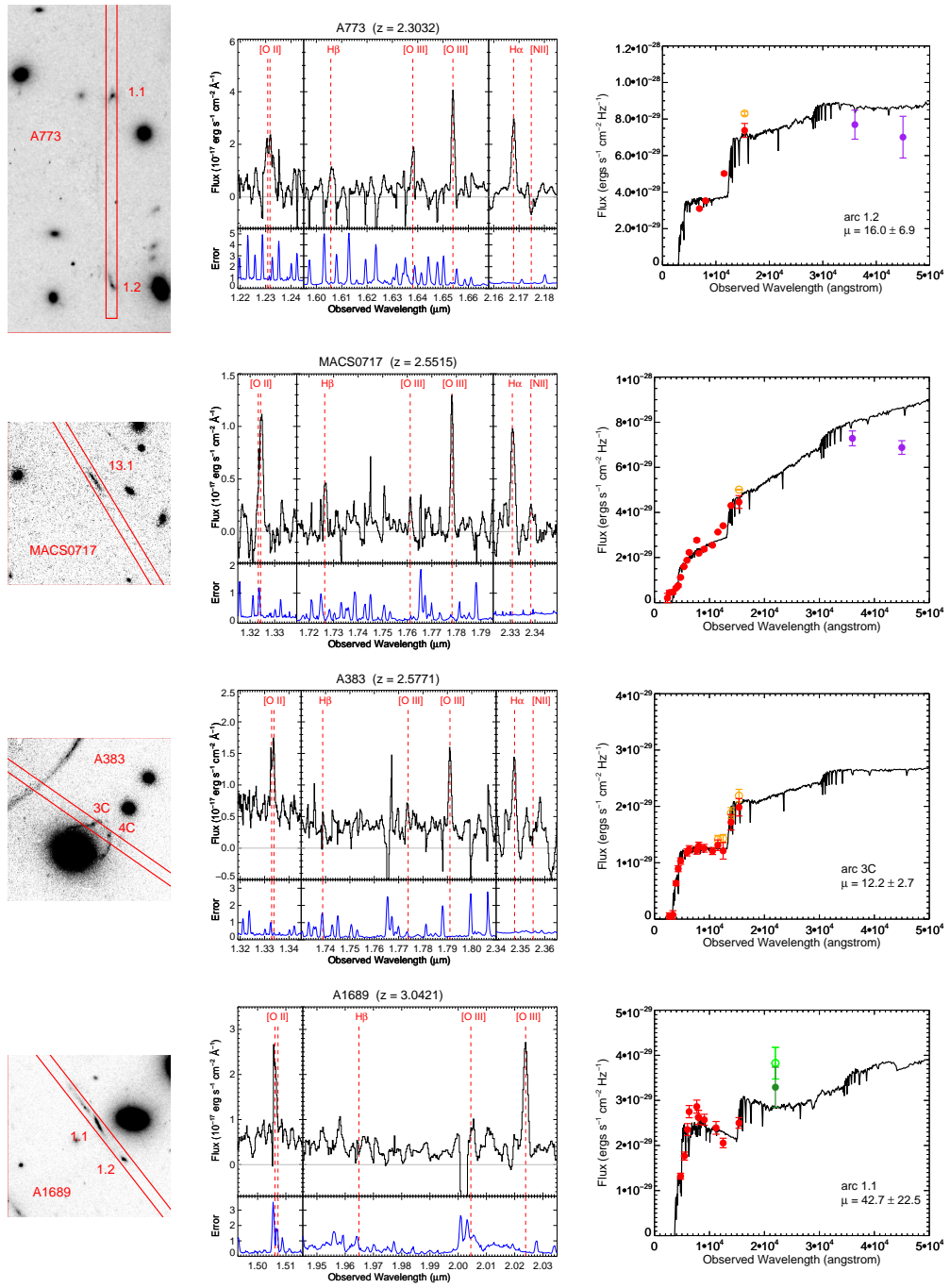


Figure 2.1 Continued.

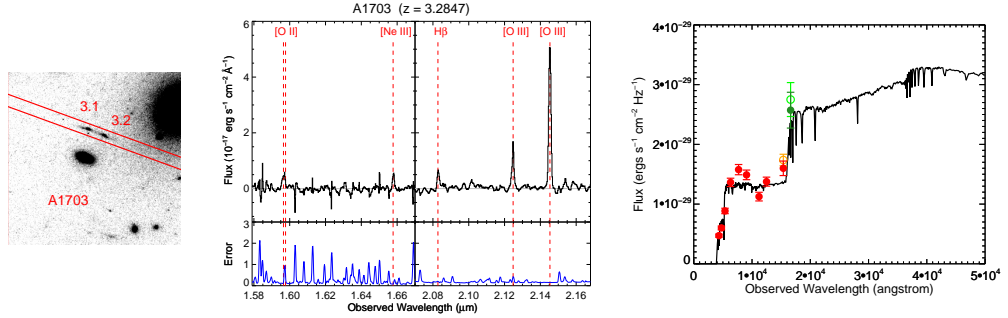


Figure 2.1 Continued.

the presence of thin clouds. This problem is mitigated by the fact that each target was observed on more than one night.

The second issue arises from the fact that every few minutes the pointing was changed according to the dithering pattern. As a result, the slit alignment is not identical in each frame, and the observed flux may depend on how the target is centered. We tested the significance of this effect using the standard star observations, where the target is bright enough to compare the flux in different frames. The discrepancy in the absolute flux between different frames is typically much less than 50%. This represents an upper limit on the flux uncertainty, since this random effect is attenuated by averaging together multiple frames for each standard star. Also, the science observations were made on much longer timescales, and the guiding was overall very stable, as we could check from the guider images taken during the exposure.

Another possible source of uncertainty is the variable seeing. However, the difference in seeing (which was almost always larger than the slit width) between the science target and the standard star observations has a much smaller effect than the slit misalignment.

For each object we separately flux-calibrated the spectra from different nights using the appropriate standard stars. This reduces the effect of seeing variation and cloud attenuation. We then measured the flux of the brightest line. Since slit misalignment and clouds tend to attenuate the line emission, we scale the spectra from different nights to match the one with the brightest line. For each object we have at least some observations with clear conditions, so that the flux uncertainty caused by cloud cover is negligible compared to the 50% uncertainty measured from the standard star misalignment. This therefore represents a conservative estimate of the overall flux calibration error. The corresponding contribution to the uncertainty in the SFR is 0.22 dex.

The calibrated spectra together with their $1\text{-}\sigma$ error are shown in Fig. 2.1. The emission line [OIII] λ 5007 is well-detected in each spectrum; other observed emission lines are $H\alpha$, $H\beta$, [OIII] λ 4959, and [OII] λ 3726, 3729. The fainter lines [NII] λ 6584 and [NeIII] λ 3870 are detected only in a few cases. The continuum emission from the arcs is never detected, but the residuals from sky subtraction or the emission from foreground galaxies can cause the observed continuum to be different from zero.

2.2.3 Imaging

We now discuss the imaging data for our sources, which will provide the essential ingredients for measuring the stellar masses and other physical properties. To accurately derive the stellar mass it is necessary to sample the spectral energy distribution (SED) redward of the rest-frame Balmer break. For $z < 2$ objects optical imaging is sufficient, but at higher redshift infrared data are needed.

2.2.3.1 Archival Data

Since we chose well-studied galaxy clusters, space-based images from *Hubble Space Telescope* (*HST*) and *Spitzer* observations are available for each target in our sample.

For four of the objects (A383, MACS0717, RXJ2129, and A611) we used publicly available data from the Cluster Lensing and Supernova Survey with Hubble (CLASH, Postman et al., 2012). This allowed us to measure the photometry for each arc in about 16 bands from UV to near-infrared. For the remaining targets we used archival *HST* images; each source has imaging available in at least four bands except A1413, for which only two bands are available.

All of the selected targets have publicly available *Spitzer* IRAC observations, but due to the faintness of the gravitational arcs not all of them are detected. The arcs with useful IRAC imaging are A611, RXJ2129, A773, and MACS0717. We used channel 1 (3.6 μm) and channel 2 (4.5 μm) observations from *Spitzer* program 60034 (PI: E. Egami) for all of the arcs, and data from program 83 (PI: G. Rieke) for A773.

Additionally, some ground-based near-infrared data have been used for a few arcs: VLT ISAAC K_S -band for A1835 (Richard et al., 2006) and A1689 (J. Richard et al., in preparation), and Subaru MOIRCS H -band for A1703 (Richard et al., 2009).

2.2.3.2 Palomar Observations

Using ground and space-based archival data we can probe the spectral region redward of the Balmer break for each arc, with the exclusion of A1413. Since this type of photometry is crucial for measuring the stellar mass, we took K_S -band imaging for A1413 using WIRC on the Palomar 200-inch telescope. We used a 9-point dithering pattern of two-minute frames for a total exposure time of 198 minutes.

2.3 Properties of Stellar Populations

2.3.1 Photometry

Since the arcs experience a large gravitational magnification, they tend to lie at short projected distances from foreground galaxies. It may then be necessary to subtract the light of the cluster galaxies in order to reliably measure the arc photometry. In these cases we used Galfit (Peng et al.,

2002), which allowed us to simultaneously fit many galaxies while taking into account the Point Spread Function (PSF) of the instrument, which was measured from bright, isolated stars in the field. This is particularly important when working with *Spitzer* IRAC images, which present a very large and asymmetric PSF.

Sometimes the gravitational arc emission is contaminated by the cluster bright central galaxy (BCG) luminous halo, and as a result the local background is hard to model. In these cases we fit the BCG using the Multi-Gaussian Expansion algorithm developed by Cappellari (2002). This method consists of fitting the surface brightness of a galaxy with a series of two-dimensional Gaussian functions, and is very effective for bright, extended galaxies.

After the subtraction of the foreground galaxies, the arc photometry is measured using polygonal apertures. The major source of uncertainty is generally the modeling of foreground galaxies and, for some IRAC images of crowded fields, confusion. The relative error in the flux is $\sim 30\%$ in the worst cases, but typically much less than that. All the photometric measurements are corrected for galactic extinction according to the map of Schlegel et al. (1998).

The photometric points are plotted for each arc in Figure 2.1 with a different color for each set of observations: red for *Hubble Space Telescope*, green for ground-based near-infrared, and purple for *Spitzer* data. When two gravitational images corresponding to the same source are available, the photometric analysis has been carried out independently on the different images, and the one less affected by foreground contamination was selected for the SED fitting. In these cases the name and the magnification factor of the chosen image are reported in Figure 2.1.

The WIRC K_S -band data for A1413 are not deep enough to detect the faint gravitational arc, because the contamination from the foreground BCG galaxy's halo is very strong. In this case we can only derive an upper limit on the flux, and we show it in Figure 2.1.

2.3.2 SED Fitting

For each target we fit the photometry from the observed UV to infrared using the stellar population models of Bruzual & Charlot (2003) in order to measure the stellar mass and other physical properties of the galaxies. We performed the fit using the chi-square minimization code FAST (Kriek et al., 2009) assuming the Calzetti et al. (2000) dust extinction law and a Chabrier (2003) initial mass function.

Since the emission lines detected in the Triplespec spectra are extremely bright compared to the continuum, we subtracted the measured line fluxes (see Section 2.4) from the appropriate photometric bands. The errors in the absolute flux calibration (see Section 2.2.2) are propagated through the corrected photometry. For targets with multiple images on the slit the correction is calculated taking the flux from the combined spectrum, which has the advantage of a better signal to noise ratio, and then appropriately scaling it using the *HST* photometry. The contribution of the emission

lines can be as high as 40% for a single band, but the effect on the stellar mass estimate is generally small: the average correction to the stellar mass is 0.10 dex. The only exception is A611, for which a combination of strong emission lines and small uncertainty on photometry causes the stellar mass to change by more than 2 sigma when applying the emission line correction.

Various stellar population parameters and degeneracies are involved in the process of SED fitting. One of the most important assumptions, and one that strongly affects the best-fit current SFR, is the star formation history. The widely used exponentially declining star formation history, or τ -model, may not be an appropriate choice since these galaxies are young and have a large gas reservoir. Sometimes an inverted τ -model is used for star-forming galaxies at high redshift. Both of these models require strong assumptions on the current state of the galaxy, i.e., that its star formation is currently at its minimum, or maximum, respectively. Also, they both introduce the free parameter τ which is usually not well-constrained by the data. For exponentially declining star formation histories, models with $\tau < 300$ Myr can give a formally acceptable fit to the data but usually fail in reproducing the SFR derived using other indicators (Wuyts et al., 2011). Since star-forming galaxies at high redshift are young, large values of τ imply a nearly flat star formation history. For these reasons we make the simplifying assumption of a constant star formation history. Shapley et al. (2005b) consider a sample of star forming galaxies at $z \sim 2$ and show that the agreement between stellar masses derived assuming τ -models or constant star formation history is very good, with no systematic offset and negligible dispersion. They also conclude that the choice of a particular SFH does not affect the uncertainty in the stellar mass measurement.

As shown by Wuyts et al. (2012a), the SED fit of low-mass star-forming galaxies tends generally to favor extremely young ages. Since a galaxy age cannot be smaller than the dynamical timescale, a lower limit on the SED age is often set. Following Wuyts et al. (2012a) we use 70 Myr as a lower limit, and the age of the Universe at the observed redshift as an upper limit. The effect of the age limit is not critical: lowering it to 20 Myr causes an average increase of 0.10 dex in both stellar mass and star formation rate.

One of the parameters involved in the SED fitting is the metallicity of the stellar population. This is different from the gas-phase metallicity, that we measure from rest-frame optical emission lines (see Section 2.4.3) and that can be higher than the stellar metallicity. The allowed values of stellar metallicity for the SED fitting are 0.2, 0.4, and 1.0 in units of solar metallicity. For some of the arcs, the best-fit value is significantly larger than the gas-phase metallicity. We attribute this unphysical result to the effect of SED fitting degeneracies. We performed a test for each arc by fitting the SED while keeping the metallicity fixed at the value closest to the one measured via emission lines. This results in slightly larger values of dust extinction, which is degenerate with metallicity. However, the effect is small: the offset is nearly always smaller than the error bar and the average change in dust extinction is $\langle \Delta E(B - V) \rangle = 0.07$. The other stellar population parameters are

Table 2.3. Emission Line Fluxes

Source	[OII] λ 3726, 3729	[NeIII] λ 3870	H β	[OIII] λ 4959	[OIII] λ 5007	H α	[NII] λ 6584
A611	15.9 \pm 4.5	34.0 \pm 8.6 ^a	90.4 \pm 4.1	43.3 \pm 6.0	< 4.1 ^a
RXJ2129	10.6 \pm 5.1 ^a	11.8 \pm 4.0 ^a	45.8 \pm 7.3	32.8 \pm 5.9	< 3.7
A1413	< 29 ^a	10.5 \pm 3.7	12.8 \pm 3.2 ^a	60.8 \pm 6.3 ^a	176 \pm 3	97.2 \pm 3.7	< 11 ^a
A1835	36 \pm 13	5.8 \pm 2.1	16.6 \pm 3.1	< 14 ^a	44.3 \pm 4.2	45.4 \pm 8.1	5.5 \pm 2.1
A773	23.8 \pm 9.7	< 24	8.3 \pm 3.5 ^a	15.3 \pm 3.4	49.0 \pm 5.2	47.2 \pm 7.6	< 9.2
MACS0717	19.3 \pm 9.0 ^a	< 9.1	8.5 \pm 2.9	4.4 \pm 1.7	18.3 \pm 2.3	18.9 \pm 4.9	< 6.0
A383	18.5 \pm 5.9	< 38 ^a	< 8.5 ^a	< 6.9 ^a	16.4 \pm 2.2	25.2 \pm 7.1	< 7.4
A1689	< 29 ^a	< 7.7 ^a	< 11 ^a	< 24 ^a	49.1 \pm 4.9
A1703	12.7 \pm 5.7	5.5 \pm 1.0	11.2 \pm 2.5	34.0 \pm 3.6	81.1 \pm 2.0

Note. — Fluxes in units of 10^{-17} erg s $^{-1}$ cm $^{-2}$. The listed uncertainties apply to flux ratios, and do not include the error in the absolute flux calibration. For undetected lines the 2- σ upper limit is given.

^aLines strongly contaminated by sky emission lines. The uncertainty on these lines does not include systematic effects due to sky residuals.

negligibly affected, and their uncertainties change only marginally.

It is important to note that among the SED fitting output parameters, stellar mass is the most robust (e.g., Wuyts et al., 2007), and is also the only one that is critical for our analysis. Star formation rate and dust extinction are more sensitive to the assumptions made, but it is possible to compare them with independent measurements from the rest-frame optical emission lines.

The best-fit spectra are shown in Figure 2.1, and the output parameters (stellar mass, dust extinction, age, and current star formation rate) for each arc are listed in Table 2.4. Stellar masses and star formation rates are corrected for the gravitational magnification. The stellar masses are in the range $7.8 < \log M_*/M_\odot < 9.4$, and are located at the low end of the mass distribution of the SDSS sample (e.g., Zahid et al., 2012a). The uncertainties are between 0.1 and 0.3 dex except for A1413, for which the low number of photometric points yields a large uncertainty in the stellar mass, $\Delta \log M_* = 0.36$ dex.

It is common practice to report the best-fit stellar mass (i.e., the one corresponding to the model that best describes the photometric data) and the 68% confidence region. The error bars are often highly asymmetric, and are very difficult to propagate when using the SED results in further analysis. In fact, a rigorous propagation of asymmetric error bars is possible only when the posterior distribution is known. Instead, we calculate the stellar mass posterior distribution from the chi-square grid output from FAST, and report the mean and the standard deviation of the distribution. The posterior distributions in $\log M_*$ are only weakly skewed and are well approximated by a Gaussian function. On the other hand, the best-fit value is often off-center, and choosing it as the best estimate would cause asymmetric error bars. Reporting the mean and standard deviation has the advantage of a straightforward propagation of the uncertainty in following calculations, which is essential for the present work. The same arguments apply to other stellar population parameters such as log SFR and dust extinction $E(B - V)$, and we follow the same method for estimating their

values. The stellar population age, however, presents a posterior distribution that is very skewed for those galaxies with a best-fit age near the lower limit, and therefore we list the best-fit value and the asymmetric 68% confidence interval, which we do not use in any further analysis.

2.4 Spectroscopic Diagnostics

The goal of this study is to explore the relation between stellar mass, star formation rate, and gas metallicity for star-forming galaxies at high redshift. In the previous section we derived the stellar masses using photometric data. In this section we use the rest-frame optical emission lines of the gravitational arcs to measure their star formation rate and metallicity.

In order to derive physical quantities from the observed spectra, we need to quantitatively analyze the emission lines. Each emission line profile was fitted with one Gaussian (two for the doublet [OII] λ 3726, 3729). For each line we derived flux, redshift, width, and continuum level from the fit. For the faintest lines we fixed one or more of these parameters using as a reference [OIII] λ 5007 or H α , which have a relatively high signal to noise ratio. The line fluxes are reported in Table 2.3. Some of the emission lines fall in the vicinity of bright sky emission features. In such cases, sky subtraction residuals may bias the Gaussian fits, because of an imperfect estimate of the error spectrum. This effect is not included in the random uncertainties given in Table 2.3; however, we mark those measurements which might be affected by a large systematic error.

The Galactic extinction is very small for all the objects considered, and negligible compared to the uncertainty on the fluxes.

The redshifts of the gravitational arcs, measured from [OIII] λ 5007, are given in Table 2.1. In two cases we found that previously published redshifts were incorrect (A611 and RXJ2129, Richard et al., 2010) due to misidentification of rest-frame UV spectral features.

2.4.1 Dust Extinction

We estimated dust reddening using the H α /H β flux ratio. Assuming a case B recombination and typical temperature (10,000 K) and density (100 cm^{-3}), the theoretical value of the ratio is 2.87 (Osterbrock & Ferland, 2006). We used the Calzetti et al. (2000) law to derive the dust extinction from the observed flux ratio. Since a negative extinction is unphysical, but can be consistent with the measured Balmer decrement because of large uncertainties, we take a Bayesian approach and use a flat, positive prior for $E(B - V)$. The results are shown in Figure 2.2 and compared to the dust extinction derived from the SED fitting. The dotted error bars indicate the measurements affected by sky emission. The two methods are in good agreement and provide very low dust extinction for most of the arcs. The only object with a large discrepancy between the two measurements of dust extinction is A1413, for which the Balmer decrement gives $E(B - V) \sim 0.8$. We attribute

Table 2.4. Physical Properties of the Sample of Star-Forming Galaxies

Source	$\log(M_*/M_\odot)^a$	$E(B - V)^a$	$\log(\text{Age}/\text{yr})^a$	$\text{SFR}_{\text{SED}}^a$ (M_\odot/yr)	$\text{SFR}_{\text{H}\alpha}^b$ (M_\odot/yr)	Line width ^b (km/s)	$12 + \log(\text{O}/\text{H})^b$	FMR residual ^c
A611	8.27 ± 0.09	0.11 ± 0.03	$8.3^{+0.3}_{-0.4}$	1.7 ± 0.5	2.0 ± 1.1	27 ± 5	7.89 ± 0.19	-0.11 ± 0.20
RXJ2129	7.80 ± 0.25	0.18 ± 0.02	$7.9^{+0.1}_{-0.0}$	0.9 ± 0.5	0.6 ± 0.4	39 ± 10	7.89 ± 0.40	0.04 ± 0.42
A1413	8.72 ± 0.36	0.07 ± 0.06	$8.0^{+0.5}_{-0.1}$	3.1 ± 1.7	7.2 ± 4.3	30 ± 3	7.89 ± 0.33	-0.26 ± 0.38
A1835	8.33 ± 0.22	0.10 ± 0.07	$8.8^{+0.4}_{-1.0}$	1.1 ± 0.7	1.0 ± 0.7	54 ± 7	8.45 ± 0.07	0.37 ± 0.14
A773	9.16 ± 0.21	0.10 ± 0.05	$8.7^{+0.4}_{-0.5}$	4.6 ± 2.7	4.4 ± 2.7	50 ± 7	8.32 ± 0.11	-0.09 ± 0.17
MACS0717	9.36 ± 0.19	0.27 ± 0.02	$7.9^{+0.1}_{-0.1}$	34 ± 15	15 ± 10	65 ± 8	8.53 ± 0.10	0.10 ± 0.15
A383	8.67 ± 0.16	0.12 ± 0.04	$8.1^{+0.6}_{-0.3}$	3.4 ± 1.3	3.8 ± 2.3	54 ± 8	8.56 ± 0.10	0.40 ± 0.14
A1689	8.27 ± 0.24	0.10 ± 0.02	$8.0^{+0.3}_{-0.2}$	2.2 ± 1.3	...	80 ± 9	7.89 ± 0.39	-0.10 ± 0.41
A1703	8.49 ± 0.27	0.09 ± 0.03	$8.6^{+0.7}_{-0.7}$	1.0 ± 0.5	4.1 ± 2.9	34 ± 3	7.84 ± 0.14	-0.23 ± 0.21

Note. — Stellar masses and star formation rates are corrected for the gravitational magnification.

^aDerived from SED fitting.

^bDerived from rest-frame optical emission lines.

^cDifference between the measured metallicity and the metallicity predicted by the FMR as formulated by Mannucci et al. (2011).

this very large value to the effect of sky emission on the $H\beta$ flux, since all the other galaxies in our sample have $E(B - V) < 0.3$. The SED fit for this galaxy, although uncertain, being based on only two photometric points, gives a dust extinction very similar to that found for the other arcs, $\langle E(B - V) \rangle = 0.13$.

The Balmer decrement probes the extinction in the HII regions, where the nebular emission originates, while the SED fit output applies to the overall stellar population of a galaxy. In principle by comparing the dust extinction obtained by the two methods it is possible to study the dust distribution, which can be concentrated in star-forming regions. Calzetti et al. (1994) found that for local starburst galaxies the nebular dust extinction is roughly twice the extinction of the stellar continuum. At $z \sim 2$ it is not clear whether there is a difference between the reddening experienced by stellar and gas emission (e.g., Erb et al., 2006b; Hainline et al., 2009; Förster Schreiber et al., 2009). Our data suggest a similar amount of attenuation for the two components, but the $H\beta$ flux determinations are too noisy to draw any conclusion. When in the following analysis we correct the emission line fluxes for dust extinction, we always use the SED fitting values, which are less affected by uncertainty. This method could underestimate the dust extinction experienced by gas emission by a factor of 2, which translates into an average increase in SFR of only 0.15 dex.

2.4.2 Lack of AGN Contribution

To exclude the possibility of any AGN contribution to the gravitational arc emission, in Figure 2.3 we show the $[\text{OIII}]\lambda 5007/H\beta$ versus $[\text{NII}]\lambda 6584/H\alpha$ line ratio diagram (BPT diagram, Baldwin et al., 1981). In this plot star-forming galaxies and AGN populate separate regions due to the different ionization mechanisms at the origin of the line emission. All the gravitational arcs lie on or near the star-forming branch of the diagram, and we can firmly exclude the presence of AGN in our sample.

It is interesting to note that the location of these $z \sim 2$ star-forming galaxies on the BPT diagram is not coincident with the region most populated by low-redshift galaxies. In particular, none of our objects lie in the region $\log([\text{OIII}]\lambda 5007/H\beta) < 0$, where the majority of local galaxies are found. A large $[\text{OIII}]\lambda 5007/H\beta$ ratio has already been reported in many studies of high-redshift star-forming galaxies (Shapley et al., 2005a; Erb et al., 2006a, 2010; Hainline et al., 2009; Richard et al., 2011; Rigby et al., 2011), and is indicative of a high ionization parameter, as extensively discussed by Erb et al. (2010).

2.4.3 Metallicities

Rest-frame optical nebular lines contain a large amount of information on the physical conditions of the gas responsible for the emission, including its metallicity. If the auroral line $[\text{OIII}]\lambda 4363$ is detected, then it is possible to calculate the electron temperature and have a direct measurement of

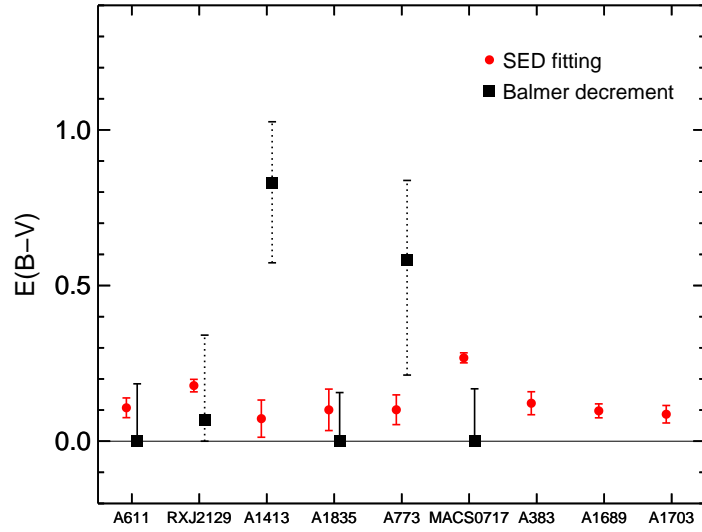


Figure 2.2 Dust extinction $E(B - V)$ derived from SED fitting (red circles) and Balmer decrement (black squares). Dotted error bars indicate measures affected by sky line contamination.

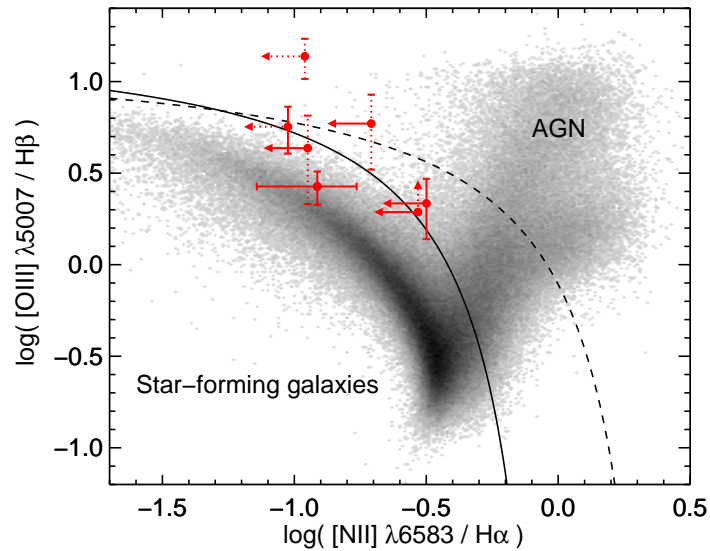


Figure 2.3 BPT diagram (Baldwin et al., 1981). Our sample (red points) is compared to the SDSS sample (gray density map, Kauffmann et al., 2003b). Also shown are the theoretical (dashed line, Kewley et al., 2001) and empirical (solid line, Kauffmann et al., 2003b) separation between active galactic nuclei and star-forming galaxies. Dotted error bars indicate the line ratios that are contaminated by sky emission.

the metallicity. Unfortunately this line is so weak that at high redshift it has been detected only for a handful of objects. Instead, we derived the gas metallicity from the flux ratio of strong emission lines. There are several well-established methods to estimate the metallicity from flux ratios, calibrated using either theoretical calculations or observations of low-redshift galaxies. The absolute metallicity obtained with these methods is highly uncertain, and the different sets of calibrations, when applied to the same observations, give results that can differ by as much as 0.7 dex (Kewley & Ellison, 2008). Although this discrepancy makes it very difficult to compare observational results obtained with different calibrations, relative measurements obtained with the same strong line method are much more reliable.

The main goal of the present study is to test whether the locally determined fundamental metallicity relation applies to high-redshift galaxies as well. The natural choice is then to use the same metallicity calibrations adopted by Mannucci et al. (2010) in the definition of the local relation. These are the empirical calibrations of Maiolino et al. (2008), which give a polynomial fit for the value of various nebular line ratios as a function of the gas metallicity. The main line ratios are $[\text{OIII}]\lambda 5007/\text{H}\beta$ and $[\text{OIII}]\lambda 5007/[\text{OII}]\lambda 3726, 3729$, while $[\text{NII}]\lambda 6584/\text{H}\alpha$ and $[\text{NeIII}]\lambda 3870/[\text{OII}]\lambda 3726, 3729$ were used only for some arcs, mostly as upper or lower limits. We also used $[\text{OIII}]\lambda 5007/\text{H}\alpha$, whose calibration we derive from $[\text{OIII}]\lambda 5007/\text{H}\beta$ assuming the theoretical value for the Balmer ratio. We note, however, that these two line ratios do not give independent measurements of the metallicity. From the plots shown in Maiolino et al. (2008) we estimate a scatter in the relations between line ratios and abundance of 0.10 dex, and we add this contribution to the uncertainty calculation.

Figure 2.4 shows the gas metallicity for our sample, derived using the available line ratios. For each arc the final metallicity is the weighted average of the single measurements, not considering upper or lower limits, and is shown in gray in the plot (and listed in Table 2.4). From this figure it is clear that the different line ratios give results that are always consistent within the error bars, and this is an important confirmation of the reliability of this method.

The relation between $[\text{OIII}]\lambda 5007/\text{H}\beta$ and the metallicity is not monotonic, and presents a maximum at $12 + \log(\text{O}/\text{H}) = 7.89$. Since this is a stationary point, any uncertainty in the line ratio is transformed into a much larger uncertainty in the metallicity. About half of our sample is found in this location, with large uncertainties on $\log(\text{O}/\text{H})$, up to 0.4 dex. The shape of this calibration also causes the existence of two possible metallicity values in some cases, but an unambiguous solution is always found thanks to the other line ratios.

In Figure 2.4 the metallicities derived from diagnostics that involve at least one line contaminated by sky emission are plotted as dotted lines. They are generally consistent with the other line ratios, although most of them have very large uncertainties and do not influence the weighted average in an appreciable way. We therefore conclude that our results do not depend on the emission lines affected by sky residuals. The only exception is A1689, for which only one upper limit and one lower

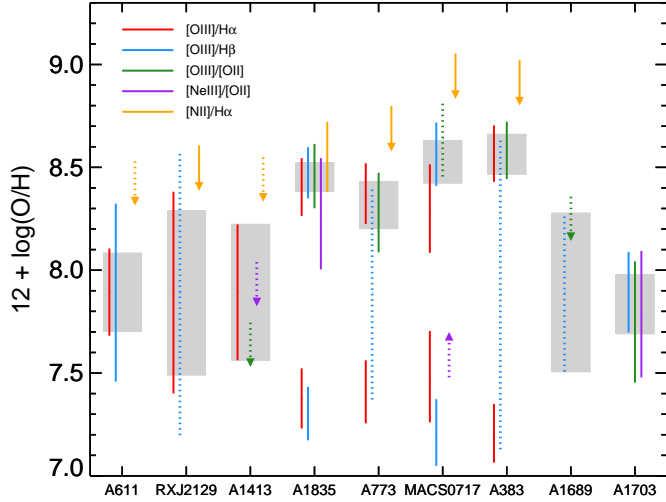


Figure 2.4 Gas metallicity derived using different line ratios adopting the calibrations of Maiolino et al. (2008). For each object the gray region shows the weighted mean. Dotted lines indicate ratios involving at least one line contaminated by sky emission.

limit on the line ratios are available, and both may be contaminated by sky emission. Although the lower limit on the $[\text{OIII}]\lambda 5007/\text{H}\beta$ ratio gives a finite confidence interval in $\log(\text{O}/\text{H})$ thanks to the non-monotonic metallicity calibration, we note that the abundance for this galaxy is not reliable.

One of the most widely used metallicity diagnostics is R_{23} , defined as the ratio between the oxygen lines ($[\text{OII}]\lambda 3726, 3729 + [\text{OIII}]\lambda 4959 + [\text{OIII}]\lambda 5007$) and $\text{H}\beta$. Although this line ratio, with the Maiolino et al. (2008) calibration, gives results that are consistent with the other diagnostics, we do not use it because it is not independent on the line ratios $[\text{OIII}]\lambda 5007/\text{H}\beta$ and $[\text{OIII}]\lambda 5007/[\text{OII}]\lambda 3726, 3729$. Using these two line ratios instead of R_{23} has the advantage of isolating the abundance determinations which are affected by sky residuals.

It is worth remarking that the ratio between the flux of two lines is independent of the absolute flux calibration even for lines that lie in very distant parts of the spectrum, since Triplespec allows us to observe the J , H , and K band simultaneously. It is also independent of gravitational magnification and slit loss. We corrected the line fluxes for dust extinction, using the SED fitting results, in a differential way: the ratio of two lines depends only on the ratio of the attenuation at the corresponding wavelengths. This results in a small correction to the metallicity estimate and its uncertainty.

The metallicity of the two gravitational arcs A1689 and A1835 has already been measured by Richard et al. (2011) from near-infrared spectra obtained with Keck NIRSPEC and using the same set of Maiolino et al. (2008) calibrations. Our results are in good agreement for both arcs. In particular, Richard et al. detect $\text{H}\beta$ and $[\text{OIII}]\lambda 5007$ in the spectrum of A1689, obtaining $12 + \log(\text{O}/\text{H}) = 8.00^{+0.44}_{-0.50}$, a value very close to our estimate. For this reason we will not exclude A1689 from our sample despite the poor quality of its spectrum.

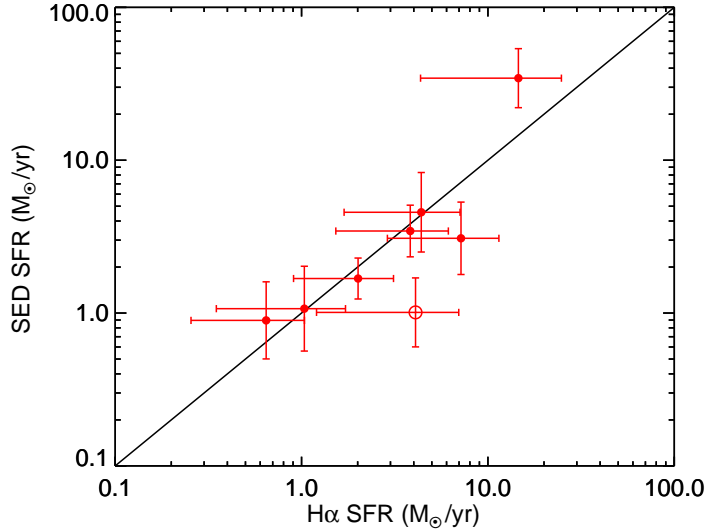


Figure 2.5 Comparison of star formation rates derived using two methods: SED-fitting and $H\alpha$ flux. The empty circle is A1703 for which $H\beta$ has been used as a proxy for $H\alpha$.

2.4.4 Star Formation Rates

We derived the current star formation rate from the extinction-corrected $H\alpha$ emission flux using the calibration given by Kennicutt (1998), dividing the result by 1.7 to convert to that appropriate for a Chabrier IMF. The resulting star formation rates, corrected for the gravitational magnification, are reported in Table 2.4.

The SFR derived from nebular emission accounts for the star formation activity in the physical region of the arc that is covered by the slit, which is different, in principle, from the star formation rate of the entire galaxy. But the narrow gravitational arcs from our sample are easily covered by the 1 arcsec wide slit, as is apparent from the image stamps in Figure 2.1. Therefore we do not attempt to correct for this effect, which is in any case less important than the uncertainty caused by slit alignment and seeing variability.

Figure 2.5 shows excellent agreement between the star formation rates calculated using SED fitting and $H\alpha$ flux. This is encouraging because it validates the numerous assumptions made in the derivation of the star formation rates. It is particularly interesting that the agreement between SED-fitting and nebular emission even holds for A1413, where only two photometric points are available. It is possible that the simplifying choice of a constant star formation history, with the consequent decrease in the number of free parameters, helped reduce the scatter in the comparison between the two methods.

In the following section we will always use the star formation rate derived from the $H\alpha$ flux. The spectra of the two objects at $z > 3$ do not include $H\alpha$, which is redshifted outside the Triplespec range. For one of them (A1703, empty circle in Figure 2.5) we use the observed flux of $H\beta$ as a proxy for $H\alpha$, assuming the theoretical line ratio discussed in Section 2.4.1 and correcting for dust

extinction. For A1689, for which both $H\alpha$ and $H\beta$ are not available, we use the SED fitting star formation rate.

2.4.5 Line Widths

The broadening of the emission lines due to the gas kinematics depends on the gravitational well of the galaxies. Measuring the line widths can then give an estimate on the gravitational arc masses that is independent of SED fitting and gravitational lensing models.

The observed velocity width of the nebular lines need to be corrected for the instrumental resolution, which was measured from the sky OH lines. For each source we extracted the spectrum of the sky using the same procedure followed to extract the arc spectrum. We measured the dispersion of the brightest, unblended OH lines, which is 40-55 km s⁻¹ depending on spectral order and wavelength. We calculated a linear fit of the ratio of the spectral resolution R to the order m as a function of wavelength, and used this to estimate the instrumental resolution for each nebular line.

Most of the arc emission lines are well-resolved. For each source we take the weighted mean of the line widths of all the well-detected lines excluding [OII] λ 3726, 3729, which is a doublet and is not completely resolved. The results are listed in Table 2.4.

Since a detailed lensing map is needed to measure the intrinsic radius of the gravitational arcs, we do not attempt to estimate the dynamical masses. The observed velocity dispersions, however, are unusually low if compared to the results of similar studies (Law et al., 2009; Förster Schreiber et al., 2009; Jones et al., 2010). This is an important confirmation of the low masses found in our sample.

2.5 Results

In this section we combine our measurements of stellar mass, gas metallicity and star formation rate to explore the properties of our sample of low-mass galaxies. In particular, the goal of this work is to test whether high-redshift galaxies follow the local fundamental metallicity relation, claimed to be valid up to at least $z \sim 2.2$ (Mannucci et al., 2010).

2.5.1 The Mass–Metallicity Relation

The mass-metallicity relation for our sample is plotted in Figure 2.6 together with the fit to the local relation from Kewley & Ellison (2008) and to the high-redshift one of Erb et al. (2006a). All the results shown in this figure have been derived using the same set of metallicity calibrations (the fits shown are taken from Maiolino et al., 2008, and are corrected for the choice of IMF).

The magnification caused by gravitational lensing allows us to probe stellar masses much smaller than those considered in previous studies of unlensed galaxies, even in the nearby Universe. This

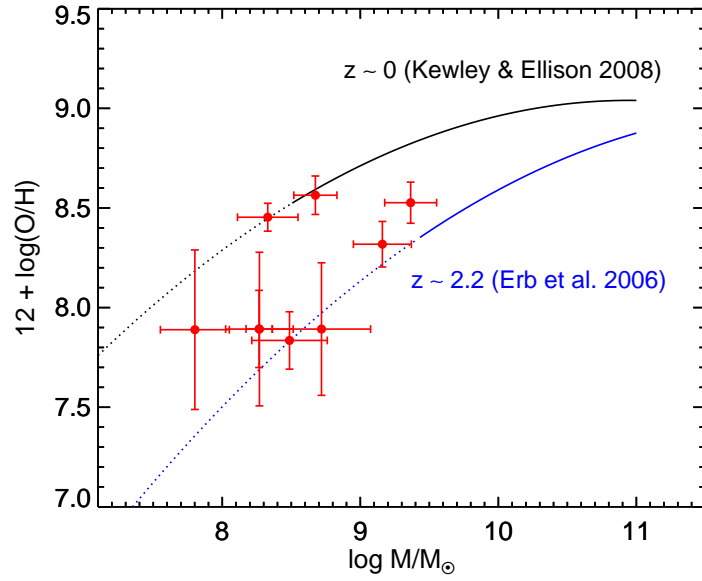


Figure 2.6 Mass-metallicity relation for our sample (red points). The fit to the relation at $z \sim 0$ (black solid line, Kewley & Ellison, 2008) and $z \sim 2.2$ (blue solid line, Erb et al., 2006a) are also shown. Note that these fits are calculated using the Maiolino et al. (2008) metallicity calibrations. The dashed lines are extrapolation at low masses.

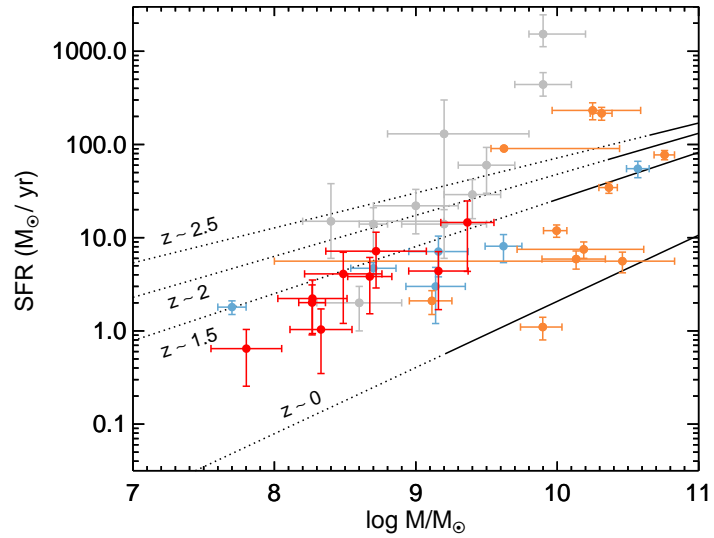


Figure 2.7 Star formation rate versus stellar mass diagram. The main sequence of star-forming galaxies is shown in black at $z \sim 0$ (Zahid et al., 2012b) and at high redshift (Whitaker et al., 2012b), with dotted lines being the extrapolation at masses below the completeness limit. Our sample (red points) is roughly on the main sequence at $z \sim 2$. Points from other studies of lensed galaxies at high redshift are shown: Richard et al. (2011) in orange, Wuyts et al. (2012b) in gray, and Christensen et al. (2012) in blue.

makes a direct comparison difficult, but it is clear from Figure 2.6 that our points do not lie on the extrapolation of neither the $z \sim 0$ nor the $z \sim 2$ relations, and have a substantial scatter, larger than the observational uncertainties.

Yuan et al. (2013) measured the mass-metallicity relation for a sample of gravitational arcs at $z \sim 2$ obtained by combining their data with results from previous studies. Although a comparison of the absolute measurements is not possible because they use a different metallicity calibration, their results are similar to ours: the lensed galaxies tend to have lower metallicities than the SDSS galaxies but do not lie on a tight sequence.

This results are consistent with the hypothesis of a mass-metallicity relation dependent on some other parameter that is not necessarily the redshift. In the remaining parts of this section we will explore the role of the star formation rate.

2.5.2 Star Formation Rate versus Stellar Mass

In Figure 2.7 we show the location of our sample in the SFR-stellar mass diagram (red points), compared to the results of other studies of lensed galaxies at high redshift: Richard et al. (2011, in orange), Wuyts et al. (2012b, in gray), and Christensen et al. (2012, in blue). Our sample populates the lower left corner, with masses and star formation rates on average lower than what probed by previous studies. In particular, we more than doubled the number of low-mass galaxies ($M_* < 10^9 M_\odot$) at this redshift with known metallicity and SFR.

In the mass-SFR plane, star-forming galaxies lie on a relatively tight relation often called the main sequence (Noeske et al., 2007). This sequence evolves strongly with redshift, with the normalization decreasing over cosmic time at least since $z \sim 2.5$ (Whitaker et al., 2012b; Zahid et al., 2012b, black lines in Figure 2.7). The gravitational arcs that we selected have star formation rates that are on or below the main sequence at $z \sim 2$. Previous studies of lensed galaxies did not reach such low values of SFR, with the exception of the work of Christensen et al. (2012).

The very low star formation rate of these arcs, between 0.6 and 15 M_\odot/yr , is of fundamental importance in this study. First, the fact that our sample lies on the main sequence means that these galaxies are representative of the typical population of star-forming galaxies. Shallower studies are biased towards luminous galaxies with star formation rates much higher than the main sequence. These objects are thought to be in a starburst phase, potentially caused by a merger, and are not representative of the typical conditions of star-forming galaxies. Secondly, it allows us to compare high and low redshift galaxies with similar star formation rates, and thereby directly address the goals of this study. From Figure 2.7 we can see that local massive galaxies ($9.5 < \log M_*/M_\odot < 11$) that lie on the main sequence at $z \sim 0$ have SFRs comparable to our sample. This is not the case for the majority of lensed galaxies considered by previous studies.

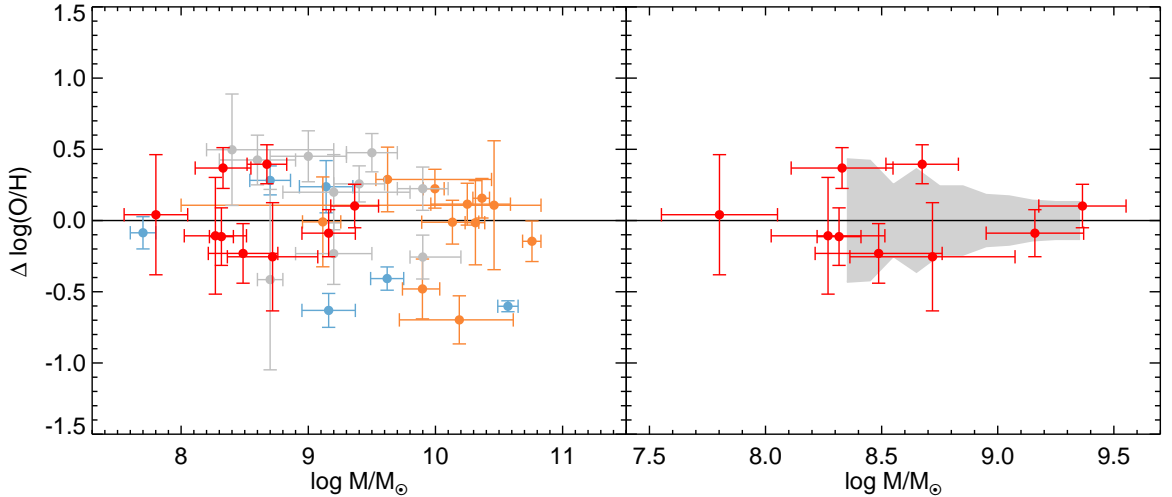


Figure 2.8 Difference between measured metallicity and the prediction of the fundamental metallicity relation. *Left:* Our residuals (red points) are compared to previous high-redshift studies, color-coded as in Figure 2.7. *Right:* Our points are compared to the SDSS low-mass sample, whose standard deviation is shown in gray. In both panels A611 is offset by 0.05 dex in mass for clarity.

2.5.3 The Fundamental Metallicity Relation

We now turn our attention to the fundamental metallicity relation, a surface in the 3D parameter space of stellar mass, metallicity and star formation rate tightly followed by the SDSS galaxies discovered by Mannucci et al. (2010) and extended to low masses by Mannucci et al. (2011). In Figure 2.8 we plot for each gravitational arc the difference between the metallicity that we measure from nebular lines and the metallicity predicted by the local FMR given its stellar mass and star formation rate. We also show the points from previous studies of lensed galaxies. Although high-redshift galaxies seem to roughly follow the local relation, some of the samples shown in Figure 2.8 show a systematic offset. Since our sample is more strictly selected in terms of star formation, we will limit the quantitative analysis to our 9 gravitational arcs.

The weighted average of the residuals for our sample is 0.12 ± 0.06 dex. However, the weighted mean is skewed toward galaxies with higher metallicity since they are measured with higher precision, because the metallicity calibrations are not linear. This is clear from Figure 2.4, where the group of galaxies aligned at $12 + \log(\text{O}/\text{H}) \sim 7.9$, the maximum of the $[\text{OIII}]\lambda 5007/\text{H}\beta$ line ratio calibration, present the largest error bars. The arithmetic mean is not affected by this bias, and gives $\langle \Delta \log(\text{O}/\text{H}) \rangle = 0.01 \pm 0.08$. The agreement of high-redshift lensed galaxies with the local fundamental metallicity relation is remarkable, and strongly suggests that these objects lie on the relation independently of their redshift at least up to $z \sim 3$. This represents the first clear result for high-redshift galaxies with $M < 10^9 M_{\odot}$, and the first time that the universality of the FMR is confirmed using galaxies at high redshift with a SFR which is observed in typical galaxies in the local Universe.

2.5.4 The Scatter in the Fundamental Metallicity Relation

Our gravitational arcs show a relatively small scatter around the local fundamental metallicity relation. The standard deviation of the metallicity offsets from the FMR is 0.24 dex, and the mean error in $\Delta \log(\text{O}/\text{H})$ is 0.25 dex. Also, none of the gravitational arcs is more than 3σ away from the local fundamental metallicity relation. These two facts suggest that the observed scatter could be in principle just a product of observational uncertainties. In contrast, the standard deviation found by Mannucci et al. (2011) for the SDSS sample is about 0.4 dex at $10^{8.4} M_{\odot}$, and is shown in gray in the right panel of Figure 2.8 as a function of stellar mass. Note that roughly 32% of the galaxies in the local sample fall outside of the shaded area, while only one among the high-redshift galaxies does not lie in this region. Although Mannucci et al. (2011) do not report the typical errors on mass, star formation rate, and metallicity, they claim that the observational uncertainties are not large enough to explain the observed dispersion. Furthermore, SDSS galaxies are selected by requiring a signal to noise ratio greater than 25 for the $\text{H}\alpha$ flux, and therefore the uncertainty in their metallicity must be much smaller than for our sample.

In order to facilitate the comparison with studies at different redshifts, we estimate the intrinsic scatter in the fundamental metallicity relation using a Bayesian framework. We assume that each measured metallicity residual $\Delta_i \equiv \Delta \log(\text{O}/\text{H})_i$ is normally distributed around its *true* value $\tilde{\Delta}_i$ with standard deviation given by the observational uncertainty σ_i :

$$p(\Delta_i | \tilde{\Delta}_i, \sigma_i) = \frac{1}{\sqrt{2\pi} \sigma_i} \exp \left[-\frac{1}{2} \frac{(\Delta_i - \tilde{\Delta}_i)^2}{\sigma_i^2} \right]. \quad (2.1)$$

We also assume that the true values $\tilde{\Delta}_i$ are normally distributed around zero with an intrinsic dispersion $\tilde{\sigma}$:

$$p(\tilde{\Delta}_i | \tilde{\sigma}) = \frac{1}{\sqrt{2\pi} \tilde{\sigma}} \exp \left[-\frac{1}{2} \frac{\tilde{\Delta}_i^2}{\tilde{\sigma}^2} \right]. \quad (2.2)$$

Note that by centering the Gaussian distribution on zero, we are setting the local FMR to hold at high-redshift. This is in agreement with our observations, as we showed in the previous section. Since we do not know the true value of each data point, we need to marginalize over $\tilde{\Delta}_i$ in order to obtain the probability density function of the observed Δ_i :

$$p(\Delta_i | \sigma_i, \tilde{\sigma}) = \int \left[p(\Delta_i | \tilde{\Delta}_i, \sigma_i) \cdot p(\tilde{\Delta}_i | \tilde{\sigma}) \right] d\tilde{\Delta}_i, \quad (2.3)$$

and we finally obtain the likelihood function:

$$\begin{aligned}\mathcal{L}(\tilde{\sigma}) &= \prod_i p(\Delta_i | \sigma_i, \tilde{\sigma}) \\ &= \prod_i \frac{1}{\sqrt{2\pi}(\sigma_i^2 + \tilde{\sigma}^2)} \exp\left(-\frac{1}{2} \frac{\Delta_i^2}{\sigma_i^2 + \tilde{\sigma}^2}\right).\end{aligned}\tag{2.4}$$

Finally, using a uniform prior, the posterior distribution for $\tilde{\sigma}$ is simply proportional to the likelihood.

The likelihood function peaks at an intrinsic dispersion of 0.20 dex, and calculating mean and standard deviation gives $\tilde{\sigma} = 0.24 \pm 0.11$ dex. This calculation shows that although a zero intrinsic dispersion is very unlikely, our data favor a value smaller than the one found in the local Universe. Despite the low number of data points, we can robustly rule out very large intrinsic dispersions: the 95% confidence interval upper limit is $\tilde{\sigma} < 0.44$ dex.

2.6 Discussion

Our data confirm that the fundamental metallicity relation applies to low-mass galaxies at $1.5 < z < 3$. This suggests that this relation is time-invariant and therefore universal.

In the equilibrium model of Finlator & Davé (2008), metallicity and star formation rates are tightly connected to gas inflows and outflows, so that a change in one implies a consequent change in the other (see also Davé et al., 2011a, 2012). If each of these processes are in equilibrium, then the FMR is naturally explained. If a galaxy is perturbed, e.g., by a minor merger, after a certain time it will return to the equilibrium configuration. The observed evolution in the mass-metallicity relation could be due to the fact that we are sampling galaxy populations with different star formation rates at different redshifts. This would explain why our points do not lie on the low-mass end of the $z \sim 2$ mass-metallicity relation from Erb et al. (2006a), that was determined using relatively high-SFR galaxies.

The analysis of the FMR scatter may provide a valuable additional constraint for numerical or analytical models of galaxy evolution. This is particularly important at low masses, where models have diverging predictions (Zahid et al., 2012a). In the equilibrium model, the observed scatter of the FMR is determined by how quickly a perturbed galaxy can return to equilibrium. This timescale in turn depends on the mass loading factor, a parameter that is fundamental for hydrodynamic simulations. The observation of the scatter in the FMR at different stellar masses and redshifts therefore gives important constraints on numerical models of galaxy evolution, even though current simulations do not resolve stellar masses below $10^9 M_\odot$ (e.g., Davé et al., 2011b).

Our results suggest a low scatter around the fundamental metallicity relation at high redshift, lower than what found by Mannucci et al. (2011) in the local Universe. In another study of low-redshift galaxies, Bothwell et al. (2013) investigated the relation between stellar mass, star formation

rate, and gas content and found that it is at least as tight as the FMR. Interestingly, they found an increase in the dispersion for $M_* < 10^9 M_\odot$, a confirmation of the results of Mannucci et al. (2011). They attribute the increase in scatter to the fact that low-mass galaxies contain a gas mass comparable to the mass of infalling neutral hydrogen clouds, with the result that the accretion process is not smooth but discontinuous and stochastic.

This trend is also confirmed by the results of Henry et al. (2013), which studied a sample of low-mass galaxies at $z = 0.6 - 0.7$ and found not only a good agreement with the local fundamental metallicity relation, but also a tight dispersion of 0.20 dex that could be explained by the observational uncertainties.

Hunt et al. (2012) analyzed a sample of 1100 galaxies at $0 < z < 3.4$ that includes many low-mass galaxies, and found a fundamental plane in the SFR, stellar mass, and metallicity space, which is independent on redshift and with a scatter of 0.17 dex. Although this dispersion is much smaller than the one found locally by other studies, Hunt et al. (2012) do not investigate the dependence of the scatter on redshift and mass. Most importantly, in contrast to the other studies mentioned so far, they do not use the Maiolino et al. (2008) metallicity calibrations, so a direct comparison is very difficult.

An interesting perspective on the issue of the FMR scatter has been pointed out by Zahid et al. (2012a). They studied the mass-metallicity relation at $z \sim 0$ using various samples from the literature and found a clear increase in the intrinsic scatter at low stellar masses. They suggest the possibility that this scatter is due to a population of low-mass, metal-rich galaxies which are near the end of their star formation. At a fixed mass, the same amount of metals would give a higher metallicity measurement, since there is little gas left. Assuming that the scatter in the FMR is directly caused by the scatter in the mass-metallicity relation, our observations agree well with this scenario, since at high redshift such a population of low-mass galaxies terminating their star-formation would not be expected. For conclusive results on the evolution of the intrinsic FMR scatter, however, a larger high-redshift sample is needed, together with a rigorous analysis of the observational uncertainties in the local sample.

2.7 Summary

We present near-infrared spectroscopic data for 9 gravitational arcs between redshift 1.5 and 3.3, and the measurement of their stellar mass, gas metallicity, and star formation rate. The use of strong gravitational lensing allows us to probe very low masses and star formation rates. Our sample more than doubles the number of galaxies with stellar masses below $10^9 M_\odot$ at $z \sim 2$ with known metallicity and SFR. Our main goal is to test whether these galaxies follow the fundamental metallicity relation discovered for local galaxies.

We find that the gravitational arcs lie above the mass-metallicity relation at $z \sim 2$ but below the local relation. However, they also have SFRs that are roughly on the main sequence of star-forming galaxies. This means that they are representative of typical star-forming galaxies, i.e., they are not in a starburst phase.

Our data are fully consistent with the local fundamental metallicity relation (Mannucci et al., 2010, 2011), with a mean metallicity offset of 0.01 ± 0.08 dex. The dispersion around the FMR of 0.24 dex is smaller than the one measured for local galaxies, and represents an important additional constraint for galaxy evolution models.

We acknowledge Kevin Bundy for providing the WIRC reduction pipeline, Eiichi Egami for the IRAC mosaic images, and Marceau Limousin and Drew Newman for some of the magnification factors. We thank Drew Newman and Gwen Rudie for useful discussions. We also thank the anonymous referee for helpful comments and suggestions. RSE and SB are supported for this work via NSF grant 0909159. JR is supported by the Marie Curie Career Integration Grant 294074.

Chapter 3

Velocity Dispersions and Dynamical Masses for a Large Sample of Quiescent Galaxies at $z > 1$: Improved Measures of the Growth in Mass and Size

Abstract

We present Keck LRIS spectroscopy for a sample of 103 massive ($M > 10^{10.6} M_{\odot}$) galaxies with redshifts $0.9 < z < 1.6$. Of these, 56 are quiescent with high signal-to-noise absorption line spectra, enabling us to determine robust stellar velocity dispersions for the largest sample yet available beyond a redshift of 1. Together with effective radii measured from deep *Hubble Space Telescope* images, we calculate dynamical masses and address key questions relating to the puzzling size growth claimed by many observers for quiescent galaxies over the redshift interval $0 < z < 2$. Our large sample provides the first opportunity to carefully examine the relationship between stellar and dynamical masses at high redshift. We find this relation closely follows that determined locally. We also confirm the utility of the locally-established empirical calibration, which enables high-redshift velocity dispersions to be estimated photometrically, and we determine its accuracy to be 35%. To address recent suggestions that progenitor bias — the continued arrival of recently-quenched larger galaxies — can largely explain the size evolution of quiescent galaxies, we examine the growth at fixed velocity dispersion assuming this quantity is largely unaffected by the merger history. Using the velocity dispersion - age relation observed in the local universe, we demonstrate that significant size and mass growth have clearly occurred in individual systems. Parameterizing the relation between mass and size growth over $0 < z < 1.6$ as $R \propto M^{\alpha}$, we find $\alpha = 1.6 \pm 0.3$, in agreement with theoretical expectations from

A version of this chapter has been published as Belli, S., Newman, A. B., & Ellis, R. S. 2014a, ApJ, 783, 117

simulations of minor mergers. Relaxing the assumption that the velocity dispersion is unchanging, we examine growth assuming a constant ranking in galaxy velocity dispersion. This approach is applicable only to the large-dispersion tail of the distribution, but yields a consistent growth rate of $\alpha = 1.4 \pm 0.2$. Both methods confirm that progenitor bias alone is insufficient to explain our new observations and that quiescent galaxies have grown in both size and stellar mass over $0 < z < 1.6$.

3.1 Introduction

Understanding the assembly history of the homogeneous population of present-day spheroidal galaxies remains an outstanding question in extragalactic astronomy. Studies of the fundamental plane of spheroidal galaxies at $z < 1$ (Treu et al., 2005a; van der Wel et al., 2005) confirmed that the most massive galaxies formed the bulk of their stars at $z > 2$, whereas less massive systems continued their assembly at later times. Deep near-infrared imaging meanwhile located a population of $z > 2$ massive quiescent galaxies (Franx et al., 2003), suggesting these are the precursors of the most massive local objects. However, surprisingly, these distant red galaxies are *physically small*, with half-light radii 3-5 times less than their local counterparts of similar stellar mass (e.g., Daddi et al., 2005; Trujillo et al., 2006b; van Dokkum et al., 2006, 2008). The inferred size expansion has been the source of much theoretical puzzlement, and dry mergers – especially involving low-mass companions – are thought to be the key growth mechanism (Naab et al., 2009; Hopkins et al., 2010).

Considerable effort has been devoted toward establishing the robustness of the relevant observations. Although stellar mass estimates are subject to uncertainties arising from assumed stellar population models, the uncertainties are thought to be insufficient to significantly change the inferred rates of growth (Muzzin et al., 2009). In an important step forward, Newman et al. (2010) inferred similar size growth rates based on more robust *dynamical* mass measures over $z \simeq 0 - 1.5$. Similarly, the arrival of Wide Field Camera 3 onboard the *Hubble Space Telescope* (WFC3/*HST*) has allowed the light profiles of $z \simeq 2$ quiescent galaxies to be traced to many effective radii, thereby confirming the compact nature of the $z \simeq 2$ sources (e.g., Szomoru et al., 2012), as well as providing large, homogeneous samples imaged at high spatial resolution in the rest-frame optical (Newman et al., 2012).

Given the robustness of the inferred masses and sizes, the key question is the growth mechanism. While the number of observed impending mergers appears consistent with that required to account for size growth over $z \lesssim 1$, the growth rate at higher redshifts is much faster, possibly suggesting an additional mechanism (Newman et al., 2012). A key difficulty arises from the continual quenching of galaxies and their arrival onto the red sequence, which implies that the average size evolution for the population need not necessarily measure that of any individual galaxy. In fact, some authors have claimed a dominant role for *progenitor bias* — the later arrival of newly-quenched, potentially larger

galaxies — in interpreting size growth observations (e.g., Carollo et al., 2013; Poggianti et al., 2013). The suggestion strikes at the heart of a fundamental problem in galaxy evolution, namely how to separate one component of a population which evolves, e.g., in size and color, over time, from a second component which joins that population at a later time. Newman et al. (2012) attempted to resolve this ambiguity using the evolving *size distribution* and *number density* of quiescent systems, arguing that the disappearance of the most compact systems could only arise from growth of individual systems. This approach requires minimal assumptions, but it is necessarily sensitive only to the compact tail of the distribution.

A number of studies indicate that the *stellar velocity dispersion* σ of a galaxy is the most fundamental tracer of its stellar populations and halo mass (e.g., Graves et al., 2009a; Wake et al., 2012) and hence can act as a valuable identifier of a consistent population over cosmic time. In the context of size evolution, the velocity dispersion is a valuable label for several reasons. First, mergers are expected to increase the radius but change the velocity dispersion relatively little (e.g., Nipoti et al., 2003; Hopkins et al., 2009b; Oser et al., 2012). Second, whereas there is evidence at $z \sim 0$ for a correlation between size and stellar age at fixed mass, there is no such correlation at fixed velocity dispersion (e.g., Graves et al., 2009b; van der Wel et al., 2009; Valentinuzzi et al., 2010). This suggests that any new arrivals onto the red sequence at a given velocity dispersion do not bias the mean size of the population. Third, the number density of the highest- σ galaxies appears to be stable over time, indicating that galaxies with $\sigma \gtrsim 280 \text{ km s}^{-1}$ are in place at early times and represent a nearly fixed population (Bezanson et al., 2012). Newman et al. (2010) found no significant difference between the rates of size growth at fixed velocity dispersion and fixed mass in a preliminary sample of 17 $z \sim 1.3$ galaxies, suggesting that the role of progenitor bias in interpreting size evolution is not large.

Relatively few velocity dispersions have been measured for quiescent galaxies at high redshifts and so it has not been possible to construct the well-defined large samples necessary for constraining their number densities. For this reason, Bezanson et al. (2011, 2012) developed a photometric method to derive *inferred* velocity dispersions for 5000 quiescent galaxies over $0 < z < 1.3$ within the Newfirm Medium Band Survey (NMBS, Whitaker et al., 2011). This approach uses the stellar masses, effective radii, and Sérsic indices of the distant sample to estimate velocity dispersions using a formula calibrated locally using SDSS data (Taylor et al., 2010a). However, given that this calibration may well evolve with redshift, direct spectroscopic measurements remain indispensable. Although the current spectroscopic datasets at $z \gtrsim 1$ appear consistent with the locally-derived calibration (e.g., van de Sande et al., 2013), the sample sizes are too small for this approach to be robust.

A further benefit of securing velocity dispersions from spectroscopic data is the ability to compare the relationship between stellar and dynamical masses for individual objects. The ratio of stellar to

dynamical mass, M_*/M_{dyn} , is a potentially valuable tracer of the likely mechanism by which galaxies grow (e.g., Hopkins et al., 2009b; Hilz et al., 2013). Specifically, under merger-driven growth, the ratio measured within the effective radius should decrease with time. This decrease would be stronger in the case of minor mergers. Some tentative support for this suggestion was discussed by van de Sande et al. (2013) using a sample of 5 galaxies with $1.5 < z < 2.1$.

To address the above issues, and building on earlier work by Newman et al. (2010), we have completed a new spectroscopic survey of over 100 $z > 1$ massive galaxies utilizing the red-sensitive CCD installed in the Keck LRIS spectrograph, thus providing nearly a four-fold increase in the sample size over earlier work. Such a large sample allows us to examine size growth at fixed velocity dispersion, thereby addressing the question of progenitor bias, as well as the relationship between stellar and dynamical mass over $0 < z < 1.5$. Chapter 4 will further address the issues of progenitor bias via spectroscopic indicators of recently-quenched galaxies.

A plan of the chapter follows. In Section 3.2 we describe the selection of the Keck LRIS sample, the spectroscopic observations and their data reduction. We also discuss the auxiliary data used for deriving sizes and stellar masses, as well as the comparison sample of local galaxies; and we present the selection of quiescent galaxies based on rest-frame colors. In Section 3.3 we derive the key physical properties: size, stellar mass, and stellar velocity dispersion, essential for our analysis, and we discuss the relevant uncertainties. In Section 3.4 we calculate the dynamical masses and discuss the stellar-dynamical mass relation and its redshift evolution. In Section 3.5 we investigate the size growth of quiescent galaxies using the stellar velocity dispersion as a tracer of populations connected over cosmic time. Finally, we summarize our main results and discuss their implications in Section 3.6. Throughout this work we use AB magnitudes, and assume a Λ CDM cosmology with $\Omega_m = 0.3$, $\Omega_\Lambda = 0.7$, and $H_0 = 70 \text{ km s}^{-1} \text{ Mpc}^{-1}$.

3.2 Data

3.2.1 Sample Selection

We selected spectroscopic targets from various photometric catalogs in three well-studied fields: COSMOS, GOODS-South, and EGS. The public photometric data are described in Section 3.2.3 and Appendix 3.A. Galaxies were selected with photometric redshifts in the range $0.9 < z_{\text{phot}} < 1.6$ and stellar masses (calculated from broad-band photometry, see Section 3.3.2) larger than $10^{10.6} M_\odot$. In designing slitmasks we gave priority to massive and red objects according to their rest-frame spectral energy distributions, and added extra sources from a less-strictly selected sample. In the first observing run (see Section 3.2.2 and Table 3.1) we used slightly different criteria: $1 < z_{\text{phot}} < 2$, magnitude in the z band brighter than 23.5, and spheroidal morphology in *HST* ACS imaging. Objects brighter than $K \sim 22$ were used as additional sources. To this sample, we added 17 galaxies

Table 3.1. LRIS Observations

Slitmask	Run ^a	Seeing (arcsec)	Exp. Time (min)
GOODS-S 1	A	0.8	420
COSMOS 1	A	1.0	420
COSMOS 2	B,C	0.8	360
COSMOS 3	C	0.9	240
COSMOS 4	D	1.0	220
EGS 1	D	1.0	260
EGS 2	D	1.6	180

^aObserving runs: A: 2011 January 6–9; B: 2011 November 21, 22; C: 2012 January 22, 23; D: 2012 April 17,18.

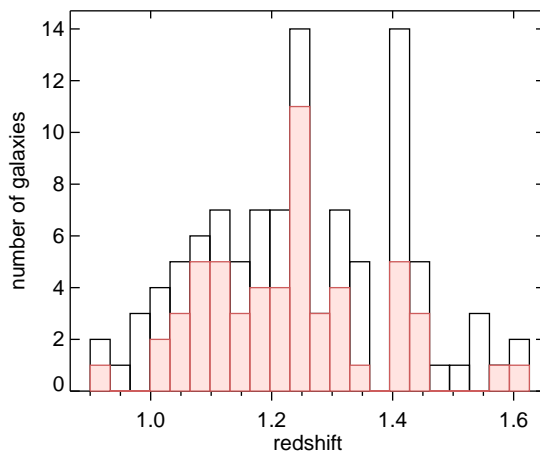


Figure 3.1 Redshift distribution of the spectroscopic sample of 103 galaxies, including the sample published by Newman et al. (2010). The subsample of 56 quiescent galaxies used in the subsequent analysis (see Section 3.2.5) is shown in red.

published by Newman et al. (2010) also observed with LRIS in the EGS, GOODS-North, and SSA22 fields. These objects were selected to have $I < 23.5$, $I - K_S > 2$, and a spheroidal morphology.

3.2.2 Spectroscopic Observations and Data Reduction

We observed the selected galaxies using the upgraded red arm (Rockosi et al., 2010) of the Low-Resolution Imaging Spectrograph (LRIS, Oke et al., 1995) on the Keck I telescope. We used $1''$ wide slits and the 600 mm^{-1} grating blazed at $1 \mu\text{m}$, with a resulting velocity resolution of $\sigma_{\text{instr}} \sim 60 \text{ km s}^{-1}$ at 9000 \AA . The spectra were taken over four observing runs in 2011 and 2012. We observed a total of seven slitmasks targeting 20–25 objects each, listed in Table 3.1. The total integration times varied from 3 to 7 hours per mask, with individual frames having a typical exposure time of 1200 seconds.

The data were reduced using a pipeline based on the code developed by Kelson (2003). Each

frame was corrected for bias and flat-fielded, and the sky emission was modeled and subtracted. The 1D spectra were then optimally extracted from the stacked frames using weights derived by fitting a Gaussian to the spatial profile of each trace. The sky spectrum was also extracted from each slit with the purpose of accurately measuring the instrumental resolution. Telluric corrections and flux calibrations were determined using observations of standard white dwarfs. To ensure a good telluric calibration, the spectra of the standard stars were broadened to match the resolution of the science observations, where necessary.

From these slitmasks we obtained 86 spectra with at least one clear feature that allows us to determine the spectroscopic redshift. To this sample we add 17 galaxies from Newman et al. (2010) which were observed with LRIS with slightly longer exposure times and reduced in a similar way. The redshift distribution of the full spectroscopic sample of 103 sources is shown in Figure 3.1. Modest overdensities are apparent at $z \sim 1.25$ and $z \sim 1.4$.

3.2.3 Auxiliary Data

In order to measure stellar masses and other properties we use photometric data for the galaxies in our sample from a number of publicly available catalogs. Space and ground-based observations from the near-UV to the near-infrared are available for every object. All except three galaxies also have *Spitzer* IRAC public data. In Appendix 3.A we describe in some detail the compilation of photometric data.

Space-based optical and near-infrared observations are critical for an accurate estimate of the size of high-redshift galaxies, and we exclusively use publicly available *HST* data for surface brightness fitting. For the GOODS-N, EGS, GOODS-S, and COSMOS fields we used the F160W data from the Cosmic Assembly Near-IR Deep Extragalactic Legacy Survey (CANDELS, Grogin et al., 2011; Koekemoer et al., 2011). Since most of our GOODS-S sample is outside the area probed by the CANDELS observations, we also used F160W data from the Early Release Science survey (Windhorst et al., 2011). For the three objects in SSA22, near-infrared *HST* observations are not publicly available, and we use the F814W data presented in Newman et al. (2010).

3.2.4 SDSS Data

We have selected a sample of galaxies from the Sloan Digital Sky Survey (SDSS DR7, Abazajian et al., 2009) that will be useful for comparing the properties of our high-redshift sample with the population of local galaxies. We make use of the NYU Value Added Catalog (Blanton et al., 2005b), which includes many derived properties. SDSS galaxies were selected with spectroscopic redshifts within the interval $0.05 < z < 0.08$, excluding objects flagged as hosting an active galactic nucleus (AGN) according to the flux ratios of emission lines. We also discarded galaxies with poor spectral

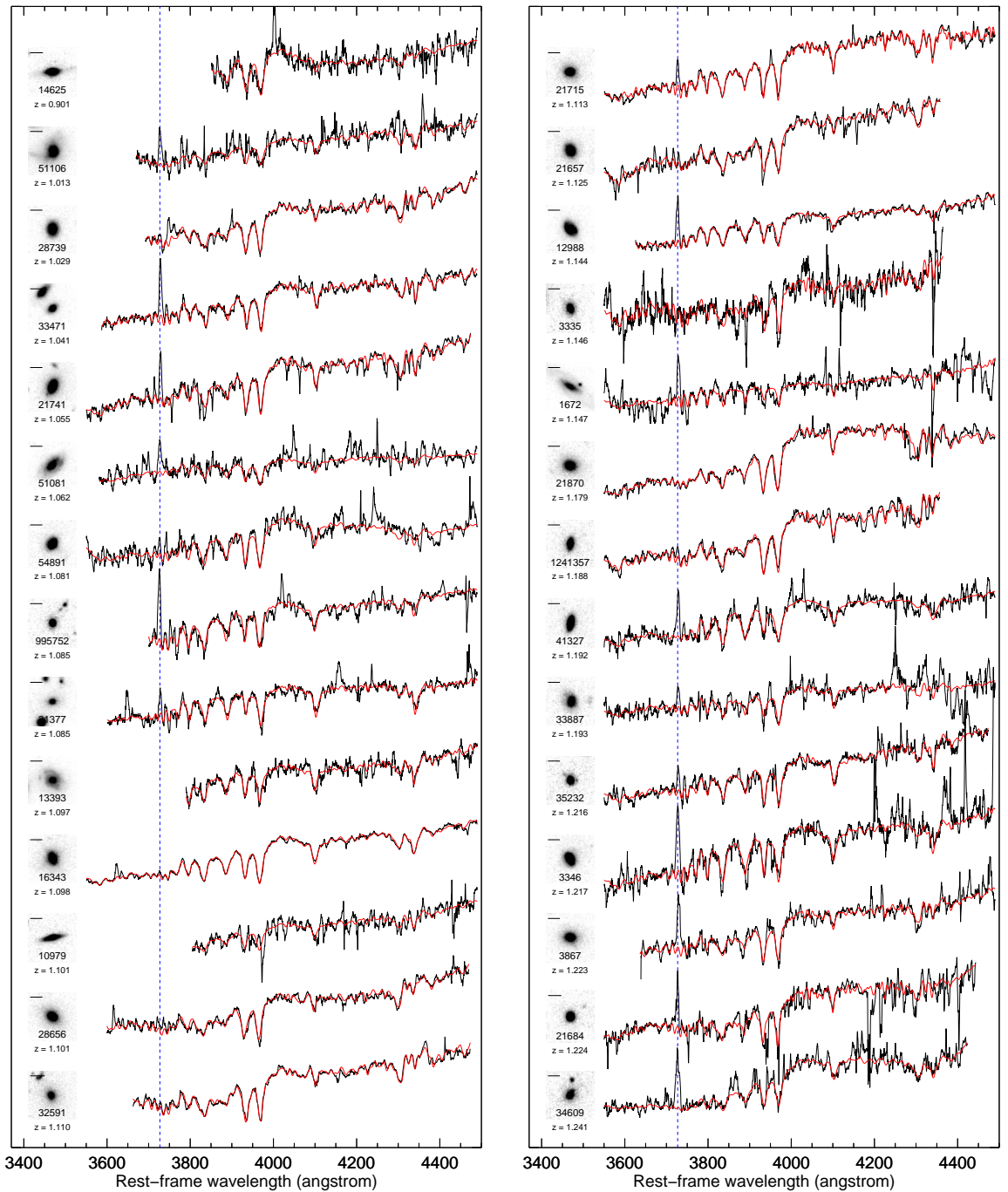


Figure 3.2 Observed LRIS spectra of the 56 quiescent galaxies for which accurate velocity dispersions were measured, sorted by redshift. The spectra are inverse-variance smoothed with a window of 21 pixels, corresponding to $\sim 7.5 \text{ \AA}$ in the rest-frame (16.8 \AA in the observed frame). The vertical blue dashed line is the expected position for the $[\text{OII}]\lambda 3726, 3729$ emission line. For each galaxy, the *HST* cutout (with a 10 kpc ruler), the ID, and the spectroscopic redshift are shown on the left, and the best-fit spectrum is overplotted in red. The *HST* images are in the F160W band except for the objects 32591 and 37085, for which we use F814W.

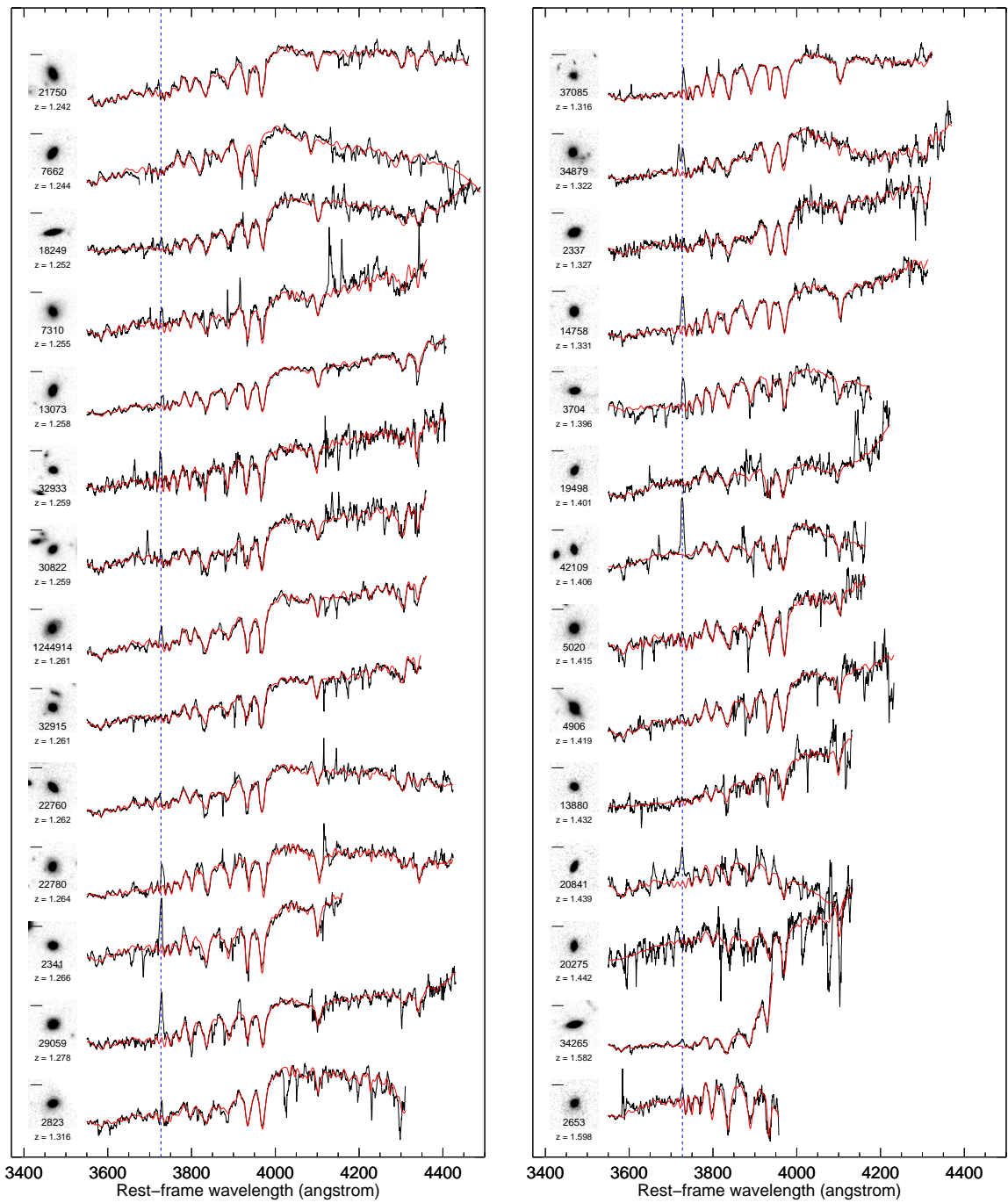


Figure 3.2 Continued.

fits, and those with a very large uncertainty on the measured velocity dispersion.

For each selected galaxy we use the NYU catalog determination of its Sérsic index and the effective radius obtained by a Sérsic profile fit to the r band imaging (Blanton et al., 2005a), the velocity dispersion measured from the optical spectrum, and the SDSS and 2MASS photometry. Since we require J band photometry for selecting quiescent galaxies in a manner similar to that adopted at high redshift (see Section 3.2.5), we only consider the subsample of galaxies detected in the 2MASS imaging survey. This survey is shallower than the SDSS, but this is not an issue for our study, since above $10^{10.6} M_{\odot}$ (which is the limiting mass for the high-redshift sample) more than 95% of the SDSS galaxies are detected in J . This selection gives a sample of 68738 objects. Finally, we match each object to the MPA-JHU catalog (Kauffmann et al., 2003a), from which we take stellar masses and star formation rates, which are calculated from the broad-band photometry assuming a Chabrier (2003) IMF.

3.2.5 Selecting Quiescent Galaxies

The main goal of this work is to study the evolution of quiescent galaxies. To identify this type of galaxy we primarily rely a color-color selection. Rest-frame UVJ magnitudes are determined by integrating the synthetic spectrum that best fits the observed SED (see Section 3.3.2). The $U - V$ versus $V - J$ plane is shown in the top panel of Figure 3.3. In this plane quiescent galaxies tend to form a tight sequence distinctly separated from the region occupied by star-forming galaxies (e.g., Williams et al., 2009). In the figure, the SED-derived specific star formation rates (sSFR, star formation rate per unit stellar mass, see Section 3.3.2) are shown for each object using a color code. The red sequence is clearly visible and composed of galaxies with low sSFR, roughly less than 0.1 Gyr^{-1} . An appropriate division between red, passive galaxies and blue, star-forming ones is shown (black line, see also Whitaker et al., 2011).

Out of the total of 103 objects, this color-color selection yields 69 quiescent galaxies, of which 56 have excellent quality, high signal-to-noise spectra (see Section 3.3.3); these form the primary sample for analysis in this chapter. Their redshift distribution is shown via the shaded histogram in Figure 3.1, and their properties are summarized in Table 3.2. The observed spectra, together with *HST* image cutouts, are shown in Figure 3.2. The rest-frame coverage is roughly centered on 4000 \AA , but changes with redshift and slit position on the mask. The Ca II H and K absorption lines are well detected for all the objects except those at $z > 1.5$, while Balmer absorption lines vary from very strong to almost absent. A detailed spectroscopic study of the total sample, including the subset of quiescent galaxies, will be presented in Chapter 4.

The [OII] λ 3726, 3729 emission line is clearly visible in a number of spectra, and could be due either to some residual star formation or to low-ionization nuclear emission-line region (LINER) activity. Out of the 53 objects for which the line falls in the observed wavelength range, 25 present

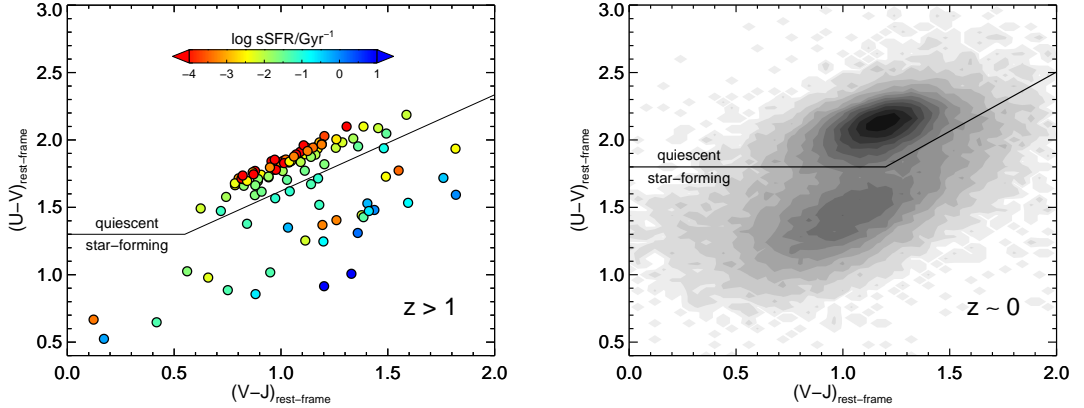


Figure 3.3 Selection of the quiescent subsample. *Top*: the total sample of 103 high-redshift galaxies in the UVJ plane. Colors denote specific star formation rates measured from SED fitting. *Bottom*: UVJ diagram for the SDSS comparison sample. In each panel, the solid line marks the adopted division between quiescent and star-forming galaxies.

clear [OII] emission, with an equivalent width larger than 3 \AA . We calculate an average equivalent width of 8 \AA (and never exceeding 15 \AA), and use the calibration of Kewley et al. (2004) to derive a rough estimate of the star formation rate. We obtain a mean value of specific star formation rate of 0.032 Gyr^{-1} , and a maximum of 0.12 Gyr^{-1} . These values are consistent with or larger than the ones resulting from the SED fitting (see Figure 3.3 and Section 3.3.2). We note that this method does not take into account the LINER contribution, which is expected to be important for this type of galaxies at $z \sim 0$ (Yan et al., 2006) as well as $z \sim 1$ (Lemaux et al., 2010), and therefore yields only an upper limit on the star formation rate. We checked that a more strict selection of quiescent galaxies that excludes objects with detected [OII] emission at both high and low redshift does not significantly change our results. Finally, we find that 3 out of 56 objects are detected in publicly available X-Ray data. These galaxies are likely to host AGN activity, and we list them in Table 3.2.

Using the same criteria as for the high-redshift galaxies, we selected a sample of quiescent galaxies from the SDSS population for comparison purposes. We use InterRest (Taylor et al., 2009) to calculate the rest-frame colors from the observed SDSS and 2MASS photometry, and we show the UVJ diagram for local galaxies in the bottom panel of Figure 3.3. In this case, galaxies present a clear bimodal distribution, even though the red sequence is shifted toward redder colors. Adopting the definition for the quiescent sample shown in the plot, we obtain 37852 objects.

3.3 Physical properties of the sample

In this section we derive the physical properties of the sample of high-redshift galaxies using photometric, imaging, and spectroscopic data.

Table 3.2. Physical Properties of the Sample of Quiescent Galaxies

Object ID	Slitmask	R.A. (J2000)	Decl. (J2000)	z	σ_e (km s ⁻¹)	R_e (kpc)	n	q	$\log M_*/M_\odot$	$\log M_{\text{dyn}}/M_\odot$
14625 ^b	COSMOS 3	150.15839	2.4154	0.901	283 ± 49	2.40	2.1	0.40	10.72 ± 0.09	11.35 ± 0.16
51106	EGS 2	214.92057	52.8659	1.013	252 ± 37	5.99	5.3	0.78	11.26 ± 0.10	11.65 ± 0.14
28739	EGS 1	214.62827	52.7157	1.029	238 ± 11	1.98	3.5	0.70	10.94 ± 0.08	11.11 ± 0.06
33471	COSMOS 3	150.15414	2.4157	1.041	176 ± 12	1.50	2.6	0.66	10.60 ± 0.02	10.73 ± 0.07
21741	N10 (EGS)	214.98510	52.9512	1.055	211 ± 14	2.28	2.2	0.53	10.93 ± 0.10	11.07 ± 0.07
51081	EGS 2	214.90243	52.8637	1.062	233 ± 58	4.36	2.2	0.53	10.89 ± 0.11	11.44 ± 0.22
54891	EGS 2	214.92122	52.8878	1.081	232 ± 37	1.27	3.2	0.73	10.72 ± 0.06	10.90 ± 0.14
995752	COSMOS 1	150.16466	2.2783	1.085	199 ± 44	1.20	4.0	0.78	10.27 ± 0.05	10.74 ± 0.20
31377	COSMOS 4	150.05580	2.2718	1.085	133 ± 18	4.88	4.9	0.63	10.83 ± 0.09	11.00 ± 0.13
13393	COSMOS 3	150.06162	2.3881	1.097	175 ± 21	7.18	3.5	0.80	11.16 ± 0.05	11.41 ± 0.12
16343	COSMOS 3	150.09793	2.4468	1.098	290 ± 8	1.95	8.0	0.65	11.04 ± 0.03	11.28 ± 0.05
10979	COSMOS 3	150.16008	2.3488	1.101	213 ± 116	2.02	1.9	0.18	10.66 ± 0.08	11.03 ± 0.47
28656	EGS 1	214.67508	52.7163	1.101	251 ± 15	2.77	5.4	0.70	11.08 ± 0.08	11.31 ± 0.07
32591 ^a	N10 (SSA22)	334.35290	0.2734	1.110	245 ± 10	4.40	2.4	0.86	11.22 ± 0.11	11.49 ± 0.06
21715 ^b	N10 (EGS)	214.97000	52.9910	1.113	109 ± 8	1.99	4.0	0.77	10.83 ± 0.07	10.44 ± 0.08
21657	N10 (EGS)	215.00590	52.9754	1.125	270 ± 13	2.14	2.5	0.74	10.97 ± 0.09	11.26 ± 0.06
12988	COSMOS 3	150.11500	2.3810	1.144	183 ± 16	2.70	3.1	0.84	10.94 ± 0.05	11.02 ± 0.09
3335	COSMOS 4	150.11756	2.2226	1.146	121 ± 19	1.33	5.1	0.61	10.67 ± 0.04	10.35 ± 0.14
1672	COSMOS 4	150.11025	2.1940	1.147	131 ± 37	5.83	1.9	0.35	11.04 ± 0.05	11.07 ± 0.25
21870	N10 (EGS)	214.98450	52.9613	1.179	230 ± 12	3.36	5.5	0.80	11.02 ± 0.07	11.32 ± 0.06
1241357	COSMOS 1	150.11053	2.3235	1.188	207 ± 13	1.06	5.0	0.43	10.86 ± 0.04	10.72 ± 0.07
41327	EGS 2	214.86345	52.8040	1.192	324 ± 41	1.17	2.9	0.35	10.80 ± 0.05	11.16 ± 0.12
33887	EGS 1	214.77293	52.7556	1.193	162 ± 33	3.76	2.1	0.75	10.74 ± 0.11	11.06 ± 0.18

Table 3.2 (cont'd)

Object ID	Slitmask	R.A. (J2000)	Decl. (J2000)	z	σ_e (km s ⁻¹)	R_e (kpc)	n	q	$\log M_*/M_\odot$	$\log M_{\text{dyn}}/M_\odot$
35232	EGS 1	214.73653	52.7618	1.216	191 ± 19	1.01	3.6	0.77	10.56 ± 0.04	10.63 ± 0.10
3346	COSMOS 4	150.11237	2.2223	1.217	185 ± 22	2.62	1.2	0.64	10.81 ± 0.05	11.02 ± 0.11
3867	GOODS-S 1	53.10946	-27.7641	1.223	184 ± 27	2.74	6.7	0.72	10.67 ± 0.08	11.03 ± 0.14
21684	N10 (EGS)	214.98130	52.9500	1.224	131 ± 23	0.95	2.2	0.80	10.55 ± 0.08	10.28 ± 0.16
34609	COSMOS 2	150.16114	2.5049	1.241	279 ± 159	6.51	8.0	0.67	11.04 ± 0.08	11.77 ± 0.50
21750	N10 (EGS)	215.03490	52.9829	1.242	264 ± 16	2.59	5.2	0.57	11.03 ± 0.07	11.32 ± 0.07
7662	N10 (GOODS-N)	189.26810	62.2264	1.244	293 ± 37	0.98	3.1	0.35	10.92 ± 0.07	10.99 ± 0.12
18249	COSMOS 2	150.10303	2.4821	1.252	286 ± 109	1.60	1.1	0.16	10.77 ± 0.04	11.18 ± 0.33
7310	COSMOS 4	150.05791	2.2904	1.255	176 ± 16	4.34	3.8	0.87	11.13 ± 0.07	11.19 ± 0.09
13073	COSMOS 3	150.12479	2.3823	1.258	265 ± 12	1.20	2.8	0.50	10.97 ± 0.03	10.99 ± 0.06
32933	COSMOS 3	150.09624	2.3770	1.259	131 ± 19	0.91	2.5	0.56	10.50 ± 0.05	10.26 ± 0.13
30822	COSMOS 4	150.09089	2.2252	1.259	271 ± 25	1.82	2.5	0.68	10.96 ± 0.07	11.19 ± 0.09
1244914	COSMOS 1	150.17400	2.3010	1.261	252 ± 13	4.99	5.5	0.79	11.18 ± 0.07	11.57 ± 0.06
32915	COSMOS 3	150.14620	2.3743	1.261	264 ± 17	1.33	6.3	0.82	10.88 ± 0.05	11.03 ± 0.07
22760	N10 (EGS)	215.13690	53.0172	1.262	232 ± 17	0.94	2.4	0.37	10.83 ± 0.06	10.77 ± 0.08
22780	N10 (EGS)	215.13170	53.0162	1.264	88 ± 18	2.28	4.2	0.77	10.75 ± 0.07	10.31 ± 0.18
2341	N10 (GOODS-N)	189.06340	62.1623	1.266	190 ± 27	1.21	3.8	0.71	10.87 ± 0.06	10.70 ± 0.13
29059	EGS 1	214.61016	52.7188	1.278	208 ± 16	1.62	4.3	0.77	10.90 ± 0.06	10.91 ± 0.08
2823	N10 (GOODS-N)	188.93450	62.2068	1.316	215 ± 21	3.26	5.4	0.64	11.01 ± 0.16	11.24 ± 0.10
37085 ^a	N10 (SSA22)	334.35020	0.3032	1.316	164 ± 14	2.51	1.8	0.94	10.60 ± 0.15	10.89 ± 0.09
34879	COSMOS 2	150.13138	2.5238	1.322	213 ± 53	5.45	8.0	0.87	11.23 ± 0.05	11.46 ± 0.22
2337	COSMOS 4	150.10076	2.2058	1.327	279 ± 20	1.54	3.5	0.70	11.04 ± 0.06	11.14 ± 0.08
14758 ^b	COSMOS 3	150.06416	2.4179	1.331	156 ± 16	0.83	2.2	0.84	10.71 ± 0.03	10.37 ± 0.10

Table 3.2 (cont'd)

Object ID	Slitmask	R.A. (J2000)	Decl. (J2000)	z	σ_e (km s ⁻¹)	R_e (kpc)	n	q	$\log M_*/M_\odot$	$\log M_{\text{dyn}}/M_\odot$
3704	N10 (GOODS-N)	189.11320	62.1325	1.396	191 ± 23	0.98	4.1	0.42	10.47 ± 0.06	10.62 ± 0.11
19498	COSMOS 2	150.11063	2.5038	1.401	250 ± 39	0.84	4.2	0.46	10.75 ± 0.07	10.79 ± 0.14
42109	N10 (EGS)	215.12170	52.9575	1.406	369 ± 48	0.73	2.3	0.41	10.77 ± 0.07	11.06 ± 0.12
5020	GOODS-S 1	53.17976	-27.7116	1.415	181 ± 54	2.07	4.6	0.88	10.83 ± 0.08	10.90 ± 0.26
4906	GOODS-S 1	53.18302	-27.7090	1.419	298 ± 26	2.33	3.7	0.59	11.34 ± 0.07	11.38 ± 0.09
13880	COSMOS 3	150.07210	2.4001	1.432	169 ± 70	0.87	2.6	0.62	10.64 ± 0.07	10.46 ± 0.36
20841	COSMOS 2	150.17009	2.5256	1.439	267 ± 52	1.43	1.3	0.35	10.65 ± 0.06	11.07 ± 0.18
20275	COSMOS 2	150.07093	2.5164	1.442	221 ± 70	1.36	4.0	0.51	10.80 ± 0.07	10.89 ± 0.28
34265	COSMOS 2	150.17016	2.4811	1.582	377 ± 54	0.92	2.9	0.22	11.33 ± 0.04	11.18 ± 0.13
2653	N10 (GOODS-N)	188.96250	62.2286	1.598	174 ± 27	0.94	8.0	0.60	10.82 ± 0.18	10.52 ± 0.14

Note. — The slitmask name N10 indicates the objects presented in Newman et al. (2010), and the field in which they were observed is given in parentheses. σ_e is the velocity dispersion within one effective radius, calculated using Equation 3.2. The effective radius R_e , Sérsic index n and axis ratio q are measured in the F160W band. We estimate the observational uncertainty on R_e to be 10%. The dynamical masses M_{dyn} are calculated using Equation 3.3.

^aThe structural parameters for these objects are measured in the F814W band instead of F160W.

^bObjects detected in the X-Ray.

3.3.1 Size Measurement

To study the size and structure of each galaxy we make use of the *HST* F160W data, which correspond to a rest-frame wavelength in the *R* or *I* band depending on the redshift. For two objects only F814W (rest-frame UV) data are available. We fit a 2D Sérsic (1963) profile to the surface brightness of every galaxy using the GALFIT code (Peng et al., 2002). Adjacent objects were identified from the SExtractor (Bertin & Arnouts, 1996) segmentation map and masked out or, when bright and close enough to influence the central region of the object, fit simultaneously. Point spread functions were derived from isolated bright stars.

The output parameters from the fitting procedure include the total flux, the Sérsic index n , the axis ratio q , and the circularized effective radius $R_e = a\sqrt{q}$, where a is the effective (i.e., half-light) semi-major axis, and are listed in Table 3.2. We adopt a 10% uncertainty on all the size measurements, in agreement with the tests performed by Newman et al. (2012), who used similar data and procedures and whose estimates are consistent with other studies (e.g., van der Wel et al., 2008).

3.3.2 SED fitting

We measure stellar masses and other properties by fitting the synthetic stellar population templates from Bruzual & Charlot (2003) to the photometric data. We perform the fit using FAST (Kriek et al., 2009), and adopt the Chabrier (2003) initial mass function and the Calzetti et al. (2000) dust extinction law, with attenuations chosen in the range $0 < A_V < 3$. We assume an exponentially declining star formation history with timescale τ and age t , and use a logarithmic grid with $10 \text{ Myr} < \tau < 10 \text{ Gyr}$ and $10 \text{ Myr} < t < t_H$, where t_H is the age of the universe at the galaxy redshift, fixed to be its spectroscopic value. Because of the well known degeneracy between age and metallicity, we kept the metallicity fixed at the solar value, as appropriate for massive early-type galaxies. For each object, we define the stellar mass and its uncertainty as the mean and standard deviation of the posterior distribution, respectively (see, e.g., Taylor et al., 2011). The random uncertainties obtained in this way range from 0.02 to 0.18 dex, with a median of 0.07 dex. However, systematic errors due to, e.g., the choice of IMF and the treatment of AGB stars in the stellar population templates are likely to dominate the uncertainty on stellar masses, particularly at high redshift.

Since we are interested in the relation between the size and the stellar mass of galaxies, we need to ensure that these two quantities are consistently derived. We measure the effective radii via fitting of the surface brightness, assuming a Sérsic profile. The flux of the best-fit Sérsic model does not necessarily correspond to the flux that one would measure from the same data using a different technique, e.g., adopting a fixed aperture or constructing the curve of growth. This is a particularly relevant issue for our sample, because the SEDs were compiled from different surveys. For this reason

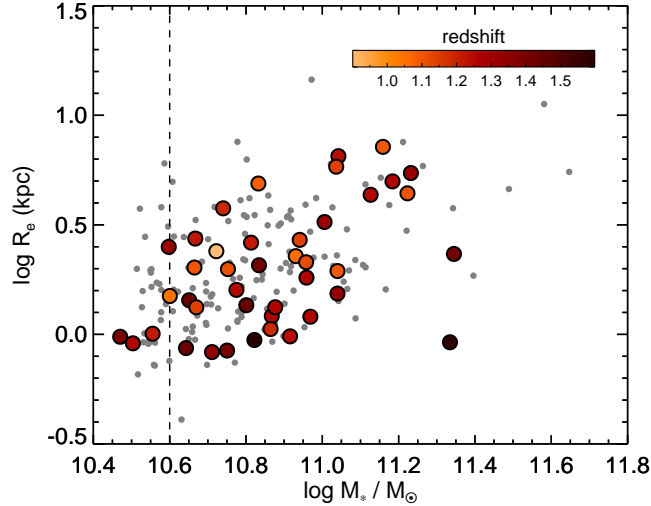


Figure 3.4 Mass-size relation for our spectroscopic sample of quiescent galaxies (large points, color-coded according to their redshift) and for a sample of photometrically selected galaxies with $1 < z < 1.6$ from Newman et al. (2012, small gray points).

we calculated a correction factor in the following way. From the FAST best-fit spectrum we calculate the expected flux $F_{160}^{(\text{FAST})}$ in the *HST* filter in which the imaging data have been taken (F160W for most of the objects). We then measure the actual flux $F_{160}^{(\text{HST})}$ by fitting a Sérsic profile to the *HST* data. Finally, we correct the stellar mass output by FAST: $M_* = M_*^{(\text{FAST})} \cdot F_{160}^{(\text{HST})} / F_{160}^{(\text{FAST})}$. We perform the same correction to the star formation rate, since these are the only parameters that depend on the overall normalization of the observed SED. The correction is generally small, with a mean and standard deviation of $\langle F_{160}^{(\text{HST})} / F_{160}^{(\text{FAST})} \rangle = 0.96 \pm 0.14$. Note that this procedure automatically corrects also for zero point differences among different catalogs, since the corrected stellar masses are normalized to the highly reliable flux calibration of *HST* data. The aperture-corrected stellar masses and their uncertainties are reported in Table 3.2.

Since our spectroscopic sample may be biased toward brighter, more compact objects, we need to check whether completeness effects are important for the subsequent analysis. In Figure 3.4 we compare the stellar masses and effective radii of our sample with those of the quiescent galaxies photometrically selected in the CANDELS fields by Newman et al. (2012). Our sample spans the whole range of size for a given stellar mass at all redshifts except for $z > 1.5$. Since only two galaxies are in this redshift range, we conclude that our spectroscopic sample is fairly representative of the population of quiescent galaxies with stellar masses above $10^{10.6} M_{\odot}$.

3.3.3 Velocity Dispersions

We derived velocity dispersions by fitting broadened templates to the observed spectra using the Penalized Pixel-Fitting method (pPXF) of Cappellari & Emsellem (2004). We used the templates from the Bruzual & Charlot (2003) library of synthetic stellar populations, and correct the observed velocity dispersions for instrumental resolution (as measured from unblended sky lines) and template resolution. During the fitting, the pixels near the expected position of the [OII] λ 3726, 3729 emission line were masked, together with the pixels contaminated by strong sky emission. The wavelength region used for the fit is within the range $3300 \text{ \AA} < \lambda < 5500 \text{ \AA}$ and depends on the rest-frame interval probed by LRIS at each redshift (with the upper limit decreasing with redshift, see Figure 3.2).

The velocity dispersion σ and its uncertainty were calculated as follows. During the template fitting we sum the observed spectrum to a polynomial of degree m to account for template mismatch, and we multiply it by a polynomial of degree n to account for the uncertainty in the relative flux calibration and dust attenuation (Cappellari et al., 2009; Bezanson et al., 2013). We adopt a grid of polynomial degrees, with $1 < m < 11$ and $1 < n < 6$, and calculate the best-fit σ_{mn} at each point on the grid. We take as fiducial model the one with $m = 8$ and $n = 3$, and the corresponding σ is our final value of velocity dispersion. Finally, we calculate the uncertainty by summing in quadrature the random error on σ output by pPXF in the fiducial model and the standard deviation of σ_{mn} after a sigma-clipping on the chi-square distribution to discard poor fits.

We conducted a number of tests to verify that the velocity dispersion measurements are stable and do not depend on the specific assumptions made. The fitting procedure was repeated many times for each object, varying each time one of the parameters. The fraction of pixels discarded due to sky emission does not influence significantly the measured dispersions. We also tested the importance of the template choice. Using the Indo-US library of observed stellar spectra (Valdes et al., 2004) yielded velocity dispersions in good agreement with the ones obtained through the Bruzual & Charlot (2003) synthetic spectra of stellar populations, with a median offset of 0.03 dex and a scatter of 0.07 dex. Finally, excluding the calcium H and K lines from the fit does not affect the velocity dispersion measurement in a significant way. We conclude that, for most of the spectra, none of the assumptions involved in the spectral fitting have an influence on the measured dispersions greater than the quoted uncertainties. This is in agreement with the extensive tests performed by van de Sande et al. (2013) on the spectra of five galaxies at $1.5 < z < 2$.

We discard spectra with a signal-to-noise ratio per resolution element smaller than 8, and we also exclude those galaxies for which the spectral fitting is not stable, i.e., the best-fit parameters change significantly when using higher degree additive and multiplicative polynomials. Our final sample comprises 56 objects (out of 69 examined) on the red sequence, with an average velocity dispersion error $\langle \delta\sigma/\sigma \rangle = 13\%$. This is the largest homogeneous sample of quiescent galaxies at

$z > 1$ for which reliable velocity dispersions have been measured.

The observed velocity dispersion σ_{obs} is the luminosity-averaged dispersion within the central region of the galaxy probed by the slit aperture. Since the angular diameter distance and effective radius are different for each object, σ_{obs} corresponds to different physical regions. To ensure an unbiased comparison, we apply an aperture correction and obtain the velocity dispersion within the effective radius R_e . One way to calculate the aperture correction is to adopt the relation between σ_e and the velocity dispersion measured within a radius R derived for nearby early-type galaxies by Cappellari et al. (2006):

$$\frac{\sigma_{\text{obs}}}{\sigma_e} = \left(\frac{R}{R_e} \right)^{-0.066}. \quad (3.1)$$

However, at high redshift the effective radius is typically much smaller than the angular size probed by the slit aperture, and the effect of seeing cannot be neglected. The model of van de Sande et al. (2013), which takes into account seeing, rectangular aperture, and optimal extraction, is more appropriate for our high-redshift observations. If the seeing is comparable to the slit aperture, as in our case, this model predicts an aperture correction which varies only by 1-2% with R/R_e . Therefore we adopt a constant correction factor for all the high-redshift galaxies, taking the average from the van de Sande et al. (2013) sample:

$$\sigma_e = 1.05 \sigma_{\text{obs}}. \quad (3.2)$$

The aperture-corrected velocity dispersions are listed in Table 3.2. For the local comparison sample, we calculate the effective velocity dispersions σ_e by applying Equation 3.1 using $R = 1''.5$, corresponding to the radius of the optical fibers used in the SDSS.

3.4 Dynamical Masses

We now turn to determining dynamical masses for our sample. From a simple virial argument, it is possible to relate the dynamical mass of a galaxy to its velocity dispersion σ_e and effective radius R_e : $GM_{\text{dyn}} = \beta \sigma_e^2 R_e$, where the virial factor β depends on the galaxy structure. Cappellari et al. (2006) showed that a constant $\beta = 5$ is a good approximation for elliptical galaxies. We then define the dynamical mass as

$$M_{\text{dyn}} = \frac{5\sigma_e^2 R_e}{G}. \quad (3.3)$$

Via this procedure we determined dynamical masses for our sample and list these in Table 3.2. We also calculate dynamical masses for the local SDSS sample using Equation 3.3.

We note that the use of Sérsic profiles to describe the surface photometry implies that galaxies with different indices n will naturally have different structures and therefore different virial factors. We explore this topic further in Appendix 3.B.

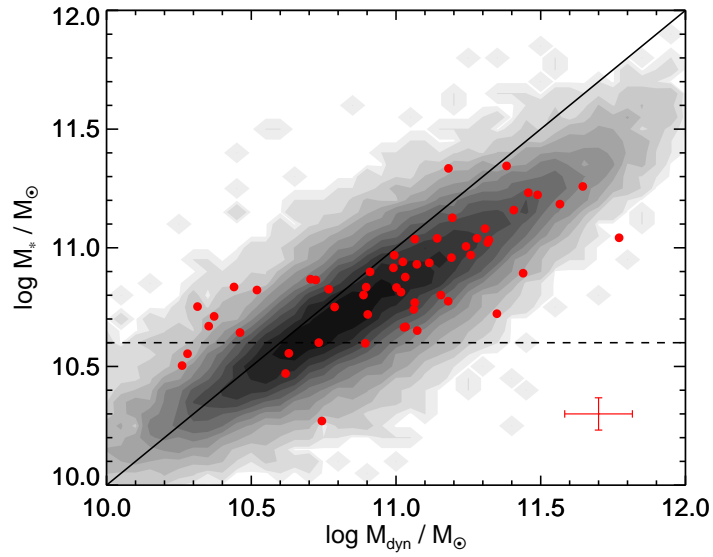


Figure 3.5 Stellar mass vs. dynamical mass. Objects from our sample are plotted as red points, and we show the SDSS sample as a grayscale map. The solid line corresponds to equal stellar and dynamical masses, while the dashed line indicates the stellar mass completeness limit. The median error bars on both axis are shown on the bottom right.

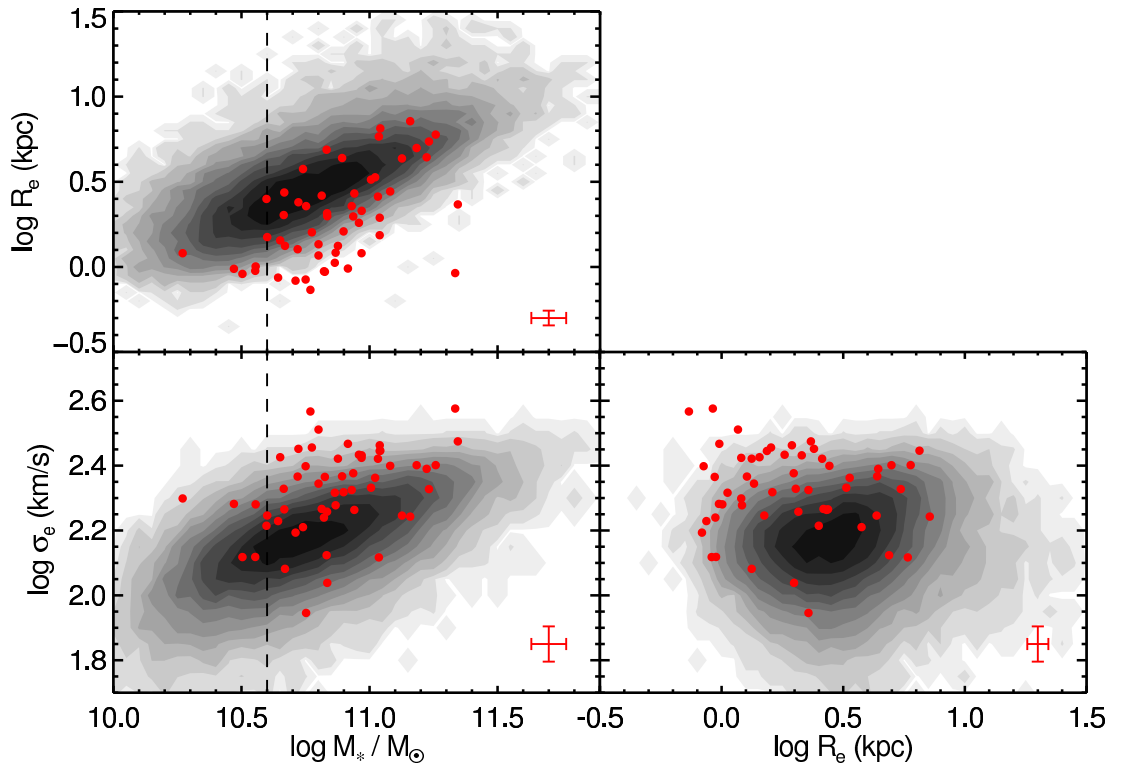


Figure 3.6 *Top*: Effective radius versus stellar mass. *Bottom left*: Velocity dispersion versus stellar mass. *Bottom right*: Velocity dispersion versus effective radius. Symbols as in Figure 3.5.

3.4.1 The Stellar Mass-Dynamical Mass Relation

In Figure 3.5 we compare the stellar masses M_* and dynamical masses M_{dyn} for our sample of quiescent galaxies (red points) and for the SDSS sample (grayscale map). The relation $M_{\text{dyn}} = M_*$ is shown by the black line. The region above this line indicates the unphysical situation where the stellar mass exceeds the dynamical mass.

It is clear that the high-redshift quiescent galaxies occupy the same region as the local population, except for a group of outliers at low masses, near our completeness threshold. Overall, the correlation between stellar and dynamical mass in Figure 3.5 is very good at both high and low redshift. In Figure 3.6 we develop the case further by showing the relation between stellar mass, size, and velocity dispersion for quiescent galaxies. Here, the high-redshift population shows a significant offset from the SDSS sample: even though there is some overlap with the local population, the systematic shift is clear. At fixed stellar mass, their effective radii are significantly smaller, and their velocity dispersions larger, compared to the local population. To quantify this offset approximately, we perform a linear fit to the SDSS data in the range $10.5 < \log M_*/M_\odot < 11.5$, and then fit a line with the same slope to the high-redshift data points. The offset obtained in this way is -0.25 ± 0.03 dex in size and $+0.12 \pm 0.02$ dex in velocity dispersion. According to Equation 3.3, an offset in size and velocity dispersion will produce a shift in the stellar-dynamical mass relation equal to $2\Delta \log \sigma_e + \Delta \log R_e$. The measured offsets, then, cancel each other almost exactly, leaving the ratio of stellar to dynamical mass unchanged, as seen in Figure 3.5. This fact is noteworthy for two reasons.

Firstly, from an observational point of view, it confirms the validity of our measurements. Since sizes, velocity dispersions, and stellar masses are measured from, respectively, *HST* imaging, Keck spectroscopy, and broad-band photometry, these three key observables are effectively independent (since the stellar mass aperture corrections, derived from the imaging data, are small; see Section 3.3.2). If any one of these were to be biased because of some observational effect, then a fine-tuned bias in the other two quantities would be required to produce the agreement seen in Figure 3.5. Thus, importantly, the relatively large velocity dispersions measured are a confirmation of the small sizes of high-redshift quiescent galaxies.

Secondly, the fact that the offsets in size and velocity dispersions do not produce an offset in dynamical mass has important implications for the evolution of early-type galaxies between $z \sim 1.3$ and today. We explore this further in the next subsection.

3.4.2 The Redshift Evolution of the Mass Ratio

As seen in Figure 3.5, the distribution of the mass ratios M_*/M_{dyn} is very similar for the high and low-redshift populations. Both samples have similar average ratios: $\langle \log (M_*/M_{\text{dyn}}) \rangle = -0.13$

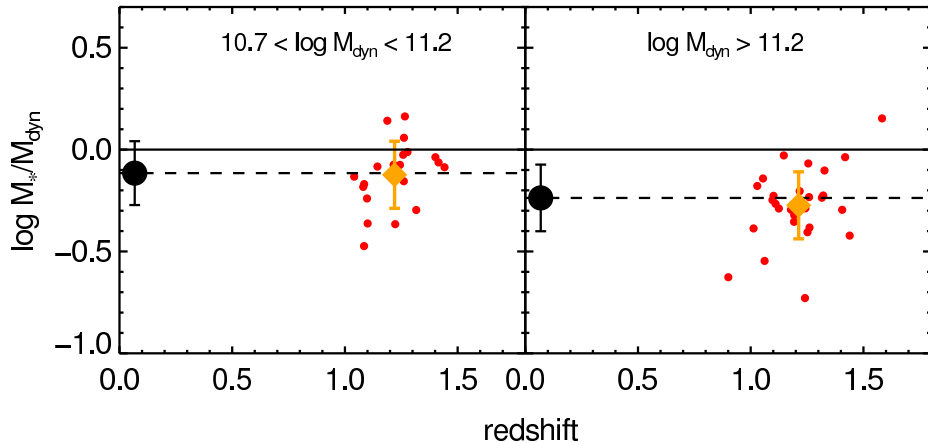


Figure 3.7 Redshift evolution of the stellar-to-dynamical mass ratio, for intermediate (left) and high mass (right) galaxies. The black points represent the SDSS sample, and the red points are galaxies from our sample, for which the average values and standard deviations are shown in orange.

for our sample and -0.12 for the SDSS population. The scatter is slightly larger at $z > 1$, with the standard deviation being 0.25 dex at high redshift and 0.18 dex at $z \sim 0$. In Figure 3.7 we consider the redshift evolution of the ratio M_*/M_{dyn} into two mass bins. The mean mass ratio for the high-redshift sample agrees with the local value in both bins. The standard deviation is also approximately unchanged from $z \sim 1.3$ to $z \sim 0$. Although van de Sande et al. (2013) found evidence for a slight evolution of the mass ratio at $z > 1.5$, within our larger sample we find no significant evolution in the relation between stellar and dynamical mass for quiescent galaxies over $0 < z < 1.6$.

Since the dynamical masses are derived independently of the synthetic stellar populations, the absence of a systematic offset in the two distributions suggests that the stellar masses at $z \sim 1.3$ are reliable. However, we cannot exclude some evolution in the intrinsic mass ratio together with a bias in the stellar masses, e.g., one caused by evolution in the initial stellar mass function (IMF) for the recently quenched galaxies, that conspire to produce this result. Nonetheless, our data are consistent with the simplest possible scenario, in which both IMF and dark matter fraction are unchanging over $0 < z < 1.6$. Of course, since galaxies evolve in mass and size with time, the fact that the stellar-dynamical mass relation is constant with redshift does not necessarily imply no evolution in the ratio M_*/M_{dyn} for individual objects. We will explore this point further in Section 3.5.

Finally, we use our data to test the scenario proposed by Peralta de Arriba et al. (2013), in which compact galaxies present dynamical masses significantly smaller than their stellar masses, an unphysical situation which they attributed to a strong non-homology in galaxy structure. From Figure 3.5 we can see that the majority of high-redshift galaxies in our sample have $M_{\text{dyn}} > M_*$, and the few exceptions lie near the completeness limit. We therefore rule out a discrepancy between dynamical and stellar mass measurements. However, we do find a clear correlation between compactness (more precisely, velocity dispersion) and mass ratio, which we will further explore in

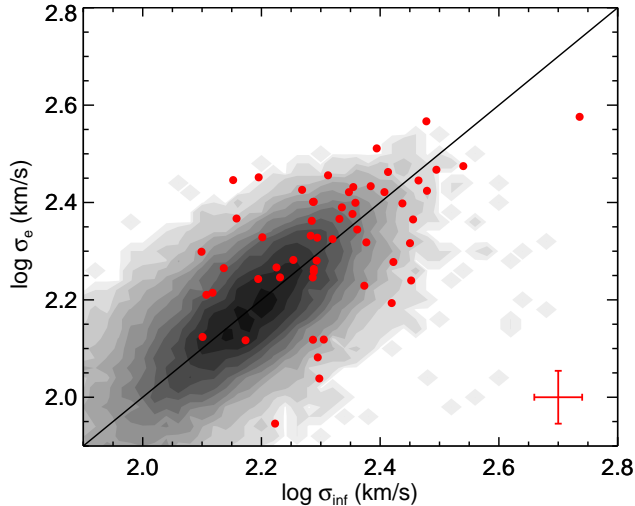


Figure 3.8 Spectroscopically observed vs. photometrically inferred velocity dispersions. Red points represent high-redshift quiescent galaxies, and the grayscale map is the distribution of the SDSS sample. The black line is the 1:1 relation. The median error bars are shown on the bottom right corner.

Section 3.5.2.1.

3.4.3 Testing Inferred Velocity Dispersions

Spectroscopic measurements of the stellar velocity dispersion for high-redshift galaxies require very long integrations and so far have been performed on a small number of objects. In fact, the present sample is the largest at redshifts $z > 1$. A more economic approach is to estimate the velocity dispersion from photometric data using a local calibration (Bezanson et al., 2011). Although this produces inferred velocity dispersions for large samples, it relies on the assumption that the local calibration is valid at all redshifts. Our spectroscopic sample presents a unique opportunity for testing this assumption.

Following Bezanson et al. (2011), we use Equation 3.3 to define the *inferred* velocity dispersion as

$$\sigma_{\text{inf}} = \sqrt{\frac{G}{5 R_e} 0.15 M_*^{1.09}}, \quad (3.4)$$

where $M_{\text{dyn}} = 0.15 M_*^{1.09}$ is the result of a linear fit to the SDSS galaxies in the mass range $10^{10.5} - 10^{11.5} M_{\odot}$. This equation differs from the one given by Bezanson et al. (2011) because we do not include the dependence of the virial factor on the Sérsic index, which we discuss in Appendix 3.B.

In Figure 3.8 we plot inferred versus spectroscopic velocity dispersions for our sample and for the SDSS local population. There is good agreement at all values of velocity dispersion, including for the very large ones, which are poorly sampled in the local distribution. The scatter is 0.13 dex and

is slightly larger than the one found in the $z \sim 0$ population, which is 0.10 dex. This difference most likely arises as a result of greater observational uncertainties at high redshift. We conclude that the local, empirical calibration for determining inferred dispersions holds reasonably well for galaxies at $1 < z < 1.6$. This can be explained physically as a consequence of the observed constancy of the relation between stellar and dynamical masses (Figure 3.5). However, the scatter of 0.13 dex, or about 35%, is much larger than the 13% typical uncertainty on the spectroscopic dispersions. This clearly limits the precision of the inferred dispersions, rendering this method less useful except for statistical studies of large populations.

3.5 The size growth of quiescent galaxies

In the previous section we presented a clear difference between the sizes and velocity dispersions of local and high-redshift galaxies, yet noted the remarkable constancy of the overall stellar-to-dynamical mass ratio. We will now explore in more detail the size evolution that high-redshift galaxies must undergo in order to match the observed properties of the $z \sim 0$ population.

3.5.1 The Progenitor Bias

There are two important effects that we need to take into account when modeling the evolution of quiescent galaxies. Firstly, even though these objects form very little stars, they can change their stellar mass and other properties through galaxy merging. Secondly, newly quiescent galaxies are continually being added to the red sequence as blue galaxies shut down their star formation and turn into red, quiescent objects. This quenching process is responsible for a population of local early-type galaxies that were not quiescent at $z > 1$. This mismatch in identification between low- and high-redshift galaxy populations is comprehensively called progenitor bias.

The effect of galaxy merging differs according to the ratio of the masses involved:

- *Major merging*, i.e., merging between two galaxies of similar mass, reduces the number density and also has a large effect on the mass and size of the galaxies. Theoretical arguments and numerical simulations (e.g., Hernquist et al., 1993; Naab et al., 2009; Hilz et al., 2013) predict that in major mergers the size and the stellar mass of individual galaxies grow at the same rate: $R_e \propto M_*$.
- *Minor merging*, on the other hand, does not have a large effect on the stellar mass of a galaxy, but can alter its size. In this case the theoretical expectation is a size growth steeper than that caused by major merging: $R_e \propto M_*^\alpha$, with $1 < \alpha < 2.5$.

The combination of these processes makes it very difficult to identify, for a given high-redshift galaxy, its potential descendants in a $z \sim 0$ population.

Moreover, the quenching of star-forming galaxies introduces the complementary issue of finding, in a low redshift population, those galaxies whose progenitors were already quiescent at $z > 1$. In fact, it has been suggested that the observed discrepancy between the sizes of local and high-redshift quiescent galaxies could be fully explained by the progenitor bias (e.g., Carollo et al., 2013; Poggianti et al., 2013). In this scenario, little physical size growth of individual galaxies is required, since the larger average radius observed at $z \sim 0$ can primarily be due to the contribution of recently formed quiescent galaxies.

3.5.2 Evolution at Fixed Velocity Dispersion

Comparing the sizes of low and high-redshift galaxies at fixed stellar mass is not particularly helpful in understanding the physical evolution of individual galaxies, since stellar masses can significantly increase after, e.g., a major merger. Taking advantage of our unique spectroscopic dataset, we therefore compare galaxy sizes *at fixed velocity dispersion*. There are several reasons why the stellar velocity dispersion is thought to remain relatively constant with cosmic time. From an observational point of view, Bezanson et al. (2012) showed that the number density of galaxies with large (inferred) velocity dispersion changed very little since $z \sim 1.5$. Also, numerical simulations show that the central velocity dispersion is weakly affected by minor or major mergers, and changes by only 10% from $z \sim 2$ to $z \sim 0$ (e.g., Hopkins et al., 2009b).

The lower panels of Figure 3.6 show that high-redshift galaxies have larger velocity dispersions and smaller radii compared to the typical SDSS values. In particular, at fixed stellar mass the velocity dispersions at high redshift are higher, as we discussed in the previous section. Assuming a constant σ_e , high-redshift galaxies are constrained to evolve along horizontal tracks, therefore they are not able to evenly populate the distribution of velocity dispersion observed locally. The only way to reproduce the local distribution would be to assume that all the newly quenched galaxies lie in the lower σ_e region of the figure. Thus it follows that, at $z \sim 0$, older galaxies have large velocity dispersions. Graves et al. (2009a) (and others, e.g., Thomas et al., 2005) studied the stellar populations of SDSS early-type galaxies and found a convincing correlation between velocity dispersion and age. In particular, they concluded that all galaxies with $\log \sigma_e > 2.35$ (aperture-corrected to our system) are older than 10 Gyr, corresponding to a formation epoch earlier than $z = 1.6$. A self-consistent picture emerges: at high redshift we observe quiescent galaxies that locally have old stellar populations and large velocity dispersions. This agrees with the simple analytical model of van der Wel et al. (2009), whereby all early-type galaxies with $\log \sigma_e = 2.40$ formed at $z \sim 1.5$.

In Figure 3.9 we re-examine the R_e - σ_e plane for low and high-redshift galaxies, this time plotting only the galaxies above our completeness limit, $\log M_*/M_\odot > 10.6$. The horizontal dot-dashed line represents the $\log \sigma_e = 2.35$ threshold from Graves et al. (2009a). In the region above this threshold

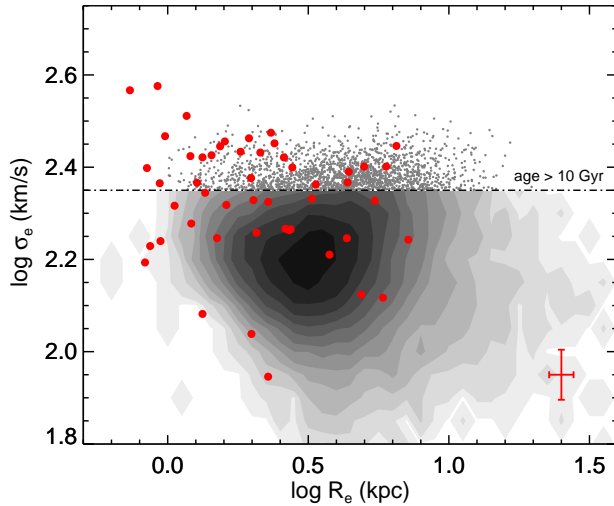


Figure 3.9 Velocity dispersion vs. effective radius, for galaxies with $\log M_*/M_\odot > 10.6$. High-redshift galaxies are shown as red points, and the SDSS sample as a grayscale map. The dot-dashed line marks the velocity dispersion above which, in the local universe, galaxies are older than 10 Gyr (Graves et al., 2009a). In this region, SDSS galaxies are plotted individually as gray small points. The median error bars for the high-redshift sample are shown on the bottom right corner.

we plot individual SDSS galaxies to better facilitate the comparison with the high-redshift sample. Since all the SDSS points above the line have very old stellar populations, we conclude that it is reasonable to connect the two distributions. The difference in size between the red and gray points is more than a factor of 2 (the mean offset is significant, viz 0.33 ± 0.05 dex), and cannot be accounted for by recently quenched galaxies of younger ages. High-redshift quiescent galaxies must *physically grow* in size in order to match the local distribution.

There is further independent evidence that progenitor bias is insufficient to explain the observed size evolution. Within the SDSS sample, Graves et al. (2009b) and van der Wel et al. (2009) independently found no correlation between size and age for quiescent galaxies at fixed velocity dispersion. In other words, considering Figure 3.9, all the $z \sim 0$ galaxies along a horizontal line have similar ages. Not only does this confirm that larger radii do not correspond to more recently-quenched galaxies, but it also extends the test to lower velocity dispersions. Since the red points preferentially occupy the portion of the figure corresponding to smaller radii also at $\log \sigma_e < 2.35$, then physical growth is essential as otherwise size and age would correlate in the SDSS sample. It is worth noting that the lack of a size-age relation holds at fixed velocity dispersion, but not at fixed stellar mass (van der Wel et al., 2009).

Finally, considering the two left panels of Figure 3.6, if the velocity dispersions remain constant and the sizes increase from $z > 1$ to $z \sim 0$, then the stellar masses must likewise increase to reproduce the local distribution.

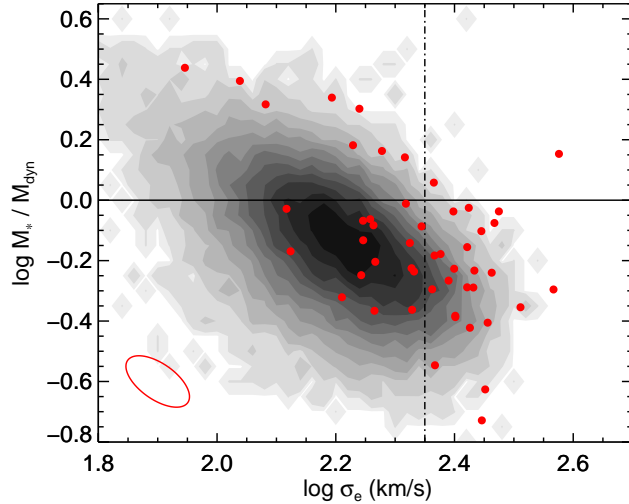


Figure 3.10 Stellar-to-dynamical mass ratio vs. velocity dispersion, for galaxies with $\log M_*/M_\odot > 10.6$. The grayscale map represents the SDSS sample, and the red points are high-redshift galaxies from our sample. The dot-dashed line indicates the threshold velocity dispersion above which galaxies are older than 10 Gyr. The median error ellipse for the high-redshift sample is shown in the bottom left corner.

To summarize, we have constructed a simple model for the evolution of quiescent galaxies over $0 < z < 1.6$ based on the following assumptions:

1. The velocity dispersions of individual galaxies do not change with cosmic time.
2. In the local universe, galaxies with larger velocity dispersions are older (Graves et al., 2009a), while at fixed velocity dispersion there is no correlation between size and age (Graves et al., 2009b).

With these assumption, observations of quiescent galaxies at low and high redshifts can be reconciled only if the sizes of individual quiescent galaxies physically grow with cosmic time. In the following, the implications of this simple model are considered.

3.5.2.1 The Evolution of Dynamical and Stellar Masses

A very interesting quantity which can be studied using our new data is the stellar-to-dynamical mass ratio. In the local universe this mass ratio shows an inverse correlation with velocity dispersion (e.g., Taylor et al., 2010a). Figure 3.10 shows this relation for both local and high-redshift samples with the restriction to galaxies more massive than our completeness limit, $\log M_*/M_\odot > 10.6$. It is important to note that the two axes are not independent, since the dynamical mass depends on velocity dispersion. Correlated errors lead to a preferred direction for the scatter of the data points as shown in the median error ellipse, calculated assuming normally distributed errors on stellar mass, radius, and velocity dispersion.

Clearly galaxies with larger σ_e tend to have smaller M_*/M_{dyn} ratios. Also, the high-redshift trend is offset from the local relation toward larger σ_e and larger mass ratios. Correlated errors can only be partly responsible for the trend seen among the red points in Figure 3.10, as the sequence spans 0.6 dex in σ_e and 0.8 dex in mass ratio, a range much larger than the observational uncertainties. Furthermore, as the error ellipse is orthogonal to the shift of the high-redshift sequence with respect to the local one, we conclude that the observed offset is real.

Figure 3.10 also marks the threshold velocity dispersion above which local galaxies have stellar populations older than 10 Gyr. To the right of the dot-dashed line, high-redshift galaxies are required to evolve until they match the SDSS distribution. Our high-redshift quiescent galaxies have slightly larger M_*/M_{dyn} ratios: at $\log \sigma_e > 2.35$ the two samples are offset by 0.05 dex. This signal is not as clear as in the velocity dispersion - size distribution, likely because of the effect of correlated errors. We expect, nevertheless, a mild evolution of the mass ratio of individual galaxies, since effective radius and stellar mass, as we showed, evolve with redshift.

Galaxies with velocity dispersion smaller than the threshold value are in general less constrained by our observations. Recently quenched objects could occupy preferentially the lower region of the figure, and in this scenario high-redshift galaxies would not be required to evolve and match the SDSS population. However, if their sizes and masses are evolving, then their mass ratio will change with time, except in the particular case of mass and size growing at the same rate, since $M_*/M_{\text{dyn}} \propto M_*/R_e$, at fixed velocity dispersion. This would correspond to evolution driven by major merging that does not affect the mass ratio since both masses change by the same amount. The evolutionary tracks would then be parallel to the one-to-one relation on the M_* versus M_{dyn} relation in Figure 3.5.

In order to constrain the evolution of high-redshift galaxies, once again we make use of the results from studies of the local universe. According to Graves & Faber (2010), at fixed velocity dispersion older galaxies have *lower* M_*/M_{dyn} ratios. This means that the high-redshift points in Figure 3.10 need to evolve toward lower mass ratios until they match the SDSS distribution, and potentially even further, in order to populate the bottom of the plot. Therefore we rule out a scenario in which stellar and dynamical mass grow at the same rate and the mass ratio of individual galaxies does not change.

Finally, we emphasize that the evolution in the mass ratio of individual galaxies is not in contradiction with the redshift-independent sequence in the stellar-dynamical mass plane. A given position on the sequence can be populated both by a galaxy at $z > 1$ and a galaxy at $z \sim 0$: they will have same stellar mass, dynamical mass, and mass ratio, but they will differ in velocity dispersion and, therefore, effective radius. According to our model, the high-redshift galaxy will then evolve at fixed velocity dispersion, increasing its size and stellar mass, but remain on the M_* - M_{dyn} sequence. At $z \sim 0$ it will occupy a different region of the sequence and will have a smaller M_*/M_{dyn} ratio. This

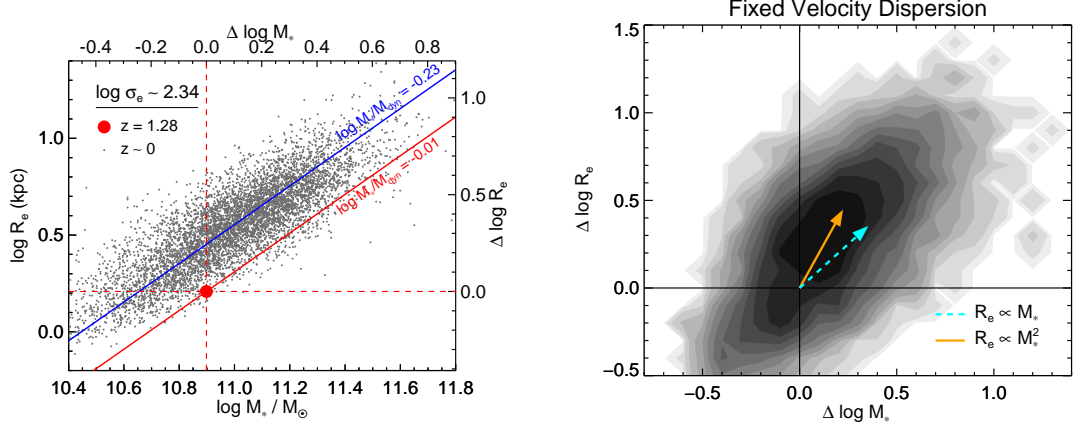


Figure 3.11 Matching at fixed velocity dispersion. *Left*: Mass-size relation. The red point is a $z = 1.28$ object in our sample with $\log \sigma_e = 2.34$, shown as example. The gray points are all the SDSS galaxies with same velocity dispersion, within 0.025 dex. The top and right axis show the logarithmic offset from the high-redshift point in stellar mass and effective radius, respectively. The diagonal lines represent fixed stellar-to-dynamical mass ratios. The blue line corresponds to the median mass ratio of the SDSS sample, and the red line corresponds to the mass ratio of the high-redshift object. *Right*: Comparison of stellar mass and effective radius at fixed velocity dispersion for the whole sample. This plot is constructed by stacking the matched low-redshift population offsets (like the one shown on the left panel) for all the LRIS objects with $\log M_*/M_\odot > 10.6$. The dashed cyan and solid orange arrows represent two example of size growth: $R_e \propto M_*$ and $R_e \propto M_*^2$, respectively.

scenario is in qualitative agreement with the prediction of numerical simulations of minor merging (e.g., Hopkins et al., 2009b; Hilz et al., 2013).

3.5.2.2 Inferring the Size Growth

We can now take full advantage of our high-quality spectroscopic data set and derive quantitatively the physical evolution in size and stellar mass of quiescent galaxies over $0 < z < 1.6$. Since we are assuming that the velocity dispersions of individual galaxies do not change with time, a natural choice is to compare the physical properties of each high-redshift galaxy of dispersion σ_0 with a subsample of the local population selected to have $\sigma_0 - h < \sigma < \sigma_0 + h$, where h is a small bin size (we take $h = 0.025$ dex). An example is shown in the left panel of Figure 3.11: the red point is a high-redshift galaxy and the gray points represent the SDSS sample selected to have a similar velocity dispersion. Here we are assuming that the red point will physically evolve to become any one of the gray points at $z \sim 0$. This allows us to determine the mean growth in size. Note that some of the $z \sim 0$ sample will be composed of galaxies that were quenched only recently, and therefore have no quiescent progenitors at $z > 1$. However, this should not bias significantly the results of our analysis since, as we discussed previously, at fixed velocity dispersion there is no correlation between size and age (Graves et al., 2009b), and therefore we can assume that young and old galaxies are evenly distributed among the SDSS points in the figure.

The $z \sim 0$ population forms a tight sequence in the mass-size plane which arises because of the relation between stellar and dynamical mass discussed previously. At fixed velocity dispersion we have:

$$\log M_* = \log M_*/M_{\text{dyn}} + \log 5/G + 2 \log \sigma_e + \log R_e. \quad (3.5)$$

Assuming a constant stellar-to-dynamical mass ratio (within a limited range in stellar mass), we obtain a linear relation between stellar mass and effective radius. The linear relation that fits the median of the SDSS sample is shown in blue in Figure 3.11. The median mass ratio for this sample is $\log M_*/M_{\text{dyn}} = -0.23$. The linear relation corresponding to the high-redshift galaxy that we took as example (shown in red) is offset by more than 0.2 dex from the local relation, despite the fact that this galaxy has, by construction, the same velocity dispersion as the $z \sim 0$ sample. As we discuss below this offset gives us a method to determine the growth in size and mass. The shift arises via the difference in the mass ratio: in Section 3.5.2.1 we demonstrated that, at a given σ_e , high-redshift galaxies have a higher mass ratio than local galaxies. For example, in this particular case the high-redshift galaxy has $\log M_*/M_{\text{dyn}} = -0.01$. We also showed that the stellar and dynamical masses of high-redshift galaxies change with time, and their mass ratio decreases. Looking at the left panel in Figure 3.11, this means that the red point must evolve onto the blue line.

For each object in the local matched sample the offset in size, $\Delta \log R_e$, and stellar mass, $\Delta \log M_*$, from the high-redshift galaxy is calculated (shown in the top and right axis in the left panel of Figure 3.11). This exercise is repeated for all the galaxies in the high-redshift sample with $\log M_*/M_\odot > 10.6$, and the distribution of mass and size offsets is summed as in the right panel of Figure 3.11. Since the distribution of σ_e in the SDSS sample falls steeply with increasing values, high-redshift galaxies with lower velocity dispersion have generally a larger number of $z \sim 0$ matching objects. In order to ensure even weighting, for each high-redshift galaxy we randomly draw from the matched $z \sim 0$ sample a fixed number of objects (250). As a small number of high-redshift galaxies have a velocity dispersion higher than any local galaxy (see Figure 3.9), we temporarily exclude them from the analysis.

The right panel of Figure 3.11 can be interpreted as the probability distribution that a galaxy at $1 < z < 1.6$ evolves in size and mass by $\Delta \log R_e$ and $\Delta \log M_*$ in order to match the local population of galaxies with same velocity dispersion. Clearly high-redshift galaxies must increase both their size and mass. A scenario in which quiescent galaxies do not increase their size over cosmic time is definitively ruled out. The mean growth is $\Delta \log R_e = 0.25 \pm 0.05$ and $\Delta \log M_* = 0.16 \pm 0.04$, corresponding to $\alpha = \Delta \log R_e / \Delta \log M_* = 1.6 \pm 0.3$. This can be compared with two examples of growth: $\alpha = 1$ (solid orange arrow) for major merging, and $\alpha = 2$ (dashed cyan arrow) for minor merging. Although the offset distribution has a shallow peak, compatible with a range in both mass and size growth of ~ 0.5 dex, the arrow corresponding to $\alpha = 1$ is only marginally consistent with

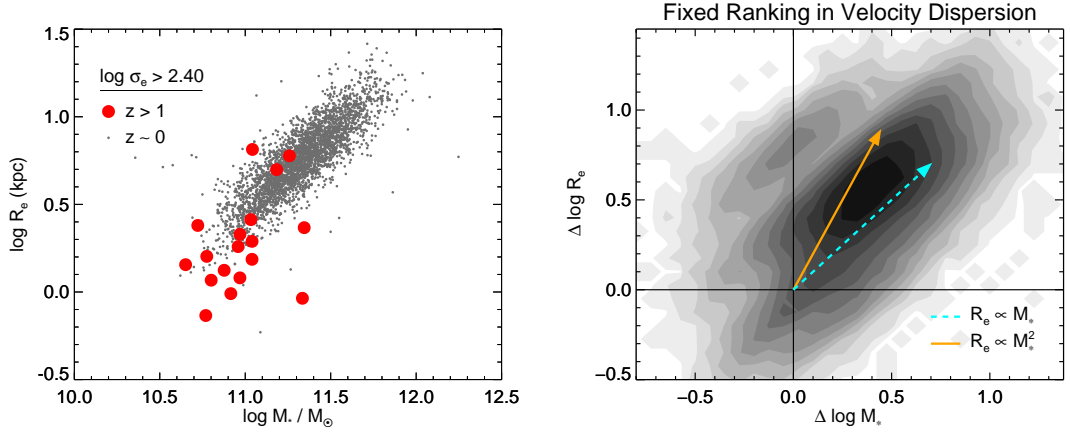


Figure 3.12 Matching at fixed velocity dispersion ranking. *Left*: Stellar mass - size plane for all the high-dispersion galaxies, defined by $\log \sigma_e > 2.40$, at high (red points) and low (gray points) redshift. *Right*: Inferred evolution in size and stellar mass of high-dispersion galaxies between $z \sim 1.3$ and $z \sim 0$. Each point represents the logarithmic offset in radius and mass of a galaxy in the SDSS sample compared to a high-redshift galaxy, both with $\log \sigma_e > 2.40$. The dashed cyan and solid orange arrows represent two examples of size growth: $R_e \propto M_*$ and $R_e \propto M_*^2$, respectively. The length of the arrows is twice the length of the arrows in Figure 3.11.

the observations. For the sample of $1 < z < 1.6$ quiescent galaxies, the size growth is steeper than $\alpha = 1$ and more consistent with minor merging. In particular, our result is in good agreement with the value $\alpha = 1.60$ found by Nipoti et al. (2012) for minor merger simulations after averaging over a cosmologically representative set of merger orbits.

3.5.3 Evolution at Fixed Ranking in Velocity Dispersion

We now confront the fact that some of the high-redshift galaxies have velocity dispersions that are larger than any found in the local universe (Figure 3.9). This raises the question of whether our assumption of a constant velocity dispersion is valid, particularly for the population with large σ_e . Also, numerical simulations do allow a weak evolution in velocity dispersion (see Section 3.5.2). For this reason we refine our matching criterion in the following way. Instead of assuming that the velocity dispersion of an individual galaxy is constant with redshift, we assume that the *ranking* of galaxies in the distribution of σ_e values is constant. A galaxy at $z > 1$ with the largest σ_e will evolve into the galaxy with the largest σ_e in a $z \sim 0$ sample drawn from an identical comoving volume. Since the volume probed by our high-redshift survey differs from that probed by the SDSS, we match galaxies at fixed cumulative number density. Such an approach is frequently used to match galaxies at different redshifts (e.g., Behroozi et al., 2013), but it is usually applied to the stellar mass function rather than to the velocity dispersion function. Although galaxy mergers can significantly change the stellar mass rank ordering, they will not affect that for the velocity dispersions significantly. We therefore expect our matching procedure to be even more robust.

Bezanson et al. (2011) have measured the velocity dispersion distribution in both the local universe and up to $z = 1.5$. They find that galaxies with very large velocity dispersions are rarer in the local universe and at about $\log \sigma_e = 2.40$ they find no evolution in the cumulative distribution, i.e., the number density of galaxies with $\log \sigma_e > 2.40$ is constant with redshift (and equals $10^{-4.5} \text{Mpc}^{-3}$). We therefore adopt this velocity dispersion threshold, $\log \sigma_{cr} = 2.40$ (corresponding to 251 km s^{-1}), and assume that high-redshift galaxies with $\sigma_e > \sigma_{cr}$ will still have $\sigma_e > \sigma_{cr}$ at $z \sim 0$. Given this large velocity dispersion threshold, incompleteness is not important, since the large- σ_e objects are the ones most easily detected as they are massive and relatively compact. However, some of the high- σ_e local galaxies are brighter than $r \sim 14.5$, and therefore affected by incompleteness due to saturation and deblending issues (Strauss et al., 2002). This problem is negligible for the main SDSS sample that we used in the previous analysis, but could be important for the much smaller population of galaxies with $\sigma_e > \sigma_{cr}$. To avoid this, we selected a secondary SDSS sample with redshift $0.10 < z < 0.15$ for this analysis. We tested that the results do not change significantly when using the main SDSS sample.

The left panel of Figure 3.12 shows the mass-size relation for the high and low-redshift samples selected with $\sigma_e > \sigma_{cr}$. The high-redshift galaxies are clearly smaller than their local counterparts. The importance of this comparison is that it represents two populations connected by a progenitor-descendent relation: the red points must physically evolve on the mass-size diagram until their distribution is similar to that of the gray points. We infer the growth in size and mass by repeating the procedure described previously: for each high-redshift galaxy we calculate the offset to the local objects, and sum the resulting distribution for the total sample in the right panel of Figure 3.12. As before there is unambiguous evolution over $0 < z < 1.6$. The growth in stellar mass and effective radius for large- σ_e galaxies is more pronounced than that found for the total sample discussed in Section 3.5.2. The mean growth is $\Delta \log M_* = 0.34 \pm 0.07$ and $\Delta \log R_e = 0.48 \pm 0.08$, with a corresponding $\alpha = 1.4 \pm 0.2$. As before the growth is steeper than $\alpha = 1$ (dashed cyan arrow), and minor merging is the preferred growth mechanism.

3.6 Summary and Discussion

Using new, deep Keck LRIS spectroscopic data we have measured velocity dispersions for 56 quiescent galaxies at $1 < z < 1.6$. Taking advantage of public *HST* imaging and multi-wavelength photometric data, we derived stellar masses and effective radii. By comparing this sample of high-redshift galaxies with a local sample drawn from the SDSS survey, we find the following results:

- Quiescent galaxies at high redshift have smaller radii and larger velocity dispersions compared to local objects at fixed stellar mass. However, the offsets in R_e and σ_e balance each other, and the dynamical masses are similar at low and high redshift, for a given stellar mass.

- We confirm the applicability at high redshift of the empirical calibration determined at $z \sim 0$ by Bezanson et al. (2011) for deriving inferred velocity dispersions from measured stellar masses and sizes. We find that the velocity dispersions measured with this method have an accuracy of 35%.
- We consider a model in which quiescent galaxies evolve over $0 < z < 1.6$ at fixed velocity dispersion. By using local observations of the velocity dispersion-age relation, we demonstrate that individual galaxies must physically evolve in size and stellar mass in order to match the $z \sim 0$ population.
- In the framework of this model, galaxies evolve at fixed velocity dispersion and increase their effective radii and stellar masses, while their stellar-to-dynamical mass ratio decreases. Quantitatively, we derive a median physical evolution of $\Delta \log R_e = 0.25 \pm 0.05$ and $\Delta \log M_* = 0.16 \pm 0.04$ over $0 < z < 1.6$ corresponding to a slope in the mass-size plane $\alpha = 1.6 \pm 0.3$. This is consistent with growth via minor merging.
- For the galaxies with the largest velocity dispersions in our sample, we perform an additional, less restrictive, comparison assuming no evolution in the velocity dispersion ranking. This results in a more convincing and stronger measure of growth, also consistent with minor merging ($\alpha = 1.4 \pm 0.2$).
- Our spectroscopic data convincingly show that the observed evolution in size and mass over $0 < z < 1.6$ arises mainly from the physical growth of individual galaxies, and cannot be explained only by progenitor bias.

Velocity dispersions represent perhaps one of the most fundamental properties of quiescent galaxies, but accurate measurement at high redshift are observationally challenging. By increasing the initial sample of Newman et al. (2010) by a factor of 4, in this work we presented the largest sample of velocity dispersion measurements at $z > 1$, from which statistically significant conclusions can be drawn. Smaller samples at similar redshifts were obtained by Bezanson et al. (2013) and van de Sande et al. (2013), who also found larger values of σ_e compared to local galaxies of similar stellar mass. By considering evolution in the mass density within a fixed radius, van de Sande et al. (2013) conclude that quiescent galaxies grow inside-out, in agreement with the minor merging scenario.

By assuming evolution at fixed velocity dispersion, we were able to derive the absolute growth in size and mass for massive quiescent galaxies over $0 < z < 1.6$. Interestingly, our results agree with the evolution inferred by van Dokkum et al. (2010) by matching galaxies at fixed number density: for galaxies with $M_* \sim 10^{11.2}$ at $z = 1.5$ they found $\Delta \log M_* = 0.25$ and $\Delta \log R_e = 0.5$. The resulting $\alpha = 2$ is consistent with evolution driven by minor merging. It is likewise encouraging that numerical simulations in the framework of Λ CDM cosmology succeed in explaining the observed

evolution of quiescent galaxies over $0 < z < 1.5$ in terms of dissipationless merging (Nipoti et al., 2012; Cimatti et al., 2012).

An alternative way to study the size growth is to compare the number density of compact objects at low and high redshift. This method does not require velocity dispersions, but relies on number density measurements, for which there are large uncertainties. As a result, different studies have found contradictory results. Trujillo et al. (2009) and Taylor et al. (2010b) did not find a population of local old objects as compact as the high-redshift ones, while Poggianti et al. (2013) claim that at least half of the $z > 1$ quiescent galaxies are found at $z \sim 0$ with similar compactness. Moreover, Carollo et al. (2013) study the evolution of the size function, finding that the size evolution is mainly driven by new arrivals, even though their conclusion is less robust for massive galaxies with $M_* > 10^{11} M_\odot$. Newman et al. (2012) consider the minimum physical growth required by the observed evolution of the smallest sizes, and infer a significant physical growth over $0 < z < 2$. They also measure the merger rate of quiescent galaxies, and conclude that for $z < 1$ the rate of minor mergers is large enough to explain the size growth.

Our approach attempts to follow a population of galaxies through cosmic time, thus avoiding the uncertainties involved in the comparison of number densities at high and low redshift. We therefore address the growth of individual galaxies rather than the evolution of the total population. Since the number of massive quiescent galaxies per unit comoving volume increases significantly from $z > 1$ to $z = 0$ (e.g., by a factor of ~ 3 according to van der Wel et al., 2009), a scenario in which newly quenched galaxies contribute significantly to the size evolution is not inconsistent with our finding of a strong physical growth of the older objects. However, we have demonstrated that progenitor bias cannot be entirely responsible for the size growth.

One further physical process has been proposed for the size growth of quiescent galaxies. A significant mass loss caused by quasar feedback (Fan et al., 2008) or stellar evolution (Damjanov et al., 2009) might in principle induce an adiabatic expansion. In this scenario the velocity dispersion is not conserved, but evolves inversely proportional to the size growth. The comparisons undertaken in this study cannot test such a process since, by construction, we assume that velocity dispersions are unchanged during the size growth. However, we note that if the size growth were entirely due to adiabatic expansion, the velocity dispersions at $z \sim 1.5$ would be about a factor of two larger than the local ones, at fixed stellar mass (Hopkins et al., 2010). Our data are in clear disagreement with this prediction (see, e.g., Figure 3.6), and rule out a dominant role of adiabatic expansion over $0 < z < 1.6$.

We acknowledge Carrie Bridge and Kevin Bundy for completing the LRIS observations for two of the slitmasks. The authors recognize and acknowledge the very significant cultural role and reverence that the summit of Mauna Kea has always had within the indigenous Hawaiian community. We are most fortunate to have the opportunity to conduct observations from this mountain.

Appendix

3.A Photometric Data

In this appendix we describe in detail the photometric catalogs used to compile the SEDs of the objects in our sample.

- GOODS-S: we use the catalog from the Multiwavelength Survey by Yale-Chile (MUSYC, Cardamone et al., 2010), which includes ground-based $U_{38}UBVRIZJHK$, 18 Subaru medium bands in the optical, and the four *Spitzer* IRAC bands.
- COSMOS: we use data from the NEWFIRM Medium-Band Survey (NMBS, Whitaker et al., 2011), which consists of deep near-infrared observations in six medium bands taken at the Kitt Peak Mayall 4 m Telescope. We also use Subaru $B_JV_Jr^+i^+z^+$, Canada-France-Hawaii Telescope (CFHT) $ugrizJHK_S$, 12 Subaru narrow bands, and *Spitzer* IRAC data, all included in the NMBS catalog.
- EGS: we make use of the catalog released by the WIRCam Deep Survey (WIRDS, Bielby et al., 2012), consisting in deep CFHT $ugrizJHK_S$ data. To this dataset we add *Spitzer* IRAC data from the Rainbow catalog (Barro et al., 2011). To avoid inconsistencies due to the difference in aperture correction and zero point between the two catalogs, we determine for each object the ratio of the flux measured by the two surveys in the same band: $f_X = F_{X,WIRDS}/F_{X,Rainbow}$, where X is one of the bands that are available in both catalogs ($griJK_S$). We then use $\langle f_X \rangle$, the flux ratio averaged over all the bands, to correct the Rainbow IRAC fluxes for that object.
- GOODS-N: three of the five objects of our sample that are located in this field fall in the region covered by the MOIRCS Deep Survey (MODS, Kajisawa et al., 2011), which includes ground-based U , *HST* $BViz$, Subaru JHK_S and *Spitzer* IRAC data. For the remaining 2 objects we use the data presented in Newman et al. (2010): *HST* $bviz$, Palomar K_S and IRAC.
- SSA22: for these galaxies we use the Subaru $BVRIZ$ and University of Hawaii 2.2 m telescope JK data described in Newman et al. (2010).

Additionally, we make use of public data from the *Chandra* and *Spitzer* archives.

3.B Galaxy Structure and Dynamical Masses

In Section 3.4 we calculated dynamical masses assuming a constant virial factor $\beta = 5$. Here we explore the possibility of a varying virial factor and its consequences on the dynamical mass calculation. The virial factor is rigorously constant only if galaxies are assumed to be identical in structure, with just a scaling in mass and size. However, since we used Sérsic profiles to describe the surface photometry, we can expect galaxies of different Sérsic indices to have different structures and therefore different virial factors. It is possible to derive a theoretical relation between β and the Sérsic index n for a spherical stellar system with an isotropic velocity dispersion distribution (Cappellari et al., 2006):

$$\beta(n) = 8.87 - 0.831n + 0.0241n^2. \quad (3.6)$$

With this definition of the virial factor, the dynamical mass is

$$M_{\text{dyn}} = \frac{\beta(n)\sigma_e^2 R_e}{G}. \quad (3.7)$$

We calculate the virial factor $\beta(n)$ for all the galaxies in our sample, obtaining an average of 6.2 and a standard deviation of 1.1. We then derive dynamical masses according to Equation 3.7 for the high-redshift galaxies and the SDSS sample, and compare them to the stellar masses in the right panel of Figure 3.13. In the left panel we show the stellar-dynamical mass comparison using a constant virial factor $\beta = 5$, as discussed in Section 3.4. In both panels we plot the objects with $n < 2.5$ as green triangles. Although the Sérsic index is not a perfect proxy for galaxy structure, low indices are considered a robust indication of the presence of a disk (Krajnović et al., 2013).

From Figure 3.13 we can see a discrepancy between the distribution of high-redshift disk galaxies and the local population. This effect is more pronounced when using a variable virial factor $\beta(n)$. In order to quantify this difference, we bin the SDSS sample in stellar mass, and calculate for each bin the average dynamical mass and its standard deviation. We then compare the distribution of high-redshift disks to the SDSS sequence. If the dynamical masses are calculated with $\beta = 5$, then 24% of the disks (4 out of 17) are outliers, as defined by being more than two standard deviations away from the $z \sim 0$ sequence. On the other hand, using $\beta(n)$ yields 47% outliers (8 out of 17) among disk galaxies. As a comparison, only 18% of the high-redshift spheroidals (i.e., objects with $n > 2.5$) are outliers, independently of which definition of β is assumed.

We chose to adopt a constant $\beta = 5$ for our analysis because it yields a better agreement between stellar and dynamical masses at both low and high redshift for the full range of Sérsic indices. The Sérsic index-dependent virial factor $\beta(n)$ seems to be a good description for spheroidal galaxies, but fails to reproduce the stellar-dynamical mass relation for disks. Although this fact is not completely unexpected, since the structure of disks is inherently different from the structure of spheroidals, it

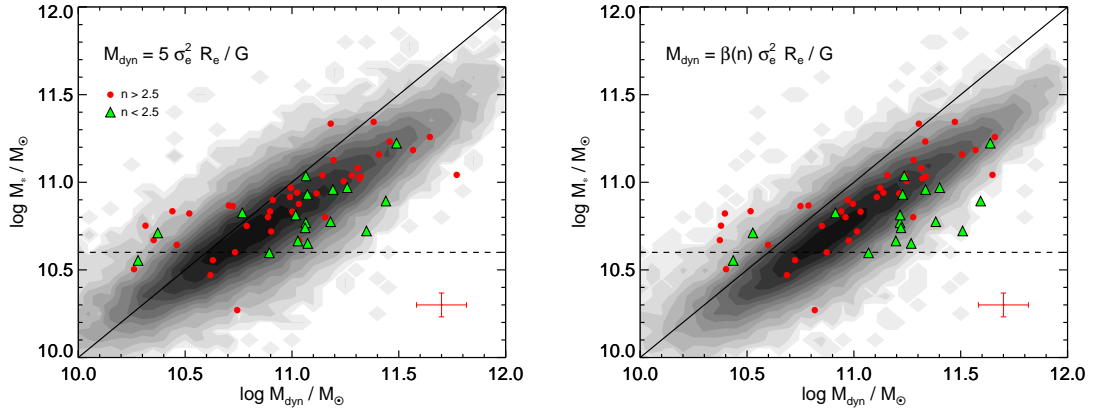


Figure 3.13 Stellar vs. dynamical mass for the SDSS sample (grayscale map) and high-redshift galaxies, divided into disks (Sérsic index $n < 2.5$, green triangles) and spheroidals ($n > 2.5$, red points). *Left*: Dynamical masses calculated using a constant virial factor $\beta = 5$ (Equation 3.3). *Right*: Dynamical masses calculated from Equation 3.7, using the Sérsic index-dependent virial factor $\beta(n)$.

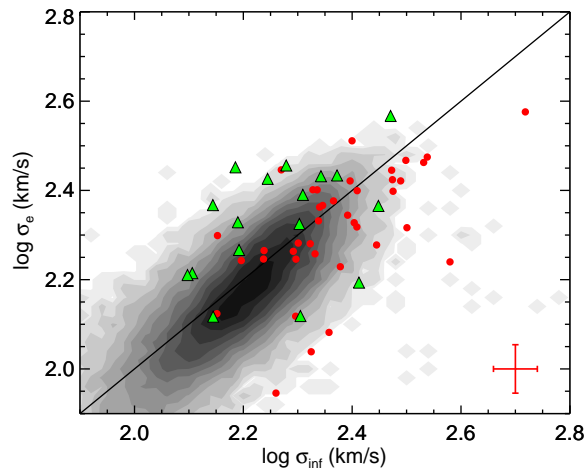


Figure 3.14 Spectroscopically observed vs. photometrically inferred velocity dispersions. High-redshift data points are divided into disks ($n < 2.5$, green triangles) and spheroidals ($n > 2.5$, red points), and the SDSS sample is shown as a grayscale map. All the inferred dispersions are calculated using Equation 3.8. The median error bars are shown on the bottom right corner.

is noteworthy that at low redshift there is a good agreement between stellar and dynamical masses, derived using Equation 3.7, even for low Sérsic indices. This difference might be caused by the fact that the SDSS fibers in most of the cases sample only the central part of a galaxy, measuring the velocity dispersion of the bulge, while at high-redshift we measure the total velocity dispersion, which includes the disk rotation.

Finally, we note that the original definition of inferred velocity dispersion given by Bezanson et al. (2011) includes the virial factor $\beta(n)$:

$$\sigma_{\text{inf}} = \sqrt{\frac{GM_*}{0.557\beta(n)R_e}}. \quad (3.8)$$

We test the agreement between the inferred dispersions derived via this equation and the spectroscopically measured dispersions in Figure 3.14. Again, we plot disk galaxies as green triangles. This definition of inferred dispersion produces a good agreement with the σ_e values, with a scatter of 35%, similar to the one that we obtained using our definition (Equation 3.4). However, there is a clear trend with the Sérsic index, and this method would underpredict the true value of velocity dispersion for most of the $n < 2.5$ objects.

Chapter 4

Stellar Populations from Spectroscopy of a Large Sample of Quiescent Galaxies at $z > 1$: Measuring the Contribution of Progenitor Bias to Early Size Growth

Abstract

We analyze the stellar populations of a sample of 62 massive ($\log M_*/M_\odot > 10.7$) galaxies in the redshift range $1 < z < 1.6$, with the main goal of investigating the role of recent quenching in the size growth of quiescent galaxies. We demonstrate that our sample is not biased toward bright, compact, or young galaxies, and thus is representative of the overall quiescent population. Our high signal-to-noise ratio Keck LRIS spectra probe the rest-frame Balmer break region which contains important absorption line diagnostics of recent star formation activity. We obtain improved measures of the various stellar population parameters, including the star-formation timescale τ , age, and dust extinction, by fitting templates jointly to both our spectroscopic and broad-band photometric data. We identify which quiescent galaxies were recently quenched and backtrack their individual evolving trajectories on the UVJ color-color plane, finding evidence for two distinct quenching routes. By using sizes measured in the previous chapter, we confirm that the largest galaxies are indeed among the youngest at a given redshift. This is consistent with some contribution to the apparent growth from recent arrivals, an effect often called *progenitor bias*. However, we calculate that recently-quenched objects can only be responsible for about half the increase in average size of quiescent

A version of this chapter has been published as Belli, S., Newman, A. B., & Ellis, R. S. 2015, ApJ, 799, 206

galaxies over a 1.5 Gyr period, corresponding to the redshift interval $1.25 < z < 2$. The remainder of the observed size evolution arises from a genuine growth of long-standing quiescent galaxies.

4.1 Introduction

In the local universe, quiescent galaxies present a particularly tight *red sequence* in the color-mass diagram (e.g., Bower et al., 1992; Blanton et al., 2003; Baldry et al., 2004). Understanding the mass assembly history of this remarkably homogeneous population remains one of the most important questions in the field of galaxy evolution. Quiescent galaxies selected at high redshift demonstrate that the red sequence seen locally was already in place at $z \sim 2$ (Cimatti et al., 2004; Labbé et al., 2005; Kriek et al., 2008). However, high redshift quiescent galaxies are significantly smaller at fixed stellar mass (e.g., Daddi et al., 2005; Trujillo et al., 2006b; van Dokkum et al., 2006, 2008; Cimatti et al., 2008) raising the question of how such size growth occurred while maintaining the uniformity of the population. Although the inferred size evolution was initially questioned, subsequent studies have confirmed the result, ruling out biases in both the mass and size measurements at high redshift (e.g., Muzzin et al., 2009; Szomoru et al., 2012).

Among the physical processes that may be responsible for this surprising size growth, theoretical arguments favor minor mergers since they represent an efficient way to increase the size of a galaxy compared to the growth of its stellar mass (e.g., Naab et al., 2009; Hopkins et al., 2010). However, as the comoving number density of quiescent galaxies increases by about an order of magnitude between $z \sim 2$ and $z \sim 0$ (e.g., Muzzin et al., 2013), most of those observed locally cannot be the descendants of those at high redshift. The remainder were likely star-forming systems whose star formation was quenched and subsequently arrived on the red sequence. As star-forming galaxies are typically larger than quiescent galaxies (e.g., Newman et al., 2012), some of the inferred growth with time in the quiescent population may be due to the later arrival of these quenched systems. It has been argued that this effect, termed *progenitor bias*, could explain part or all of the surprising size evolution in the quiescent population (e.g., Carollo et al., 2013; Poggianti et al., 2013).

Detailed spectroscopic studies provide the most effective way to make progress in understanding both the physical origin of the size growth in quiescent objects as well as in disentangling the contribution from progenitor bias. In Chapter 3 we investigated the size growth of quiescent galaxies to $z \sim 1.6$ using deep Keck LRIS spectroscopy of over 100 massive galaxies with $z > 1$. We considered size evolution at fixed velocity dispersion arguing that the latter quantity should remain relatively constant with time even in the event of minor mergers (e.g., Hopkins et al., 2009b). By matching each high redshift galaxy to local samples with equivalent velocity dispersions, we concluded that physical size growth must have occurred and that progenitor bias alone cannot explain the observations. Moreover, the *growth efficiency* $d \log R / d \log M$ we inferred over $0 < z < 1.6$ is consistent with that

expected for minor mergers, a conclusion in agreement with the frequency of likely associated pairs observed over this redshift interval in deep CANDELS data (Newman et al., 2012).

The present chapter addresses the more challenging aspect of the observations. At redshifts above $z \sim 1.5$, the rate of size growth accelerates significantly. Specifically, in Newman et al. (2012) we found the growth at fixed stellar mass over $1.5 < z < 2.5$, an interval of only 2 Gyr, is comparable to that which occurred in the subsequent 9 Gyr to the present epoch. However, in this redshift range, the frequency of likely minor mergers is insufficient to explain the rapid growth. To verify this remarkably rapid size growth, we recently extended our spectroscopic study to a smaller sample of $2 < z < 2.5$ quiescent galaxies using MOSFIRE, a new near-infrared multi-object spectrograph at the Keck observatory (see Chapter 5). Combining dispersion measures for this new sample with the limited number of similar $z > 2$ measures in the literature (van Dokkum et al., 2009; Toft et al., 2012; van de Sande et al., 2013) enabled us to measure the growth efficiency, which is too high to be consistent with the minor merging scenario. In addition to the shortage of observed associated pairs during this early period (Newman et al., 2012), numerical simulations in the Λ CDM framework are also unable to explain the fast growth rate (Nipoti et al., 2012; Cimatti et al., 2012). Given the fast rise in the comoving number density of quiescent systems, progenitor bias is likely to become more important at higher redshift, and is conceivably a significant factor in explaining growth in the $1.5 < z < 2.5$ interval.

A direct way to estimate the contribution of newly-quenched galaxies to the size growth of quiescent sources is to examine the size distribution as a function of the *age* of the stellar population. This tests whether the most compact objects are the oldest as would be the case if the growth is mostly due to progenitor bias. Luminosity weighted stellar ages can be inferred from the detailed absorption features seen in the rest-frame optical spectra. However, as high quality spectra are required for accurate age measures, limited work has so far been possible at $z > 1$ (e.g., Kriek et al., 2006, 2009; Onodera et al., 2012; Whitaker et al., 2013). The LRIS spectra of $1 < z < 1.6$ galaxies obtained for our velocity dispersion study (see Chapter 3) are ideal for this purpose. In addition to being the largest systematic spectroscopic study of quiescent galaxies above $z \sim 1$ to date, the rest-frame optical spectra include important features such as the Balmer absorption lines, the 4000Å break, and the [OII] emission line, that are sensitive to the past star formation activity on various timescales that probe earlier activity out to $z \sim 2-2.5$. As we will show in this chapter, we can improve the age constraints by combining our spectroscopic measures with those derived from the spectral energy distributions derived over a wide wavelength range from publicly available multi-band photometric surveys. We undertake a comprehensive Bayesian analysis that takes into account simultaneously both photometric and spectroscopic data (see Newman et al., 2014). This allows us to secure accurate stellar population parameters for a large representative sample of quiescent galaxies at $z > 1$.

The main goal of the present work is therefore to study the size-age relation for quiescent galaxies at $1 < z < 1.6$ and thereby to infer the past size evolution of the red sequence population, disentangling genuine physical growth of old sources from the contribution of newly-quenched sources (progenitor bias). Additionally, by reconstructing the past star formation of individual objects now observed on the red sequence, we can explore the mass assembly history and obtain new insights into the physical processes responsible for the quenching that transformed star-forming galaxies into passive objects.

An overview of the chapter follows. In Section 4.2 we review the sample, briefly discussing the LRIS spectra and the auxiliary photometric data. In Section 4.3 we derive the stellar population properties by fitting templates to our Keck spectra, demonstrating the value of additional constraints that arise from the presence of [OII] 3727 Å emission. In Section 4.4 we analyze in detail various components of the color-color diagram for our LRIS sample and use our stellar population parameters to reconstruct the past trajectories of individual quiescent galaxies, measuring how recently they arrived on the red sequence. This enables us to investigate the role of quenching in the observed size growth over $1.25 < z < 2$, and hence to quantify the effect of progenitor bias, in Section 4.5. Finally, we summarize our results and discuss them in the context of galaxy quenching scenarios in Section 4.6. Throughout this chapter we use the AB magnitude system, and assume a Λ CDM cosmology with $\Omega_m = 0.3$, $\Omega_\Lambda = 0.7$, and $H_0 = 70 \text{ km s}^{-1} \text{ Mpc}^{-1}$.

4.2 Data

The present analysis is drawn from the spectroscopic sample of 103 galaxies presented in Chapter 3. In brief, most of the galaxies in the sample were selected to have photometric redshifts in the range $0.9 < z_{\text{phot}} < 1.6$ and stellar masses, derived from broad-band photometry, larger than $10^{10.7} M_\odot$. Massive and quiescent objects were given a higher priority when designing the slitmasks. All targets were observed with the LRIS Spectrograph (Oke et al., 1995) and its red-sensitive CCD on the Keck I telescope, with integration times ranging from 3 to 11 hours per mask. Examples of the LRIS spectra are shown in Chapter 3.

All except three galaxies in our sample lie in fields observed by the Cosmic Assembly Near-IR Deep Extragalactic Legacy Survey (CANDELS, Grogin et al., 2011; Koekemoer et al., 2011). Therefore, high-quality *HST* F160W observations, together with a wealth of broad-band photometric data, are publicly available. For each object, we collate space and ground-based observations from the near-UV to the near-infrared, including *Spitzer* IRAC data (Cardamone et al., 2010; Whitaker et al., 2011; Bielby et al., 2012; Barro et al., 2011; Kajisawa et al., 2011; Newman et al., 2010) and MIPS data from the *Spitzer* archive.

In Appendix 4.A we demonstrate that, for stellar masses above $10^{10.7} M_\odot$, our sample is fully

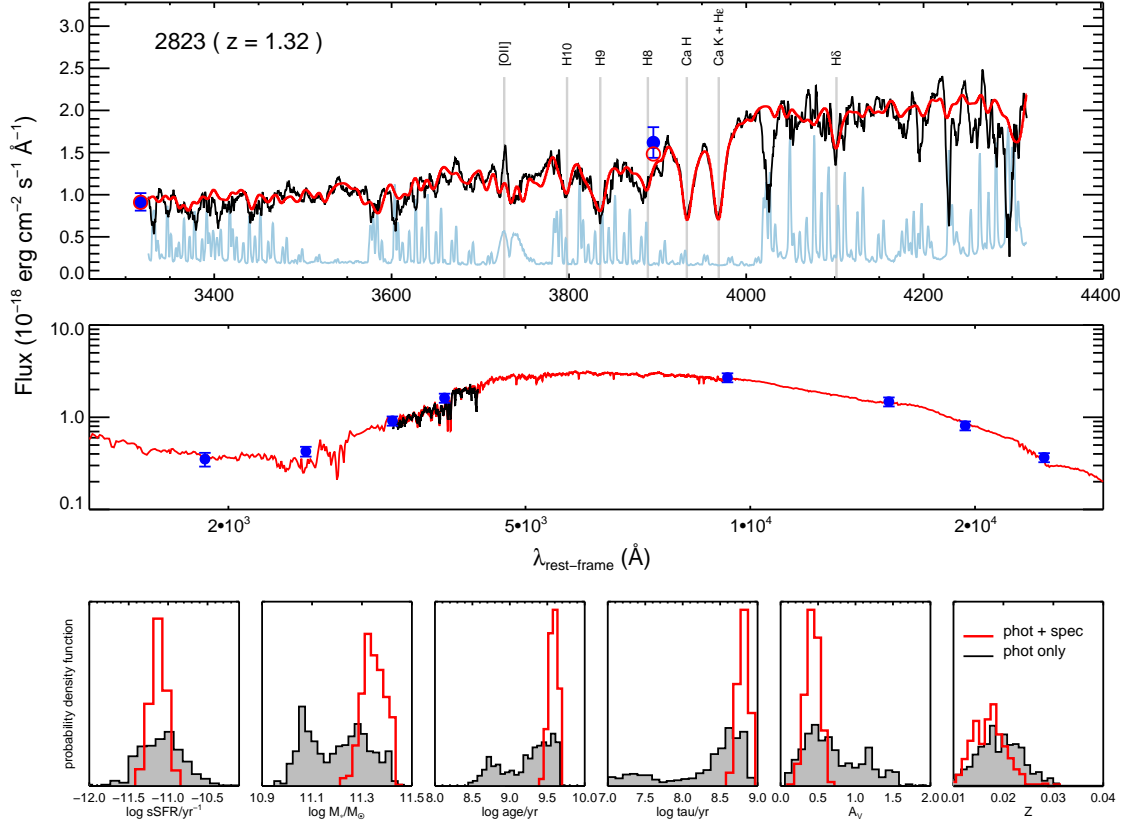


Figure 4.1 An illustration of our spectral fitting technique for the object 2823 ($z = 1.32$) which has a signal-to-noise ratio representative of the sample. Top two panels: observed Keck LRIS spectrum (black), error spectrum (cyan), observed multi-band photometry (blue) and best-fit model (red). In the top panel, empty red circles show the flux in the observed passbands expected from the best-fit model, and vertical gray lines mark the most important spectral features. Bottom: the posterior distributions output by `pyspecfit` are shown for the five stellar population parameters and the specific star formation rate. Gray histograms represent those obtained by fitting the photometric data alone, while the red histograms show the same distribution when the LRIS spectrum is included.

representative of the population of quiescent galaxies in this redshift range in terms of both colors and sizes. In the following analysis we will consider those 62 objects with stellar masses above this threshold. This remains the largest $z > 1$ unbiased sample with high signal-to-noise spectra.

4.3 Derivation of Physical Properties

4.3.1 Stellar Populations

Stellar population properties of high redshift galaxies are usually derived by model fitting of either broad-band photometry or a spectrum. Our LRIS spectra probe a rest-frame region rich in diagnostics of recent star formation activity, such as the Balmer lines and the 4000Å break. Older stellar populations, however, contribute mainly to the near-infrared emission. To take advantage of both our high quality Keck spectra and the wealth of photometry available for our sample, we fit stellar population templates jointly to both the spectroscopic and photometric data. We use the Bayesian code `pyspecfit` presented by Newman et al. (2014), which performs a Markov Chain Monte Carlo sampling of the parameter space and outputs the posterior distributions, from which uncertainties and degeneracies can be properly estimated.

We mask out the spectral region around [OII] emission and those pixels most contaminated by sky emission. We allow a polynomial correction to the observed spectrum in order to match the broad-band spectral energy distribution. We also add in quadrature a 5% contribution to represent systematic errors to the photometry, and we exclude the IRAC datapoint at 8 μm , which is susceptible to contamination by dust emission. In order to give appropriate weighting to the spectra and photometry, we run an initial fit that we use only to calculate the chi-square, which we then use to rescale the error spectra.

We selected stellar population templates from the library of Bruzual & Charlot (2003), and assume a Chabrier (2003) initial mass function (IMF) and the Calzetti et al. (2000) dust extinction law. We adopt exponentially decreasing star formation histories (or τ models), characterized by the age t_0 and timescale τ (with star formation rate proportional to $e^{-(t-t_0)/\tau}$), which have log-uniform priors in the range $10^8\text{yr} < t_0 < t_H$ and $10^7\text{yr} < \tau < 10^{10}\text{yr}$, where t_H is the age of the universe corresponding to the galaxy redshift, which is fixed to its spectroscopic value. The templates depend on two further parameters: the dust attenuation A_V , with the uniform prior $0 < A_V < 4$, and the metallicity Z , with a normal prior centered on the solar value $Z_\odot = 0.02$ and with a width of 0.005. The final output of the fitting procedure includes also the stellar mass M_* , obtained by scaling the best-fit template to the observed photometric data. The specific star formation rate (i.e., star formation rate per unit stellar mass) is not a free parameter, but is uniquely determined by the combination of t_0 and τ .

Figure 4.1 illustrates the procedure for a representative galaxy at $z = 1.32$. The template provides

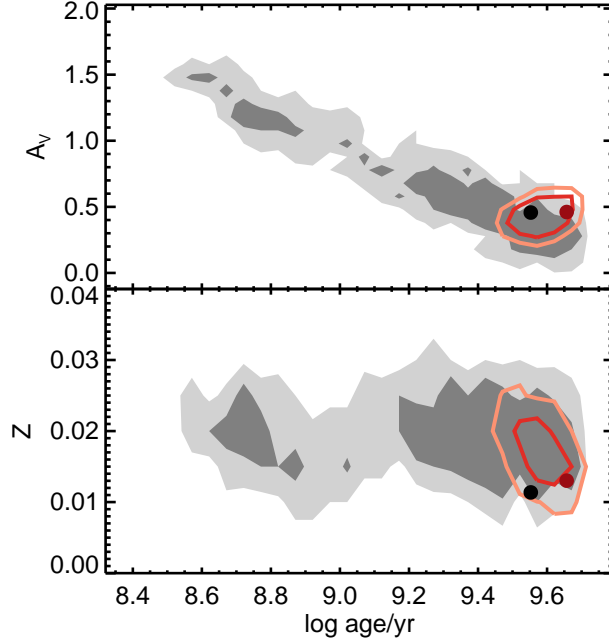


Figure 4.2 2D posterior distributions for the object shown in Figure 4.1: dust extinction versus age (top panel) and stellar metallicity versus age (bottom panel). Grayscale contours represent the 68 and 95% confidence levels for fit to the photometry alone with the black point marking the best-fit parameters. Red lines and points represent the fit to both the photometric and spectroscopic data. Combining both datasets is successful in breaking the dust-age degeneracy but less so for the metallicity-age degeneracy.

an excellent fit to the observed photometry from the rest-frame UV to the near-infrared and also the detailed Keck spectrum. The fit is fully described by the five stellar population parameters t_0 , τ , A_V , Z , and M_* . The posterior distributions output by `pyspecfit` for each parameter are shown in red in the bottom panels of Figure 4.1. The posterior distribution for the specific star formation rate, derived from the posteriors of t_0 and τ , is also shown. In each panel, the posterior distribution obtained by fitting only the photometric data (but keeping the redshift fixed to its spectroscopic value) is shown as a gray histogram. The advantage of including the spectroscopic data in the fit is clear: the posterior distributions become much narrower. For example, the median uncertainty on the ages in our sample decreases from 0.10 dex to 0.05 dex when including the spectra. The stellar population parameters and their uncertainties are listed in Table 4.1.

Including the rest-frame spectra in the fitting procedure breaks degeneracies between some of the stellar population parameters. A familiar degeneracy is that between age and dust extinction, each of which has a similar reddening effect on the spectral energy distribution. The Balmer absorption lines and other features in the rest-frame optical spectrum, marked in Figure 4.1, are only sensitive to the age. Once the age is well determined spectroscopically, the amount of dust extinction is much more effectively constrained. The top panel of Figure 4.2 shows the two-dimensional (2D) posterior

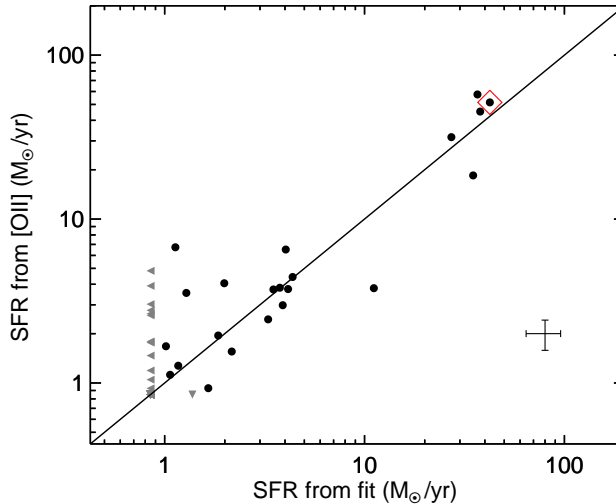


Figure 4.3 A comparison of the star formation rate as derived from our spectral fitting technique with that estimated from the strength of [OII] 3727 Å emission. Median uncertainties are shown in the bottom right corner, and upper limits are marked as gray triangles. Objects for which the IRAC colors imply the presence of an AGN are marked with red diamonds.

distribution of dust extinction and age for the galaxy presented in Figure 4.1 and how inclusion of the spectrum improved estimates of both. A further degeneracy is that between age and metallicity, for which the 2D posterior distribution is shown in the bottom panel. In this case our technique is somewhat less successful.

The fitting procedure usually yields posterior distributions that are smooth and well separated from the edges of the prior. In only three cases (that we will discuss in Section 4.4.1) the age and τ parameters have the minimum allowed values. We discard these objects from our sample, since their star formation histories are unreliable. Broadly speaking the uncertainties in each parameter are comparable with those given in the example in Figure 4.1 and this is important to remember in the following section.

4.3.2 [OII] Emission

Many galaxies in our sample show [OII] λ 3726,3729 emission, which is useful as an additional diagnostic of the current star formation rate, independent of the fitting procedure described above. Accordingly, we measured the [OII] rest-frame equivalent width for each spectrum by first subtracting the best-fit model spectrum from the observed one and fitting a double Gaussian to the residual. Both components of the [OII] doublet were assumed to have a fixed relative wavelength and identical width. Line emission with an equivalent width larger than 2\AA is seen for 40 out of 58 objects for which the observed spectra cover the appropriate wavelength range.

To derive star formation rates, we convert the equivalent widths to luminosities using the con-

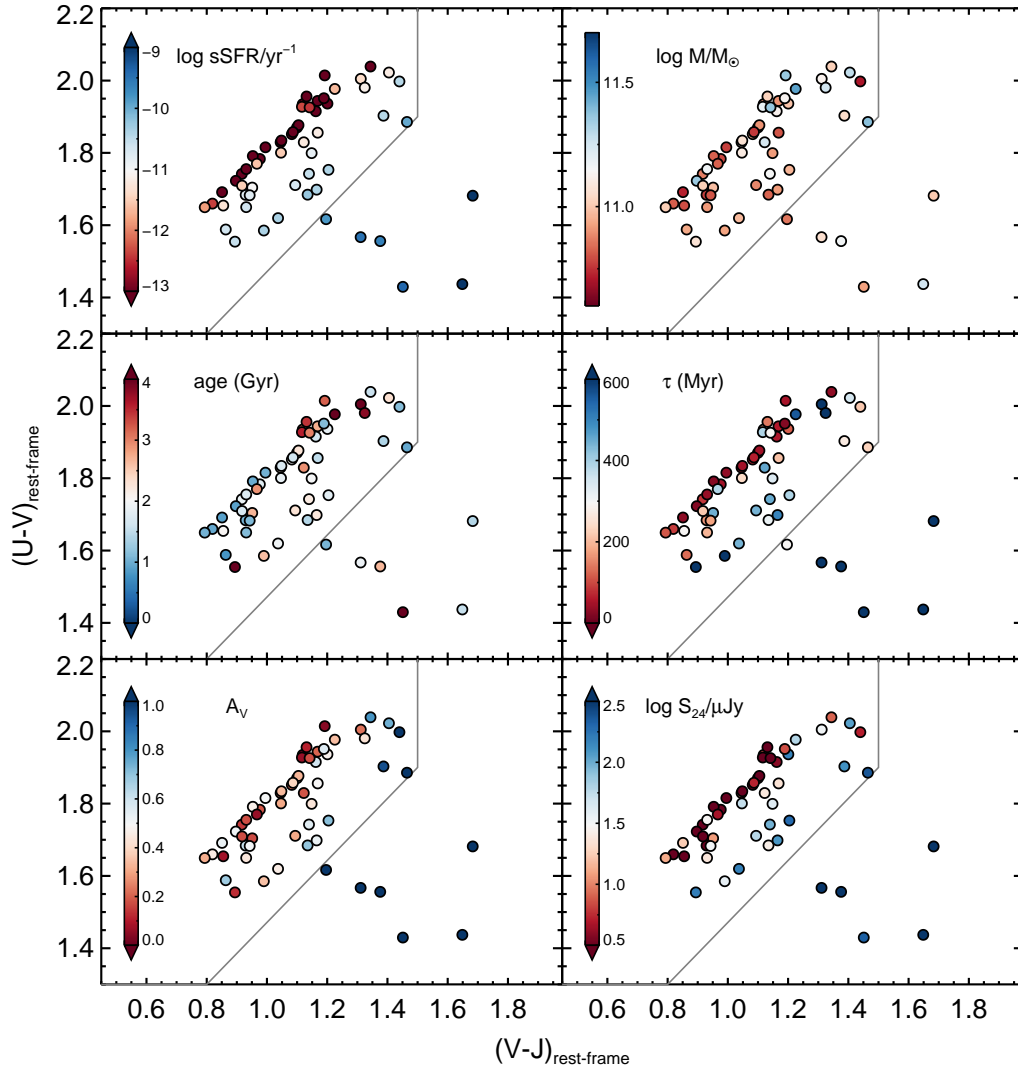


Figure 4.4 The distribution on the UVJ plane of the physical properties of the LRIS sample. Panels show the stellar population parameters obtained via spectral fitting for each galaxy, and the $24\ \mu\text{m}$ flux. The gray line indicates the division between quiescent and star-forming galaxies adopted by Muzzin et al. (2013). In the last panel, only galaxies with available MIPS data are shown.

tinuum flux given by our best-fit model spectra. We use the Kewley et al. (2004) calibration to derive the star formation rate, which we then correct for dust extinction. Figure 4.3 compares the star formation rates obtained in this way with those obtained via spectral fitting. For galaxies with a significant level of star formation (i.e., above $\sim 1 M_{\odot}/\text{yr}$), the spectral fitting star formation rates are in good agreement with the ones derived from [OII] emission. Although we do not use the star formation rates in our main analysis, the agreement between the two estimates represents an important independent confirmation of the stellar population parameters obtained with `pyspecfit`.

A number of galaxies that are not forming stars according to the spectral fitting show weak, but clearly detected emission lines. Other than star formation, possible causes for the presence of an [OII] line are AGN and LINER emission. We use IRAC colors to identify strong AGNs, following Donley et al. (2012), and find only two. Both are star-forming objects, and one has [OII] in the observed range and is marked with a red diamond in Figure 4.3. The [OII] lines detected in quiescent galaxies are therefore due to LINER emission, in agreement with what found at $z \sim 0$ (Yan et al., 2006; Graves et al., 2007) and $z \sim 1$ (Lemaux et al., 2010). Such emission might be caused by hot old stars and is not necessarily associated with AGNs (Singh et al., 2013).

In the subsequent analysis, we exclude the two strong AGNs from our sample. We also checked the X-ray emission using Chandra data, and found four detections in addition to the two strong AGNs (also detected). As these targets do not show any peculiarity, we keep them in our sample.

4.4 The Red Sequence

As discussed in Chapter 3, quiescent galaxies in our LRIS sample can be identified using a UVJ color-color diagram (e.g., Wuyts et al., 2007; Williams et al., 2009). Figure 4.4 shows how the stellar population parameters obtained via spectral fitting (as described in Section 4.3) are distributed according to the location of the galaxy in this diagram (see Appendix 4.A for details on the rest-frame colors). In each panel the solid line indicates the division between quiescent and star-forming galaxies adopted by Muzzin et al. (2013).

Even in the redshift range $1 < z < 1.6$ a familiar picture emerges. A tight red sequence is clearly visible with a sharp upper envelope. Red sequence galaxies have low specific star formation rates, mature ages and relatively short τ parameters. Moreover, they have little to no dust extinction. Elsewhere in the diagram, ‘blue cloud’ galaxies present significant star formation rates and dust extinction with larger τ parameters.

The last panel of Figure 4.4 show the distribution of the *Spitzer* MIPS 24 μm flux. As with the earlier discussion of [OII] λ 3726,3729 emission, this measure is completely independent of the spectral fit and supports the above picture. In particular, we note that the objects that comprise the tightest part of the red sequence have very low mid-infrared emission. Clearly they are genuinely quiescent galaxies and their red colors are not due to the effect of dust extinction.

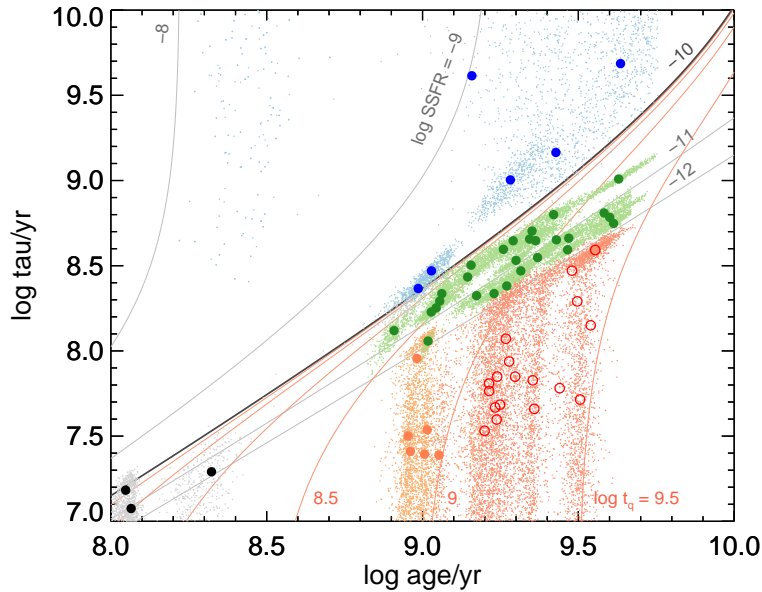


Figure 4.5 Distribution of the stellar population parameters τ and age obtained via our fitting technique (Section 4.3.1). Large points indicate the best-fit values, and the posterior distributions are plotted using small dots. The colors represent different galaxy populations: blue cloud (blue), green valley (green), red sequence (red, open symbols), and post-starburst galaxies (orange) - see text for definitions. The objects shown in black have posterior distributions limited by the prior boundaries, and we consider these to be less reliable. The gray lines mark regions of the plot of constant specific star formation rate, while the red lines mark regions of constant quiescent time (as defined in Section 4.5.1).

4.4.1 Diversity among Quiescent Galaxies

Our high quality spectra allow us to go beyond the simple division of the population into star-forming and quiescent galaxies that is conventionally done at high redshift. Thus we depart briefly from our goal of analyzing the nature of size evolution of the quiescent population to illustrate this surprising diversity in the quiescent population. From Figure 4.4 we see that *perpendicular* to the red sequence, the star formation rate increases progressively. Objects with intermediate values of specific star formation rate are often considered to be transitional objects moving toward the red sequence, particularly at high redshift (e.g., Gonçalves et al., 2012). This population shows similar ages to the red sequence, but larger τ values, consistent with elevated levels of star formation.

On closer examination, our stellar population parameters indicate there is some diversity even within the red sequence population itself. Figure 4.4 shows there is a clear gradient in the age along the sequence, from ~ 1 Gyr at the blue end to ~ 3 Gyr at the red end. The redder galaxies also tend to be more massive and less dusty. To better understand how this diversity might arise, we consider their distribution in the τ versus age plane in Figure 4.5. For each object we plot the best-fit value as a large data point and the full posterior distribution with small dots which is helpful in indicating

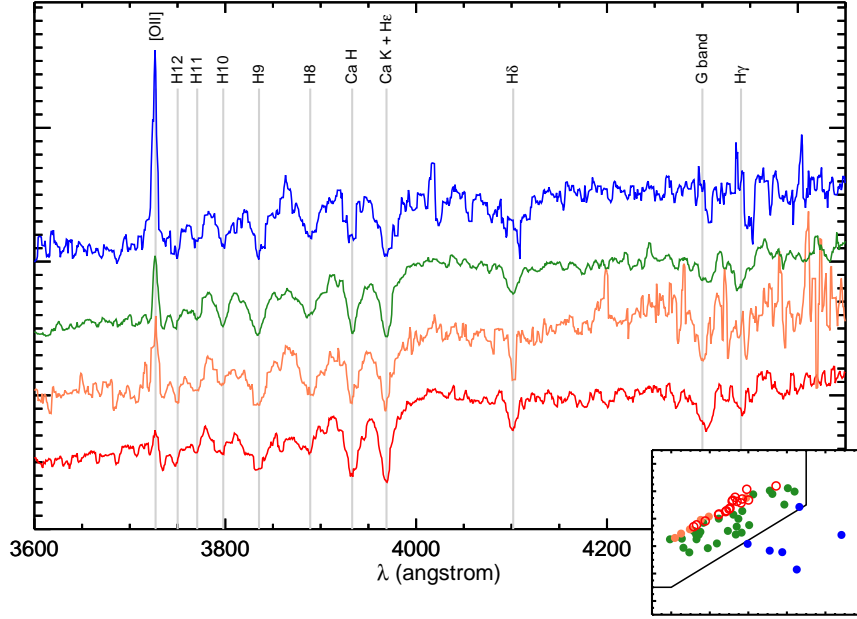


Figure 4.6 Stacked spectra for the four galaxy populations defined in Section 4.4.1. Gray vertical lines mark the location of important spectral features. The inset shows the distribution of the populations on the UVJ diagram. Colors and symbols as in Figure 4.5.

the uncertainties. Lines of constant specific star formation rate are indicated. We identify different galaxy populations in Figure 4.5:

- Galaxies above the bold line, which marks a specific star formation rate of 10^{-10} yr^{-1} , are *star-forming* (blue points, 6 objects). As a reference, the main sequence at this redshift corresponds to a specific star formation rate of 10^{-9} yr^{-1} (Speagle et al., 2014).

We call *quiescent* all the galaxies below the bold line. We adopt the value 10^{-10} yr^{-1} because it is roughly equivalent to a mass doubling time twice the age of the universe at $z \sim 1.3$. This threshold in specific star formation rate is almost exactly equivalent to the UVJ selection box shown in Figure 4.4. We further divide quiescent galaxies into three groups:

- *Green valley* galaxies are defined as having a specific star formation rate between 10^{-12} and 10^{-10} yr^{-1} (green points, 27 objects). The posterior distributions of these galaxies are elongated, following lines of constant specific star formation rate. This indicates that the measurement of star formation activity is robust but there is a small degeneracy between age and τ .
- The *red sequence* consists of genuinely old, passive galaxies, with ages above 1.25 Gyr and specific star formation rates below 10^{-12} yr^{-1} (red empty points, 18 objects). The posterior distributions are vertical: for these objects we have a good measure of the age but only an

upper limit on τ , and therefore we can only obtain an upper limit on the star formation rate.

- The remaining passive galaxies, i.e., those with ages below 1.25 Gyr and specific star formation rates below 10^{-12} yr^{-1} , are *post-starburst galaxies* (orange points, 6 objects). We use this term to indicate quiescent galaxies that show signs of recent star formation activity; this is different from the often used definition in terms of absence of [OII] emission and presence of strong Balmer absorption lines (e.g., Dressler et al., 2013).

Finally, the points in black represent three galaxies whose determined τ and age are unphysically small and represent limits governed only by the boundary of the priors. We discard these objects from our analysis of the quiescent sample, since their colors are clearly in the star-forming region of the *UVJ* diagram.

A striking way to further visualize this diversity in the population of quiescent galaxies is via stacked spectra for the four populations (Figure 4.6) defined above. For each galaxy within the relevant population, we convolve the spectrum with a Gaussian kernel to yield a fixed velocity dispersion of 400 km s^{-1} , normalize to a median flux at $4000\text{\AA} < \lambda < 4050\text{\AA}$, and produce a median-stack. No weighting is applied to avoid biasing the results to more luminous objects. The spectra show a very clear decline in activity from blue cloud to old red sequence sources as indicated in a declining level of [OII] emission but an increasing 4000\AA break, more prominent G band and deep Calcium absorption lines, the latter being features associated with older stars. Importantly, however, these trends continue within the red sequence itself from the younger end (populated by post-starburst galaxies) to the older end. In the inset of Figure 4.6 we plot the four populations on the *UVJ* diagram. Clearly the post-starburst galaxies occupy the blue side of the red sequence (e.g., Whitaker et al., 2013).

The purpose of this interlude in our goal to address size evolution will become clearer when we attempt to physically understand how these various subsets of quiescent galaxies fit into an evolutionary picture in Section 4.6.

4.4.2 Reconstructing the Quiescent Population

The availability of ages and τ parameters for each LRIS galaxy in Figure 4.4 enables us to reconstruct their past star formation histories and hence their earlier trajectories on the *UVJ* color-color diagram. This provides the basic means by which we can disentangle which quiescent sources are truly old and possibly growing in physical size, and which sources became quiescent more recently and may contribute to apparent growth with time via progenitor bias.

We use the star formation history to calculate the stellar population parameters, including the rest-frame colors, at various periods earlier in time. In Figure 4.7 we plot the distribution for the epoch of observation, t_{obs} (final panel), and at five earlier times $t_{\text{obs}} - \Delta t$, with Δt in increments

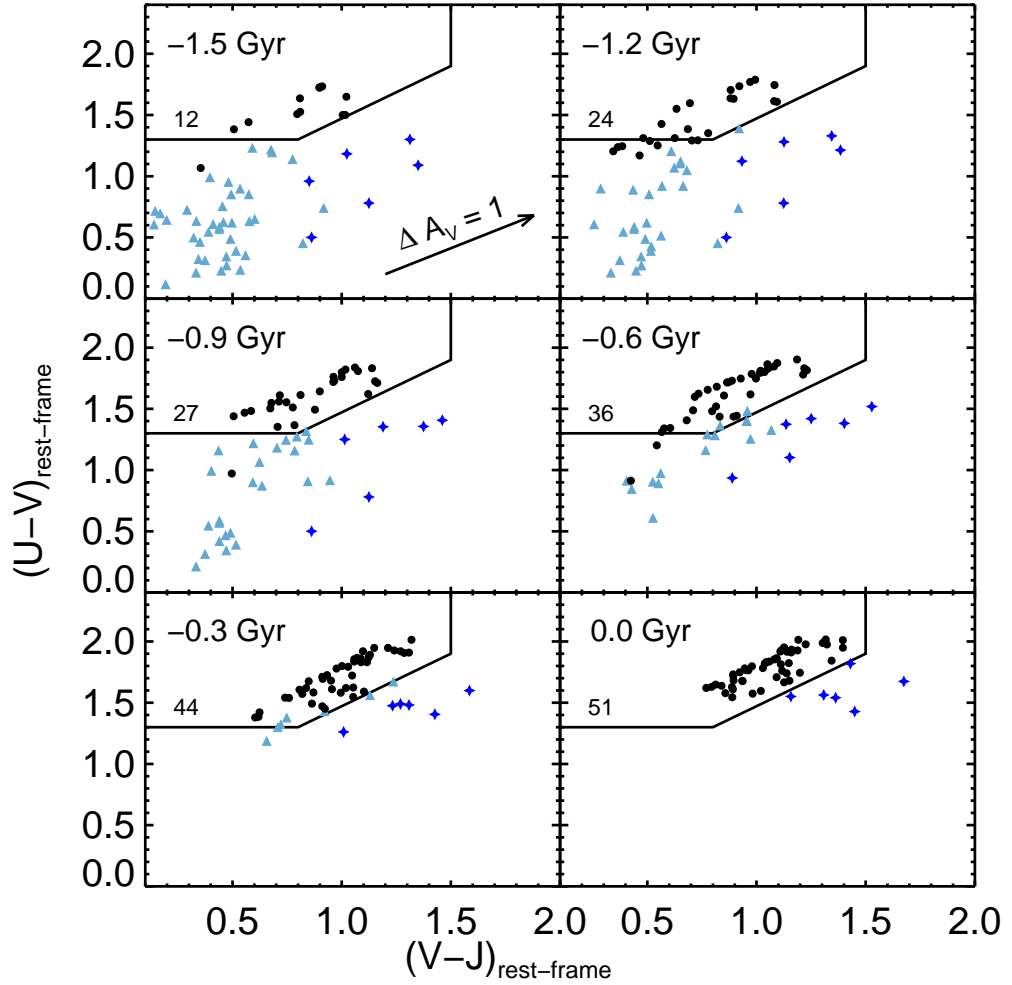


Figure 4.7 Reconstructed evolution of the LRIS sample on the UVJ diagram in a series of time snapshots 300 Myr apart up to the epoch of observation in the final panel (corresponding to the median redshift of our sample: $z = 1.25$). For each time snapshot, black points represent quiescent galaxies, while light blue triangles are star-forming galaxies that will become quiescent by the end of the simulated evolution (i.e., at the time of observations). Blue stars represent galaxies that are star-forming throughout the simulation. The number of quiescent galaxies, defined as those with a specific star formation rate less than 10^{-10} yr^{-1} (Section 4.4.1), is shown in each panel.

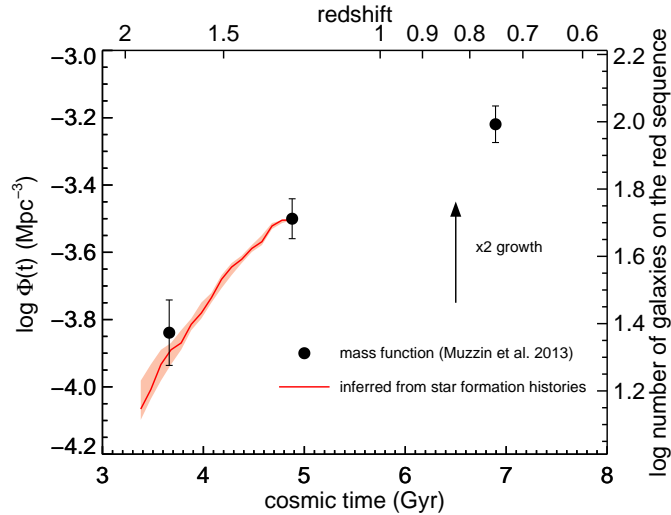


Figure 4.8 The evolving number density of quiescent galaxies with $\log M_*/M_\odot > 10.7$ from the stellar mass function study of Muzzin et al. (2013, black points) with respect to the left ordinate axis. The red line represents the evolution inferred from the star formation history analysis of our LRIS spectroscopic sample of quiescent galaxies whose median redshift is $z = 1.25$ with respect to the right ordinate axis. The shaded area shows the effect of the uncertainties on the star formation histories. The vertical offset between the two samples is arbitrary given the uncertain volume probed by our spectroscopic survey.

of 300 Myr. These panels show clearly how the currently-observed red sequence of LRIS galaxies assembled over the previous 1.5 Gyr. At each time snapshot, we define galaxies with specific star formation rate under 10^{-10} yr^{-1} as quiescent, and we show them with black points in Figure 4.7. The reason we prefer to make this definition in terms of the specific star formation rate as opposed to directly selecting quiescent sources from the UVJ diagram is that in calculating the evolutionary tracks we must assume that dust content and metallicity do not evolve. Since star-forming galaxies are observed to be on average more dust-rich than quiescent galaxies, quenching must to some extent also be associated with a decline in extinction. This means that our predicted past colors will generally be too blue for those galaxies that are quiescent at $\Delta t = 0$, but that are still forming stars at earlier epochs (shown as blue triangles in Figure 4.7). The effect of dust extinction is shown by the arrow in the first panel. Clearly, a reasonable amount of dust can shift the population of transitional objects and bring it closer to the green valley, where galaxies are observed to lie. In the figure we also show the reconstructed evolution for the sample of 6 star-forming galaxies. However, we do not include these objects in the subsequent analysis as this sample is small and biased toward bright objects, unlike our quiescent sample.

We are now in a position to understand the rate at which the population of quiescent population is being enriched by recent arrivals. For each past time step we count the number of quiescent objects defined as above (numbers shown in black in each panel). Out of 51 quiescent galaxies at the

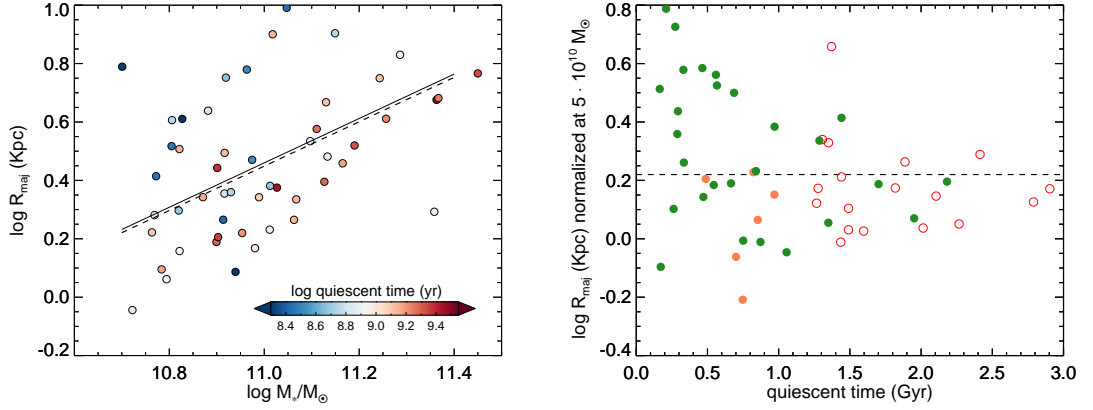


Figure 4.9 Left: Stellar mass-size relation for quiescent galaxies in the LRIS sample. The color indicates the quiescent time t_q , which is the interval since the object became quiescent. The dashed line represents the relation derived from the 3D-HST sample at $z \sim 1.25$ (van der Wel et al., 2014), and the solid line is the relation obtained for our sample assuming the same slope. Right: Size trends with quiescent time for both red sequence and green valley galaxies. The ordinate represents the size normalized to a fixed stellar mass of $5 \cdot 10^{10} M_\odot$ using the mass-size relation shown in the left panel. The dashed line represents the median mass-normalized size: galaxies above this line lie above the mass-size relation. The points are color coded according to their stellar population properties as discussed in Section 4.4.1: old red sequence (red), post-starburst galaxies (orange), and green valley (green).

epoch of observation, only 12 have been quiescent for more than 1.5 Gyr, thus the population grew by roughly a factor of four in a short period. Given we have shown that our sample is representative (Appendix 4.A), we can thus compare the rate at which the quiescent population is growing from our simulated evolution to the results of photometrically-based stellar mass function studies, which are approximately volume-limited.

Muzzin et al. (2013) derive the stellar mass function for quiescent and star-forming galaxies over $0 < z < 4$ using a UVJ color selection. This definition of the quiescent sample is in excellent agreement with the specific star formation rate threshold that we adopt, as we already discussed and as also evident from Figure 4.7. Using the Schechter function fits from Muzzin et al. (2013) we integrate over stellar masses larger than our adopted limit, $10^{10.7} M_\odot$, to yield $\Phi(t)$, the number density of massive quiescent galaxies per unit comoving Mpc^3 , as a function of cosmic time (Figure 4.8). This must be compared to the number evolution inferred from the star formation histories of our spectroscopic sample, shown in red, up to the median epoch of observation at $z = 1.25$. As we cannot rigorously calculate the cosmic volume probed by our spectroscopic observations, there is an unknown vertical offset in Figure 4.8. Thus we should compare only the *rate of increase* in the quiescent population, which is in remarkable agreement with the mass function results. To estimate the uncertainty, we recalculate the number evolution many times, using slightly different star formation histories extracted from the posterior distribution of each galaxy, and plot the 68%

confidence region in light red. From our analysis we obtain a number density growth rate from $z = 1.75$ to $z = 1.25$ of 0.39 ± 0.03 dex, which compares favorably to 0.34 ± 0.11 derived from the stellar mass function study. This growth rate is not particularly sensitive to the selection of the quiescent population: shifting the UVJ selection box of ± 0.1 mag changes the rate derived from the Muzzin et al. data by less than 0.08 dex. We note that our comparison neglects the effect of galaxy mergers, which can increase the stellar mass of quiescent galaxies that are just below the mass threshold, thus causing a growth in the number of massive quiescent galaxies that is not due to quenching. However, at this redshift the merger rate is much smaller than the quenching rate (e.g., Newman et al., 2012), and this effect can be neglected.

The agreement between the number growth of the quiescent population that we reconstruct and the one directly observed as a function of redshift suggests our best-fit star formation histories are a reasonable description of the actual evolution of quiescent galaxies.

4.5 Size Evolution on the Red Sequence

We have used our technique to reconstruct the development of the quiescent population over a period of 1.5 Gyr prior to the median epoch of observation. This corresponds roughly to the redshift range $1.25 < z < 2$, where the size growth rate is particularly rapid. We are thus now in a position to directly estimate how recently-quenched galaxies that arrive on the red sequence during this time interval affect the size growth. In measuring physical sizes R_{maj} (effective radii measured along the major axis, listed in Table 4.1) for the LRIS sample, we use the methods described in detail in Chapter 3.

4.5.1 The Size-Age Relation

Figure 4.9 (left panel) shows the stellar mass-size relation for the quiescent galaxies in our sample. For convenience we compare this to the relation found at $z \sim 1.25$ by van der Wel et al. (2014) using the 3D-HST data (dashed line) as this survey also selected quiescent galaxies via their UVJ colors. Although there is significant scatter, assuming the same slope we find the normalization for our sample differs from that for 3D-HST by only 0.01 dex (as shown by the solid line). The data points are color-coded according to their *quiescent time* t_q , defined as the time interval since the object's specific star formation rate fell below 10^{-10} yr^{-1} , following the discussion in Section 4.2. The value of t_q is uniquely determined by age and τ , as shown in Figure 4.5 (red lines). Figure 4.9 shows that galaxies which have been quiescent the longest, i.e., with the largest t_q , are physically more compact.

In the right panel of Figure 4.9 we plot the deviation of galaxies from the mean mass-size relation as a function of their quiescent time. The deviation is simply the vertical distance of each data

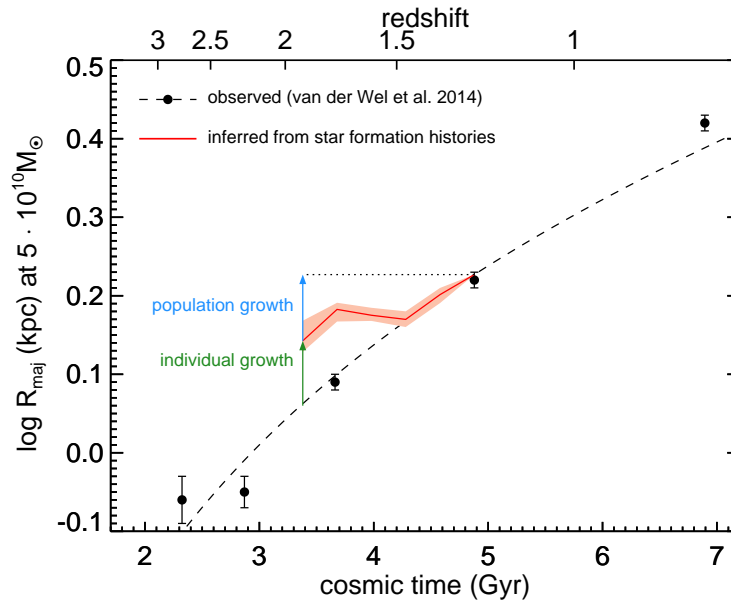


Figure 4.10 Growth measured in terms of the normalization of the stellar mass-size relation for red sequence galaxies (parameterized as the average size at $M_* = 5 \cdot 10^{10} M_\odot$), as a function of cosmic time. Black points represent the observations of van der Wel et al. (2014) and the dashed line is their fit to the data. The red line is the evolution inferred by measuring the sizes of the galaxies in our sample that were quiescent at a given cosmic time. The effect of taking different star formation histories that are still consistent with the observations is shown by the shaded area. Our method is sensitive only to the growth due to the change in the composition of the quiescent population (blue arrow). The difference with the observed overall size evolution, then, must be due to the growth of individual galaxies (green arrow).

point to the dashed line in Figure 4.9, normalized to the mean size at $5 \cdot 10^{10} M_\odot$. In the right panel, points above the dashed line indicate galaxies which lie above the mass-size relation. Here we color code the galaxies according to whether they lie in the green valley, in the red sequence, or in the post-starburst region. This figure shows two important points. First, as we already saw in the left panel, older galaxies tend to be smaller, and vice-versa. Second, we now see that among young galaxies, the ones on the green valley are significantly larger than the post-starburst systems. In fact, the young and old halves of the red sequence have quite similar size distributions.

4.5.2 The Contribution of Progenitor Bias to the Size Growth

The overall goal of this chapter is to use our reconstructed history of the red sequence to separate two modes of size growth in the redshift interval $1.25 < z < 2$. We will use the term *individual size growth* to indicate a genuine increase in size for galaxies that have been on the red sequence throughout this period. *Population size growth*, instead, refers to the apparent growth in size of red sequence galaxies arising from more recent arrivals which were larger prior to their quenching;

this is the contribution from progenitor bias. As we have seen in the previous section, the oldest quiescent galaxies are typically the most compact and so, given we can reconstruct the rate of arrival of newly-quenched systems following our analysis in Section 4.2, we are ready to quantify the two modes of size growth.

In Figure 4.10 we illustrate the size evolution via a red line, that we obtain in the same way as for the red line in Figure 4.8, but measuring at each time step the average size (as opposed to just counting the number) of the quiescent galaxies. Again, the shaded area is obtained by varying the star formation histories according to the posterior distributions. The black points in the figure represent the evolution with redshift in the normalization of the mass-size relation from van der Wel et al. (2014), and the dashed line is a fit to the points. Since we are principally interested in the growth rate, we normalize the red line so it matches the van der Wel et al. (2014) fit at $z = 1.25$. This required shift is negligible as we already showed that our mass-size relation is in close absolute agreement with that of van der Wel et al. (2014).

Figure 4.10 shows the principal result of our study: size evolution due to the arrival of larger, newly-quenched galaxies - i.e., ‘population growth’ - is insufficient to explain the observations. The size evolution of quiescent galaxies directly observed is 0.167 ± 0.014 dex over a 1.5 Gyr period, which is larger than that obtained above by measuring the sizes of the oldest galaxies at $z \sim 1.25$, 0.084 ± 0.020 dex over the same period. The remainder (0.083 ± 0.024 dex) must be due to individual size growth in long-standing quiescent objects. We show the relative contributions of individual and population size growth in Figure 4.10 with, respectively, blue and green arrows. In linear units, each process causes a relative size increase, at fixed mass, of 21% over 1.5 Gyr. A more direct way to view this is to see that even the oldest, smallest objects at $z < 1.5$ are larger than the average quiescent galaxies observed at $z > 1.5$, a point first made by Newman et al. (2012), which estimated the minimum individual growth by measuring the size increase of the smallest quiescent objects, obtaining a value in agreement with ours (0.096 ± 0.018 dex over 1.5 Gyr). The only possible explanation for this difference is that physical growth of individual quiescent galaxies has occurred.

This result is very robust in terms of size measurements, which are accurate to the 10% level for both our sample and the 3D-HST reference sample (Newman et al., 2012; van der Wel et al., 2012). Due to the high quality of our spectroscopic data, this result is also robust against random errors in the age estimates, as shown in Figure 4.10. These do not include systematic effects, due, e.g., to the assumption of simple declining star formation histories, which do not include the effect of secondary bursts. However, the agreement between our reconstructed number evolution of the red sequence with the evolution directly observed by Muzzin et al. (2013, shown in Figure 4.8) strongly suggests that our ages are not significantly biased. Regarding the size evolution we also made the implicit assumption that the *observed* size of a galaxy does not change during the quenching process. The size, however, might decrease because of disk instability (that causes a change in the mass distribution)

or because of the removal of dust (which would cause a change in the light distribution). In both cases the effect of newly quenched galaxies on the mean mass-size relation would be smaller than what assumed in our analysis, and therefore our measurement of the progenitor bias would be an upper limit.

4.6 Summary and Discussion

Taking advantage of deep LRIS spectra, together with associated imaging and broad-band photometry, we have investigated the stellar population parameters of an unbiased sample of quiescent galaxies within the redshift range $1 < z < 1.6$. By reconstructing their star formation histories, we were able to reproduce the evolution in number density of quiescent galaxies measured independently in deep photometric surveys. We measured the relation between size and mass, and found that older galaxies are significantly smaller. We then reconstructed the evolution of the mean size in the 1.5 Gyr prior to the time of observation. Comparing this to the mean sizes measured at different redshifts from the HST CANDELS survey, we found that the oldest galaxies in our sample must have been growing in size since $z \sim 2$.

Our result is in agreement with the conclusions of dynamical studies undertaken at higher redshift. In Chapter 5 we measure velocity dispersions for a small sample of quiescent galaxies at $2 < z < 2.5$, and by comparing their sizes and masses to those of local galaxies with same velocity dispersion, we conclude that physical growth occurred. It is noteworthy that the physical growth of quiescent galaxies over the period corresponding to $1 < z < 2$, first suggested by number density arguments (e.g., Bezanson et al., 2009; Newman et al., 2012), has now been confirmed by two independent techniques and datasets.

As the apparent growth over $1.25 < z < 2$ can now be dissected into a near-equal combination of genuine (physical) growth and that arising from recently-quenched arrivals (progenitor bias), the question arises as to the mechanism by which the older quiescent galaxies are growing. In Chapter 3 we showed that minor mergers are likely to be the primary mechanism for the size growth over $0 < z < 1.5$ (see also van Dokkum et al., 2010; Nipoti et al., 2012; Posti et al., 2014). However, at $z \sim 2$ spectroscopic observations suggest that the growth in mass and size is steeper (see Chapter 5). Moreover, the merger rate inferred from *HST* imaging (Newman et al., 2012) appears to be insufficient to account for the physical growth even after accounting for progenitor bias. Hopefully improved estimates of the minor merger rate together with larger spectroscopic samples beyond $z \sim 2$ will enable us to address this important remaining question in the evolution of compact quiescent galaxies.

Our result was made possible by the high quality of the spectroscopic data, which allowed us to derive accurate stellar population parameters. An earlier attempt to measure the relation between

size and age at $1 < z < 2$ used the UVJ colors as proxy for age. By splitting the red sequence into blue and red halves, Whitaker et al. (2012a) did not detect any difference in size. As we showed in Section 4.4, the post-starburst objects that populate the blue side of the red sequence do, in fact, show similar sizes to the oldest galaxies. The main contribution to the size growth of the population comes instead from galaxies in the green valley.

4.6.1 Two Pathways to Quenching?

One of the unexpected findings of this study was the distinction between green valley galaxies and post-starburst systems, both of which lie within the quiescent population defined in Section 4.3.1. Given the different levels of star formation rate for these two populations, one might conclude that green valley and post-starburst phase represent successive stages in the overall evolution from the blue cloud to the red sequence. This is clearly not the case. All the post-starburst galaxies have ages around 1 Gyr, and very small values of τ , therefore their quiescent times are also around or slightly below 1 Gyr (see Figure 4.5). However, green valley galaxies have ages between 1 and 4 Gyr, and quiescent times that span the entire range between 0 and 4 Gyr. Our data are inconsistent with a simple picture in which quenched galaxies first cross the green valley before moving through a post-starburst phase and arriving on the red sequence. The more likely explanation is one in which the green valley and the post-starburst phase represent two independent evolutionary paths. The main difference is the quenching timescale: the low values of τ for post-starburst galaxies correspond to a fast quenching, whereas for the green valley galaxies, τ is comparable to the age, resulting in slowly declining star formation rates. This difference in timescales results in different levels of star formation rates for galaxies of identical ages.

Interestingly, this picture is consistent with the studies of Patel et al. (2013) and Marchesini et al. (2014) which follow the evolution of a galaxy population by matching number densities at different redshifts. These authors find that at high redshift the progenitors of local massive quiescent galaxies are located both on the blue end of the red sequence and on the green valley. More importantly, the progenitors on the red sequence move toward the red end with cosmic time, while at the same time the green valley remains significantly populated. This implies that the post-starburst phase is not just the endpoint of the evolution of green valley galaxies, but constitutes an independent path, which in the case of ultra-massive galaxies ends by $z \sim 1.5$ (see, e.g., Figure 2 of Marchesini et al. 2014).

The star formation histories are not the only properties that are distinct across the two quiescent sub-populations. Green valley systems are typically large and dusty, while post-starburst galaxies have little dust and smaller sizes. Although the best-fit dust extinction can be degenerate with stellar population ages, the sizes are clearly independently measured. Furthermore, using independent mid-IR emission as a proxy for dust extinction does not significantly change our results, thus confirming

the robustness of our conclusions (see Figure 4.4).

The possibility of two quenching channels with different timescales has also been proposed at low redshift by Schawinski et al. (2014, see also Yesuf et al., 2014), who suggest that major mergers produce a fast quenching and a morphological transformation, while the slow quenching might be caused by some process, such as AGN feedback, that interrupts gas accretion. On the theoretical side, a number of simulations are consistent with quenching being caused by two essentially unrelated physical processes (e.g., Woo et al., 2014; Wellons et al., 2015).

Potential progenitors of compact quiescent galaxies have been identified by Barro et al. (2013), which selected a sample of compact star-forming galaxies at $z > 2$. Among these galaxies, the ones near the blue end of the *UVJ* red sequence tend to be small and dust-free (Barro et al., 2014a). These objects are likely to be the immediate progenitors of the post-starburst systems that we identified at $z < 1.5$. Dusty star-forming objects, such as sub-mm galaxies, might on the other hand be the progenitors of the galaxies on the green valley (Toft et al., 2014; Nelson et al., 2014). However, further studies of transitional galaxies, including more detailed analysis of their star formation histories and morphologies, are needed in order to understand the physical processes responsible for galaxy quenching.

We acknowledge Danilo Marchesini for useful discussions. The authors recognize and acknowledge the very significant cultural role and reverence that the summit of Mauna Kea has always had within the indigenous Hawaiian community. We are most fortunate to have the opportunity to conduct observations from this mountain.

Appendix

4.A The Spectroscopic Sample is Unbiased

Spectroscopic samples are typically biased, because of the combined effects of target selection and the need to identify spectral features. It is therefore critical to assess whether our sample is biased. For this purpose, it is necessary to use a larger catalog that can be considered complete down to masses below $\sim 10^{10.7} M_{\odot}$. For this task we use the public catalog from the 3D-HST survey (Brammer et al., 2012; Skelton et al., 2014), that presents two important advantages. Firstly, it was obtained in the same CANDELS fields in which the majority of our targets lie, allowing a more direct comparison; secondly, the 3D-HST team adopts the UVJ plane for dividing galaxies into quiescent and star-forming, and this ensures consistency in the definition of the samples.

The 3D-HST catalog contains, among other properties, photometric redshift, stellar mass, and rest-frame colors for every object. We selected all the objects with $1 < z < 1.6$ and $M_* > 10^{10.7} M_{\odot}$, and call this the reference sample. We also identify 58 of our 62 objects in the 3D-HST catalog by matching the coordinates. Rather than comparing the properties that we derived for our objects with those published for the reference sample, we carry out a self-consistent comparison by using only the properties from the 3D-HST catalog.

The left panel of Figure 4.11 shows the distribution of our sample (red points) and the reference sample (gray points) in the UVJ diagram. Only the objects in the quiescent selection box are shown. The two histograms compare the rest-frame $U - V$ and $V - J$ colors for our sample and for the reference population. The two samples are remarkably similar, and a K-S test confirms that the two distributions are formally consistent with each other, in both $V - J$ ($p = 0.43$) and $U - V$ ($p = 0.63$).

We note that when we use the rest-frame colors derived from our best-fit models we obtain slightly different results. Comparing the colors calculated by us to the ones calculated by the 3D-HST team *for the same objects* in our sample, we find a mean shift $\Delta(V - J) = 0.12$ and $\Delta(U - V) = 0.03$. This discrepancy is probably caused by a difference in the templates used: we calculate the colors by integrating our best-fit template, while the 3D-HST colors are obtained from the EAZY templates (Brammer et al., 2008), which include emission lines. As a consequence, the sample shown in Figure

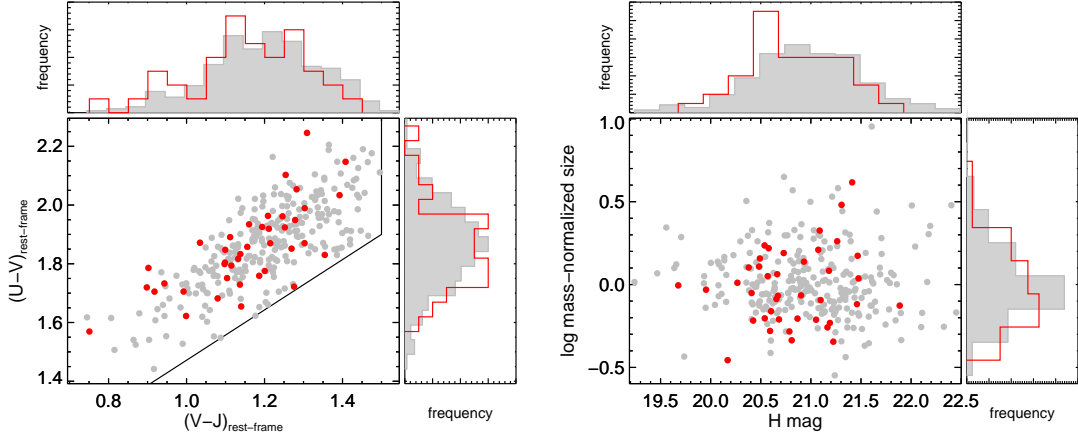


Figure 4.11 Left: Comparison of the distribution on the UVJ diagram for our sample (red) and for the the 3D-HST reference sample, defined by $\log M_*/M_\odot > 10.7$ and $1 < z < 1.6$ (gray). Only galaxies in the quiescent selection box are shown. The top and right panels show the histograms of the rest-frame colors for the two samples. Right: Comparison of the magnitude and mass-normalized distributions. In both panels, the properties of our sample are taken from the 3D-HST catalog, to ensure a consistent comparison.

4.11 is slightly different from the sample used in the rest of the present chapter, as the slightly different rest-frame colors can cause some objects to fall inside or outside the selection box. We note that the star-forming galaxies are the ones most affected by this issue, while the objects on the red sequence show the smallest discrepancy.

In the right panel of Figure 4.11 we compare the distribution of our sample in H magnitude and mass-normalized size with the reference sample. Again, we can see that our spectroscopic sample is unbiased compared to the parent population, as is confirmed by the K-S test ($p = 0.29$ for the H distributions and $p = 0.19$ for the size distributions).

We conclude, therefore, that our sample of quiescent galaxies is unbiased, and represents well the underlying galaxy population.

Table 4.1. Stellar Population Properties of the Sample of Quiescent Galaxies

Object ID	z	$\log \text{sSFR}$ (yr^{-1})	$\log M_*$ (M_\odot)	$\log \text{Age}$ (yr)	$\log \tau$ (yr)	A_V	$Z/0.02$	R_{maj} (kpc)
19826	1.008	-10.55 ± 0.06	11.07 ± 0.04	9.63 ± 0.06	9.01 ± 0.06	0.13 ± 0.04	0.44 ± 0.04	2.2
51106	1.013	-11.18 ± 0.09	11.29 ± 0.03	9.37 ± 0.05	8.55 ± 0.06	0.75 ± 0.08	0.89 ± 0.17	6.8
28739	1.029	< -12	11.03 ± 0.03	9.54 ± 0.04	8.15 ± 0.55	0.11 ± 0.05	0.66 ± 0.10	2.4
21741	1.055	< -12	10.92 ± 0.03	9.24 ± 0.05	7.85 ± 0.42	0.41 ± 0.07	0.74 ± 0.17	3.1
49418	1.061	< -12	11.37 ± 0.04	9.48 ± 0.07	8.47 ± 0.46	0.17 ± 0.09	0.79 ± 0.17	4.8
51081	1.062	-10.37 ± 0.10	10.96 ± 0.04	9.26 ± 0.06	8.60 ± 0.07	0.71 ± 0.09	0.91 ± 0.18	6.0
31377	1.085	-10.43 ± 0.13	10.70 ± 0.02	9.06 ± 0.02	8.34 ± 0.04	1.42 ± 0.09	0.61 ± 0.15	6.2
13393	1.097	-10.52 ± 0.05	11.15 ± 0.03	9.34 ± 0.05	8.66 ± 0.05	0.56 ± 0.06	0.67 ± 0.17	8.0
16343	1.098	-11.84 ± 0.19	11.01 ± 0.01	9.02 ± 0.01	8.06 ± 0.09	0.32 ± 0.03	1.02 ± 0.03	2.4
28656	1.101	< -12	11.19 ± 0.03	9.55 ± 0.04	8.59 ± 0.40	0.06 ± 0.04	0.79 ± 0.09	3.3
32591	1.110	< -12	11.36 ± 0.02	9.51 ± 0.03	7.71 ± 0.49	0.04 ± 0.05	1.01 ± 0.05	4.7
21715	1.113	-10.85 ± 0.07	10.92 ± 0.03	9.30 ± 0.03	8.53 ± 0.04	0.44 ± 0.05	1.06 ± 0.12	2.3
21657	1.125	-11.38 ± 0.09	11.13 ± 0.04	9.60 ± 0.05	8.78 ± 0.06	0.23 ± 0.07	1.14 ± 0.17	2.5
12988	1.144	-10.33 ± 0.05	10.97 ± 0.02	9.29 ± 0.03	8.65 ± 0.04	0.46 ± 0.05	0.84 ± 0.16	3.0
1672	1.147	-10.44 ± 0.07	11.05 ± 0.03	9.14 ± 0.04	8.43 ± 0.05	0.95 ± 0.06	1.18 ± 0.17	9.8
21870	1.179	< -12	11.11 ± 0.02	9.35 ± 0.03	7.83 ± 0.43	0.26 ± 0.05	0.53 ± 0.08	3.8
1241357	1.188	< -12	10.90 ± 0.02	9.50 ± 0.03	8.29 ± 0.46	0.03 ± 0.03	0.89 ± 0.11	1.6
41327	1.192	< -12	10.82 ± 0.03	8.98 ± 0.04	7.96 ± 0.32	0.46 ± 0.10	0.84 ± 0.28	2.0
33887	1.193	-10.66 ± 0.10	10.88 ± 0.04	9.36 ± 0.06	8.65 ± 0.07	0.31 ± 0.09	1.05 ± 0.23	4.4
45759	1.196	-10.37 ± 0.12	10.92 ± 0.05	9.35 ± 0.08	8.70 ± 0.09	0.53 ± 0.12	0.96 ± 0.20	5.6
3346	1.217	-10.75 ± 0.08	10.80 ± 0.02	9.04 ± 0.04	8.25 ± 0.04	0.51 ± 0.09	1.05 ± 0.24	3.3
3867	1.223	-11.59 ± 0.11	10.82 ± 0.02	9.47 ± 0.04	8.59 ± 0.09	0.07 ± 0.04	0.62 ± 0.12	3.2
34609	1.241	< -12	11.02 ± 0.02	9.20 ± 0.04	7.53 ± 0.37	0.80 ± 0.06	0.81 ± 0.15	7.9

Table 4.1 (cont'd)

Object ID	z	$\log \text{sSFR}$ (yr^{-1})	$\log M_*$ (M_\odot)	$\log \text{Age}$ (yr)	$\log \tau$ (yr)	A_V	$Z/0.02$	R_{maj} (kpc)
21750	1.242	-11.51 ± 0.10	11.10 ± 0.03	9.27 ± 0.05	8.38 ± 0.05	0.31 ± 0.06	0.96 ± 0.22	3.4
7662	1.244	< -12	10.95 ± 0.00	9.30 ± 0.00	7.85 ± 0.00	0.21 ± 0.00	0.98 ± 0.00	1.7
18249	1.252	-11.18 ± 0.12	10.81 ± 0.04	9.17 ± 0.05	8.32 ± 0.06	0.49 ± 0.06	1.24 ± 0.19	4.0
7310	1.255	< -12	11.13 ± 0.02	9.21 ± 0.03	7.76 ± 0.40	0.60 ± 0.05	0.54 ± 0.13	4.7
13073	1.258	-11.50 ± 0.09	11.01 ± 0.02	9.23 ± 0.03	8.34 ± 0.03	0.18 ± 0.04	0.90 ± 0.15	1.7
30822	1.259	< -12	10.99 ± 0.04	9.27 ± 0.08	8.07 ± 0.45	0.48 ± 0.10	0.97 ± 0.43	2.2
1244914	1.261	-11.22 ± 0.05	11.24 ± 0.02	9.47 ± 0.03	8.66 ± 0.04	0.19 ± 0.05	0.94 ± 0.19	5.6
32915	1.261	-11.01 ± 0.05	10.98 ± 0.02	9.43 ± 0.03	8.65 ± 0.04	0.17 ± 0.05	0.54 ± 0.11	1.5
22760	1.262	< -12	10.90 ± 0.01	9.36 ± 0.02	7.66 ± 0.37	0.33 ± 0.06	0.54 ± 0.09	1.5
22780	1.264	-10.77 ± 0.10	10.77 ± 0.01	9.03 ± 0.02	8.23 ± 0.03	0.62 ± 0.06	0.84 ± 0.14	2.6
2341	1.266	< -12	10.82 ± 0.02	9.01 ± 0.01	7.39 ± 0.26	0.47 ± 0.06	1.08 ± 0.12	1.4
29059	1.278	-10.62 ± 0.09	10.91 ± 0.02	9.06 ± 0.04	8.29 ± 0.05	0.44 ± 0.08	1.10 ± 0.22	1.8
2823	1.316	-11.12 ± 0.12	11.26 ± 0.04	9.58 ± 0.05	8.81 ± 0.07	0.42 ± 0.09	0.86 ± 0.17	4.1
34879	1.322	-11.64 ± 0.10	11.45 ± 0.03	9.61 ± 0.04	8.75 ± 0.04	0.35 ± 0.06	0.61 ± 0.10	5.8
2337	1.327	< -12	11.06 ± 0.06	9.23 ± 0.07	7.67 ± 0.41	0.34 ± 0.06	0.75 ± 0.25	1.8
14758	1.331	< -12	10.72 ± 0.02	8.95 ± 0.02	7.50 ± 0.27	0.53 ± 0.05	0.73 ± 0.14	0.9
33786	1.352	-10.21 ± 0.11	10.83 ± 0.03	9.16 ± 0.06	8.50 ± 0.07	0.70 ± 0.10	0.94 ± 0.21	4.1
25374	1.397	< -12	10.90 ± 0.09	9.44 ± 0.10	7.78 ± 0.47	0.20 ± 0.16	0.83 ± 0.23	2.8
19498	1.401	< -12	10.78 ± 0.04	9.25 ± 0.07	7.68 ± 0.42	0.19 ± 0.07	0.79 ± 0.25	1.2
5835	1.405	-10.35 ± 0.07	10.93 ± 0.02	9.42 ± 0.05	8.80 ± 0.05	0.35 ± 0.07	0.58 ± 0.15	2.3
42109	1.406	-11.29 ± 0.08	10.79 ± 0.03	9.32 ± 0.05	8.47 ± 0.05	0.08 ± 0.06	0.62 ± 0.14	1.2
5020	1.415	< -12	10.87 ± 0.03	9.28 ± 0.08	7.94 ± 0.45	0.15 ± 0.06	0.51 ± 0.08	2.2
4906	1.419	< -12	11.13 ± 0.07	9.05 ± 0.08	7.39 ± 0.27	0.57 ± 0.08	1.04 ± 0.11	3.0

Table 4.1 (cont'd)

Object ID	z	$\log \text{sSFR}$ (yr^{-1})	$\log M_*$ (M_\odot)	$\log \text{Age}$ (yr)	$\log \tau$ (yr)	A_V	$Z/0.02$	R_{maj} (kpc)
20275	1.442	< -12	10.77 ± 0.03	9.02 ± 0.08	7.54 ± 0.30	0.50 ± 0.13	1.12 ± 0.20	1.9
40620	1.478	< -12	11.17 ± 0.03	9.24 ± 0.06	7.60 ± 0.34	0.18 ± 0.07	0.67 ± 0.16	2.9
17468	1.529	< -12	10.76 ± 0.09	9.21 ± 0.17	7.81 ± 0.42	0.39 ± 0.14	0.87 ± 0.25	1.7
34265	1.582	< -12	11.36 ± 0.01	8.96 ± 0.02	7.41 ± 0.24	0.52 ± 0.04	0.95 ± 0.09	2.0
2653	1.598	-10.60 ± 0.31	10.94 ± 0.02	8.91 ± 0.04	8.12 ± 0.09	0.68 ± 0.11	0.83 ± 0.15	1.2

Chapter 5

New MOSFIRE Spectroscopy of Quiescent Galaxies at $1.5 < z < 2.5$. Evolution of Stellar Populations and Dynamical Properties

Abstract

We present a sample of 24 deep near-infrared spectra of quiescent galaxies at $1.5 < z < 2.5$ obtained with Keck MOSFIRE. These high-quality spectra show numerous absorption features such as Balmer and CaII lines and the 4000 Å break. Our analysis is composed of two parts. First, we derive velocity dispersions and dynamical masses and explore the structural evolution of quiescent galaxies. By matching galaxies at fixed velocity dispersion across different cosmic times, we demonstrate that there is significant physical size growth of individual objects over $0 < z < 2.5$. The slope of growth $d \log R_e / d \log M_*$ steepens at higher redshift, but remains consistent with the theoretical expectations for minor mergers. We also investigate the stellar-to-dynamical mass ratio, and find a marginal evolution with redshift. In the second part we analyze the stellar population properties by fitting templates simultaneously to the spectroscopic and photometric data. We find a diversity of ages within the quiescent population, with both young and old systems at each redshift. We detect for the first time at this redshift, and in agreement with local studies, a downsizing in the formation epoch, where more massive galaxies are systematically older. Finally, we explore in detail the star formation history of a very massive galaxy at $z = 2.09$ for which we have a spectrum with high signal-to-noise ratio. We find that the galaxy is well described by a simple burst that is 1 Gyr old, implying the progenitor formed most of its stellar mass through intense activity at $z \sim 3$. We estimate that less than 20% of its mass was formed in the last Gyr, which constitutes a strong constraint on the quenching mechanism.

Part of this chapter has been published as Belli, S., Newman, A. B., Ellis, R. S., & Konidaris, N. P. 2014b, ApJ, 788, L29

5.1 Introduction

Simulations of galaxy formation and evolution in the context of the Λ CDM cosmological model show that structure formation follows a hierarchical assembly (e.g., Springel et al., 2005). However, in the last decade this picture has been challenged by the discovery of a population of high-redshift massive galaxies (Franx et al., 2003; Daddi et al., 2004b). Furthermore, part of this population consists of quiescent objects (Cimatti et al., 2004; Daddi et al., 2005), which have formed at even earlier times and subsequently quenched. These massive quiescent galaxies are also physically compact (Trujillo et al., 2006b; Cimatti et al., 2008; van Dokkum et al., 2008; Szomoru et al., 2012), and current models of structure formation find it difficult to reproduce their properties or their evolution. There are in fact many open questions regarding this population, and significant observational efforts are being directed toward improving our understanding of their evolution. We can broadly divide the life of a typical massive compact galaxy into three phases: initial star-formation, quenching, and passive evolution. Therefore the questions that need to be addressed are:

1. How did these massive and compact objects form in the first place? What are their star-forming progenitors?
2. How and when did they stop forming new stars? What drives this quenching process?
3. What governs their subsequent size evolution? And what is their current level of star-formation activity?

One of the most direct ways to explore the physical properties of galaxies is by observing their spectra. The strong absorption features found in the rest-frame optical spectra of quiescent galaxies allow us to measure their stellar velocity dispersion, which represents a fundamental parameter for spheroidal systems (e.g., Franx et al., 2008; Wake et al., 2012). As velocity dispersions should remain stable through merger episodes, spectroscopic observations can link high-redshift progenitors with their local descendants (see Chapter 3). The physical size growth of individual systems needs to be confirmed using velocity dispersions to connect galaxies at different redshifts, particularly at $z > 1.5$ where the evolution is claimed to be surprising rapid (e.g., Newman et al., 2012).

Rest-frame optical spectroscopy also represents a reliable way to study the stellar populations of quiescent galaxies (Conroy, 2013, and references therein). A substantial improvement of the stellar population templates (e.g., Bruzual & Charlot, 2003; Maraston, 2005) together with the adoption of the full spectrum fitting technique (e.g., Cid Fernandes et al., 2005; Conroy et al., 2014) have led to significant progress in our understanding of quiescent galaxies in the local universe. This *archaeological* approach has allowed detailed studies of the composition and star formation history of the local population. One of the most important results is their anti-hierarchical assembly: the most massive objects formed earlier and on shorter timescales (Thomas et al., 2005). Given the very

high signal-to-noise ratio achievable for nearby objects, the stellar chemical composition can also be measured to unprecedented levels of details: the state-of-the-art analysis of local quiescent galaxies includes measured abundances for 16 chemical elements (Conroy et al., 2014).

However, if we want to understand the early evolution of quiescent galaxies, the archaeological approach presents significant limitations. First, the analysis of spectra observed in local galaxies is plagued by the so-called outshining effect, i.e., the large difference in luminosity between young and old stars. Most of the light observed in old massive galaxies can in principle be due to a small amount of recently-formed stars, whose contribution to the total mass is negligible. As a result, spectral analysis can only yield a lower limit on the age of the stellar population. Then, even in the ideal case where no contamination from younger stars took place, measuring the ages of old galaxies is challenging because of the lack of evolution in the spectra of old populations, particularly for the strongest features such as Balmer absorption lines. This is due to the fact that the oldest stars are also the ones with the slowest evolution, and is at the origin of the remarkable homogeneity of the local red sequence (Bower et al., 1992). As a result, ages become increasingly uncertain for older systems. Distinguishing between a formation redshift of, e.g., $z = 2$ and $z = 3$, corresponding to lookback times of ~ 10 and ~ 11 Gyr respectively, is clearly a very difficult task if based entirely on spectra from local galaxies. Finally, a third problem is the degeneracy between the mass *formation* history and the mass *assembly* history. Even when a reliable star formation history is found, it is not possible to know whether the various episodes were due to *in-situ* star formation or to the contribution of stars formed in other systems that then merged with the galaxy under study. Being able to directly probe these different scenarios is fundamental for our understanding of galaxy formation.

The limitations of galactic archaeology can be overcome by observations of galaxies at high redshift. Since the galaxies' oldest populations are limited by the age of the universe, the outshining effect and the lack of evolution in the spectral features become less important at higher redshift. At $z \sim 1$ there cannot be populations older than 6 Gyr; at $z \sim 2$ the upper limit is 3 Gyr. In some sense, measuring ages and star formation histories becomes increasingly easier at higher redshift. Furthermore, tracing the stellar populations as a function of redshift allows us to reconstruct, in a statistical way, the star formation history for galaxies of a given stellar mass or velocity dispersion, and break the degeneracy between formation and assembly of stellar mass.

At least up to $z \sim 0.7$ there is now agreement among independent studies of large, high-quality spectroscopic samples (Choi et al., 2014; Gallazzi et al., 2014). Both metallicities and ages of quiescent galaxies are consistent with passive evolution. However, at higher redshift the quality of the data is significantly lower, partly because the spectral region of interest (the rest-frame optical) is redshifted into the observed red and near-infrared bands. Strong, variable sky emission and absorption, together with poor detector sensitivity, have made it almost impossible to obtain

the high signal-to-noise ratio required to measure absorption features for targets at $z > 1$. For this reason, most studies of high-redshift quiescent galaxies are based on broad- or medium-band photometry, which is sufficient for measuring stellar masses, but yields unreliable age estimates because of the age-dust degeneracy.

The recent progress in detector technology is finally allowing us to obtain high-quality spectroscopic data in the near-infrared. The upgrade of the red-sensitive detector on the LRIS spectrograph at Keck allowed us to collect the largest number of spectra with clearly detected absorption lines for objects at $1 < z < 1.5$ (see Chapter 3). In order to make the best use of all the available information, we fit simultaneously the Keck spectra with the publicly available broad-band photometric data, and derived ages assuming an exponentially declining star formation history (see Chapter 4).

The most massive objects, however, were formed at $z > 1.5$, where more challenging near-infrared observations are needed. So far, only a handful of absorption line spectra of individual galaxies have been studied at these redshifts (van Dokkum et al., 2009; Kriek et al., 2009; Toft et al., 2012; van de Sande et al., 2013; Barro et al., 2015). In order to achieve the required signal for significative samples, different strategies have been successfully applied. These include the use of narrow-band photometry as a substitute for spectroscopic data (Pérez-González et al., 2013); the stacking of spectra obtained with large, ground-based telescopes (Onodera et al., 2012, 2014; Mendel et al., 2015); and the use of low-resolution grism observations with the *Hubble* Space Telescope (*HST*) (Whitaker et al., 2013; Bedregal et al., 2013; Krogager et al., 2014; Newman et al., 2014). For a direct measurement of the stellar population properties, however, the analysis of a large number of individual spectra is needed.

Taking advantage of the high sensitivity of the new multi-object near-infrared spectrograph MOSFIRE at Keck (McLean et al., 2012), and following our pilot campaign presented in Belli et al. (2014b), we have collected the largest sample of absorption line spectra at $1.5 < z < 2.5$. In this work we present the analysis of the stellar populations and dynamical properties of these objects, which we use to explore both their size growth and the details of their formation and evolution.

This chapter is organized as follows. In Section 5.2 we present the sample selection and describe the spectroscopic observations and data reduction. In Section 5.3 we derive structural and dynamical properties of the sample and discuss the stellar population analysis. The analysis of the dynamical data, including the evolution of velocity dispersions, dynamical masses, and effective sizes, is discussed in Section 5.4, while the results relative to the stellar populations are discussed in Section 5.5. Finally, we summarize and discuss the main results of the present study in Section 5.6.

Throughout the chapter we use AB magnitudes and assume a Λ CDM cosmology with $\Omega_M=0.3$, $\Omega_\Lambda=0.7$ and $H_0= 70 \text{ km s}^{-1} \text{ Mpc}^{-1}$.

5.2 Data

5.2.1 Target Selection and Ancillary Data

A careful selection of the spectroscopic targets is critically important for deep observations of faint objects. The choice of the targets is determined by two requirements: the presence of deep high-resolution imaging from which the structural parameters can be robustly measured even for $z > 2$ compact galaxies, and the public availability of photometric data that cover as many photometric bands as possible. We therefore selected targets in the fields observed by the Cosmic Assembly Near-IR Deep Extragalactic Survey (CANDELS, Grogin et al., 2011; Koekemoer et al., 2011), for which deep *HST* *F160W* observations are available, and used the photometric catalog assembled by the 3D-HST team (Brammer et al., 2012; Skelton et al., 2014), that includes derived properties such as stellar mass and photometric redshift.

We assigned a weight to each target in the parent catalog according to the likelihood of yielding a detection of one or more rest-frame absorption lines. Since the observations were carried out in the *Y* and *J* bands, we constructed two different catalogs, one per band. For each catalog, the weight of an object was calculated as the combination of different factors:

- *Photometric redshift*: highest priority was given to redshift values that would result in an ideal visibility of the main absorption features within the observed wavelength range. The ideal ranges are $1.5 < z < 1.8$ for the *Y* band and $2 < z < 2.4$ for the *J* band. In order to account for the uncertainty in the photometric redshifts, we gave intermediate priority to those targets with a redshift in the vicinity of the ideal range.
- *Observed near-infrared magnitude*: larger weights were given to brighter objects, for which the observations are more likely to succeed.
- *Position on the UVJ diagram*: our previous spectroscopic survey at lower redshift (see Chapter 3 and Chapter 4) showed that this is a very robust method to identify quiescent galaxies. Objects closer to the center of the red sequence were given the top priority.

These criteria ensure that the top priority objects are massive, quiescent galaxies at $1.5 < z < 2.5$.

Finally, we identified the regions in the sky where the largest number of targets with high priority are located, and manually designed the MOSFIRE slitmasks. Two of our masks (COSMOS2 and COSMOS3) partially overlap with the $z \sim 2.1$ protocluster discovered by Spitler et al. (2012).

5.2.2 MOSFIRE Spectroscopy

We obtained spectroscopic observations using Keck MOSFIRE during two observing runs in November 2014 and April 2015. We observed a total of four slitmasks in different CANDELS fields, and

Table 5.1. MOSFIRE Observations

Slitmask	Band	Seeing ^a (arcsec)	Exp. Time (min)
COSMOS2 ^b	<i>J</i>	0.5–0.9	484
COSMOS3	<i>J</i>	0.5–0.8	534
UDS1	<i>Y</i>	0.6–0.7	330
UDS1	<i>H</i>	0.6–0.9	90
EGS2	<i>Y</i>	0.5–0.8	240
EGS2	<i>H</i>	0.5	152
COSMOS6	<i>Y</i>	0.6–0.7	312
COSMOS6	<i>H</i>	0.6	84

^aThe seeing is calculated from the trace of a star in the slitmask

^bFrom Belli et al. (2014b)

we used only data obtained in good conditions (clear sky or thin clouds, $0''.5 - 0''.9$ seeing). Table 5.1 lists the details of the observations for each slitmask. The exposure times varied between four and nine hours per mask. We adopted a two-point dithering pattern, with exposure times for individual frames between 120 and 180 s, and used a $0''.7$ slit width which yields a spectral resolution $R \sim 3500$. We observed one mask in *J* and three masks in *Y*. For these, we also obtained shallower *H* band observations with the goal of measuring H α emission lines for targets at $z < 1.7$.

The data were reduced using the Data Reduction Pipeline¹ (DRP). The pipeline performs flat fielding, sky subtraction, cosmic ray removal, and wavelength calibration, and outputs the rectified 2D spectra. From these we optimally extracted the 1D spectra (Horne, 1986), adopting the light profile (i.e., the 2D flux integrated along the wavelength direction) as the weight for each target.

Although the near-infrared sky presents strong emission lines, the AB dithering pattern allows the DRP to perform an accurate sky subtraction. However, the atmosphere also introduces strong absorption features. To account for these telluric features, we observed A0V standard stars, and derived the correction by comparing them to a high-resolution model spectrum of Vega. We use the method of Vacca et al. (2003) and Cushing et al. (2004) to broaden and shift the Vega model in order to match the intrinsic spectrum of the standard stars. Using this technique, we obtain a telluric correction for each standard star observation, typically two per night in each band. By comparing these data obtained during multiple observing runs, we conclude that the telluric correction is generally very stable with airmass and time (both within one night and among different nights), but varies at the edges of the near-infrared bands, where the absorption is significantly stronger. This can potentially cause an imperfect correction if the standard star and the science targets were not observed in the same exact conditions. We estimate the spectral error due to this mismatch in the following way. We downloaded the ATRAN models (Lord, 1992) of the telluric spectrum from the

¹<https://github.com/Mosfire-DataReductionPipeline>

Gemini website², and selected the two examples that represent extreme conditions of the atmosphere: airmass 1 and 1 mm of water vapor, and airmass 2 and 3 mm of water vapor. We take half of their difference as an approximate measure of the typical variation in the telluric spectrum between the standard star and the science observations. We checked that this telluric error spectrum is a good description of the variations between telluric corrections obtained at different times, and we found good agreement. When applying the telluric correction to the science targets, we add this relative error in quadrature to the error spectrum generated by the DRP. This procedure significantly affects the error spectra of our targets only in few cases, where the redshift and the spatial position of the object on the mask require us to use the part of the spectrum near the edge of the near-infrared bands.

The telluric correction described so far also accounts for the relative flux calibration, but not for the absolute flux calibration since slit loss, air mass, seeing, and transmission typically vary between the observation of the standard star and the observation of the science targets. We derive a correction factor in the following way: in each mask we position one slit on a relatively bright star; we then extract its spectrum in the same way as for the science targets, and integrate over the entire bandpass to obtain a photometric measurement. The absolute calibration factor is then obtained by requiring this photometric measurement to match the one from the CANDELS-3DHST catalog for the same star.

The total sample consists of rest-frame spectroscopy for 29 galaxies in the range $1.5 < z < 2.5$. For each target we detect at least one among of the Balmer or CaII (H and K) lines. Other detected features include the G band and the [OII] λ 3726, 3729 emission line. Of these 29 targets, we exclude 5 because of low signal-to-noise spectra, as described in Section 5.3.2. The final sample of 24 spectra is shown in Figure 5.1.

In Figure 5.2 we show the sample on the UVJ diagram, i.e., the rest-frame $U - V$ versus $V - J$ color-color plot, which is very effective in distinguishing between star-forming and quiescent galaxies (Williams et al., 2009). The rest-frame colors were taken from the 3D-HST catalog, and were derived from fitting models to the observed photometry. We plot all the galaxies that were targeted by our MOSFIRE observations; the ones for which we successfully identified absorption features in the spectrum are shown in red. Remarkably, virtually all the successful targets are found in the selection box used defined by Muzzin et al. (2013) and used to identify quiescent galaxies. It is also interesting to note that most of the objects in the quiescent box yielded a spectroscopic detection, confirming the effectiveness of our selection methods. This sample represents a significant step forward in the study of high-redshift quiescent galaxies, since only a few absorption-line spectra at $z > 1.5$ have been published to date (van Dokkum et al., 2009; Toft et al., 2012; van de Sande et al., 2013).

²<http://www.gemini.edu>

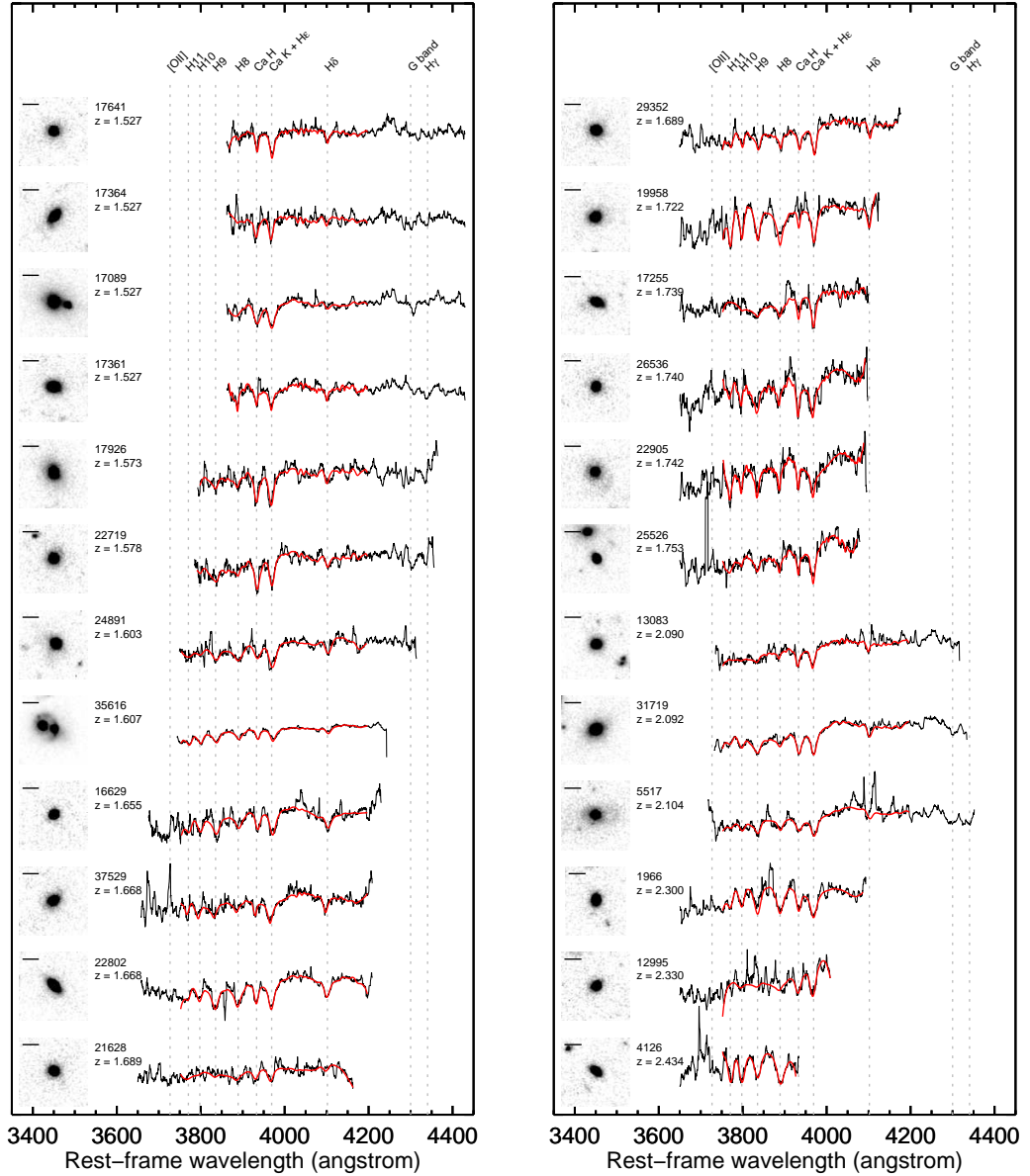


Figure 5.1 *HST* images and MOSFIRE spectra for our sample of quiescent galaxies. For each object, the ID and spectroscopic redshift are indicated; the 4'' cutout shows the F160W image with a 10 kpc ruler; the observed spectrum (in black) and the best-fit model (in red) are plotted. Gray dashed lines mark important spectral features.

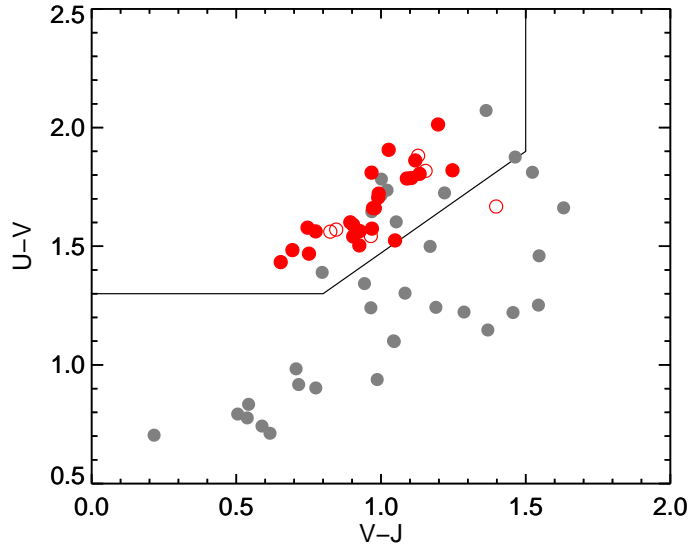


Figure 5.2 UVJ diagram for the targeted sample. Red points represent objects for which absorption lines were successfully observed. The open circles are objects with low signal-to-noise spectra, which we exclude from our final sample (see Section 5.3.2). The selection box is from Muzzin et al. (2013).

5.3 Physical Properties

The main physical properties that we will use in our analysis of the sample are the sizes (derived from public *HST* imaging), the velocity dispersions (calculated from the MOSFIRE spectroscopy), and the stellar population properties such as stellar masses and star formation histories (which we measure by fitting simultaneously the MOSFIRE spectra and the public photometry). In this section we explain how these properties were derived. For the sizes and velocity dispersions we follow closely the methods outlined in Chapter 3, while for the stellar population parameters we expand on the technique presented in Chapter 4.

5.3.1 Structural Properties

The size and other basic structural properties were derived for each galaxy using the public *HST* data in the F160W band, which corresponds to the rest-frame optical emission. We use GALFIT (Peng et al., 2002) to fit a two-dimensional Sérsic profile to the observed surface brightness for each object. Neighboring objects are identified using SExtractor Bertin & Arnouts (1996) and are either masked out or fit simultaneously, according to their distance and brightness. We combined isolated bright stars to derive the point-spread function (PSF).

The fitting procedure outputs a number of parameters for each galaxy, of which the most physically interesting are the Sérsic index n , the axis ratio q , and the half-light semi-major axis a . Instead of using the semi-major axis, we define the circularized effective radius $R_e = a\sqrt{q}$. We assume an

uncertainty of 10% on the size measurement, which has been shown to be a good approximation to the true error (van der Wel et al., 2008; Newman et al., 2012).

5.3.2 Velocity Dispersions

Velocity dispersions were measured by fitting broadened templates to the observed MOSFIRE spectra using the Penalized Pixel-Fitting routine (pPXF) of Cappellari & Emsellem (2004). The instrumental resolution was measured for each object from by fitting a Gaussian profile to the sky emission lines. The measured dispersion was corrected for both the instrumental resolution (40 – 50 km s⁻¹) and the resolution of the template spectra (~ 95 km s⁻¹). Only the wavelength region $3750\text{\AA} < \lambda < 4200\text{\AA}$ was considered for the fit (so to exclude the emission line [OII] λ 3726, 3729), but the exact wavelength range used varies for each object depending on redshift and physical position on the slitmask. Within the range used, the spectral pixels that are significantly contaminated by sky emission were masked out.

We adopted the Bruzual & Charlot (2003) library of synthetic spectra of stellar populations, allowing for a combination of single bursts with different ages. In principle, the choice of templates can have a large impact on the measurement of the velocity dispersion, and for this reason we test our results by performing the same fit with the Indo-US library of observed stellar spectra (Valdes et al., 2004). We also test for the effect of the wavelength range, the masking of the sky emission, and the degree of the additive and multiplicative polynomials used in the spectral fit. Of the 29 galaxies for which absorption lines are detected, we discard five whose fits are not robust due to low signal-to-noise ratio. For a detailed discussion of the fit and the estimate of the uncertainty on the velocity dispersion, which is due to both systematic and random errors, we refer the reader to Chapter 3.

5.3.3 Stellar Populations

We derive stellar population properties from a simultaneous fit to the MOSFIRE spectroscopic data and to the publicly available broad-band photometry collected in the 3D-HST catalog. We use the Bayesian code `pyspecfit` (Newman et al., 2014) which outputs, for each galaxy, the posterior distribution of the stellar population parameters. By fitting both the spectrum and the broadband photometry we make sure to include in the analysis all the available information for each target, which helps significantly in breaking the degeneracy between age and dust extinction. We already successfully applied this method to the $1 < z < 1.6$ LRIS sample in Chapter 4, to which we refer the reader for a detailed discussion of the fitting procedure.

In brief, we adopt the stellar population templates from Bruzual & Charlot (2003), the initial mass function from Chabrier (2003), and the dust extinction law from Calzetti et al. (2000). We

assume that the star formation history is exponentially declining and is described by the age t_0 and the timescale τ , both with log-uniform priors. For each object we set the redshift to its spectroscopic value, and we assume the age of the universe to be the upper limit to the age of the stellar population. Other free parameters are the dust extinction A_V and the stellar metallicity Z , where the solar value is assumed to be $Z_\odot = 0.02$. Finally, we calculate the stellar mass M_* by scaling the best-fit template to the observed photometry.

5.3.4 Emission Lines

In addition to the absorption line spectra, for the galaxies at $z < 1.7$ we also have H -band MOSFIRE data covering the $H\alpha$ line. All the quiescent galaxies in our sample except one (discussed below) do not show any emission, which is particularly important as it represents one of the most direct methods to test that star formation in these objects is, in fact, turned off. An accurate upper limit on the $H\alpha$ flux is therefore very helpful for constraining the recent activity. We emphasize that our dataset presents a unique opportunity: by measuring the spectroscopic redshift from the absorption lines, we can pinpoint the exact location of $H\alpha$, and obtain a reliable upper limit. Without spectroscopic redshifts, the measurements would be significantly limited by the uncertainty in the emission line wavelength because of the uneven noise due to strong near-infrared sky emission.

We derive the $3\text{-}\sigma$ upper limit on the equivalent width by calculating the average flux uncertainty in a window of 300 km s^{-1} centered on the expected wavelength position. Since we carefully calibrated the absolute scale in our MOSFIRE spectra (see Section 5.2.2), we can then convert the equivalent width (or its upper limit) to an absolute flux. However, it is notoriously difficult to achieve a high level of accuracy on the absolute flux calibration of spectroscopic observations, so we obtain the conversion from equivalent width to flux using the best-fit model output by `pyspecfit` (see Section 5.3.3).

In converting from observed equivalent width to intrinsic line fluxes we need to take into account two effects. First, the stellar continuum typically presents $H\alpha$ in absorption, so that the observed emission is actually smaller than the intrinsic one. We correct for this effect by measuring the equivalent width of the $H\alpha$ absorption line from the best-fit spectrum and adding this to the observed value. The equivalent width in absorption is typically 2.5 to 4 Å. The other correction we need to apply to the observed $H\alpha$ emission is the effect of dust extinction. We assume the attenuation A_V (and its uncertainty) obtained with `pyspecfit`, calculate the extinction at the wavelength of $H\alpha$, and use this value to correct the effect of dust on the line flux.

We obtain upper limits on the $H\alpha$ equivalent width in the range 2 to 6 Å, which we convert to values of star formation rate following Kennicutt (1998). The result is an upper limit on the instantaneous star formation rate of a few M_\odot/yr , confirming the quiescent nature of these objects.

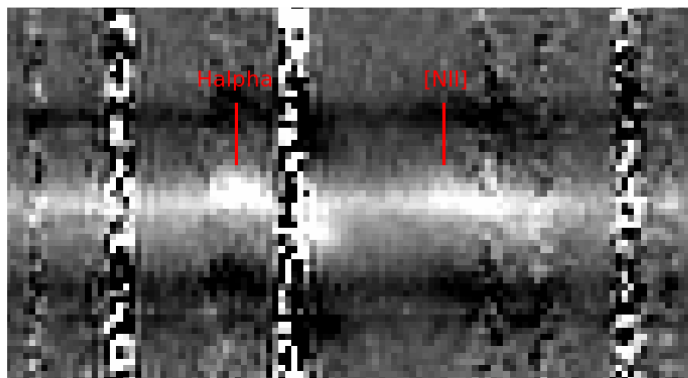


Figure 5.3 The H band MOSFIRE spectrum for 35616. The red lines mark the expected position for $H\alpha$ and $[\text{NII}]\lambda 6584$, assuming the spectroscopic redshift obtained from the absorption lines.

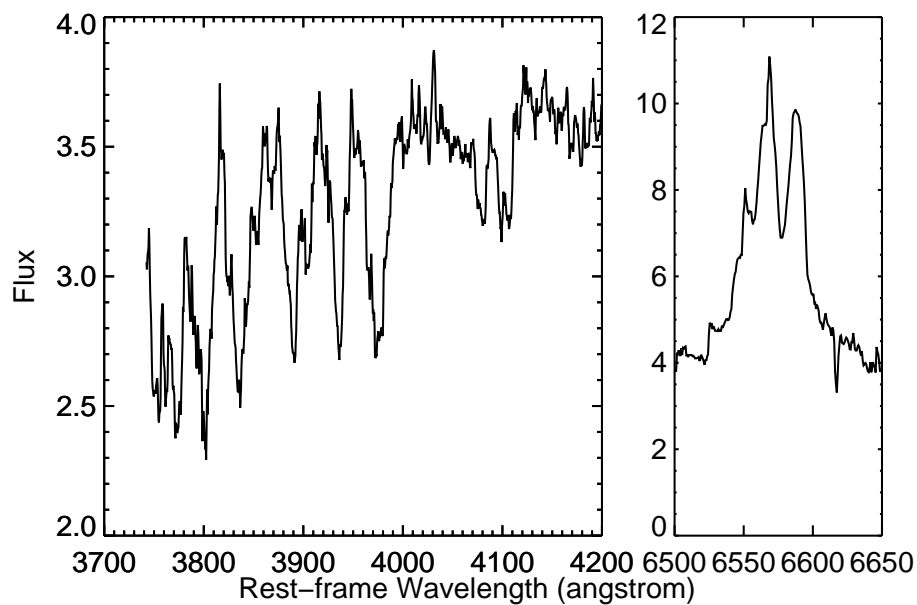


Figure 5.4 Extracted spectra for 35616 from the Y (left) and H (right) band. The Balmer and CaII absorption lines indicate a passive object. The $H\alpha$ emission clearly shows a broad and a narrow component, typical of AGN emission.

5.3.5 AGN activity in 35616

The only quiescent galaxy in our sample with strong line emission is 35616. Figure 5.3 shows the 2D spectrum for this object, obtained with MOSFIRE in the H band. The extracted 1D spectra for both Y and H band are shown in Figure 5.4. A broad $H\alpha$ emission is clearly visible, together with significant emission corresponding to the $[\text{NII}]\lambda 6584$ line. The flux ratio $[\text{NII}]\lambda 6584/H\alpha \sim 0.8$ is high, suggesting a contribution from AGN activity. This is consistent with the existence of a broad component of the $H\alpha$ line, with $\sigma \sim 1000 \text{ km s}^{-1}$ (see Genzel et al., 2014a), and with the fact that the absorption lines in the Y band spectrum indicate an old stellar population, and show no signs of on-going star formation activity. We therefore conclude that the emission is consistent with being entirely due to AGN activity.

Interestingly, the *HST* imaging shows that this galaxy is in a very close pair, with some signs of interaction (see cutout in Figure 5.1). According to the 3D-HST catalog, the companion has a spectroscopic redshift $z = 1.592$, very similar to the redshift we find for 35616 ($z = 1.607$), thus confirming that the objects are in a merger. Since the UVJ colors of the companion puts it at the center of the star-forming region, it is reasonable to assume that this object is gas-rich. This suggests that the emission we detected in 35616 is due to AGN activity triggered by inflowing gas, which was tidally stripped from the companion. This scenario would explain why 35616 is the only system in our sample of quiescent galaxies for which we detect $H\alpha$ emission.

5.4 Dynamical Analysis

In this section we use our new dynamical measurements, together with those from lower-redshift observations, to constrain the evolution of the size and structure of massive quiescent galaxies. After presenting the dynamical and structural properties for our sample, we discuss their implications for the evolution of the stellar-to-dynamical mass ratio and for the size growth of quiescent galaxies.

Figure 5.5(a) shows the mass-size relation for similarly-selected UVJ -quiescent galaxies over $0 < z < 2.5$. We show the local population from the Sloan Digital Sky Survey (SDSS DR7, Abazajian et al., 2009, grayscale map), the sample at $1 < z < 1.6$ from Chapter 3 (small orange points), the MOSFIRE sample observed in the Y band ($1.5 < z < 2$, red circles), and the MOSFIRE sample observed in the J band ($2 < z < 2.5$, red stars). Clearly, the mass-size relation evolves with redshift. At fixed stellar mass, galaxies at $z \sim 1.3$ are about 0.25 dex smaller than the local population. At $z > 1.5$, the logarithmic offset from the local sample is even larger, implying that the evolution accelerates at earlier cosmic times. Moreover, almost all of the $z > 2$ objects are more compact than the other MOSFIRE targets at $1.5 < z < 2$, in agreement with previous photometric studies, particularly the mass-size relation at $z \sim 2.2$ from Newman et al. (2012, red line). The only exception is 5517, which has a very large size and lies almost on the local mass-size relation. This

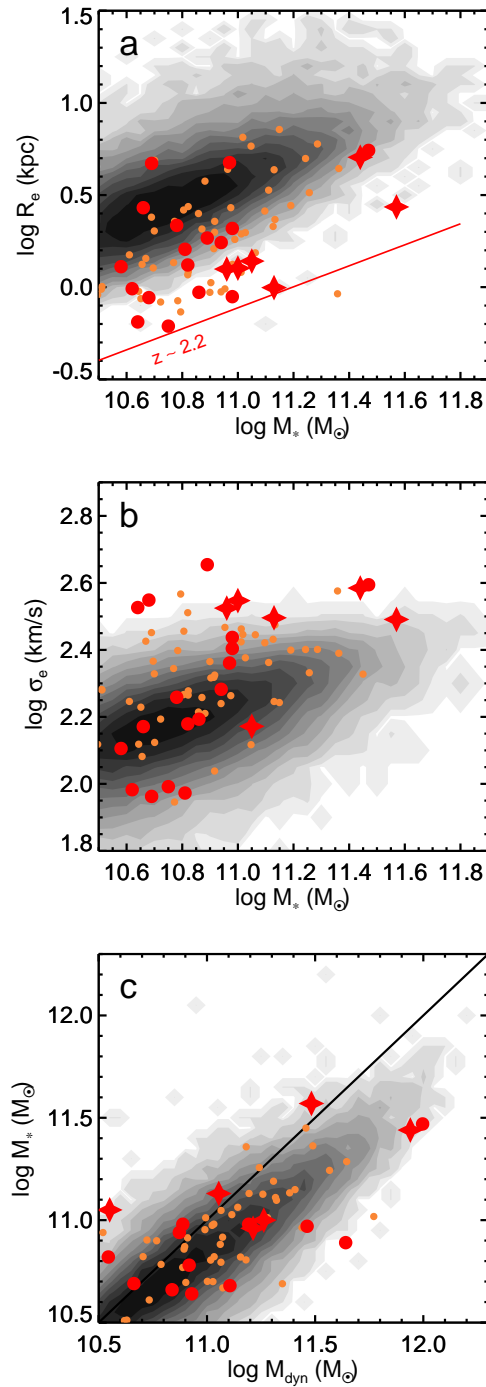


Figure 5.5 Relations between stellar mass and structural and dynamical properties for quiescent galaxies at $0 < z < 2.5$. The local SDSS population is shown in gray, the $1 < z < 1.6$ LRIS sample is in orange, and the MOSFIRE sample is in red (circles at $1.5 < z < 2$, stars at $2 < z < 2.5$). a) Mass-size relation. The red line indicates the $z \sim 2.2$ relation derived by Newman et al. (2012). b) Stellar mass vs. velocity dispersion. c) Dynamical vs. stellar mass. The black line is the one-to-one relation.

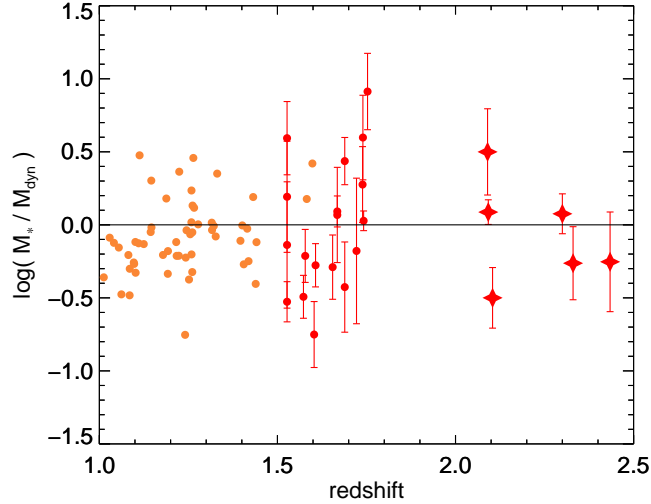


Figure 5.6 Stellar-to-dynamical mass ratio as a function of redshift. Symbols as in Figure 5.5.

object is the brightest galaxy (BCG) of the protocluster discovered by Spitler et al. (2012). This observation suggests that such systems have large sizes already at $z \sim 2$, in agreement with other studies at $z \lesssim 1.8$ (Papovich et al., 2012; Stanford et al., 2012; Newman et al., 2014).

The main advance of this study is that we can now explore the dynamical properties of galaxies at $z > 2$. Figure 5.5(b) shows high-redshift galaxies have significantly larger velocity dispersions than lower redshift objects of similar stellar mass. Also, there is a clear trend with redshift: all the $z > 2$ objects have very high dispersions, $\sigma_e \approx 300 \text{ km s}^{-1}$, with one exception, 4126. This galaxy is the only $z > 2$ object in our sample for which the UVJ colors indicate a post-starburst nature, and presents an elongated morphology and low Sérsic index, $n = 1.4$, typical of disk-like galaxies.

Velocity dispersions enable us to calculate dynamical masses, via $M_{\text{dyn}} = 5\sigma_e^2 R_e / G$. Finally, figure 5.5(c) compares the dynamical and stellar masses. The $z \sim 1.3$ sample closely follows the local distribution, and now for the first time we can show that $z > 1.5$ galaxies are also in agreement with the $z \sim 0$ population, albeit with larger scatter.

5.4.1 The Stellar-to-Dynamical Mass Ratio

In order to test whether the stellar-to-dynamical mass ratio evolves with redshift, we plot M_*/M_{dyn} for our samples in Figure 5.6. Although the scatter increases at $z > 1.5$, we find a broad agreement between the mass ratio distribution obtained from the new MOSFIRE sample and the one from the LRIS spectra. However, if we calculate the weighted average value for the three redshift bins, we obtain $\log M_*/M_{\text{dyn}} = -0.09 \pm 0.03$ at $z < 1.5$, -0.04 ± 0.04 at $1.5 < z < 2$, and 0.02 ± 0.06 at $z > 2$. These results are marginally inconsistent with a constant stellar-to-dynamical mass ratio: at fixed dynamical mass, the stellar mass is slightly larger at higher redshift.

An evolution of the mass ratio was first suggested by Toft et al. (2012) and van de Sande et al. (2013) on the basis of a few objects. If confirmed, such evolution could arise if $z > 2$ quiescent galaxies have a reduced dark matter fraction, a heavier stellar IMF or different structure compared to their lower-redshift counterparts. Although it is difficult to pinpoint the exact physical origin, a change in the stellar-to-dynamical mass ratio would suggest an evolution in the physical properties of quiescent galaxies between $z \sim 2$ and $z \sim 1.3$, as opposed to the remarkable similarity that we found in Chapter 3 between the population at $z \sim 1.3$ and the one at $z \sim 0$.

5.4.2 Galaxy Evolution at Fixed Velocity Dispersion

We now use our dynamical measurements to infer the rate of size growth for high-redshift quiescent galaxies beyond $z \sim 2$ for the first time. Following Chapter 3, we assume that we can link progenitor and descendant galaxies by selecting populations at *fixed velocity dispersion*. This follows the results of numerical simulations that show that velocity dispersion is minimally affected during merger events (e.g., Hopkins et al., 2009b; Oser et al., 2012), and the observed unchanging velocity dispersion function (Bezanson et al., 2012). In particular, we focus on the most massive targets in our sample, and consider the bin in velocity dispersion defined by $\log \sigma_e > 2.40$. In Figure 5.7 we show all the quiescent galaxies with such high values of velocity dispersions in the mass-size plane. The local population forms a clear sequence whereas objects at high redshift show an offset towards smaller sizes and masses. The new MOSFIRE data confirm the existence of physical growth of individual quiescent galaxies up to $z \sim 2$, in agreement with what we found at lower redshift in Chapter 3.

A powerful method to constrain the physical processes responsible for this size growth is to measure the slope $\alpha = d \log R_e / d \log M_*$ of the evolutionary tracks on the mass-size plane and compare it with theoretical predictions. Simple virial arguments (Naab et al., 2009; Bezanson et al., 2009) give $\alpha = 1$ for identical mergers and $\alpha = 2$ for the limiting case of mergers with infinitely diffuse satellites. More realistic numerical simulations, which include the effect of dark matter, gas, and a distribution of orbits, indicate that minor mergers are less efficient than the theoretical limit, and yield values in the range $1.4 < \alpha < 1.8$ (Hopkins et al., 2009b; Nipoti et al., 2012; Oser et al., 2012; Posti et al., 2014). The simulations of Hilz et al. (2013), in which massive dark matter halos enhance the efficiency of minor merging up to $\alpha = 2.4$, are the only exception. However, the large dark matter fraction at the center of these simulated galaxies disagrees with the observed stellar-to-dynamical mass ratios at both low and high redshift.

Assuming evolution at fixed velocity dispersion, we measure α by considering the tracks that high-redshift points must follow in order to match the local distribution. Using this technique, the $z \sim 1.3$ sample yields $\alpha = 1.4 \pm 0.2$ (see Chapter 3). Merging can therefore readily explain the size growth over $0 < z < 1.5$. If we repeat this calculation for the new MOSFIRE sample, we obtain $\alpha = 2.1 \pm 0.8$. This confirms a steepening of the growth at $z > 1.5$, but given the

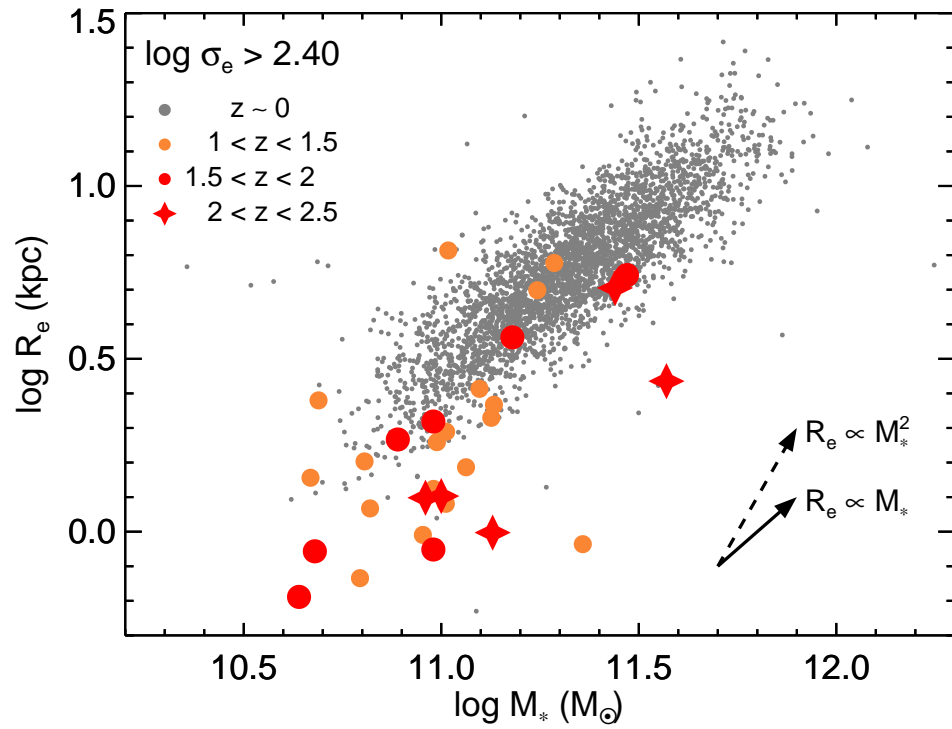


Figure 5.7 Evolution in the mass-size plane for quiescent galaxies with $\log \sigma_e > 2.40$. The high-redshift samples are clearly offset from the local population toward smaller radii at fixed stellar mass. The solid and dashed arrows represent the cases for $\alpha = 1$ and 2, respectively.

increased uncertainty the result is still in agreement with the expectations from minor mergers. We note that the preliminary results from our MOSFIRE campaign, together with the few objects previously observed (van Dokkum et al., 2009; Toft et al., 2012; van de Sande et al., 2013) suggested a much steeper growth at $z > 2$, not compatible with mergers (Belli et al., 2014b). Our new, larger sample shows that this was probably due to low number statistics and uncertainties in the velocity dispersions (in our preliminary analysis we used one of the objects that here we have excluded due to a low signal-to-noise ratio).

5.5 Analysis of the Stellar Populations

While in Section 5.4 we investigated the evolution of quiescent galaxies over $0 < z < 2$, in this section we will explore the earlier star formation history of these systems, by taking advantage of the first representative sample at $z > 1.5$ for which robust stellar population properties derived via spectral fitting are available. We first consider the overall population and its age distribution, and then we have a detailed look at one particular galaxy, and try to constrain its past star formation history.

5.5.1 The Ages of High-Redshift Quiescent Galaxies

In Section 5.3.3 we discussed the derivation of stellar population parameters from a fit to the photometric and spectroscopic data, assuming an exponentially declining star formation history characterized by age t_0 and timescale τ . We plot the galaxy ages t_0 as a function of the age of the universe at the corresponding redshift, for our entire sample, in Figure 5.8. The diagonal line marks the upper edge of the physically allowed region; by construction, each model considered during the fit has an age younger than the age of the universe. Interestingly, quiescent galaxies occupy virtually the entire allowed region on this diagram: at each cosmic time it is possible to find both young and old quiescent galaxies. Naturally, younger galaxies must have a correspondingly shorter timescale τ in order to have negligible on-going star formation rate. Nevertheless, we see that quiescent galaxies as young as 1 Gyr consistently populate all redshifts from $z \sim 1$ to $z \sim 2.5$. This is a direct evidence for the continuing growth of the red sequence population: at each redshift new galaxies are quenched and become quiescent. It is this continuous addition of new systems to the quiescent population that makes it difficult to trace back the evolution of the red sequence: selecting quiescent galaxies at $z \sim 2$ and $z \sim 1$ clearly gives two different populations.

An interesting effect that has been known for some time is the downsizing in star formation: in the local universe, massive galaxies are systematically older than less massive systems (e.g., Thomas et al., 2005). We can directly test for this trend in Figure 5.9, where we color-code the points by stellar mass. Since our sample is biased towards brightest targets for which the spectroscopic

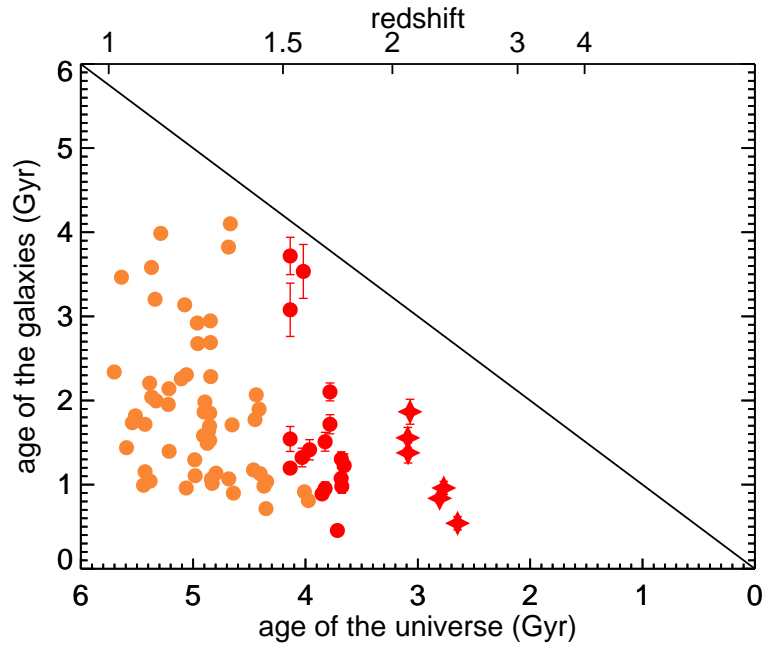


Figure 5.8 Galaxy age vs. age of the universe for the LRIS and MOSFIRE samples. The top x axis indicates the redshift at which each galaxy is observed, and the corresponding age of the universe is shown on the bottom x axis. Symbols as in Figure 5.5. The region above the solid line is unphysical, since galaxies cannot be older than the age of the universe at the corresponding redshift.

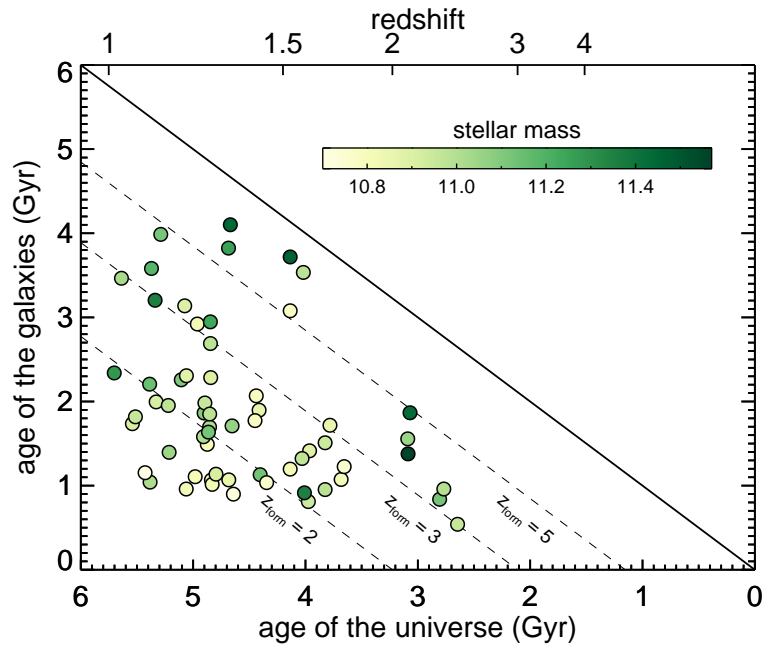


Figure 5.9 Galaxy age vs. age of the universe, color-coded according to stellar mass. Only galaxies with $M_* > 10^{10.7} M_\odot$ are shown. The dashed lines represent the traces for purely passive evolution corresponding to three formation redshifts: $z_{\text{form}} = 2, 3, \text{ and } 5$.

observations were successful, and this effect is particularly important for fainter objects with low signal-to-noise ratio, here we plot only galaxies above $10^{10.7} M_{\odot}$, which at least for the LRIS sample is a safe limit, as we showed in Chapter 4. In the figure we see a clear trend: at fixed redshift, massive galaxies tend to be older. In fact, massive galaxies tend to lie very close to the diagonal line, meaning that they are almost maximally old. On this diagram, passively evolving galaxies move on diagonal lines: we show three representative traces for three choices of formation redshifts. The most massive galaxies are consistent with a formation at $z > 5$, while intermediate-mass objects formed later, at $z \sim 2-3$.

This is the first direct spectroscopic observation of downsizing in stellar ages at $z > 1$, and is consistent with a passive evolution of the stellar population in massive quiescent galaxies since $z \sim 2$. However this does not rule out a possibly large contribution from mergers to the evolution of these objects, as long as the merging events are gas-poor (*dry* merging) and do not trigger new star formation.

5.5.2 Constraining the Recent Star Formation Activity of a Massive Galaxy at $z = 2.09$

The use of τ models is very convenient for a simple description of the star formation history of a galaxy population. However, the quality of our data allows a more detailed analysis of the past star formation activity. In order to illustrate the possibilities of our spectroscopic data, we consider COSMOS-31719, a very massive ($M_{*} \sim 10^{11.6} M_{\odot}$) object located in the $z = 2.09$ protocluster. Due to its unusual brightness, this object is ideal for a detailed study, and in fact an independent spectrum taken with VLT X-Shooter has been presented by van de Sande et al. (2013).

We start by showing the results from a τ model fit in Figure 5.10. The best-fit model is clearly a good description of both the spectrum and the photometry. The posterior distributions show an age of ~ 1 Gyr and a τ shorter than ~ 100 Myr, with little dust extinction and super-solar metallicity. We note that given the very short τ the exponentially declining model in this case is effectively a simple burst. However, this star formation history does not allow secondary bursts, and cannot simultaneously constrain the past and recent activity in an independent way. For this reason we repeat the fit using a slightly more complex star formation history, composed of a τ model and a completely independent burst. The burst is fully described by two parameters: its age and the total mass formed, which we express as a fraction of the total stellar mass of the galaxy at the observed cosmic time. The posterior distribution for these two parameters, marginalized over the τ model parameters, is shown in Figure 5.11.

There are two important results that we obtain from this simple exercise. First, we note that the age of the burst is consistent with the value obtained for a simple τ model, $t_0 \sim 1$ Gyr, and

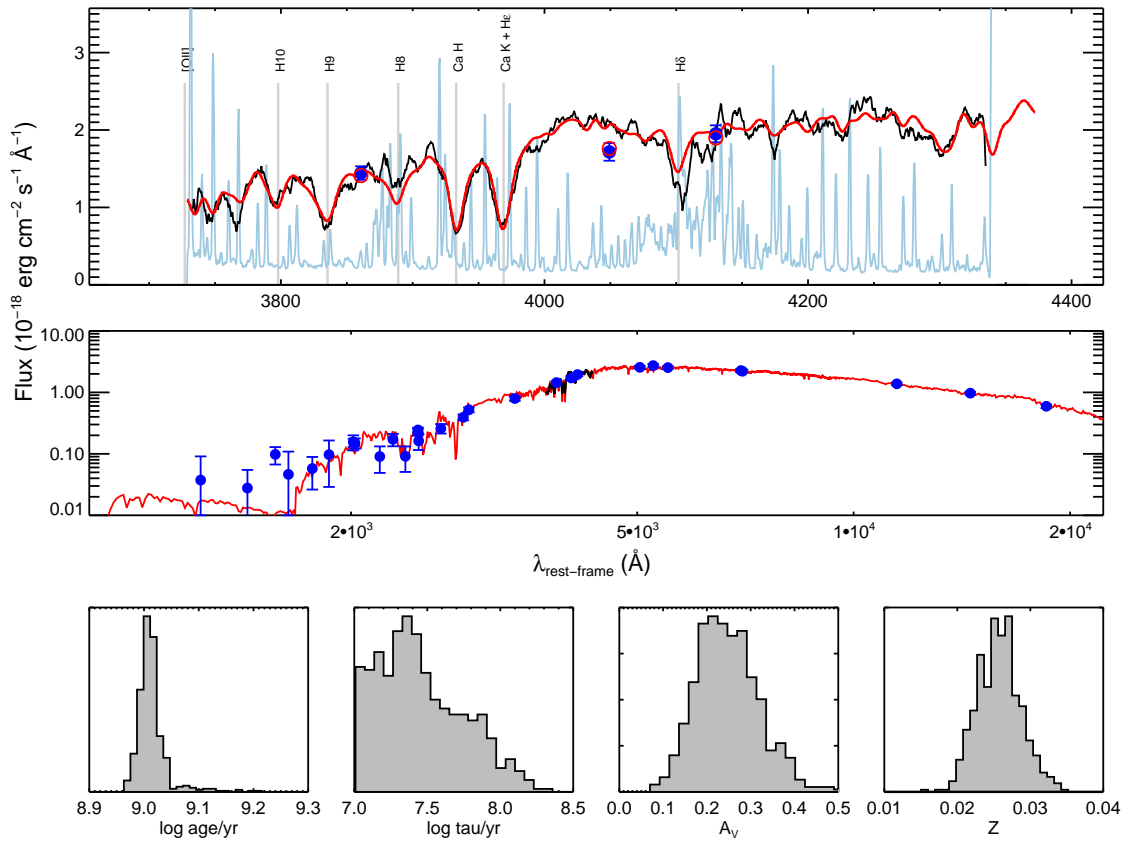


Figure 5.10 Spectral fit to COSMOS-31719. Top: MOSFIRE spectrum (black) with its observational uncertainty (cyan), and public photometric data points (blue). The most important spectral features are marked in gray. Center: Observed photometry (blue points) from the public 3D-HST catalog. In both panels, the best-fit τ model is shown in red. Bottom: Posterior distribution for age, τ , dust extinction, and stellar metallicity.

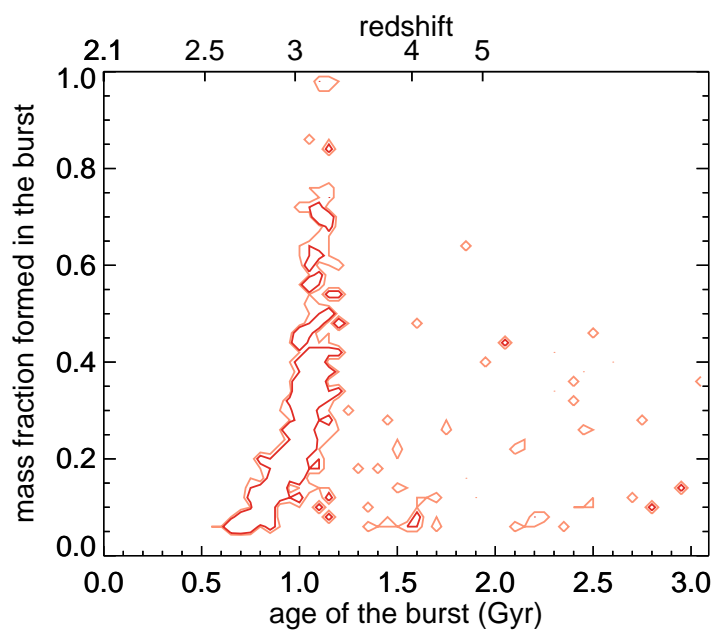


Figure 5.11 Result of fitting the combination of a τ model and a simple burst to the spectroscopic and photometric data for COSMOS-31719. The plot shows the posterior distribution for the age and intensity of the burst, measured as the fraction of the galaxy stellar mass that was formed during the burst. The top axis converts the age of the burst to the corresponding redshift, with zero coinciding with the observed value $z = 2.09$.

does not depend strongly on the burst intensity. This means that COSMOS-31719 had a star formation history that is remarkably well described by a ~ 1 Gyr old simple burst (or, equivalently, an exponentially declining model with a very short τ and $t_0 \sim 1$ Gyr). Second, even allowing an unconstrained secondary burst, we see that at most 20% of the total mass was formed in the last 800 Myr. The remaining 80% must have been formed earlier, at cosmic times corresponding to $z > 3$. This confirms the results of archaeological studies of local ellipticals, and at the same time sets a useful constraint on the timescale of the quenching mechanism. Not only such massive galaxy must have assembled its mass by $z = 2.09$, but most of its stars must have formed by $z \sim 3$, with only minor star formation continuing at later times.

One important unsolved problem related to the formation of massive quiescent galaxies is the identification of their star-forming progenitors. Since we found that the bulk of star formation for COSMOS-31719 happened at $z > 3$, when the universe was only 2 Gyr old, we can calculate a lower limit on the maximum star formation rate that the progenitor of this object must have reached at some point in the past. By dividing 80% of the stellar mass of COSMOS-31719 by 2 Gyr we obtain $160 M_{\odot}/\text{yr}$. This value is consistent with the distribution of star formation rates of compact star-forming galaxies at a similar redshift, which ranges between 10 and $350 M_{\odot}/\text{yr}$ (Barro et al., 2014a), in agreement with the idea of an evolutionary link between these two populations (Barro et al., 2013). Of course it is always possible to obtain a much larger value by choosing a shorter timescale: if most of the stars were formed over 200 Myr then the progenitor must have reached $\sim 1000 M_{\odot}/\text{yr}$, similar to the values measured for sub-millimeter galaxies, which have also been suggested as possibly being an early phase in the life of compact quiescent galaxies (Toft et al., 2014).

5.6 Summary and Discussion

We present a spectroscopic sample of 24 quiescent galaxies at $1.5 < z < 2.5$ that we observed using the new MOSFIRE multi-object near-infrared spectrograph at Keck. By targeting the rest-frame optical region these spectra allow the study of both the kinematics and the stellar populations for individual galaxies at $z > 1.5$. At this redshift, only a few individual spectra of comparable quality have been available before (Toft et al., 2012; van de Sande et al., 2013). We divided our analysis into two parts: a study of the dynamical and structural evolution; and an investigation of the stellar population properties.

In the first part, we extended our previous work (Chapter 3) started with the LRIS spectra of $1 < z < 1.6$ galaxies to higher redshift. We found that quiescent galaxies at higher redshift have larger velocity dispersions, as expected from their smaller sizes. By assuming that the velocity dispersion of a massive galaxy does not change significantly with cosmic time, we matched objects

with $\log \sigma_e > 2.40$ at high and low redshift and inferred their size and mass evolution. We showed that physical growth of individual galaxies happened at all redshifts, and by measuring the slope of growth α on the mass-size plane we found that, despite a steepening at high redshift, its value is consistent with the theoretical expectations for minor mergers even at $z \sim 2$.

Observational studies based primarily on photometric data have shown that, while at $z < 1.5$ the merger rate can explain the inferred size growth of quiescent galaxies, this may not be true at higher redshift (Newman et al., 2012). Our spectroscopic data are consistent with minor mergers driving the size growth even at $z \sim 2$, however, we note that the measurement of the slope of growth $\alpha = 2.1 \pm 0.8$ allows the possibility of a value outside the range obtained by numerical simulations of mergers. Moreover, the tentative evidence for an evolution in the stellar-to-dynamical mass ratio at $z > 1.5$ may point toward a partial change in the growth mechanism. Perhaps minor mergers are not the *only* process responsible for the size growth at $z \sim 2$.

In the second part of our analysis, we fit stellar population templates to the observed spectroscopic and photometric data, following the procedure presented in Chapter 4. We derived the ages for the population of quiescent galaxies assuming exponentially declining star formation histories. At each redshift we found a range of ages, from ~ 1 Gyr up to the age of the universe, and concluded that the population of quiescent galaxies is continuously replenished by recently quenched systems. We also detected a clear trend in which more massive galaxies are older. Our results suggest a scenario in which massive galaxies are formed at early times and then evolve passively (i.e., without new star formation). Less massive galaxies follow the same path but with a later formation epoch. This downsizing scenario is in qualitative agreement with the results of detailed studies of the stellar populations in local quiescent galaxies (e.g., Thomas et al., 2005). However, we note that most archaeological studies find much later formation epochs. For example, Choi et al. (2014) find that quiescent galaxies up to $z \sim 0.7$ are passively evolving and have ages much smaller than the age of the universe, corresponding to a formation redshift $z < 1.5$. In order to reconcile our results with the ages found in low-redshift galaxies, either new star formation or mixing due to mergers are required. Since dry merging is required to explain other aspects of galaxy evolution, including the size evolution as we showed in the first part of this study, we suggest that the ages of massive quiescent galaxies are continuously *rejuvenated* by the accretion of smaller systems which, in agreement with the downsizing picture, host much younger stars, despite being quiescent. In this scenario, our $z \sim 2$ sample contains objects that are almost maximally old because perhaps at these early times there has not been enough merging with much younger systems.

Despite the τ model being widely used for its simplicity, it is still unclear whether this assumption is appropriate for quiescent galaxies, particularly at high redshift, where a departure from the simple exponential law should have a stronger impact on the observed emission given the relatively young ages. For this reason we explored in detail the star formation history of COSMOS-31719,

a particularly massive galaxy at $z = 2.09$, for which the spectroscopic data present a high signal-to-noise ratio. By adding a simple burst on top of the τ model, we explored the possibility of a secondary peak in the star formation history. We find that adding complexity to the model does not help; in fact the result of the fit suggests that the best description of the star formation history is a simple burst with an age of 1 Gyr. By exploring the posterior distribution of the parameters describing the secondary burst, we conclude that at least 80 % of the observed stellar mass was formed by $z \sim 3$, with very little star formation activity thereafter. This result represents a powerful constraint on the quenching mechanism: models of physical processes such as merging and AGN feedback that are thought to be responsible for shutting off star formation must be able to reproduce such early formation and on such short timescales. Furthermore, because of the limited amount of time available for the formation of this object, we are able to estimate the typical star formation rate of the progenitor, which is $\sim 160 M_{\odot}/\text{yr}$, in agreement with the idea that compact star-forming galaxies are the immediate progenitors of compact quiescent galaxies (Barro et al., 2013).

Our analysis of COSMOS-31719 is an illustration of what is now possible in the study of stellar populations at high redshift. Applying the same method to larger samples will certainly help constrain the formation of massive galaxies, including understanding their progenitors and the quenching process. One caveat is that we cannot know whether the progenitor of this galaxy is just one, or perhaps the star formation happened in two or more less massive systems that then quenched and merged. This possibility of course would change the inferred star formation rate of the progenitors. However, since the timescale for major mergers is of the order of a Gyr, at this redshift it is unlikely that one or more major mergers already took place without leaving visible signs in the *HST* imaging.

Finally, we note that the lack of $\text{H}\alpha$ in emission found in our sample (see Section 5.3.4) confirms the analysis of COSMOS-31719: quiescent galaxies at $z \sim 2$ are truly passive and the amount of star formation activity is negligible. This is in agreement with studies on deep stacks of radio or infrared data at similar redshift (Fumagalli et al., 2014; Man et al., 2014). It is noteworthy that in this study we contributed with two independent lines of evidence to the emerging picture of an early formation and immediate quenching for massive galaxies.

We thank Chuck Steidel, Ian McLean, and their team for their work in producing the remarkable MOSFIRE instrument. The authors recognize and acknowledge the very significant cultural role and reverence that the summit of Mauna Kea has always had within the indigenous Hawaiian community. We are most fortunate to have the opportunity to conduct observations from this mountain.

Chapter 6

Conclusions and Future Work

Since the first spectroscopic studies of massive quiescent galaxies at $z \sim 2$ a decade ago (Cimatti et al., 2004; Glazebrook et al., 2004), much effort has been devoted to the study of these systems. Although many questions about the *formation* of this population still remain open, significant progress has been made on understanding their *evolution*. In this section we first summarize the recent observational studies, including the ones presented in this thesis, that investigated the size growth of quiescent galaxies in the last 10 Gyr. A consistent explanation for the evolution of quiescent galaxies has emerged from a variety of independent observations. We then discuss the more uncertain aspects of the formation of these systems, namely the properties of their progenitors and the nature of quenching. We conclude presenting an observational plan that, using the facilities currently available, will give us new insights on the early phases of galaxy formation.

6.1 The Growth of Massive Galaxies

Explaining the inferred growth of quiescent galaxies has been one of the main goals of extragalactic studies in recent years. After the robustness of the $z \sim 2$ observations was confirmed (Muzzin et al., 2009; Szomoru et al., 2012), two main types of explanations for the size growth have been proposed: either the compact galaxies physically grow in size, perhaps because of mergers or some puffing-up due to AGN feedback, or the inferred size evolution is due to progenitor bias, and the high-redshift red nuggets remain physically small until $z \sim 0$.

Many studies tried to compare the number density of compact galaxies at different redshifts, but they often obtained contradictory results (Trujillo et al., 2009; Taylor et al., 2010b; Carollo et al., 2013; Poggianti et al., 2013; Damjanov et al., 2014, 2015). Although this represents the most direct method to probe the size growth, there are many issues that make it extremely difficult to obtain a robust measurement. First, the various studies adopt different definitions of compactness, either in physical units or in relative terms (compared to the mass-size relation). Besides the difficulty of comparing different studies, selecting sources below a given size threshold cannot constrain the

behavior of the entire population, since there can always be size growth within the population of arbitrarily-defined compact galaxies. The second important issue is that compact galaxies are often mistaken for unresolved stars in seeing-limited surveys, such as the SDSS, with the result of an incompleteness that is difficult to quantify and that varies with redshift.

A complementary method that does not involve comparing number densities is to obtain spectroscopic data for samples of red nuggets, and to infer the size growth by using the kinematics to match galaxies at different redshifts. The technological improvement in near-infrared detectors in the last few years allowed for the first time the measurement of velocity dispersions for individual quiescent galaxies at high redshift (van Dokkum et al., 2009; Toft et al., 2012; van de Sande et al., 2013; Bezanson et al., 2013). Continuing the survey initiated by Newman et al. (2010) using the upgraded red detector on the LRIS instrument at Keck, we collected a large number of deep spectra of quiescent galaxies at $1 < z < 1.6$, which constitutes the largest sample at high redshift to date. By comparing these galaxies with the local population at fixed velocity dispersion we showed that individual quiescent galaxies grow in size and mass, thus proving that progenitor bias cannot explain the totality of the observed size evolution (see Chapter 3). Furthermore, by comparing the growth in mass with the growth in size it is possible to constrain the physical mechanism that drives the observed evolution. The measured slope of growth $d \log R_e / d \log M_*$, again derived by matching galaxies in velocity dispersion, is consistent with the theoretical expectations for minor mergers, and significantly steeper than what expected for major mergers (e.g., Nipoti et al., 2012; Hilz et al., 2013). Therefore our study indicates that the physical mechanism behind the size growth is likely minor merging. The puffing-up scenario is ruled out because it predicts an increase in velocity dispersion by a factor of two between $z \sim 2$ and $z \sim 0$ (Hopkins et al., 2010), which is not observed, together with an increase in the scatter of the mass-size relation with redshift, which is also in disagreement with the observations (e.g., Trujillo et al., 2009).

The fact that individual galaxies undergo significant size and mass growth does not necessarily exclude a contribution of progenitor bias to the observed size evolution. Using the same deep spectra, we derived reliable stellar population parameters, including the star formation history, for each object in our sample. The main result of this study (see Chapter 4) is that the ages are tightly correlated to the sizes, with larger objects being systematically younger. This is, in fact, the first direct observation of progenitor bias at high redshift: galaxies that were recently quenched tend to be larger, and will increase the typical size of the quiescent population over time. If this were the only effect in place, then we would be able to correctly predict the sizes of quiescent galaxies at $z \sim 2$ by taking the average size of all the galaxies in our $z \sim 1.25$ sample that are older than 1.5 Gyr (the cosmic time elapsed between the two redshift values). However, we obtain a size growth that is only half of the one directly observed by comparing the sizes at $z \sim 2$ with the sizes at $z \sim 1.25$. This means that progenitor bias accounts for only about half of the size growth; the remaining half

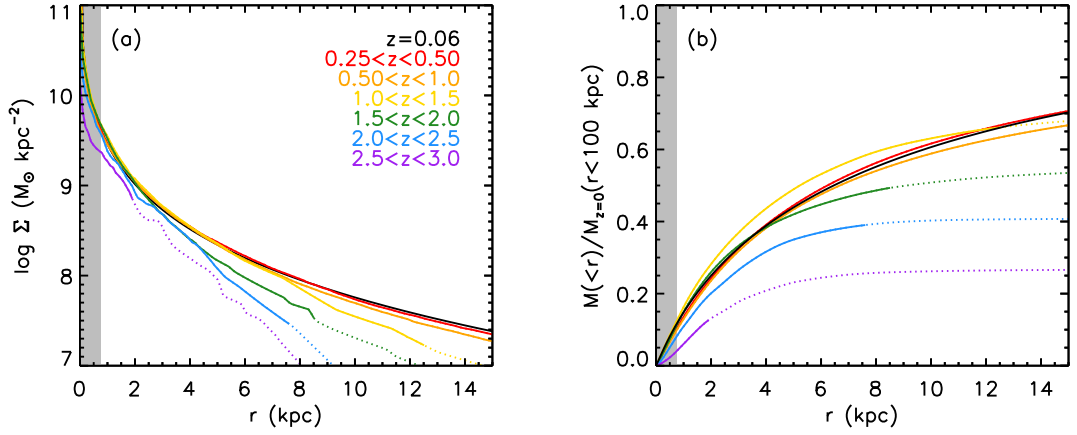


Figure 6.1 Growth of massive galaxies at fixed cumulative number density, from Patel et al. (2013). The lines show the median, mass-normalized profiles, in different redshift bins, for the galaxy population at a cumulative number density of $n_c = 1.4 \times 10^{-4} \text{ Mpc}^{-3}$, corresponding to a mass of $10^{11.2} M_\odot$ at $z = 0$. The left panel shows the stellar mass surface density, while the right panel shows the stellar mass enclosed in a given radius. The dotted parts indicate where the uncertainty on the profile is larger than 20%, and the central shaded area marks the spatial scale unresolved with *HST*.

must be due to individual galaxies that are physically getting larger, in agreement with our previous investigation.

Both studies using independent methods on the same dataset give a consistent result: the size growth of quiescent galaxies is partly due to minor mergers, and partly due to the arrival on the red sequence of larger, recently quenched systems. One independent test of this picture can be obtained by calculating whether the observed minor merger rate is sufficient to explain the size growth. Newman et al. (2012) derive the minor merger rate from the number of close pairs, and measure the redshift evolution of the mass-size relation, using the same *HST* imaging from the CANDELS survey. They conclude that, for reasonable values of merger timescales, the observed rate is high enough to explain the size growth of quiescent galaxies, at least since $z \sim 1.5$. Independent analyses of the effect of dry mergers on the size growth reached the same conclusions (Nipoti et al., 2012; Cimatti et al., 2012).

Remarkably, there is yet another confirmation of the picture presented above, from a fully independent method. With the advent of large surveys, it is now possible to obtain an accurate measurement of the galaxy stellar mass function at different redshifts (e.g., Ilbert et al., 2013; Muzzin et al., 2013). Assuming that the ranking in stellar mass is roughly preserved, it is possible to find the progenitors of a given population of local galaxies by selecting systems at constant cumulative number density. For each stellar mass value at $z = 0$, mass function studies give us the stellar mass of the corresponding main progenitor population as a function of redshift. Although this method does not account for scatter in the mass growth rate, it still gives a good approximation to what is

the true evolutionary track of a galaxy population (Leja et al., 2013). Using a cumulative number density selection, van Dokkum et al. (2010) explored the structural evolution of massive galaxies, finding that the difference between $z \sim 0$ objects and their high-redshift progenitors is only in the outer parts, while the cores are virtually unchanged. Further studies confirmed this trend (see Figure 6.1) using data from wider and higher-resolution surveys (Patel et al., 2013; Marchesini et al., 2014; van Dokkum et al., 2014). This *inside-out* growth is in excellent agreement with the theoretical expectations for minor mergers (e.g., Hopkins et al., 2009a), which are thought to add material only to the outskirts of massive galaxies. Furthermore, the growth in mass and size determined at fixed number density gives a slope $d \log R_e / d \log M_* \sim 2$ (van Dokkum et al., 2010), similar to our results obtained with a selection at constant velocity dispersion.

A consistent picture of galaxy growth driven by minor mergers is supported by observations up to $z \sim 1.5$. However, at higher redshift the inferred growth is significantly faster, and the observed merger rate might not be high enough to sustain it (Newman et al., 2012). Taking advantage of the new MOSFIRE spectrograph at Keck, we carried out another survey in the near-infrared with the aim of expanding our previous study at higher redshift (see Chapter 5). By matching massive galaxies at $1.5 < z < 2.5$ with local objects of equal velocity dispersion, we show that a significant physical growth of individual systems took place. This is the first time that such physical growth is probed at $z > 1.5$. We also calculate the slope of growth on the mass-size plane, obtaining a value that is steeper than what found at $z < 1.5$, but still consistent with the prediction of minor merger simulations.

6.2 The Formation and Quenching of the First Galaxies

Although we now have a reliable picture of the evolution of massive quiescent systems (at least for $z < 1.5$), we still know very little about the manner in which they formed. Particularly, there are two fundamental issues with important implications for models of galaxy formation: what are the progenitors of red nuggets? And what is the physical mechanism that shuts off star formation at these early cosmic epochs?

In a merger event, the size of the remnant is strongly influenced by the amount of dissipation involved (e.g., Khochfar & Silk, 2006; Hopkins et al., 2006). In order to produce compact remnants, the progenitors must be very rich in gas. Alternatively, it is also possible to produce a compact galaxy via violent disk instability, triggered by intense gas inflows (e.g., Dekel et al., 2009; Dekel & Burkert, 2014; Zolotov et al., 2015). Both major merger and disk instability activities need to be highly dissipational in order to leave a very compact remnant. This is in agreement with the observational fact that compact galaxies are only formed at high redshift, since the typical gas fraction strongly declines with cosmic time. Different formation mechanisms need not to be mutually exclusive; in

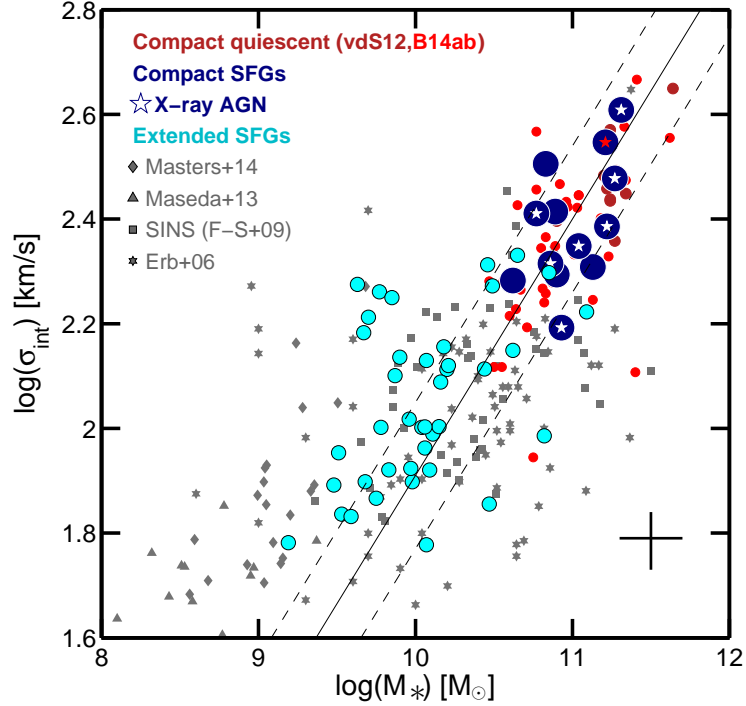


Figure 6.2 Distribution of velocity dispersions and stellar masses for star-forming galaxies at $z \sim 2$, from Barro et al. (2014b). The cyan points represent normal-size galaxies, while the blue points are compact galaxies (i.e., blue nuggets). Regular star-forming galaxies from other studies are shown in gray. The red points are quiescent galaxies (i.e., red nuggets), for which the velocity dispersions have been measured from absorption lines by van de Sande et al. (2013); Belli et al. (2014a,b). The distribution of the blue nuggets matches remarkably well the one of the red nuggets, and suggests a direct evolutionary link between these two populations.

fact, cosmological simulations suggest that there might be multiple channels for the formation of compact systems (Wellons et al., 2015).

Once a compact galaxy is formed via some gas-rich process, the star-formation needs to be shut off before a red nugget can be formed. The problem of galaxy quenching is therefore different from the issue of the compact sizes, but necessarily connected to it. The large amount of gas that collapses to the center might trigger intense star formation followed by supernova, stellar, or AGN feedback (Zolotov et al., 2015). Another possibility is that the fast growth of the bulge leads to gravitational quenching (e.g., Genzel et al., 2014b).

If the above scenario is correct, there is one straightforward prediction that is relatively easy to test: the existence of a population of *compact star-forming* galaxies at $z \sim 2$. These systems, which are the intermediate step between large gas-rich galaxies and compact quiescent objects, have been called *blue nuggets* (Barro et al., 2013). Such population has been identified in observations from wide surveys and, remarkably, its number density is approximately in agreement with the one found for red nuggets at a similar redshift (Barro et al., 2013, 2014a). Spectroscopic follow-up (Barro et al., 2014b; Nelson et al., 2014) yields velocity dispersions, as measured from emission lines, that

are much larger than the typical values for star-forming galaxies at $z \sim 2$, and match the velocity dispersions measured from absorption lines in quiescent compact galaxies, as shown in Figure 6.2. The agreement on the kinematics is an important additional clue towards the identification of blue nuggets as the immediate progenitors of red nuggets. However, comparing emission lines with the absorption lines of different systems might not give consistent results. Ideally, the velocity dispersion should be measured from both absorption and emission lines in the same system, which must be observed during the quenching phase. To date, only two such measurements have been performed (Barro et al., 2014b, 2015), and the results are still inconclusive. A different approach is to try to reconstruct the properties of the progenitor by observing the quenched population. As an illustration of this method, we showed that by accurately constraining the star formation history of a $z \sim 2$ quiescent galaxy it is possible to estimate the star formation rate of its progenitor. We found a value of $\sim 160M_*/\text{yr}$, remarkably consistent with the typical star formation rates of blue nuggets.

Sub-millimeter galaxies are another population suggested as the progenitors of red nuggets. These high-redshift systems are characterized by very large star formation rates and have been shown to be related to gas-rich mergers (e.g., Tacconi et al., 2008). Their kinematics and sizes at $3 < z < 6$ match the distributions found for massive quiescent galaxies at $z \sim 2$, and the number densities and star formation rates are also consistent with the expectations from simple models (Toft et al., 2014, see Figure 6.3). This possibility is not in contrast with the idea that blue nuggets are the progenitors of compact quiescent galaxies, as the two populations might represent different evolutionary phases and/or phases for objects of different masses, since the sub-millimeter galaxies have generally higher redshifts and masses compared to blue nuggets.

Although substantial uncertainty remains, particularly for the early phases, a coherent picture for the formation and evolution of massive galaxies is emerging from theoretical and observational studies. Massive systems form at very early cosmic times in gas-rich mergers or in disk instabilities fed by massive gas inflows; they go through a sub-millimeter and/or a blue nugget phase; they are quenched possibly because of supernova or AGN feedback, and they turn into compact quiescent galaxies. After this point, their evolution is dominated by dry minor mergers, which cause a substantial size growth, until they appear at $z \sim 0$ as massive elliptical galaxies.

Understanding the formation of the earliest quiescent galaxies is also important for testing current models based on the Λ CDM cosmology. While the downsizing in star formation has been satisfactorily explained by recent models, a possible discrepancy about the downsizing in mass assembly remains. As quiescent massive objects are photometrically detected at higher and higher redshifts (Straatman et al., 2014; Spitler et al., 2014), it is not clear whether a hierarchical formation of structure, in which the more massive dark matter halos are assembled last, can explain the observations (e.g., Steinhardt et al., 2015).

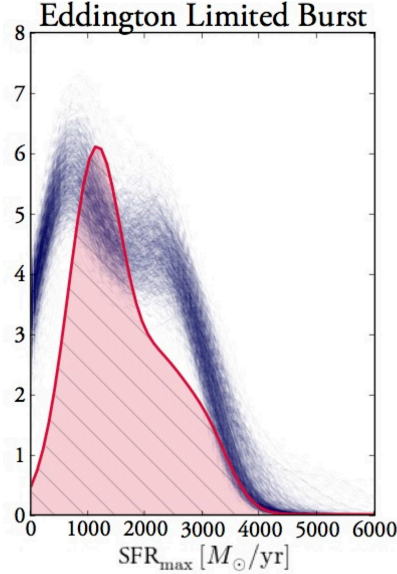


Figure 6.3 Comparison of the star formation rate distribution for sub-millimeter galaxies and compact quiescent systems, from Toft et al. (2014). Assuming that $z \sim 2$ red nuggets form in Eddington limited starbursts, it is possible to calculate the expected distribution for the star formation rate of their progenitors, which is shown in red. The blue curves are 1000 realizations of the observed star formation rate (derived from the infrared luminosity) for $z > 3$ sub-millimeter galaxies. The two distributions are in good agreement, consistent with the idea that sub-millimeter galaxies represent an evolutionary phase in the formation of compact quiescent galaxies.

6.3 Future Work

On the observational side the main way forward is to obtain increasingly deep spectra and study in detail the dynamics and stellar populations of early galaxies. Velocity dispersions can help match quenched galaxies with their progenitors, and the study of stellar populations can shed light on the quenching mechanism. For example, in our study of the LRIS sample (Chapter 4), we find evidence for two quenching paths at $z \sim 1.25$, possibly suggesting the existence of two independent physical processes responsible for quenching, as proposed by other works (e.g., Schawinski et al., 2014). Pushing these studies to even earlier epochs can put powerful constraints on models of galaxy formation, particularly considering that at $z \sim 3$ the star formation history is relatively easy to measure, since stars cannot be older than 2 Gyr. However, the largest impact on the current understanding of galaxy formation will come from new observational constraints of physical properties that have not been previously measured at high redshift. In this section, we describe our current efforts toward obtaining the first measurements of rotation velocities and stellar metallicities for red nuggets at $z > 2$.

In the local universe, massive ellipticals are typically pressure-supported, and present very little rotation (Emsellem et al., 2011). However, at high redshift there seems to be a significant fraction of

quiescent galaxies that are morphologically elongated, consistent with being dominated by a disk (van der Wel et al., 2011; Bruce et al., 2012; Chang et al., 2013). This is in agreement with some theoretical predictions for the remnants of major mergers (Wuyts et al., 2010). Clearly, a direct measure of the rotation in compact massive galaxies at $z \sim 2$ would be very helpful in constraining the formation mechanism and the properties of the progenitors. Furthermore, if rotation is indeed present, it would be a further confirmation of the fact that the subsequent evolution of these systems is far from being purely passive, since some process (perhaps minor mergers) would be needed to disrupt the disks and generate pressure-supported ellipticals at $z \sim 0$. Additionally, these observations would also have important repercussions on the interpretation of the measured velocity dispersions, which would then contain a significant component of unresolved rotation. This could help explain the far steeper slope of growth $d \log R_e / d \log M_*$ observed at $z > 2$ by matching galaxies at velocity dispersions (see Chapter 5), since the observed values of σ at these early epochs would be overestimated due to the rotational component.

Unfortunately, given the small physical sizes of quiescent galaxies at $z \sim 2$, together with the fact that spectra for these faint targets can only be obtained using large ground-based telescopes, so far it has not been possible to obtain *resolved* spectroscopic data for red nuggets. However, this can be achieved with current facilities by targeting galaxies that happen to be gravitationally lensed by foreground clusters. Strong gravitational lensing can spatially magnify the source and boost its observed flux. This technique has been extensively used to explore the properties of faint star-forming systems, and in Chapter 2 we gave an example of a near-infrared survey that was specifically designed to study emission-line spectra for lensed sources at $1.5 < z < 3$. However, at high redshift massive quiescent galaxies have a much smaller number density compared to intermediate- and low-mass star-forming galaxies, therefore the chances of a random alignment between a foreground cluster and a background red nugget are much smaller. Furthermore, quiescent galaxies are intrinsically less bright than star-forming objects, particularly in the blue and optical wavelengths, and therefore they are more difficult to find in wide surveys, that tend to be relatively shallow. Nonetheless, the first few examples of lensed massive quiescent galaxies have been recently found (Muzzin et al., 2012; Geier et al., 2013), although their faintness makes spectroscopic followup observations very challenging.

In order to investigate this important aspect of the kinematic structure of massive quiescent galaxies, we started a new survey, led by Andrew Newman, aimed at measuring rotation velocities for a few examples of $z > 2$ lensed red nuggets. We selected targets that are ideal for followup spectroscopy by systematically searching the *HST* archival images of galaxy clusters, and also by taking new Magellan imaging data. Using Keck MOSFIRE, we already observed the first target, a very massive galaxy at $z = 2.64$, shown in Figure 6.4. By positioning the slit along the axis of maximum lensing magnification, we are able to extract spectra of the galaxy from two spatially independent

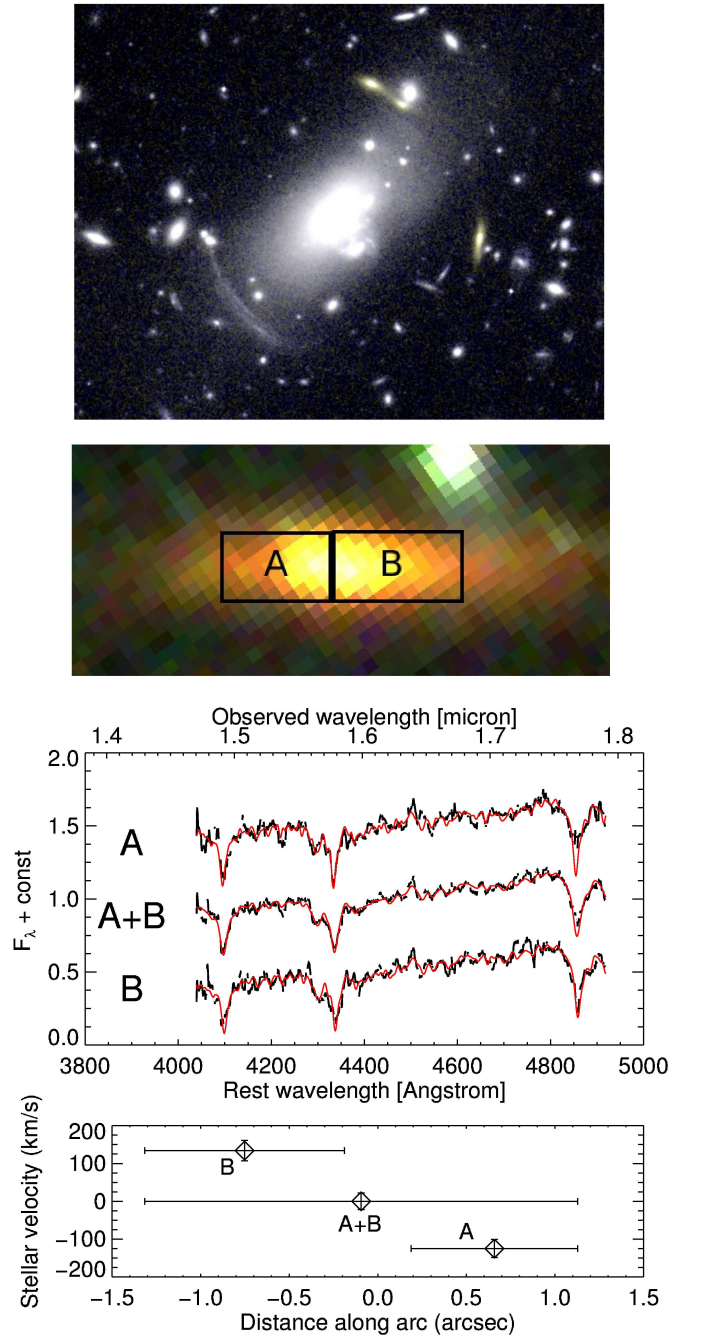


Figure 6.4 Illustration of the possibilities offered by gravitational lensing, from Newman et al. (2015, in prep.). a) *HST* image of a cluster gravitationally lensing a quiescent $z = 2.64$ galaxy. b) Strong lensing stretches the image preferentially along one direction, allowing ground-based resolved observations. c) Keck MOSFIRE spectra of the target extracted from the two apertures marked in panel b) as A and B. The red lines represent the best-fit models, from which the velocity shifts are calculated. d) Velocity shifts derived from the two apertures as a function of their spatial position. This represents the first rotation curve determined from the absorption lines of a quiescent galaxy at $z > 2$.

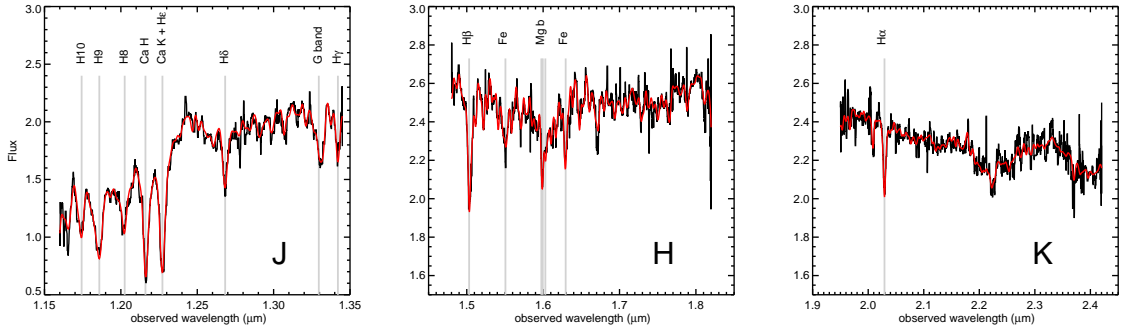


Figure 6.5 A simulated Keck NIRES spectrum with an 8-hour exposure time for a $z = 2.092$ galaxy drawn from our MOSFIRE sample (Belli et al., 2014b). The best-fit stellar model (shown in red) to the observed MOSFIRE spectrum and photometry was used to generate the simulated data (in black). The NIRES spectrograph will allow us to observe simultaneously the near-infrared J , H , and K bands, which at this redshift contain important spectral features (marked in the figure) that can be used to derive accurate measurements of the stellar metallicity.

apertures. We then measure the spectral shifts by fitting models to the spectroscopic data, and use these to make a crude rotation curve. This represents the very first velocity measurement for a quiescent system at $z > 2$. We detect a rotation of hundreds of km/s, confirming the presence of a disk in this particular quiescent galaxy. This preliminary result is clearly very promising, and suggests that our ongoing study will be able to give us meaningful constraints on the rotation of red nuggets.

Another important physical quantity that can be used to connect galaxies with their progenitors is the metallicity. The progenitors of compact quiescent galaxies must be very gas-rich, and for these systems the gas-phase metallicity is now routinely measured up to $z \sim 3$ via strong emission line ratios (e.g., see Chapter 2; Maiolino et al., 2008; Steidel et al., 2014; Sanders et al., 2015), although a substantial uncertainty on the calibrations remain. Quiescent galaxies, on the other hand, are typically gas-poor, and their spectra do not present most of the nebular lines needed for a measurement of the gas-phase metallicity. This leaves only the possibility of deriving the *stellar* abundance from fitting templates to the observed absorption-line spectra. Observations in the local universe show a clear relation between stellar metallicity and stellar mass (Gallazzi et al., 2005), similarly to what found for star-forming galaxies (Tremonti et al., 2004). However, the stellar metallicity is a proxy for the past star formation history rather than the present state of the gas. In fact, it can be used to pinpoint the duration of the starburst event (e.g., Thomas et al., 2005), and to set critical constraints on theoretical models (Muñoz & Peeples, 2015). Measuring the stellar metallicity in $z \sim 2$ massive quiescent galaxies would represent a novel, independent method to link these systems with their star-forming progenitors. At the same time, these measurements would offer a way to constrain the forward evolution, by matching high-redshift red nuggets with local ellipticals of equal metallicity.

Due to the very high signal-to-noise ratio required on the spectroscopic data, currently stellar metallicities have been measured only up to $z \sim 0.7$ (Choi et al., 2014; Gallazzi et al., 2014). In order to extend these studies to higher redshifts, extremely deep near-infrared exposures are needed. Such observations become feasible with current telescopes if one targets only the brightest galaxies, or selects gravitationally lensed sources. We are planning to obtain the first measurements of stellar metallicities at $z > 2$ by taking advantage of the wide wavelength range of NIRES, a new near-infrared instrument that is currently being installed at Keck. Featuring the same high-sensitivity detector as MOSFIRE, this spectrograph will be able to observe a single object in the J , H , and K bands simultaneously. This is critical for such study, since the observable wavelength range contains most of the metallicity-sensitive spectral features for objects at $z \sim 2$. Our simulation, shown in Figure 6.5, confirms that an ~ 8 -hour exposure will reach signal-to-noise ratios sufficiently high for a metallicity measurement with 0.1 dex precision, using the stellar population templates of Conroy et al. (2009). These measurements will open the path to a completely new method for matching galaxies at different evolutionary phases and will help us understand the processes that lead to the formation of compact massive galaxies in the early universe.

The recent development of sensitive near-infrared detectors opened up the $z \sim 2$ universe and allowed us for the first time to explore the physical properties of early massive systems. By targeting the brightest objects and taking advantage of gravitational lensing, it is now possible to constrain important properties such as rotation and stellar metallicity for $z \sim 2$ galaxies, but for only a few objects. For a comprehensive look at the galaxy population in its entirety, we need to wait for the next generation of facilities such as the James Webb Space Telescope and the 30-40 m ground-based telescopes, which will let us explore even earlier epochs, and directly observe the formation of the very first galaxies in the universe.

Bibliography

- Abazajian, K. N., et al. 2009, *ApJS*, 182, 543
- Arimoto, N., & Yoshii, Y. 1987, *A&A*, 173, 23
- Auger, M. W., Treu, T., Bolton, A. S., Gavazzi, R., Koopmans, L. V. E., Marshall, P. J., Moustakas, L. A., & Burles, S. 2010, *ApJ*, 724, 511
- Baade, W. 1944, *ApJ*, 100, 137
- Baldry, I. K., Glazebrook, K., Brinkmann, J., Ivezić, Ž., Lupton, R. H., Nichol, R. C., & Szalay, A. S. 2004, *ApJ*, 600, 681
- Baldwin, J. A., Phillips, M. M., & Terlevich, R. 1981, *PASP*, 93, 5
- Barro, G., et al. 2011, *ApJS*, 193, 13
- . 2013, *ApJ*, 765, 104
- . 2014a, *ApJ*, 791, 52
- . 2014b, *ApJ*, 795, 145
- . 2015, ArXiv e-prints
- Baum, W. A. 1959, *PASP*, 71, 106
- Bedregal, A. G., et al. 2013, *ApJ*, 778, 126
- Behroozi, P., Marchesini, D., Wechsler, R., Muzzin, A., Papovich, C., & Stefanon, M. 2013, ArXiv e-prints
- Bell, E. F., et al. 2004, *ApJ*, 608, 752
- Belli, S., Jones, T., Ellis, R. S., & Richard, J. 2013, *ApJ*, 772, 141
- Belli, S., Newman, A. B., & Ellis, R. S. 2014a, *ApJ*, 783, 117
- . 2015, *ApJ*, 799, 206

- Belli, S., Newman, A. B., Ellis, R. S., & Konidaris, N. P. 2014b, *ApJ*, 788, L29
- Bender, R., Ziegler, B., & Bruzual, G. 1996, *ApJ*, 463, L51
- Bertin, E., & Arnouts, S. 1996, *A&AS*, 117, 393
- Bertin, G., Ciotti, L., & Del Principe, M. 2002, *A&A*, 386, 149
- Bezanson, R., van Dokkum, P., & Franx, M. 2012, *ApJ*, 760, 62
- Bezanson, R., van Dokkum, P., van de Sande, J., Franx, M., & Kriek, M. 2013, *ApJ*, 764, L8
- Bezanson, R., van Dokkum, P. G., Tal, T., Marchesini, D., Kriek, M., Franx, M., & Coppi, P. 2009, *ApJ*, 697, 1290
- Bezanson, R., et al. 2011, *ApJ*, 737, L31
- Bielby, R., et al. 2012, *A&A*, 545, A23
- Blanton, M. R., Eisenstein, D., Hogg, D. W., Schlegel, D. J., & Brinkmann, J. 2005a, *ApJ*, 629, 143
- Blanton, M. R., et al. 2003, *ApJ*, 594, 186
- . 2005b, *AJ*, 129, 2562
- Bolton, A. S., Burles, S., Treu, T., Koopmans, L. V. E., & Moustakas, L. A. 2007, *ApJ*, 665, L105
- Bothwell, M. S., Maiolino, R., Kennicutt., R., Cresci, G., Mannucci, F., Marconi, A., & Cicone, C. 2013, *ArXiv e-prints*
- Bower, R. G., Lucey, J. R., & Ellis, R. S. 1992, *MNRAS*, 254, 601
- Brammer, G. B., van Dokkum, P. G., & Coppi, P. 2008, *ApJ*, 686, 1503
- Brammer, G. B., et al. 2012, *ApJS*, 200, 13
- Brinchmann, J., & Ellis, R. S. 2000, *ApJ*, 536, L77
- Bruce, V. A., et al. 2012, *MNRAS*, 427, 1666
- Bruzual, G. 1983, *ApJ*, 273, 105
- Bruzual, G., & Charlot, S. 2003, *MNRAS*, 344, 1000
- Buitrago, F., Trujillo, I., Conselice, C. J., Bouwens, R. J., Dickinson, M., & Yan, H. 2008, *ApJ*, 687, L61
- Burstein, D., Faber, S. M., Gaskell, C. M., & Krumm, N. 1984, *ApJ*, 287, 586

- Calzetti, D., Armus, L., Bohlin, R. C., Kinney, A. L., Koornneef, J., & Storchi-Bergmann, T. 2000, *ApJ*, 533, 682
- Calzetti, D., Kinney, A. L., & Storchi-Bergmann, T. 1994, *ApJ*, 429, 582
- Cappellari, M. 2002, *MNRAS*, 333, 400
- Cappellari, M., & Emsellem, E. 2004, *PASP*, 116, 138
- Cappellari, M., et al. 2006, *MNRAS*, 366, 1126
- 2009, *ApJ*, 704, L34
- 2013, *MNRAS*, 432, 1709
- Cardamone, C. N., et al. 2010, *ApJS*, 189, 270
- Carollo, C. M., et al. 2013, *ApJ*, 773, 112
- Cassata, P., et al. 2010, *ApJ*, 714, L79
- Chabrier, G. 2003, *PASP*, 115, 763
- Chang, Y.-Y., et al. 2013, *ApJ*, 773, 149
- Choi, J., Conroy, C., Moustakas, J., Graves, G. J., Holden, B. P., Brodwin, M., Brown, M. J. I., & van Dokkum, P. G. 2014, *ApJ*, 792, 95
- Christensen, L., et al. 2012, *MNRAS*, 427, 1953
- Cid Fernandes, R., Mateus, A., Sodré, L., Stasińska, G., & Gomes, J. M. 2005, *MNRAS*, 358, 363
- Cimatti, A., Nipoti, C., & Cassata, P. 2012, *MNRAS*, 422, L62
- Cimatti, A., et al. 2002, *A&A*, 381, L68
- 2004, *Nature*, 430, 184
- 2008, *A&A*, 482, 21
- Ciotti, L. 2009, *Nuovo Cimento Rivista Serie*, 32, 1
- Ciotti, L., Lanzoni, B., & Renzini, A. 1996, *MNRAS*, 282, 1
- Coe, D., Benítez, N., Broadhurst, T., & Moustakas, L. A. 2010, *ApJ*, 723, 1678
- Cole, S., Lacey, C. G., Baugh, C. M., & Frenk, C. S. 2000, *MNRAS*, 319, 168
- Conroy, C. 2013, *ARA&A*, 51, 393

- Conroy, C., Graves, G. J., & van Dokkum, P. G. 2014, *ApJ*, 780, 33
- Conroy, C., Gunn, J. E., & White, M. 2009, *ApJ*, 699, 486
- Cowie, L. L., Songaila, A., Hu, E. M., & Cohen, J. G. 1996, *AJ*, 112, 839
- Croton, D. J., et al. 2006, *MNRAS*, 365, 11
- Cushing, M. C., Vacca, W. D., & Rayner, J. T. 2004, *PASP*, 116, 362
- Daddi, E., Cimatti, A., Renzini, A., Fontana, A., Mignoli, M., Pozzetti, L., Tozzi, P., & Zamorani, G. 2004a, *ApJ*, 617, 746
- Daddi, E., et al. 2004b, *ApJ*, 600, L127
- . 2005, *ApJ*, 626, 680
- Damjanov, I., Geller, M. J., Zahid, H. J., & Hwang, H. S. 2015, *ApJ*, 806, 158
- Damjanov, I., Hwang, H. S., Geller, M. J., & Chilingarian, I. 2014, *ApJ*, 793, 39
- Damjanov, I., et al. 2009, *ApJ*, 695, 101
- Davé, R., Finlator, K., & Oppenheimer, B. D. 2011a, *MNRAS*, 416, 1354
- . 2012, *MNRAS*, 421, 98
- Davé, R., & Oppenheimer, B. D. 2007, *MNRAS*, 374, 427
- Davé, R., Oppenheimer, B. D., & Finlator, K. 2011b, *MNRAS*, 415, 11
- Dayal, P., Ferrara, A., & Dunlop, J. S. 2012, *ArXiv e-prints*
- De Lucia, G., Kauffmann, G., & White, S. D. M. 2004, *MNRAS*, 349, 1101
- De Lucia, G., Springel, V., White, S. D. M., Croton, D., & Kauffmann, G. 2006, *MNRAS*, 366, 499
- Dekel, A., & Burkert, A. 2014, *MNRAS*, 438, 1870
- Dekel, A., Sari, R., & Ceverino, D. 2009, *ApJ*, 703, 785
- Djorgovski, S., & Davis, M. 1987, *ApJ*, 313, 59
- Donley, J. L., et al. 2012, *ApJ*, 748, 142
- Dressler, A., Lynden-Bell, D., Burstein, D., Davies, R. L., Faber, S. M., Terlevich, R., & Wegner, G. 1987, *ApJ*, 313, 42

- Dressler, A., Oemler, Jr., A., Poggianti, B. M., Gladders, M. D., Abramson, L., & Vulcani, B. 2013, *ApJ*, 770, 62
- Driver, S. P., et al. 2006, *MNRAS*, 368, 414
- Drory, N., Bender, R., Feulner, G., Hopp, U., Maraston, C., Snigula, J., & Hill, G. J. 2004, *ApJ*, 608, 742
- Drory, N., Salvato, M., Gabasch, A., Bender, R., Hopp, U., Feulner, G., & Pannella, M. 2005, *ApJ*, 619, L131
- Eggen, O. J., Lynden-Bell, D., & Sandage, A. R. 1962, *ApJ*, 136, 748
- Elias, J. H., Frogel, J. A., Matthews, K., & Neugebauer, G. 1982, *AJ*, 87, 1029
- Ellis, R. S., Smail, I., Dressler, A., Couch, W. J., Oemler, Jr., A., Butcher, H., & Sharples, R. M. 1997, *ApJ*, 483, 582
- Ellison, S. L., Patton, D. R., Simard, L., & McConnachie, A. W. 2008, *ApJ*, 672, L107
- Emsellem, E., et al. 2011, *MNRAS*, 414, 888
- Erb, D. K., Pettini, M., Shapley, A. E., Steidel, C. C., Law, D. R., & Reddy, N. A. 2010, *ApJ*, 719, 1168
- Erb, D. K., Shapley, A. E., Pettini, M., Steidel, C. C., Reddy, N. A., & Adelberger, K. L. 2006a, *ApJ*, 644, 813
- Erb, D. K., Steidel, C. C., Shapley, A. E., Pettini, M., Reddy, N. A., & Adelberger, K. L. 2006b, *ApJ*, 647, 128
- Faber, S. M., & Jackson, R. E. 1976, *ApJ*, 204, 668
- Faber, S. M., et al. 2007, *ApJ*, 665, 265
- Fan, L., Lapi, A., Bressan, A., Bernardi, M., De Zotti, G., & Danese, L. 2010, *ApJ*, 718, 1460
- Fan, L., Lapi, A., De Zotti, G., & Danese, L. 2008, *ApJ*, 689, L101
- Feldmann, R., & Mayer, L. 2015, *MNRAS*, 446, 1939
- Finlator, K., & Davé, R. 2008, *MNRAS*, 385, 2181
- Förster Schreiber, N. M., et al. 2009, *ApJ*, 706, 1364
- Franx, M., van Dokkum, P. G., Schreiber, N. M. F., Wuyts, S., Labbé, I., & Toft, S. 2008, *ApJ*, 688, 770

- Franx, M., et al. 2003, *ApJ*, 587, L79
- Fumagalli, M., et al. 2014, *ApJ*, 796, 35
- Gallazzi, A., Bell, E. F., Zibetti, S., Brinchmann, J., & Kelson, D. D. 2014, *ApJ*, 788, 72
- Gallazzi, A., Charlot, S., Brinchmann, J., White, S. D. M., & Tremonti, C. A. 2005, *MNRAS*, 362, 41
- Garnett, D. R. 2002, *ApJ*, 581, 1019
- Geier, S., Richard, J., Man, A. W. S., Krühler, T., Toft, S., Marchesini, D., & Fynbo, J. P. U. 2013, *ApJ*, 777, 87
- Genzel, R., et al. 2014a, *ApJ*, 796, 7
- . 2014b, *ApJ*, 785, 75
- Glazebrook, K., et al. 2004, *Nature*, 430, 181
- Gonçalves, T. S., Martin, D. C., Menéndez-Delmestre, K., Wyder, T. K., & Koekemoer, A. 2012, *ApJ*, 759, 67
- Graves, G. J., & Faber, S. M. 2010, *ApJ*, 717, 803
- Graves, G. J., Faber, S. M., & Schiavon, R. P. 2009a, *ApJ*, 693, 486
- . 2009b, *ApJ*, 698, 1590
- Graves, G. J., Faber, S. M., Schiavon, R. P., & Yan, R. 2007, *ApJ*, 671, 243
- Grogin, N. A., et al. 2011, *ApJS*, 197, 35
- Hainline, K. N., Shapley, A. E., Kornei, K. A., Pettini, M., Buckley-Geer, E., Allam, S. S., & Tucker, D. L. 2009, *ApJ*, 701, 52
- Henry, A., Martin, C. L., Finlator, K., & Dressler, A. 2013, *ArXiv e-prints*
- Hernquist, L., Spergel, D. N., & Heyl, J. S. 1993, *ApJ*, 416, 415
- Herter, T. L., et al. 2008, in *Society of Photo-Optical Instrumentation Engineers (SPIE) Conference Series*, Vol. 7014, *Society of Photo-Optical Instrumentation Engineers (SPIE) Conference Series*
- Hilz, M., Naab, T., & Ostriker, J. P. 2013, *MNRAS*, 429, 2924
- Hopkins, P. F., Bundy, K., Hernquist, L., Wuyts, S., & Cox, T. J. 2010, *MNRAS*, 401, 1099

- Hopkins, P. F., Bundy, K., Murray, N., Quataert, E., Lauer, T. R., & Ma, C.-P. 2009a, *MNRAS*, 398, 898
- Hopkins, P. F., Cox, T. J., Kereš, D., & Hernquist, L. 2008, *ApJS*, 175, 390
- Hopkins, P. F., Hernquist, L., Cox, T. J., Di Matteo, T., Robertson, B., & Springel, V. 2006, *ApJS*, 163, 1
- Hopkins, P. F., Hernquist, L., Cox, T. J., Keres, D., & Wuyts, S. 2009b, *ApJ*, 691, 1424
- Horne, K. 1986, *PASP*, 98, 609
- Hubble, E. P. 1925, *Popular Astronomy*, 33, 252
- . 1936, *Realm of the Nebulae*
- Hunt, L., et al. 2012, *MNRAS*, 427, 906
- Ilbert, O., et al. 2013, *A&A*, 556, A55
- Ishibashi, W., Fabian, A. C., & Canning, R. E. A. 2013, *MNRAS*, 431, 2350
- Jones, T. A., Swinbank, A. M., Ellis, R. S., Richard, J., & Stark, D. P. 2010, *MNRAS*, 404, 1247
- Kajisawa, M., et al. 2011, *PASJ*, 63, 379
- Kauffmann, G. 1996, *MNRAS*, 281, 487
- Kauffmann, G., et al. 2003a, *MNRAS*, 341, 33
- . 2003b, *MNRAS*, 346, 1055
- Kelson, D. D. 2003, *PASP*, 115, 688
- Kelson, D. D., Illingworth, G. D., Franx, M., & van Dokkum, P. G. 2001, *ApJ*, 552, L17
- Kelson, D. D., Illingworth, G. D., van Dokkum, P. G., & Franx, M. 2000, *ApJ*, 531, 184
- Kennicutt, Jr., R. C. 1998, *ApJ*, 498, 541
- Kewley, L. J., Dopita, M. A., Sutherland, R. S., Heisler, C. A., & Trevena, J. 2001, *ApJ*, 556, 121
- Kewley, L. J., & Ellison, S. L. 2008, *ApJ*, 681, 1183
- Kewley, L. J., Geller, M. J., & Jansen, R. A. 2004, *AJ*, 127, 2002
- Khochfar, S., & Silk, J. 2006, *ApJ*, 648, L21
- Kodama, T., & Arimoto, N. 1997, *A&A*, 320, 41

- Koekemoer, A. M., et al. 2011, *ApJS*, 197, 36
- Kormendy, J. 1977, *ApJ*, 218, 333
- Krajnović, D., et al. 2013, *MNRAS*, 433, 2812
- Kriek, M., van der Wel, A., van Dokkum, P. G., Franx, M., & Illingworth, G. D. 2008, *ApJ*, 682, 896
- Kriek, M., van Dokkum, P. G., Labbé, I., Franx, M., Illingworth, G. D., Marchesini, D., & Quadri, R. F. 2009, *ApJ*, 700, 221
- Kriek, M., et al. 2006, *ApJ*, 649, L71
- Krogager, J.-K., Zirm, A. W., Toft, S., Man, A., & Brammer, G. 2014, *ApJ*, 797, 17
- Labbé, I., et al. 2005, *ApJ*, 624, L81
- Lara-López, M. A., et al. 2010, *A&A*, 521, L53
- Larson, R. B. 1974, *MNRAS*, 169, 229
- Law, D. R., Steidel, C. C., Erb, D. K., Larkin, J. E., Pettini, M., Shapley, A. E., & Wright, S. A. 2009, *ApJ*, 697, 2057
- Leja, J., van Dokkum, P., & Franx, M. 2013, *ApJ*, 766, 33
- Lemaux, B. C., Lubin, L. M., Shapley, A., Kocevski, D., Gal, R. R., & Squires, G. K. 2010, *ApJ*, 716, 970
- Lequeux, J., Peimbert, M., Rayo, J. F., Serrano, A., & Torres-Peimbert, S. 1979, *A&A*, 80, 155
- Lilly, S. J., Tresse, L., Hammer, F., Crampton, D., & Le Fevre, O. 1995, *ApJ*, 455, 108
- Limousin, M., et al. 2011, *ArXiv e-prints*
- Longhetti, M., et al. 2007, *MNRAS*, 374, 614
- Lord, S. D. 1992, *NASA Technical Memorandum*, 103957
- Maiolino, R., et al. 2008, *A&A*, 488, 463
- Man, A. W. S., et al. 2014, *ArXiv e-prints*
- Mancini, C., et al. 2010, *MNRAS*, 401, 933
- Mannucci, F., Cresci, G., Maiolino, R., Marconi, A., & Gnerucci, A. 2010, *MNRAS*, 408, 2115
- Mannucci, F., Salvaterra, R., & Campisi, M. A. 2011, *MNRAS*, 414, 1263

- Mannucci, F., et al. 2009, MNRAS, 398, 1915
- Maraston, C. 2005, MNRAS, 362, 799
- Marchesini, D., et al. 2014, ApJ, 794, 65
- McLean, I. S., et al. 2012, in Society of Photo-Optical Instrumentation Engineers (SPIE) Conference Series, Vol. 8446, Society of Photo-Optical Instrumentation Engineers (SPIE) Conference Series
- Mendel, J. T., et al. 2015, ApJ, 804, L4
- Mo, H., van den Bosch, F. C., & White, S. 2010, Galaxy Formation and Evolution
- Muñoz, J. A., & Peebles, M. S. 2015, MNRAS, 448, 1430
- Muzzin, A., van Dokkum, P., Franx, M., Marchesini, D., Kriek, M., & Labbé, I. 2009, ApJ, 706, L188
- Muzzin, A., et al. 2012, ApJ, 761, 142
- . 2013, ApJ, 777, 18
- Naab, T., Johansson, P. H., & Ostriker, J. P. 2009, ApJ, 699, L178
- Nelson, E., et al. 2014, Nature, 513, 394
- Newman, A. B., Ellis, R. S., Andreon, S., Treu, T., Raichoor, A., & Trinchieri, G. 2014, ApJ, 788, 51
- Newman, A. B., Ellis, R. S., Bundy, K., & Treu, T. 2012, ApJ, 746, 162
- Newman, A. B., Ellis, R. S., Treu, T., & Bundy, K. 2010, ApJ, 717, L103
- Newman, A. B., Treu, T., Ellis, R. S., & Sand, D. J. 2011, ApJ, 728, L39
- Newman, A. B., Treu, T., Ellis, R. S., Sand, D. J., Richard, J., Marshall, P. J., Capak, P., & Miyazaki, S. 2009, ApJ, 706, 1078
- Nipoti, C., Londrillo, P., & Ciotti, L. 2003, MNRAS, 342, 501
- Nipoti, C., Treu, T., Leauthaud, A., Bundy, K., Newman, A. B., & Auger, M. W. 2012, MNRAS, 422, 1714
- Noeske, K. G., et al. 2007, ApJ, 660, L43
- Oke, J. B., et al. 1995, PASP, 107, 375
- Onodera, M., et al. 2012, ApJ, 755, 26

- . 2014, ArXiv e-prints
- Oser, L., Naab, T., Ostriker, J. P., & Johansson, P. H. 2012, *ApJ*, 744, 63
- Osterbrock, D. E., & Ferland, G. J. 2006, *Astrophysics of gaseous nebulae and active galactic nuclei* (University Science Books)
- Papovich, C., et al. 2012, *ApJ*, 750, 93
- Patel, S. G., et al. 2013, *ApJ*, 766, 15
- Peng, C. Y., Ho, L. C., Impey, C. D., & Rix, H.-W. 2002, *AJ*, 124, 266
- Peralta de Arriba, L., Balcells, M., Falcón-Barroso, J., & Trujillo, I. 2013, ArXiv e-prints
- Pérez-González, P. G., et al. 2013, *ApJ*, 762, 46
- Poggianti, B. M., Moretti, A., Calvi, R., D’Onofrio, M., Valentinuzzi, T., Fritz, J., & Renzini, A. 2013, *ApJ*, 777, 125
- Posti, L., Nipoti, C., Stiavelli, M., & Ciotti, L. 2014, *MNRAS*, 440, 610
- Postman, M., et al. 2012, *ApJS*, 199, 25
- Pozzetti, L., et al. 2003, *A&A*, 402, 837
- . 2010, *A&A*, 523, A13
- Rees, M. J., & Ostriker, J. P. 1977, *MNRAS*, 179, 541
- Renzini, A. 2006, *ARA&A*, 44, 141
- Renzini, A., & Ciotti, L. 1993, *ApJ*, 416, L49
- Richard, J., Jones, T., Ellis, R., Stark, D. P., Livermore, R., & Swinbank, M. 2011, *MNRAS*, 413, 643
- Richard, J., Pei, L., Limousin, M., Jullo, E., & Kneib, J. P. 2009, *A&A*, 498, 37
- Richard, J., Pelló, R., Schaerer, D., Le Borgne, J.-F., & Kneib, J.-P. 2006, *A&A*, 456, 861
- Richard, J., et al. 2010, *MNRAS*, 404, 325
- Rigby, J. R., Wuyts, E., Gladders, M. D., Sharon, K., & Becker, G. D. 2011, *ApJ*, 732, 59
- Rockosi, C., et al. 2010, in *Society of Photo-Optical Instrumentation Engineers (SPIE) Conference Series*, Vol. 7735, *Society of Photo-Optical Instrumentation Engineers (SPIE) Conference Series*
- Sandage, A. 1972, *ApJ*, 176, 21

- Sanders, R. L., et al. 2015, *ApJ*, 799, 138
- Saracco, P., et al. 2005, *MNRAS*, 357, L40
- Savaglio, S., et al. 2005, *ApJ*, 635, 260
- Schawinski, K., et al. 2014, *MNRAS*, 440, 889
- Schlegel, D. J., Finkbeiner, D. P., & Davis, M. 1998, *ApJ*, 500, 525
- Sérsic, J. L. 1963, *Boletin de la Asociacion Argentina de Astronomia La Plata Argentina*, 6, 41
- Shapley, A. E., Coil, A. L., Ma, C.-P., & Bundy, K. 2005a, *ApJ*, 635, 1006
- Shapley, A. E., Steidel, C. C., Erb, D. K., Reddy, N. A., Adelberger, K. L., Pettini, M., Barmby, P., & Huang, J. 2005b, *ApJ*, 626, 698
- Shen, S., Mo, H. J., White, S. D. M., Blanton, M. R., Kauffmann, G., Voges, W., Brinkmann, J., & Csabai, I. 2003, *MNRAS*, 343, 978
- Singh, R., et al. 2013, *A&A*, 558, A43
- Skelton, R. E., et al. 2014, *ArXiv e-prints*
- Somerville, R. S., & Davé, R. 2014, *ArXiv e-prints*
- Speagle, J. S., Steinhardt, C. L., Capak, P. L., & Silverman, J. D. 2014, *ArXiv e-prints*
- Spitler, L. R., et al. 2012, *ApJ*, 748, L21
- . 2014, *ApJ*, 787, L36
- Springel, V., et al. 2005, *Nature*, 435, 629
- Stanford, S. A., Eisenhardt, P. R., & Dickinson, M. 1998, *ApJ*, 492, 461
- Stanford, S. A., et al. 2012, *ApJ*, 753, 164
- Steidel, C. C., et al. 2014, *ApJ*, 795, 165
- Steinhardt, C. L., Capak, P., Masters, D., & Speagle, J. S. 2015, *ArXiv e-prints*
- Straatman, C. M. S., et al. 2014, *ApJ*, 783, L14
- Strauss, M. A., et al. 2002, *AJ*, 124, 1810
- Szomoru, D., Franx, M., & van Dokkum, P. G. 2012, *ApJ*, 749, 121
- Szomoru, D., et al. 2010, *ApJ*, 714, L244

- Tacconi, L. J., et al. 2008, *ApJ*, 680, 246
- Tassis, K., Kravtsov, A. V., & Gnedin, N. Y. 2008, *ApJ*, 672, 888
- Taylor, E. N., Franx, M., Brinchmann, J., van der Wel, A., & van Dokkum, P. G. 2010a, *ApJ*, 722, 1
- Taylor, E. N., Franx, M., Glazebrook, K., Brinchmann, J., van der Wel, A., & van Dokkum, P. G. 2010b, *ApJ*, 720, 723
- Taylor, E. N., et al. 2009, *ApJS*, 183, 295
- . 2011, *MNRAS*, 418, 1587
- Thomas, D., Maraston, C., Bender, R., & Mendes de Oliveira, C. 2005, *ApJ*, 621, 673
- Toft, S., Gallazzi, A., Zirm, A., Wold, M., Zibetti, S., Grillo, C., & Man, A. 2012, *ApJ*, 754, 3
- Toft, S., et al. 2007, *ApJ*, 671, 285
- . 2014, *ApJ*, 782, 68
- Toomre, A. 1977, in *Evolution of Galaxies and Stellar Populations*, ed. B. M. Tinsley & R. B. G. Larson, D. Campbell, 401
- Tremonti, C. A., et al. 2004, *ApJ*, 613, 898
- Treu, T., Ellis, R. S., Liao, T. X., & van Dokkum, P. G. 2005a, *ApJ*, 622, L5
- Treu, T., et al. 2005b, *ApJ*, 633, 174
- Trujillo, I., Burkert, A., & Bell, E. F. 2004, *ApJ*, 600, L39
- Trujillo, I., Cenarro, A. J., de Lorenzo-Cáceres, A., Vazdekis, A., de la Rosa, I. G., & Cava, A. 2009, *ApJ*, 692, L118
- Trujillo, I., Conselice, C. J., Bundy, K., Cooper, M. C., Eisenhardt, P., & Ellis, R. S. 2007, *MNRAS*, 382, 109
- Trujillo, I., et al. 2006a, *MNRAS*, 373, L36
- . 2006b, *ApJ*, 650, 18
- Tully, R. B., & Fisher, J. R. 1977, *A&A*, 54, 661
- Vacca, W. D., Cushing, M. C., & Rayner, J. T. 2003, *PASP*, 115, 389
- . 2004, *PASP*, 116, 352

- Valdes, F., Gupta, R., Rose, J. A., Singh, H. P., & Bell, D. J. 2004, *ApJS*, 152, 251
- Valentinuzzi, T., et al. 2010, *ApJ*, 712, 226
- van de Sande, J., et al. 2013, *ApJ*, 771, 85
- van der Wel, A., Bell, E. F., van den Bosch, F. C., Gallazzi, A., & Rix, H.-W. 2009, *ApJ*, 698, 1232
- van der Wel, A., Franx, M., van Dokkum, P. G., Rix, H.-W., Illingworth, G. D., & Rosati, P. 2005, *ApJ*, 631, 145
- van der Wel, A., Holden, B. P., Zirm, A. W., Franx, M., Rettura, A., Illingworth, G. D., & Ford, H. C. 2008, *ApJ*, 688, 48
- van der Wel, A., et al. 2011, *ApJ*, 730, 38
- . 2012, *ApJS*, 203, 24
- . 2014, *ApJ*, 788, 28
- van Dokkum, P. G., & Ellis, R. S. 2003, *ApJ*, 592, L53
- van Dokkum, P. G., & Franx, M. 1996, *MNRAS*, 281, 985
- van Dokkum, P. G., Kriek, M., & Franx, M. 2009, *Nature*, 460, 717
- van Dokkum, P. G., et al. 2006, *ApJ*, 638, L59
- . 2008, *ApJ*, 677, L5
- . 2010, *ApJ*, 709, 1018
- . 2014, *ApJ*, 791, 45
- Vazdekis, A., Sánchez-Blázquez, P., Falcón-Barroso, J., Cenarro, A. J., Beasley, M. A., Cardiel, N., Gorgas, J., & Peletier, R. F. 2010, *MNRAS*, 404, 1639
- Wake, D. A., van Dokkum, P. G., & Franx, M. 2012, *ApJ*, 751, L44
- Wellons, S., et al. 2015, *MNRAS*, 449, 361
- Whitaker, K. E., Kriek, M., van Dokkum, P. G., Bezanson, R., Brammer, G., Franx, M., & Labbé, I. 2012a, *ApJ*, 745, 179
- Whitaker, K. E., van Dokkum, P. G., Brammer, G., & Franx, M. 2012b, *ApJ*, 754, L29
- Whitaker, K. E., et al. 2011, *ApJ*, 735, 86
- . 2013, *ApJ*, 770, L39

- White, S. D. M., & Frenk, C. S. 1991, *ApJ*, 379, 52
- White, S. D. M., & Rees, M. J. 1978, *MNRAS*, 183, 341
- Williams, R. J., Quadri, R. F., Franx, M., van Dokkum, P., & Labbé, I. 2009, *ApJ*, 691, 1879
- Williams, R. J., Quadri, R. F., Franx, M., van Dokkum, P., Toft, S., Kriek, M., & Labbé, I. 2010, *ApJ*, 713, 738
- Windhorst, R. A., et al. 2011, *ApJS*, 193, 27
- Woo, J., Dekel, A., Faber, S. M., & Koo, D. C. 2014, *ArXiv e-prints*
- Wuyts, E., Rigby, J. R., Gladders, M. D., Gilbank, D. G., Sharon, K., Gralla, M. B., & Bayliss, M. B. 2012a, *ApJ*, 745, 86
- Wuyts, E., Rigby, J. R., Sharon, K., & Gladders, M. D. 2012b, *ApJ*, 755, 73
- Wuyts, S., Cox, T. J., Hayward, C. C., Franx, M., Hernquist, L., Hopkins, P. F., Jonsson, P., & van Dokkum, P. G. 2010, *ApJ*, 722, 1666
- Wuyts, S., et al. 2007, *ApJ*, 655, 51
- . 2011, *ApJ*, 738, 106
- Yan, R., Newman, J. A., Faber, S. M., Konidaris, N., Koo, D., & Davis, M. 2006, *ApJ*, 648, 281
- Yates, R. M., Kauffmann, G., & Guo, Q. 2012, *MNRAS*, 422, 215
- Yesuf, H. M., Faber, S. M., Trump, J. R., Koo, D. C., Fang, J. J., Liu, F. S., Wild, V., & Hayward, C. C. 2014, *ApJ*, 792, 84
- Yuan, T.-T., Kewley, L. J., & Richard, J. 2013, *ApJ*, 763, 9
- Zahid, H. J., Bresolin, F., Kewley, L. J., Coil, A. L., & Davé, R. 2012a, *ApJ*, 750, 120
- Zahid, H. J., Dima, G. I., Kewley, L. J., Erb, D. K., & Davé, R. 2012b, *ApJ*, 757, 54
- Zahid, H. J., Kewley, L. J., & Bresolin, F. 2011, *ApJ*, 730, 137
- Zirm, A. W., et al. 2007, *ApJ*, 656, 66
- Zolotov, A., et al. 2015, *MNRAS*, 450, 2327